INVESTIGATION OF IMPACT FACTORS FOR PERMIT VEHICLES

CONTRACT NUMBERS: BD543 (FDOT) and 020555 (FSU)

DRAFT FINAL

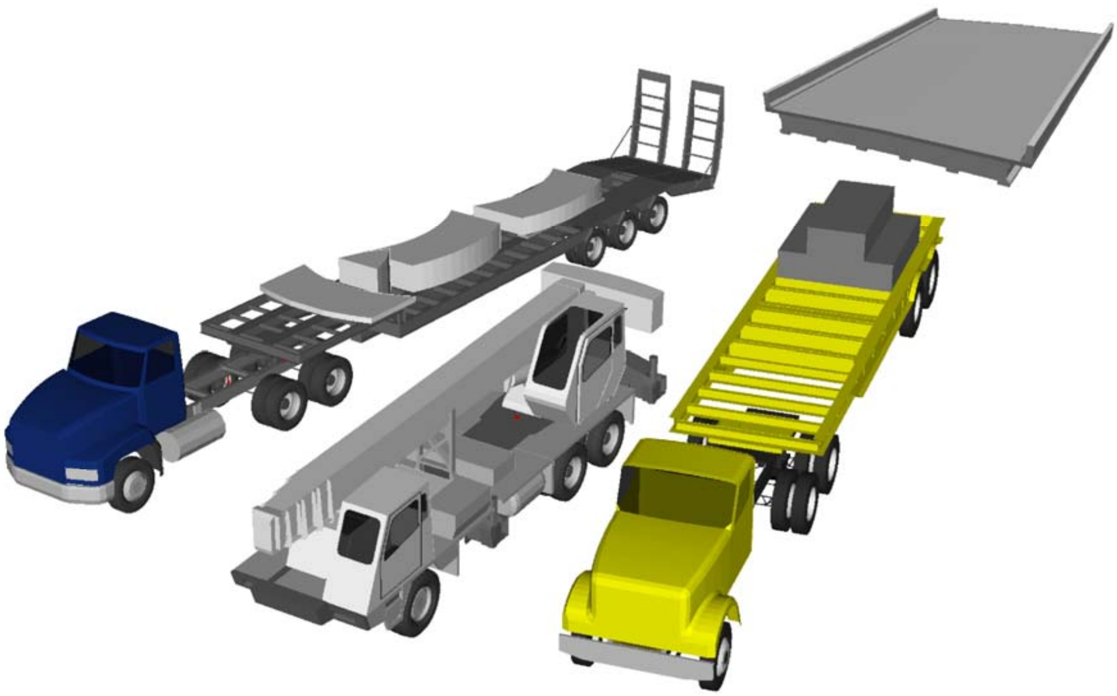

Submitted to:
Mr. Marc Ansley, PE
FDOT Structures Design Office

by
Jerry Wekezer, Ph.D. P.E., Principal Investigator
Piotr Szurgott, M.S.
Leslaw Kwasniewski, Ph.D.
Jeff Siervogel, B.S.

Tallahassee, December 2008

DISCLAIMER

The study described in this final report was supported by a contract from the Florida Department of Transportation titled: "Investigation of Impact Factors for Permit Vehicles", contract number BD543, work order number 15. Opinions, findings and views expressed in this report are those of the writers and not necessarily those of the sponsoring agency.

CONVERSION TABLES

Table 1. Approximate conversions to US Customary Units

Symbol	When You Know	Multiply by	to Find	Symbol
		LENGTH		
mm	millimeters	0.039	inches	in
m	meters	3.28	feet	ft
m	meters	1.09	yards	yd
km	kilometers	0.621	miles	mi
		AREA		
mm^2	square millimeters	0.0016	square inches	in^2
m^2	square meters	10.764	square feet	ft^2
m^2	square meters	1.195	square yards	yd^2
ha	hectares	2.47	acres	ac
km^2	square kilometers	0.386	square miles	mi^2
		VOLUME		
mL	milliliters	0.034	fluid ounces	fl oz
L	liters	0.264	gallons	gal
m^3	cubic meters	35.314	cubic feet	ft^3
m^3	cubic meters	1.307	cubic yards	yd^3
		MASS		
g	grams	0.035	ounces	oz
kg	kilograms	2.202	pounds	lb
Mg (or "t")	megagrams (or "metric ton")	1.103	short tons (2000 lb)	T
		FORCE and PRESSURE or STRESS		
N	newtons	0.225	poundforce	lbf
kPa	kilopascals	0.145	poundforce per square inch	lbf/in^2

Table 2. Approximate conversions to SI Units

Symbol	When You Know	Multiply by	to Find	Symbol
		LENGTH		
in	inches	25.4	millimeters	mm
ft	feet	0.305	meters	m
yd	yards	0.914	meters	m
mi	miles	1.61	kilometers	km
		AREA		
in^2	square inches	645.2	square millimeters	mm^2
ft^2	square feet	0.093	square meters	m^2
yd^2	square yard	0.836	square meters	m^2
ac	acres	0.405	hectares	ha
mi^2	square miles	2.59	square kilometers	km^2
		VOLUME		
fl oz	fluid ounces	29.57	milliliters	mL
gal	gallons	3.785	liters	L
ft^3	cubic feet	0.028	cubic meters	m^3
yd^3	cubic yards	0.765	cubic meters	m^3
		MASS		
oz	ounces	28.35	grams	g
lb	pounds	0.454	kilograms	kg
T	short tons (2000 lb)	0.907	megagrams (or "metric ton")	Mg (or "t")
		FORCE and PRESSURE or STRESS		
lbf	poundforce	4.45	newtons	N
lbf/in^2	poundforce per square inch	6.89	kilopascals	kPa

ACKNOWLEDGEMENTS

This study was completed under direction and in cooperation with Mr. Marc Ansley, the Project Manager and a Director of the FDOT Structures Laboratory. All experimental tests were professionally conducted by Marc Ansley, Stephen Eudy, William Potter and Paul Tighe from FDOT Structures Lab at Broadmoor Estate (speed bump calibration and testing) and on the bridge #500133 over Mosquito Creek on US 90. The guidance, comments, advice, and technical support provided by this group of professionals are highly appreciated.

Dr. Hongyi Li participated in the initial phase of the project working on the final element model of a heavy crane. Cezary Bojanowski, a Ph.D. candidate in the Department of Civil and Environmental Engineering, provided his support and advice in development of finite element models of heavy vehicles and in LS-DYNA analyses during this project. The authors are grateful for their assistance.

EXECUTIVE SUMMARY

The main purpose of this project was to develop numerical models of the heavy vehicle applicable for transient analysis of dynamic vehicle-bridge interaction. Two completely new FE models of a tractor-trailer and a crane were developed and validated. Validation included checking the mass distribution and determining a spring constant and a damping coefficient of the suspension systems.

Afterwards, FE models of heavy vehicles were used for analysis of their dynamic interaction with the bridge FE model. This analysis reflected a full scale experimental test carried out on the actual bridge. Results obtained by both methods were compared; their conformity is quite good for most cases. Therefore, existing FE models of the vehicle and the bridge can be successfully used in further multi-variant analysis instead of conducting expensive and time consuming experimental tests.

The dynamic load allowance (impact factor) was determined based on data obtained from the experimental tests and FE analysis as well. An influence of the vehicle velocity on the impact factor was considered. In addition, an assessment of the influence of railing barriers on bridge strength and its behavior under dynamic interaction with the crossing vehicle were performed using FE analysis.

TABLE OF CONTENTS

LIST OF FIGURES

Chapter 2

Chapter 3

Chapter 4

Chapter 5

Chapter 6

Chapter 7

Chapter 8

LIST OF TABLES

Chapter 1

Chapter 4

Chapter 5

Chapter 6

Chapter 7

Chapter 8

Technical Report Documentation Page

1. Report No.	2. Government Accession No.	3. Recipient's Catalog No.
FDOT BD543		

4. Title and Subtitle	5. Report Date
INVESTIGATION OF IMPACT FACTORS FOR PERMIT VEHICLES	December 31, 2008
	6. Performing Organization Code
7. Author(s) Jerry Wekezer (PI), Piotr Szurgott, Leslaw Kwasniewski, Jeff Siervogel	8. Performing Organization Report No.
9. Performing Organization Report No. FSU Project number 020555 Crashworthiness and Impact Analysis Laboratory FAMU-FSU College of Engineering	10. Work Unit No. (TRAIS) 11. Contract or Grant No.
12. Sponsoring Agency Name and Address Florida Department of Transportation 605 Suwannee Street, MS Tallahassee, FL 32399	13. Type of Report and Period Covered Draft Final 01/01/2007 – 12/31/2008 14. Sponsoring Agency Code

15. Supplementary Notes

16. Abstract

The major goal of this project was to develop numerical models of several heavy permit vehicles for subsequent transient analysis of dynamic vehicle-bridge interaction. Two completely new finite element (FE) models of a tractor-trailer and a crane were developed and validated. Validation process included checking for the correct mass distribution, and determining spring constants and damping coefficients of the suspension systems.

Developed FE models of heavy vehicles were used for analysis of their dynamic interaction with the bridge FE model. This analysis reflected a full scale experimental test carried out on the actual bridge. Results obtained by both methods were compared with good correlation between analytical and experimental results. Therefore, the FE models of the vehicle and the bridge developed can be successfully used in further multi-variant analysis instead of conducting expensive and time consuming experimental tests.

Dynamic load allowance (or: impact) factors were determined based on data obtained from the experimental tests and FE analysis as well. An influence of the vehicle velocity on the impact factor was considered. In addition, an assessment of the influence of railing barriers on bridge strength and its behavior under dynamic interaction with the crossing vehicle were performed using FE analysis and LS-DYNA computer code.

17. Key Word	18. Distribution Statement
Finite element analysis, LS-DYNA, vehicle - bridge interaction, dynamic interaction.	

19. Security Classif. (of this report)	20. Security Classif. (of this page)	21. No. of Pages	22. Price
Unclassified.	Unclassified.	244.	

Form DOT F 1700.7 (8-72) Reproduction of complete page authorized

1. INTRODUCTION

1.1. Problem Statement

This project responds to the FDOT mission, which calls for providing "… a safe transportation system that ensures the mobility of people and goods…" making travel in Florida safer and more efficient. According to the 2020 Florida Transportation Plan, Safety and System Management including bridge repairs and replacements (operation and maintenance) will cost about 30 percent of all state and federal revenues between 2003 and 2020. Therefore, knowledge of the actual load effects and structure resistance is necessary. This information can be very helpful for determination of the load carrying capacity and condition of structures. Moreover, it can help to make management decisions, such as establishing permissible weight limits, and can have important economic and safety implications. Advanced structural analysis and evaluation procedures can also be applied to structures with behavior that is difficult to explain, such as excessive vibration, deflection, and others.

Very often, the evaluation of bridges on the basis of traditional inspection methods and simplified static analysis is difficult or even impossible. The dynamic nature of live loads and vehicle-bridge interaction is not sufficiently considered in the design process. Impact factors suggested by bridge design codes usually lead to conservative solutions, especially for overloaded vehicles. Accurate and inexpensive methods are needed for diagnostics and verification of the actual dynamic effects of the bridges and the impact factors.

Traditional bridge analysis is based on several simplifications of geometry, material models, boundary conditions and loading. Bridge live load is considered as one of the most questionable simplifications. The interaction between a vehicle and bridge structure is usually represented by concentrated and uniformly distributed static loads. Dynamic effects of the actual live loads are considered by scaling static loads by impact factors. The magnitude of the dynamic load allowance (impact factor) is usually determined based on the simplifications and is related only to the length of the bridge, without reference to the bridge surface roughness and the dynamic characteristics of the vehicles.

The increasing computational capability of computers and development of commercial finite element programs allows for more advanced numerical, 3-D dynamic analysis of bridge structures. Nowadays, it is possible to create more detailed three dimensional models of bridges containing a large number of finite elements with consistent stiffness and mass distribution. Commercial software offers advanced material models for steel and concrete, rebar options for modeling of reinforcement, application of different types of constraints, and damping options allowing for more accurate descriptions of actual bridge behavior. On the other hand, there are finite element models of different vehicles, including trucks, available in the public domain. These models are ready to use, with different levels of detailed representation for suspension systems, kinematical characteristics of vehicle components and wheel models. After improvements, they can be used successfully for simulation of truck passes through the bridge structure. Application of these models would allow consideration of complex mechanical phenomena, such as contact between wheels and pavement surface, impact forces caused by surface discontinuities, and time dependence of moving live loads caused by dynamic interaction among suspended masses representing vehicle components. Actual live loads caused by overloaded heavy vehicles can also be modeled.

1.2. Research Objective

Emphasis of the current project emphasis was placed on the development of numerical models of the heavy vehicle applicable for transient analysis of dynamic vehicle-bridge interaction. Such a model provides a reliable approximation of dynamic loading exerted by the wheels on the bridge. It is expected that the procedure developed here would be easily adaptable for a wide range of heavy vehicles with different gross vehicle weights (GVW), suspension characteristics, and speeds. Full scale suspension tests were carried out to develop and validate of the spring and damping characteristics for all suspension systems of the vehicle models. During the experimental tests, a heavy vehicle was driven across a speed bump at different speeds. Relative displacement and acceleration histories were collected for several points located on axles and frame. Afterwards, these tests were reflected in numerical simulations based on non-linear, explicit, dynamic, finite element (FE) computational mechanics using the LS-DYNA computer code.

Three different heavy vehicles were taken into consideration for this research. Selection of the test vehicles was determined by the following criterion: the heaviest vehicle permitted for crossing a selected bridge in conjunction with a relatively small outer bridge length which is defined as distance from the steering axle to the last axle of the vehicle. This assumption allows obtaining the maximum load of the bridge span because the total weight of the vehicle is concentrated on a short distance.

In addition to suspension testing, experimental testing of selected vehicles was conducted on bridge #500133 on US 90 over Mosquito Creek. The finite element model of this bridge was already developed and validated under the previous BD 493 contract. The first span of the bridge was instrumented with strain gages and displacement sensors, and accelerometers glued to the bridge slab. Several accelerometers were attached also to the test vehicle. This experimental testing provided strain, deflection and acceleration histories for selected runs used later on for validation of the FE models.

The results have been documented in Monthly Progress Reports and this Final Report submitted to the FDOT. Conclusions and practical recommendations for further tests and analysis are presented in Chapter 9.

1.3. Research Tasks

The following research tasks proposed for the study:

- Task 1 — Literature Review
- Task 2 — Survey of Selected Surface Irregularities
- Task 3 — FE Bridge Model
- Task 4 — Suspension Testing for Selected Heavy Vehicles
- Task 5 — Development of FE Models of Heavy Vehicles with Suspension Systems
- Task 6 — Bridge Testing
- Task 7 — FE Analysis and Validation
- Task 8 — Monthly Reports and Final Report
- Task 9 — Milestone Meetings

Research activities by task as of December 18, 2008 are presented in Table 1.1.

Table 1.1. Research activities by task

	1 Jan	2 Feb	3 Mar	4 Apr	5 May	6 Jun	7 Jul	8 Aug	9 Sep	10 Oct	11 Nov	12 Dec	13 Jan	14 Feb	15 Mar	16 Apr	17 May	18 Jun	19 Jul	20 Aug	21 Sep	22 Oct	23 Nov	24 Dec	% Completion
Task 1: Literature review	4	4	4	4	4	4	4	4	4	4	4	4	4	4	4	4	4	4	5	5	5	5	4	4	100
Task 2: Survey of selected surfaces		15	20						15					25		25									100
Task 3: FE bridge model					20	20											60								100
Task 4: Suspension testing												20	10	40					30						100
Task 5: FE models of heavy vehicles										30	20				30	20									100
Task 6: Bridge testing																		30	70						100
Task 7: FE analysis and validation															15	15			20	20	20	10			100
Task 8: Monthly and final reports	3	3	3	3	3	3	3	3	3	3	3	3	3	3	3	3	3	3	3	12	12	10	6	3	100
Task 9: Milestone meeting								20				30						50							100

2. LITERATURE REVIEW

Literature relevant to the current work has been reviewed continuously throughout the whole project. The review focused on the following: AASHTO specification of bridge dynamic effect, FE modeling of bridges and vehicles, suspension testing and vehicle-bridge interaction.

2.1. Bridge Dynamic Effect in AASHTO Specification

Highway bridges are subjected to dynamic influences by vehicles driving over them. They can result in deterioration of bridges that increases maintenance costs and decreases their working life (Green & Cebon, 1997). Therefore, the dynamic effects are should be taken into consideration when evaluating existing bridges or designing new ones. An impact factor (now called dynamic allowance) is frequently used to assess the dynamic effects of wheel loads on bridges. These effects can result from the two following sources:

– hammering effect or dynamic response of the wheel assembly to riding surface discontinuities such as deck joints, cracks, potholes and delaminations,

– dynamic response of the whole bridge to passing vehicle.

In AASHTO (American Association of State Highway and Transportation Officials) standard specifications for highway bridges (AASHTO Standard Specifications for Highway Bridges, 2002), the impact factor is expressed as the increment of the static response of the wheel load and is determined by the formula:

$$I = \frac{50}{L + 125} \tag{2.1}$$

where L = the length (feet) of the portion of the span that is loaded to produce the maximum stress in the member.

Equation (2.1) is based on field tests and theoretical analysis for specific trucks. It is not clear if the equation can be used for bridges subjected to oversized and overweight vehicles. Therefore, this research is being conducted to accurately evaluate the wide range of bridge dynamic responses using advanced numerical methods and to determine the actual impact factor.

2.2. FE Modeling of Bridges

There are several levels of bridge models in use for studying dynamic response. With regard to interaction effects and changing contact points between wheels and deck, there are no close solutions when the truck is modeled as a vibrating system including mass and elasticity (Baumgaertner, 1998).

In some cases, bridges are modeled as simple or continuous beams. The beam analogy is relatively efficient if the bridge is straight, non-skewed and symmetric about the centerline with large length to width ratio, uniform stiffness and mass distribution, and symmetric loads. However, a beam model excludes the torsional and transverse modes, which in reality can be excited when the truck does not travel along the centerline of the bridge.

Grillage models (see Figure 2.1) allow for better approximation of the response of a slab since both flexural and torsional stiffness are taken into account. This model was determined to be a suitable analytical tool for bridge analysis (Tan, Brameld, & Tambiratnam, 1998). Figure 2.7 shows a grillage element and a grillage model of a bridge.

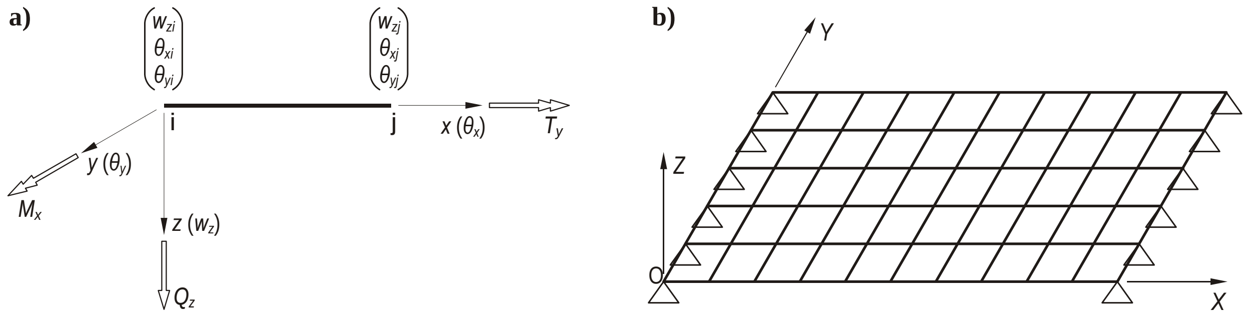

Figure 2.1. Grillage model: a) a single grillage element, b) grillage model of bridge

The model is made up of a series of discrete elements, including longitudinal beams (girders) and transverse elements (diaphragms). The elements are connected at joints where loads and constraints can be applied. The stiffness and spacing of girders were determined so that the deflection of the model and the actual bridge were the same. The more girders are used, the more accurate results can be achieved. However it will increase computation time. Today with the increasing computing power, the number of elements is no longer a major limit. It is possible to develop detailed three dimensional FE models with a large number of elements.

More and more frequently, commercial FE programs are used for modeling of complex civil structures in detail and more accurately. The Federal Highway Administration and the National Crash Analysis Center have focused on developing highly realistic and detailed numerical models of highway bridges to conduct health monitoring (Marzougui, Jin, & Livingston, 2001). By the FE method, some key features in a bridge can be accurately modeled compared with the analytical method. These features include component geometry, constitutive material models, component connections, boundary conditions, and dynamic loading conditions.

In a simplified analytical model, some structural components have been ignored, which is the major reason to explain the significant discrepancy between the results of the analytical model and the real response of the bridge. The precise geometry of the concrete deck, girders and cross members has a direct impact on the overall dynamic response of a bridge. Because all the components in FE models are modeled with a large number of shell and solid elements rather than beam elements, the bridge characteristics like mass, inertia, center of gravity and stiffness of structural components are more accurately represented. The detailed 3D model can also predict the buckling and torsional deformation of structural components.

When the bridge is subjected to extreme traffic loads, it is possible for the bridge to undergo nonlinear response, either locally or globally due to plastic deformation, time varying dependency of materials and aging degradation. Commercial FE codes provide many material models which can describe the nonlinear properties of materials and provide the opportunity to define a curve relating stress and strain.

Connections between components such as bolts and welds in a bridge can be correctly modeled in an FE model. LS-DYNA, 3D explicit FE software, provides several options to model the connections with failure.

The superstructure of a bridge is connected to the piers through rollers and bearing pads. Each roller limits the relative translational motion between the girder and the pier. The bearing device allows for translation motion along the longitudinal direction of the bridge girder. In an FE model, all these supports can be modeled with their real geometry and by applying an appropriate material model. An exemplary FE model of a bridge in shown in Figure 2.2.

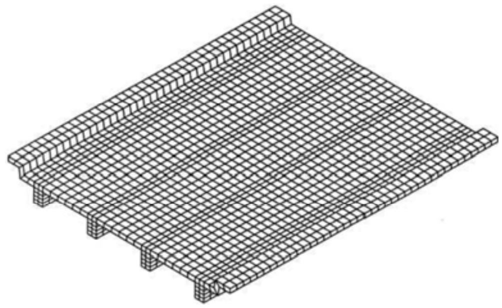

Figure 2.2. 3D finite element model of the bridge (Tedesco, Stallings, & El-Mihimy, 1999)

2.3. FE Modeling of Vehicles

There are several different approaches for vehicle modeling, with different levels of complexity. Analytical vehicle models are simple for mathematical convenience but consist of the most essential elements of the vehicle such as the body, wheels and suspension systems. Bodies are commonly represented by masses subjected to rigid body motions. Suspensions are assumed to be the combination of springs and dampers dissipating energy during oscillation. The simplest two-dimensional analytical models are depicted in Figure 2.3. In the first case, the body is modeled with a rigid bar while the suspension unit is composed of a spring and a damper (Yang & Lin, 1995). Further simplification can be achieved by using lumped masses at the ends of the bar with the rotation degrees of freedom excluded (Yang, Chang, & Yau, 1999).

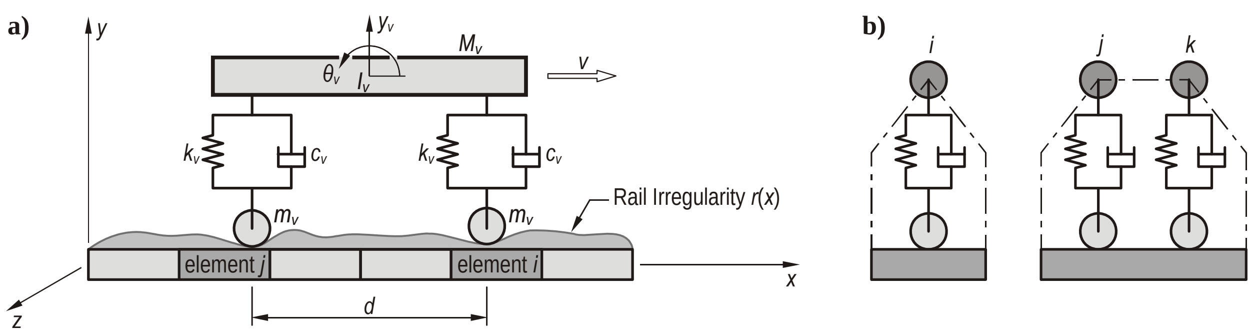

Figure 2.3. Simple analytical vehicle models (Yang & Lin, 1995), (Yang, Chang, & Yau, 1999)

A three dimensional vehicle model (see Figure 2.4) is slightly more complex. It is modeled as a rigid chassis subjected to rigid body motions including pitching and rolling rotations (Tan, Brameld, & Tambiratnam, 1998). There are a total of seven degrees of freedom in this model: vertical displacement at the chassis center, pitching and rolling rotation about the two axles of the chassis, and four vertical displacements at each of its axle locations. The tires (wheels) are modeled as point followers with springs under the axles. Suspension systems are represented by springs with a nonlinear relationship between load and deflection.

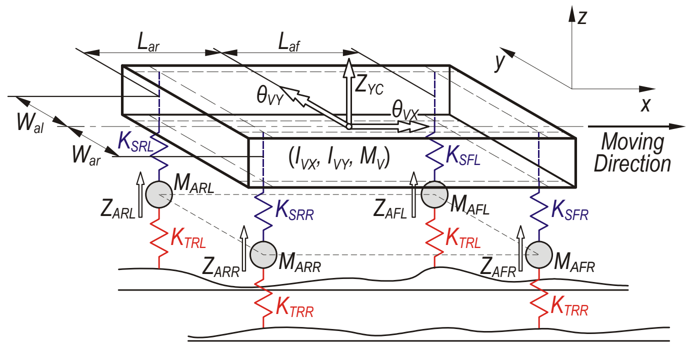

Figure 2.4. Three dimensional analytical vehicle models (Tan, Brameld, & Tambiratnam, 1998)

An analytical model of an AASHTO HS20-44 truck with 11 degrees of freedom was used by Florida International University and the Florida Department of Transportation to evaluate the dynamic response of highway girder bridges (Wang, Huang, Shahawy, & Huang, 1996). This model is illustrated in Figure 2.4. The nonlinear vehicle model comprises five rigid bodies, which represent the tractor, semi-trailer, steer-wheel-axle set, tractor-wheel-axle set and trailer-wheel-axle set. The tractor and semi-trailer are each assigned 3 degrees of freedom corresponding to vertical displacement, pitching and rolling. Two degrees of freedom in rolling and vertical displacement are assigned to each wheel-axle set. The tractor and the semi-trailer are connected at the pivot point. The suspension system is modeled with springs and dampers. Similar models to that described above can be found in the literature (Valášek, Stejskal, Šika, Vaculín, & Kovanda, 1998), (Letherwood & Gunter, 2001).

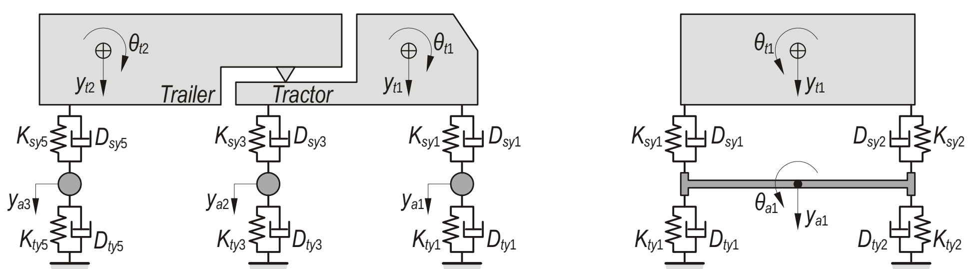

Figure 2.5. Analytical model of an AASHTO HS20-44 truck (Wang, Huang, Shahawy, & Huang, 1996)

An analytical model is treated as a multi-body system and is convenient for studying the vehicle-bridge interaction theoretically. However, the number of degrees of freedom is limited for mathematical convenience. More and more frequently, MBS models are developed in commercial software, e.g. ADAMS (Lehtonen, 2005), (Previati, Gobb, & Mastinu, 2007). Most of parts in such models are assumed to be rigid, except for the tires. In addition, MBS software allows modeling complicated transmission, suspension systems, etc. using appropriate modules available in the database.

The next step in the vehicle modeling is finite element modeling. Very often, FE models are available in public domains and ready to use. They consist of most structural components with different levels of detailed representation for suspension systems, kinematical characteristics of components and wheel models with airbags applied. Such models are developed for crashworthiness analysis mostly. Therefore, some additional modifications are necessary before they would be applied for simulation of the vehicle-bridge interaction. Exemplary FE models available on-line (Finite Element Model Archive, 2008) are presented in Figure 2.6.

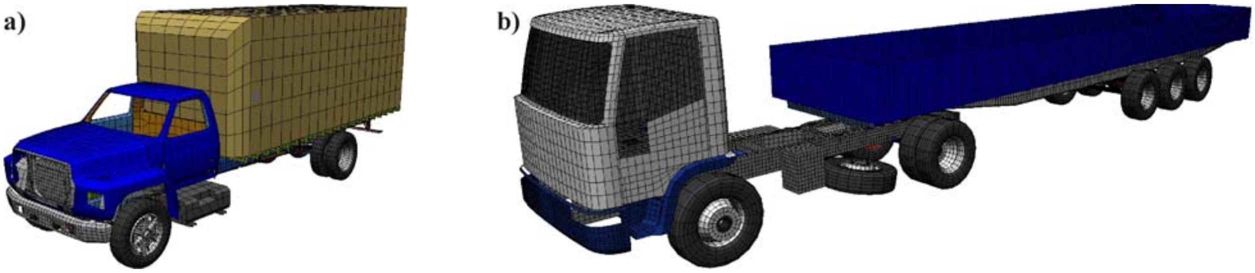

Figure 2.6. Finite element models available in public domain (Finite Element Model Archive, 2008): a) Ford single unit truck FE model, b) heavy goods vehicle FE model (developed by CM/E Group)

2.4. Suspension Testing

Characteristics of the vehicle suspension can be determined through experimental compression tests conducted either on an isolated suspension system (Marzougui, Zink, Zaouk, Kan, & Bedewi, 2004) or indirectly through field experiments conducted on an entire vehicle (Valášek, Stejskal, Šika, Vaculín, & Kovanda, 1998), (Previati, Gobb, & Mastinu, 2007), (Lehtonen, 2005), (Letherwood & Gunter, 2001). The purpose of each test is to determine a spring constant k and a damping coefficient c of the suspension. The first method is expensive as it requires removal of the suspension from the existing vehicle or a purchase of a new one. Velocity of the piston of the shock absorber is measured and recorded as a function of the load applied. This relationship is non-linear and is usually simplified by piecewise linear functions. Idealized, perfectly fixed boundary conditions in direct suspension testing do not account for sometimes worn out and partially loose connections between the suspension and the vehicle. In addition, testing of a new suspension system will often result in different suspension characteristics as compared with those in actual and used vehicles.

In the indirect method the tests are conducted on an entire vehicle which moves along predefined road surface profiles with different loads and at different speeds. Typical data acquisition from such tests usually includes time histories of accelerations and relative displacements between selected points. Filtered experimental output is analyzed and used for validation of analytical or numerical models. The first approximation of the suspension characteristics can also be obtained for some of the technical solutions using a simplified formula developed by the automotive industry. Such formulas allow for calculation of linear stiffness of leaf spring suspension based on dimensions of leaves and their number. The disadvantage of the indirect method is the difficulty in measuring dynamic interaction forces between suspension components or between wheels and the road surface.

Literature search led to several publications describing procedures used for the indirect method of vehicle suspensions testing. Different types of vehicles were considered including: a platform truck (Valášek, Stejskal, Šika, Vaculín, & Kovanda, 1998), agricultural tractors (Previati, Gobb, & Mastinu, 2007), (Lehtonen, 2005), military tactical trucks (Letherwood & Gunter, 2001), etc. Tests and simulations in each of these cases were performed for different types of obstacles. Sometimes, such obstacles (called a calibrated bump) are used for correlation studies between the test and simulation (Edara, Shih, Tamini, Palmer, & Tang, 2008). The suspension parameters in the FE model are adjusted until simulation data is matched with experimental results.

The vehicle speeds were varied between 10 and 30 mph. Accelerators were mostly placed on the axles to determine the time when the truck was driven over the bump. Displacement sensors were also used to measure relative displacement between the chassis and the axle. Results of suspension tests from the literature are presented in Fig.5 as an example.

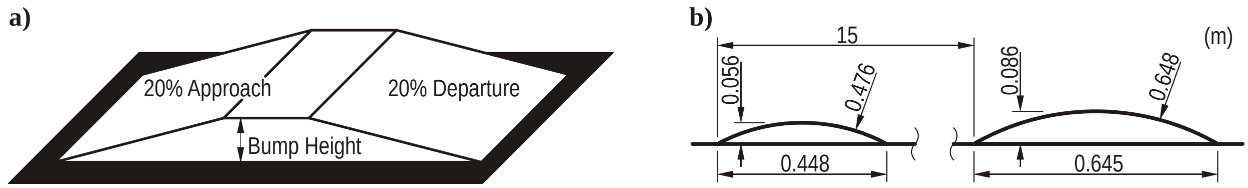

Figure 2.7. Different types of obstacles (bumps) used in the suspension tests for following vehicles: a) heavy 5-axle tactical military truck (Letherwood & Gunter, 2001), b) agricultural tractor (Lehtonen, 2005)

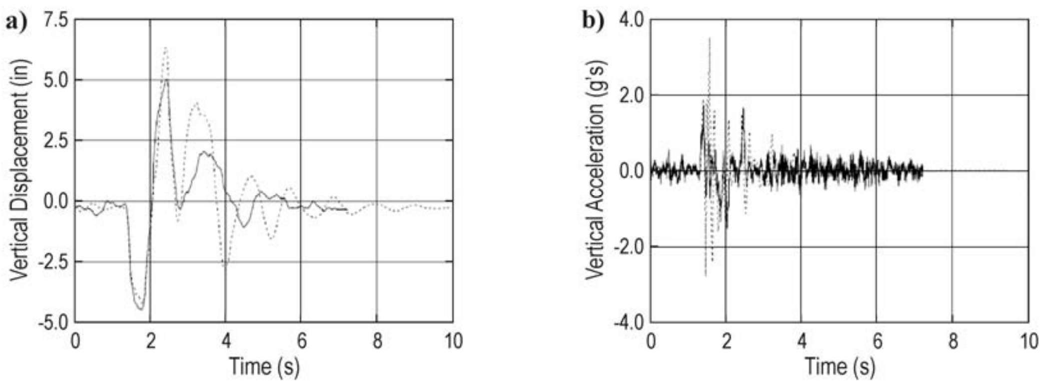

Figure 2.8. Comparison between the results from field tests (continuous line) and numerical simulation (dashed line) for the front axle of the heavy 5-axle tactical military truck driven over 18 inch high bump (Figure 2.7) at velocity of 12 mph: a) vertical displacement, b) acceleration (Letherwood & Gunter, 2001)

2.5. Vehicle-Bridge Interaction

Once the analytical models of the bridge and vehicle are developed, the direct method used to conduct interaction analysis is to formulate the governing equations of motion. The vehicle has contact points with the bridge deck and maintains that contact as it moves along the deck. For example, for a spring mass system moving along the bridge deck, two equations of motion have to be formulated. The first equation represents the dynamic equilibrium of the bridge; the second equation is for the dynamic equilibrium of the spring mass system. The interaction force between the pavement and the spring mass system depends upon the deck displacement. Hence the two equations are coupled and need to be solved simultaneously. The system governing equations are nonlinear because of the physical characteristics of the system and the components.

Henchi, Fafard, Talbot and Dhatt (1998), give two ways to simulate the vehicle-bridge interaction, as depicted in Figure 2.9.

Today’s large nonlinear finite element programs allow for effective modeling of the dynamic behavior of bridge structural system. In Baumgaertner (1998), the bridge and the truck are modeled separately to simulate three different situations. In the first case, the truck is running on the rough road before reaching the bridge. In the second one, the truck is crossing the bridge with a rough surface. In the third, the truck has left the bridge and the bridge is in a free vibrating state.

In Marzougui, Jin and Livingstonn (2001), the bridge was modeled in detail in LS-DYNA while the moving traffic flow was simplified by using concentrated nodal forces with appropriate load curves. The pressure due to tire contact with the road surface is assumed to act at the centerline of the tire and move at the same speed as the vehicle. Load curves are assigned to the nodes in the path of the vehicle motion. This simulation did not include the effects of the vehicle suspension system. The same method is also used in Tedesco, Stallings and El-Mihimy (1999).

Many similar models are discussed and used to study the dynamic interactions between vehicles and bridges in Green and Cebon (1997), Zaman, Taheri and Khanna (1996), and Das, Dutta and Talukdar (2004).

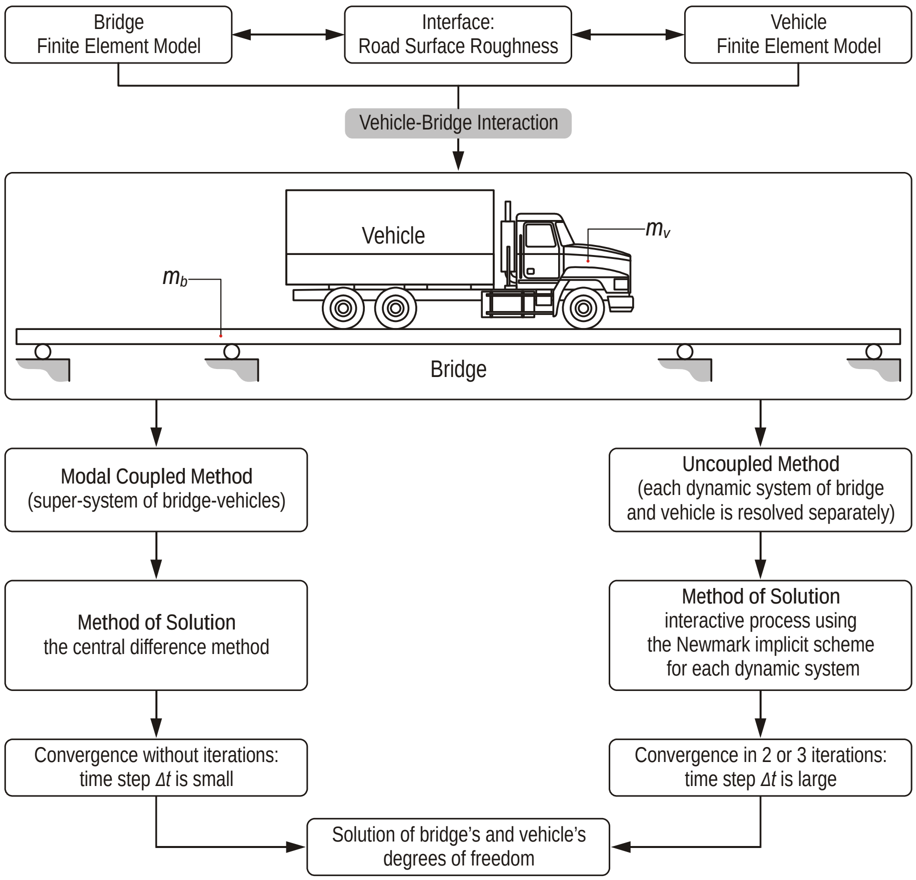

Figure 2.9. Dynamic analysis procedures of vehicle and bridge interaction.

3. SELECTION OF OBJECTS FOR THE TESTS

3.1. Selection of the Bridge

The main objective of the project was to conduct experimental tests on a relatively new highway bridge in Florida. Hence, bridge #500133 was considered for this study. It is a 3-span bridge with two lanes of traffic, as presented in Figure 3.1. It was built over Mosquito Creek in 1999 on US 90, just to the east of Chattahoochee (Figure 3.2). The total length of the bridge is 65.1 m (213'-7"); each span is 21.7 m (71'-2.33") long and 14.15 m (46'-5.09") wide. Each span of the bridge consists of six AASHTO type III prestressed girders, which are simply supported and spaced at 2.4 m (7'-10.5"). The concrete slab is cast as continuous. The bridge structure is still in good condition without any significant deterioration. However, the bridge approach is characterized by a slight depression which may have an influence on the bridge's behavior when driving over it. In addition, a protrusion on the boundary of the asphalt pavement and concrete bridge (Figure 3.3) may cause additional vibration on the bridge structure.

The elevation of the bridge and its typical cross-section are depicted in Figure 3.4 and Figure 3.5, respectively.

Figure 3.1. The bridge #500133 over Mosquito Creek used for the field tests

Figure 3.2. Localization of the tested bridge (Google Maps, 2008)

Figure 3.3. Bridge approach depression and a protrusion on the boundary of asphalt pavement and concrete slab

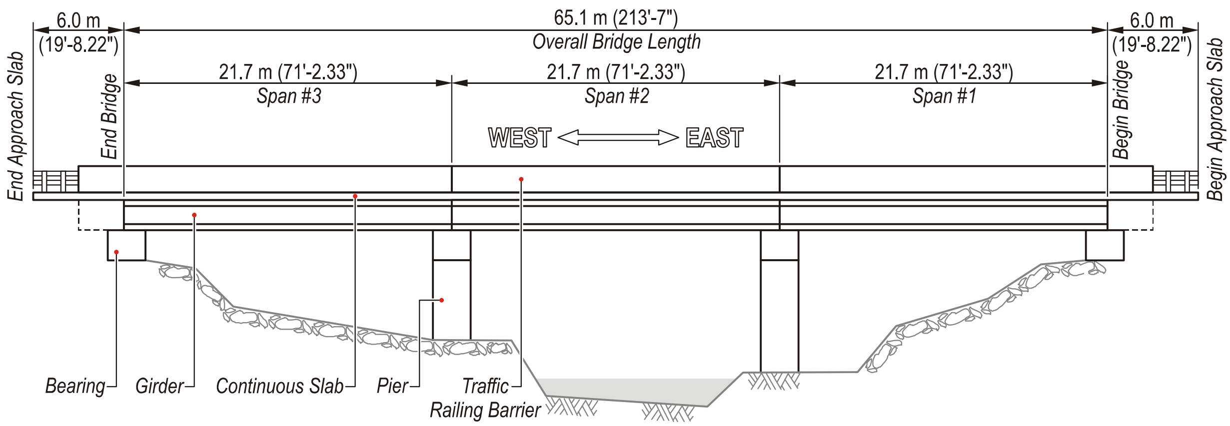

Figure 3.4. Elevation of the tested bridge

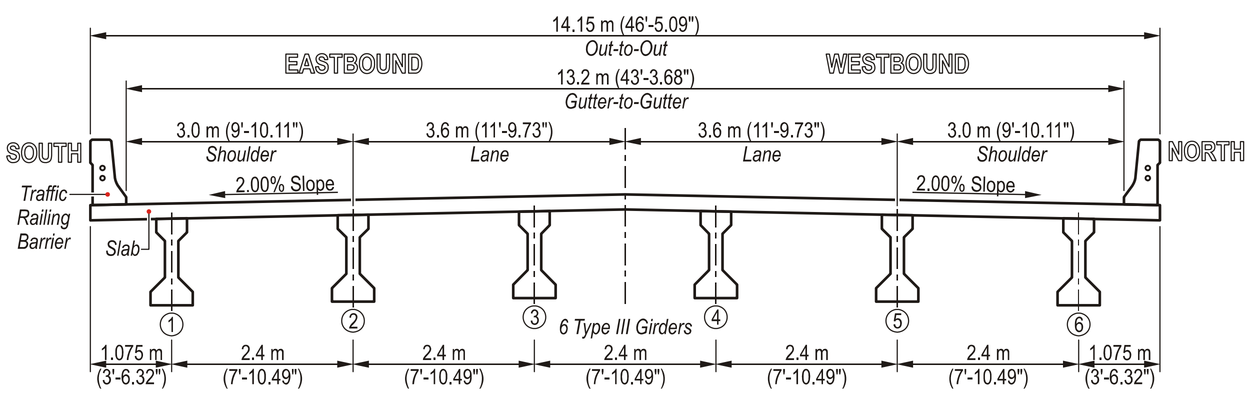

Figure 3.5. Bridge cross-section

3.2. Selection of the Vehicles

Three different heavy vehicles were selected and used during the tests. They are shown with their overall dimensions in Figure 3.6. Selection of the tested vehicle was determined by the following criteria – the heaviest vehicle permitted for crossing the bridge #500133 in conjunction with a relatively small outer bridge length which is defined as distance from the steering axle to the last axle of the vehicle. This assumption allows obtaining the maximum load of the bridge span because the total weight of the vehicle is concentrated on a short distance. The considered bridge belongs to the group of short span bridges; therefore it was quite difficult to select the appropriate vehicle for the tests.

Based on information obtained from the FDOT Permit Office the gross weights of the heaviest vehicles permitted for crossing the bridge #500133 were 90,265 kg, 89,358 kg, and 77,111 kg (199,000 lb, 197,000 lb and 170,000 lb). All vehicles had large outer bridge length—31.1 m, 29.3 m, and 26.8 m (102", 96", and 88")—and multiple axles – 11, 10, and 9, respectively. This information was taken into consideration during the selection of the vehicle. It was decided to choose a truck tractor hauling a loaded lowboy trailer. Another group of vehicles which meets above-mentioned criteria is the cranes. Therefore, a three axle mid-size crane was also used in the tests. The Terex T-340 crane, as well as the truck tractor with the single drop lowboy trailer, was rented from the Jackson-Cook, LC Company. In addition, the FDOT truck was tested to compare current results with those from the previous project (Wekezer, Li, Kwasniewski, & Malachowski, 2004).

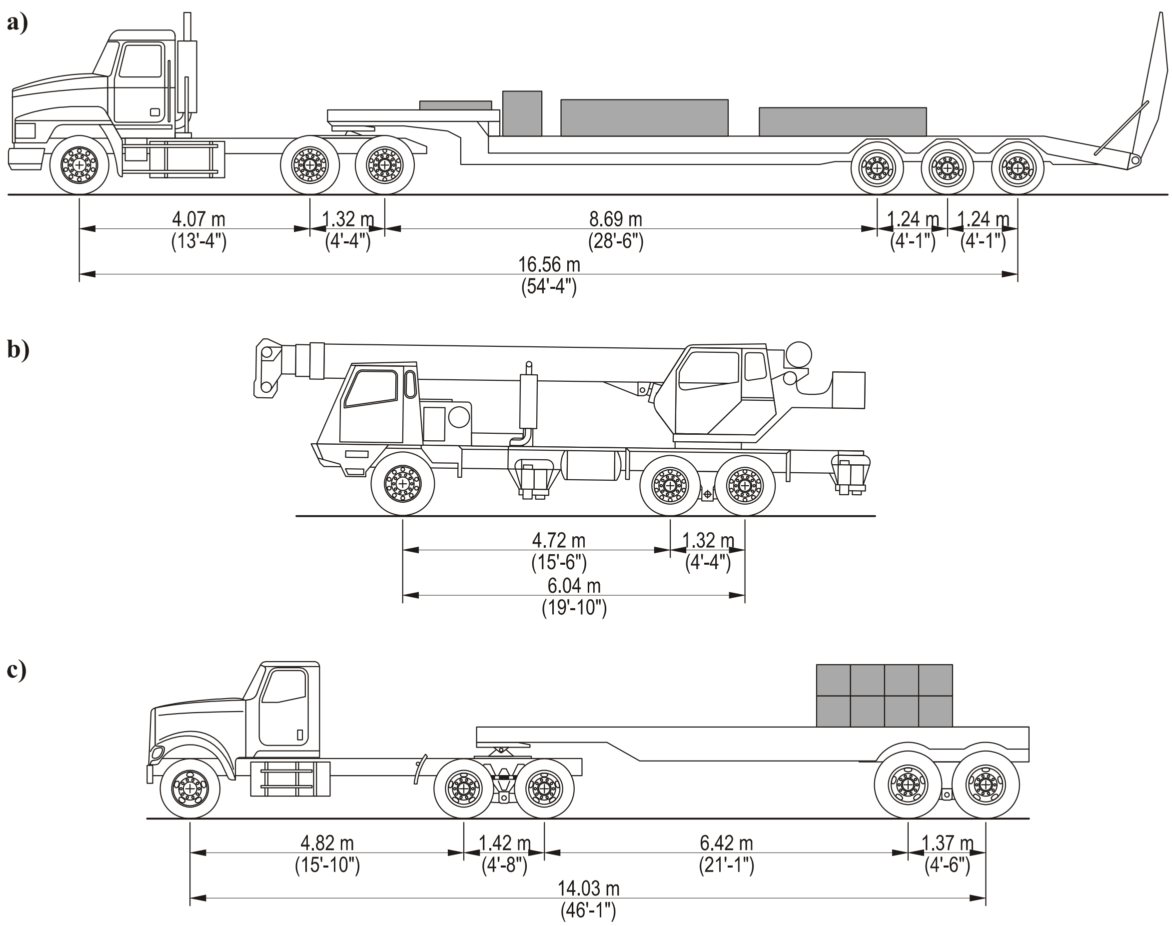

Figure 3.6. Configurations, axles spacing and outer bridge lengths of the heavy vehicles used in the tests: a) truck tractor with a single drop lowboy trailer, b) Terex T-340 crane, and c) FDOT truck

Tractor-Trailer

The first of the tested vehicles was Mack CH613 truck tractor with a three axle single drop lowboy trailer (Figure 3.7), and with a total weight of 53 tons (117,000 lb). This vehicle was fully suspended and was the heaviest one used during the tests. Additional cargo (counterweights taken from a heavy crane) was placed evenly on a load deck of the trailer.

Figure 3.7. Mack CH613 truck tractor with a three axle single drop lowboy trailer used in the tests

Terex T-340 Crane

A three axle mid-size crane, Terex T-340 (Figure 3.8), was the last heavy vehicle used in the bridge tests. Its total mass during testing was 27.7 tons (61,000 lb). It included an auxiliary boom head and other addition components. It was equipped with a simple suspension system including leaf springs and shocks in the front and walking beams with no springs in the rear.

Figure 3.8. The Terex T-340 three axle crane used in the tests

FDOT Truck

The FDOT truck, as shown in Figure 3.9, used in the current project was a later version of the vehicle tested in the previous one. Major differences were associated with the truck tractor only. They included different axle spacing and a new fully suspended driver cab. The trailer remained the same, as well as the number of concrete blocks used for loading. Both tandem axles, in the rear of the truck and in the trailer, were equipped with walking beams. Such suspension results in more even load distribution for each axle. Moreover, the suspension system of the trailer was very stiff. It did not include any springs or shock absorbers, thereby resulting in the most severe impact loading on the bridge.

Figure 3.9. The FDOT truck tractor and the trailer used in the tests

3.3. Selection of a Testing Track

The primary objective of the this research was to develop representative and reliable FE models of two heavy vehicles mentioned in the previous sub-chapter – the truck tractor with the trailer and the mid-size crane. Therefore, some experimental tests were necessary to provide approximate data on spring stiffness and damping coefficients implemented in the FE models. Vehicles usually drive over a different type of obstacle or at a special testing track during such tests. Accelerations and displacements for selected points located on the tested vehicle are compared with corresponding values from computational analysis allowing validating the suspension model.

It was decided to use an existing speed bump as the obstacle for the tests in this project. An appropriate test track was selected on the basis of following criteria:

- safety during the test with heavy vehicles (testing track was supposed to be located at a gated area),
- close proximity to Tallahassee, to save money and time,
- a long, straight and flat section of a road, which allowed for developing desirable vehicle speed.

A former trailer park, also known as old Broadmoor Estate in Tallahassee, was selected for the test. It met all criteria mentioned above and additionally it had several one-foot width speed bumps which could be used in the tests.

4. DEVELOPMENT OF THE FE MODELS

Two completely new FE models of heavy vehicles were developed for the current project. Necessary geometric data were taken from original blueprints and drawings, and datasheets available on manufacturer websites, but some of them were also collected from direct measurements. Additionally, FE models of speed bumps and bridge approach depression were developed from on-site laser scanning. The three dimensional FE model of the bridge was exactly the same as the model used in the previous project, *Analytical and Experimental Evaluation of Existing Florida DOT Bridges* – FDOT Project No. BD493 (Wekezer, Li, Kwasniewski, & Malachowski, 2004). Moreover, the FE model of the FDOT truck used earlier in the BD493 project was adopted and slightly modified for the current project.

Altair HyperMESH was used as a preprocessor for developing all the FE models from geometric data (HyperMesh 8.0 User's Guide, 2007). Several developer tools and options make this software very convenient for creating and modifying geometric objects for further FE analyses. The objects were then meshed either automatically or manually with several meshing blocks for one-, two- and three-dimensional objects. Complete FE models were exported as a key file with the LS-DYNA preferences.

The FE models were subsequently developed using the LS-PrePost program (LS-PrePost Online Documentation, 2008) in which all necessary parameters including boundary conditions, element properties, material properties, solution type, and many others were defined. An updated key file was used as an input deck for LS-DYNA solver. The latest available version 971 of the LS-DYNA was used for the FE analysis (LS-DYNA Keyword User's Manual, 2007). Preliminary analyses, including simulations with the isolated FE models of the vehicles, were performed on 8 GB workstation with 4 Dual-Core processors. A 32-node cluster was used when a large number of finite elements and long real time analyses were required for a complete vehicle-bridge interaction studies.

The LS-PrePost is an interactive and commonly used post-processor for the LS-DYNA. It was used to read the binary plot files generated by the LS-DYNA analysis code. LS-PrePost allows plotting contours, time histories, and deformed shapes as well. It also allows for database processing, including filtering, mathematical operations, etc.

All dimensions and material properties declared in the FE model were expressed in SI units. One of the sets of consistent units presented in the LS-DYNA User's Manual was used for current analysis (Table 4.1). All material properties applied in the FE models, and the model summaries, were provided in Appendix A.

Table 4.1. Sets of units adopted for FE analysis in this study (LS-DYNA Keyword User's Manual, 2007)

Length unit	Time unit	Mass unit	Force unit	Stress unit
millimeter (mm)	*second* (s)	*megagram* (Mg)	*Newton* (N)	*megapascal* (MPa)

4.1. Development of a FE Model for the Bridge

A finite element (FE) model of the bridge being considered was developed during the previous FDOT project: *Analytical and Experimental Evaluation of Existing Florida DOT Bridges* – FDOT Project No. BD493 (Wekezer, Li, Kwasniewski, & Malachowski, 2004). Geometric data was extracted from blueprints provided by the FDOT. The following five structural components of a single bridge span were developed as parts of its FE model: a slab, traffic railing barriers, AASHTO type III beams, diaphragms, and neoprene pads. Three types of bars were used as reinforcement in the bridge structure (see Table 4.2).

Table 4.2. Nominal dimensions of the ASTM standard reinforcing bars used in the bridge structure (Nawy, 2005)

Bar Size Designation	Mass (kg/m) / (lb/ft)	Diameter (mm) / (in)	Area (mm^2) / ($in.^2$)
10M	0.785 / 0.527	11.3 / 0.445	100 / 0.155
15M	1.570 / 1.055	16.0 / 0.630	200 / 0.310
20M	2.355 / 1.582	19.5 / 0.768	300 / 0.465

The dimension of most finite elements and location of nodes in the FE model were determined by the location of the reinforcement, requirements for contact between tires and top surface of the deck, and a total number of elements. Detailed description of the FE model of each structural component follows.

The bridge model was verified and validated in the previous project (Wekezer, Li, Kwasniewski, & Malachowski, 2004). Behavior of the girder FE model subjected to prestress forces was checked at the beginning of the validation process. The next step was to determine a static response of the bridge FE model and to compare it with experimental data. The last element of the bridge model validation consisted of verifying of natural frequencies and modes from LS-DYNA implicit algorithm as compared with experimental field test measurements.

Summary of the complete FE model of one span of the bridge is provided in Table 4.3. Parts, elements and nodes were renumbered to avoid problems during integration of two FE models (the bridge model and the vehicle model) into one file. Material properties and additional detailed information related to the bridge FE model are provided in Appendix A.1.

Table 4.3. Summary of the complete FE model of one span of the bridge

Specification		Specification	
Number of parts	13	Total number of elements	145,600
Number of nodes	107,378	– solid elements	84,694
Number of material models	8	– beam elements	60,906

Concrete Slab

A reinforced concrete slab of the bridge was modeled with four layers of 8-node solid, fully integrated elements. Elastic material model was selected for FE analysis and its properties were obtained from laboratory tests conducted by the FDOT Structure Lab. The actual material properties of the concrete slab, as tested, are provided in Table 4.4.

Two types of the reinforcing bars were used in the slab structure – size 10M and 15M. They were modeled using 1D beam elements with the elastic material model applied. The FE model of the slab including concrete and reinforcement is presented in Figure 4.1.

Table 4.4. Material properties of the concrete slab (Wekezer, Li, Kwasniewski, & Malachowski, 2004)

Specification	Unit	Value	Comments
Young's modulus, *E*	(GPa) / (ksi)	40.5 / 5871.8	
Poisson's ratio, ν	—	0.20	
Specify compressive strength, f_c'	(MPa) / (ksi)	55.9 / 8.11	

a)
b)

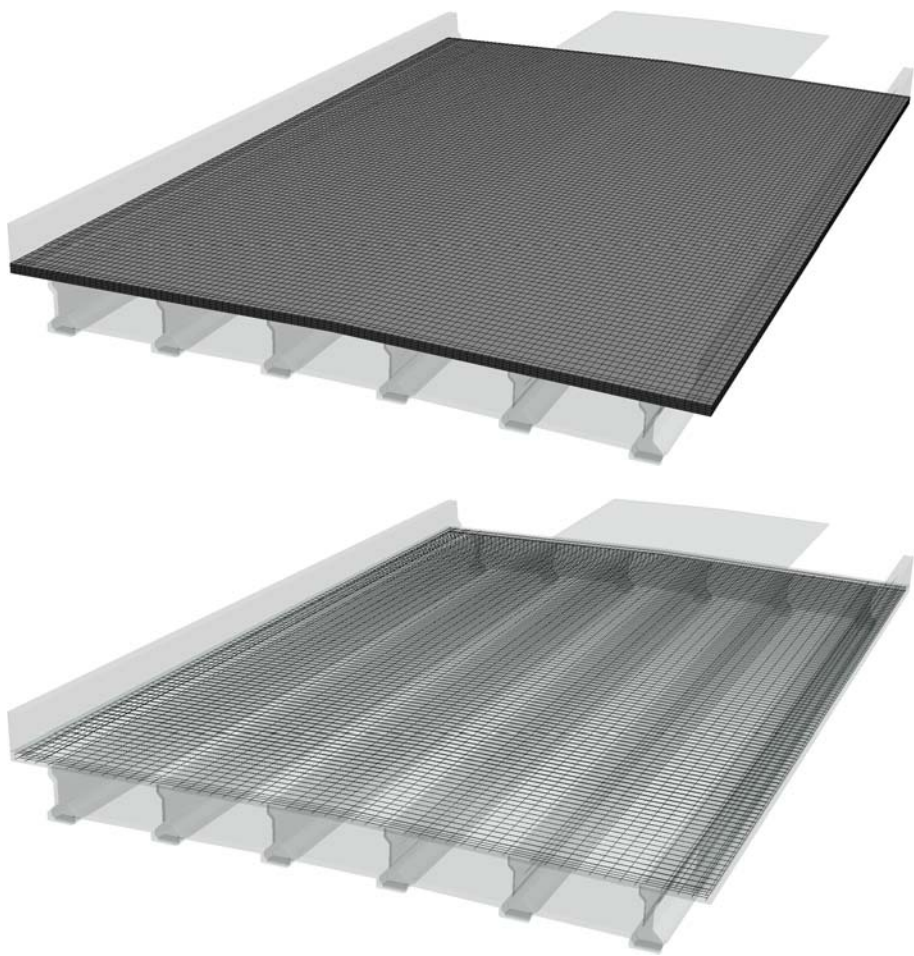

Figure 4.1. FE model of the bridge slab:
a) concrete, b) detailed reinforcement

Traffic Railing Barriers

Reinforced concrete barriers were modeled using 3D solid, fully integrated elements. Two types of reinforcing bars: 10M and 15M were designed for the actual barriers. Minor geometric adjustments were necessary due to finite dimensions of elements used for the barrier model, as depicted in Figure 4.2. The complete FE model of the traffic railing barrier, including concrete and reinforcement, is presented in Figure 4.3.

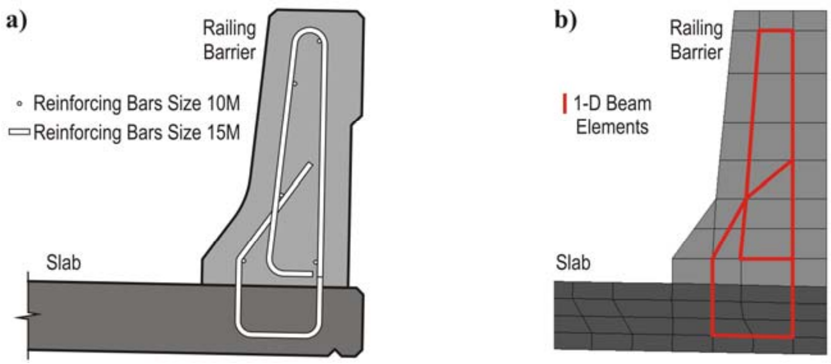

Figure 4.2. Cross-section of the traffic railing barrier: a) actual object, b) FE model

a)

b)

Figure 4.3. FE model of the traffic railing barriers: a) concrete, b) reinforcement

AASHTO Type III Beams

Six prestressed AASHTO type III beams were used for each of the three spans of the bridge considered. The concrete beams were modeled using 8- and 6-node solid, fully integrated elements. An elastic material model was selected for FE analysis. Its properties are provided in Table 4.5. Several reinforcing bars (Figure 4.4a) and strands (Figure 4.5a) were used in each beam. They were represented as 1D beam and rod elements, respectively.

Each beam includes two No. 9 strands at the top and 24 No. 13 strands at the bottom. Only one equivalent strand at the top and eleven equivalent strands at the bottom were modeled due to discrete location of the nodes in the cross-section of the beam FE model. Selected strands were grouped and their properties were distributed into equivalent ones (Figure 4.5c) to make sure that the FE model well represents the real beam.

A special material model type 071 (*MAT_CABLE_DISCRETE_BEAM) was applied to introduce prestressing force in the rod elements. This model allows elastic cables to carry tensile loads only, with no stiffness for compression (LS-DYNA Keyword User's Manual, 2007). The complete FE model of the beams including concrete, reinforcement and strands is presented in Figure 4.6.

Table 4.5. Material properties of the concrete beams (Wekezer, Li, Kwasniewski, & Malachowski, 2004)

Specification	Unit	Value	Comments
Young's modulus, E	(GPa) / (ksi)	37.5 / 5441.9	
Poisson's ratio, ν	—	0.22	
Specify compressive strength, f_c'	(MPa) / (ksi)	63.7 / 9.24	

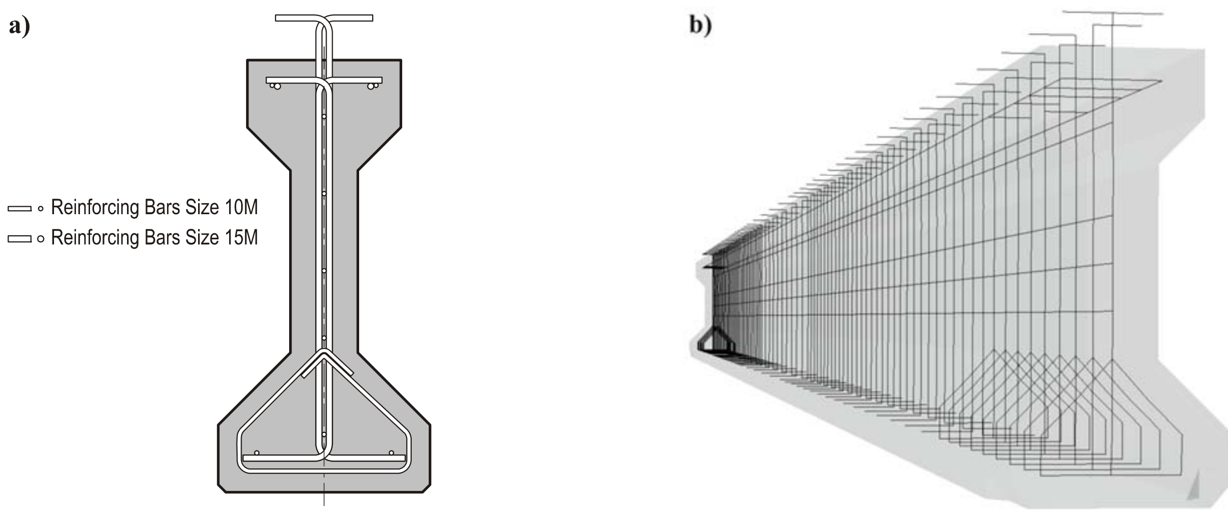

Figure 4.4. Reinforcing bars in the AASHTO Type III beam:
a) location of the bars in the cross-section, b) 1D beam elements used for the bars modeling

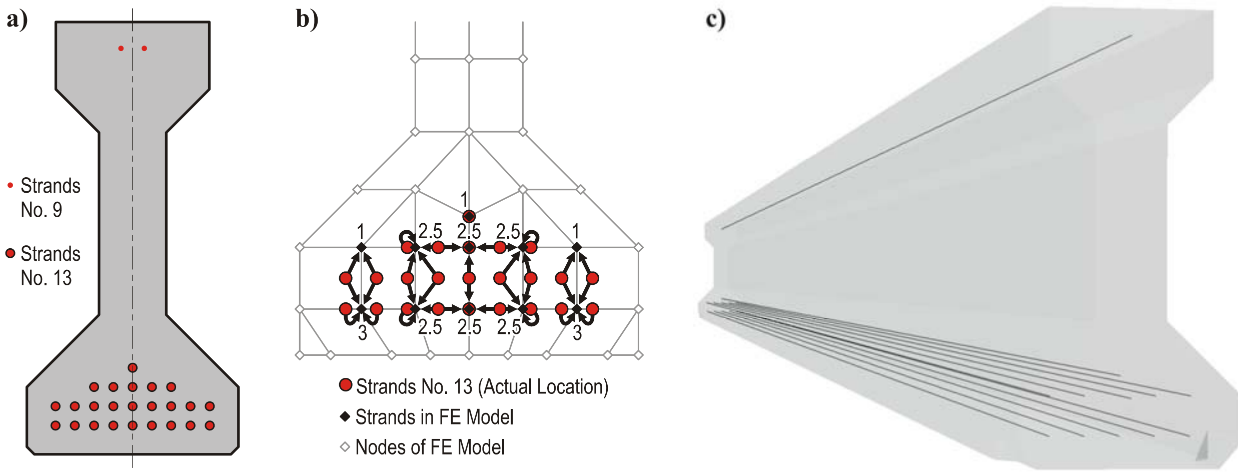

Figure 4.5. Strands in the AASHTO Type III beam:
a) location of strands, b) distribution of strand properties between adjacent nodes,
c) 1D rod elements used for strand modeling

Figure 4.6. FE model of the beams:
a) concrete, b) reinforcing bars and strands

Diaphragms

Concrete diaphragms for the bridge were modeled using 3D solid elements with reinforcing bars represented by 1D beam elements. A complete FE model of the beams, including concrete and reinforcement, is presented in Figure 4.7.

a)

b)

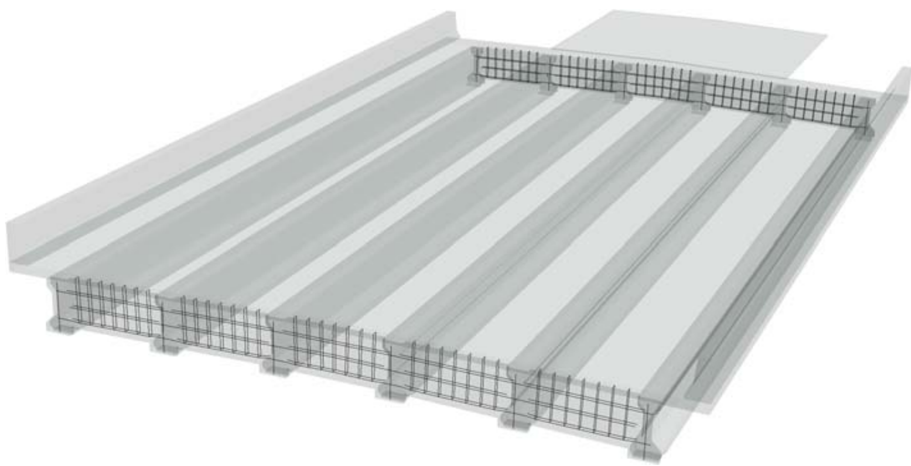

Figure 4.7. FE model of the diaphragm: a) concrete; b) reinforcement

Neoprene Pads

Neoprene pads were used to support each girder on bridge piers. Three dimensional solid element and material model type 006 (*MAT_VISCOELASTIC) were adopted to model the neoprene pads. The location of all neoprene pads for each span of the FE model of the bridge is shown in Figure 4.8.

Concrete Bridge Approach

The importance of modeling bridge approach imperfections were indicated and stressed in earlier studies (*Analytical and Experimental Evaluation of Existing Florida DOT Bridges* – FDOT Project No. BD493, Wekezer, Li, Kwasniewski, & Malachowski, 2004). The concrete bridge approach was modeled with three dimensional 8-node solid elements (Figure 4.9).

In addition, a short section of the asphalt pavement next to the beginning of the concrete approach was included based on actual geometry. This geometry was scanned using a laser scanner as a part of this project. Methodology of the FE model development of the asphalt approach is described in section 4.2. in detail.

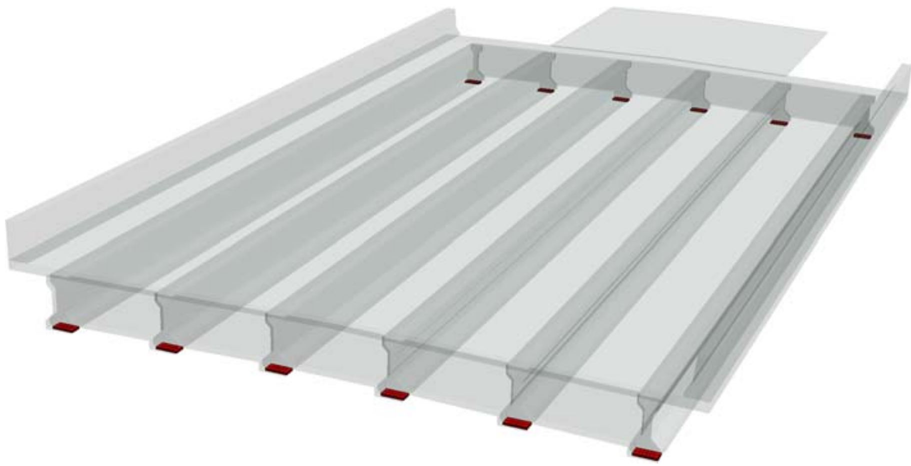

Figure 4.8. FE model of the neoprene pads

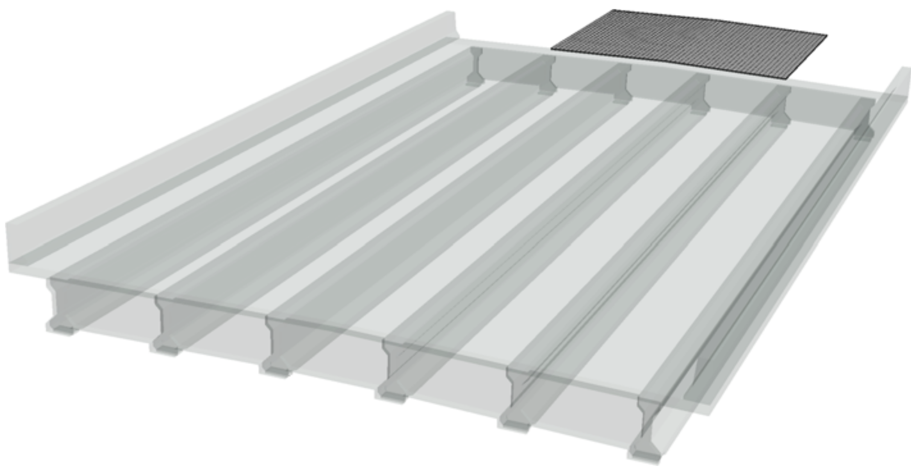

Figure 4.9. FE model of the bridge approach slab

4.2. Development of a FE model for the Asphalt Approach

The Optech's Intelligent Laser Ranging and Imaging System (ILRIS) scanner was used to capture an actual road profile next to the concrete bridge slab (Figure 4.10a). The laser scanner was used for mapping geometry of a depression located on the asphalt pavement next to the bridge slab, and a "dip" (a joint between the bridge approach slab and asphalt pavement) as presented in Figure 4.10b.

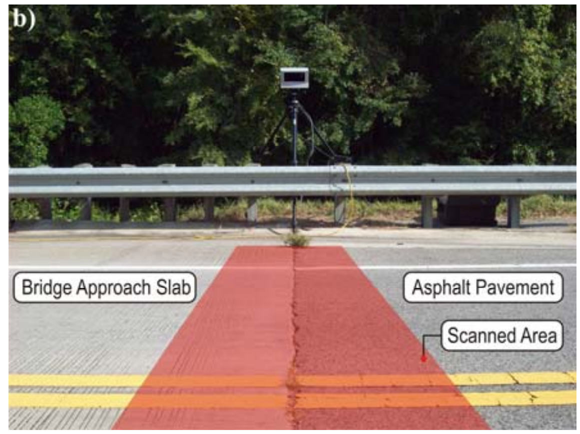

Figure 4.10. a) Optech's ILRIS laser scanner used to capture an actual road profile, b) scanned area (highlighted)

An FE model of the asphalt approach was developed from a point cloud obtained from the scanner. Six-node solid elements were selected with dimensions similar to those of elements used for the bridge and the wheels models. Penta FE elements with triangular faces on the top and bottom were selected to avoid warped faces of the element due to relatively high roughness of the approach. The FE model of the bridge approach consists of two sections, as presented in Figure 4.11.

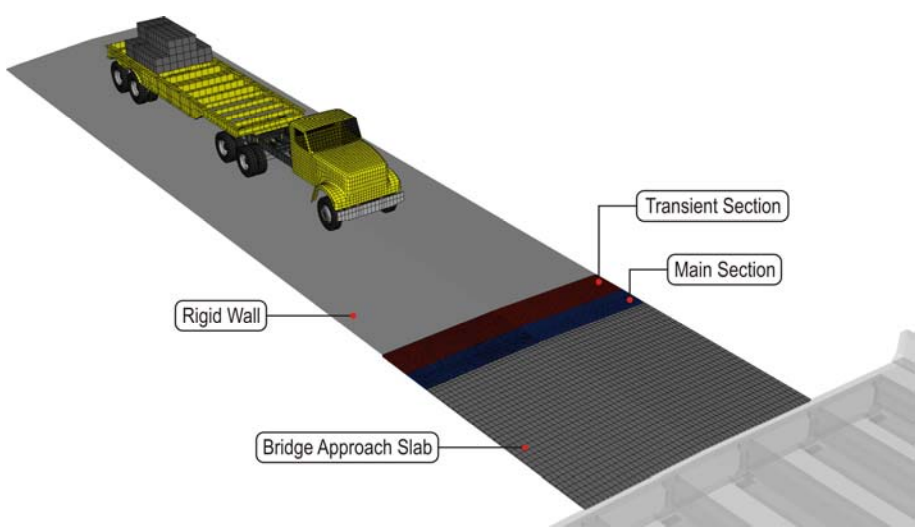

Figure 4.11. The FE model of the bridge approach consists of the main and the transient sections

The main section, closer to the bridge slab, was developed from actual, scanned geometry, while the second part was used as a transient section. It ensured a smooth transition between two completely flat rigid walls used for accelerating the vehicle FE models, and the main section. The right side (westbound lane) and the left side (eastbound lane) of the FE approach model were developed separately. Methodology of the bridge approach modeling was presented in Figure 4.12.

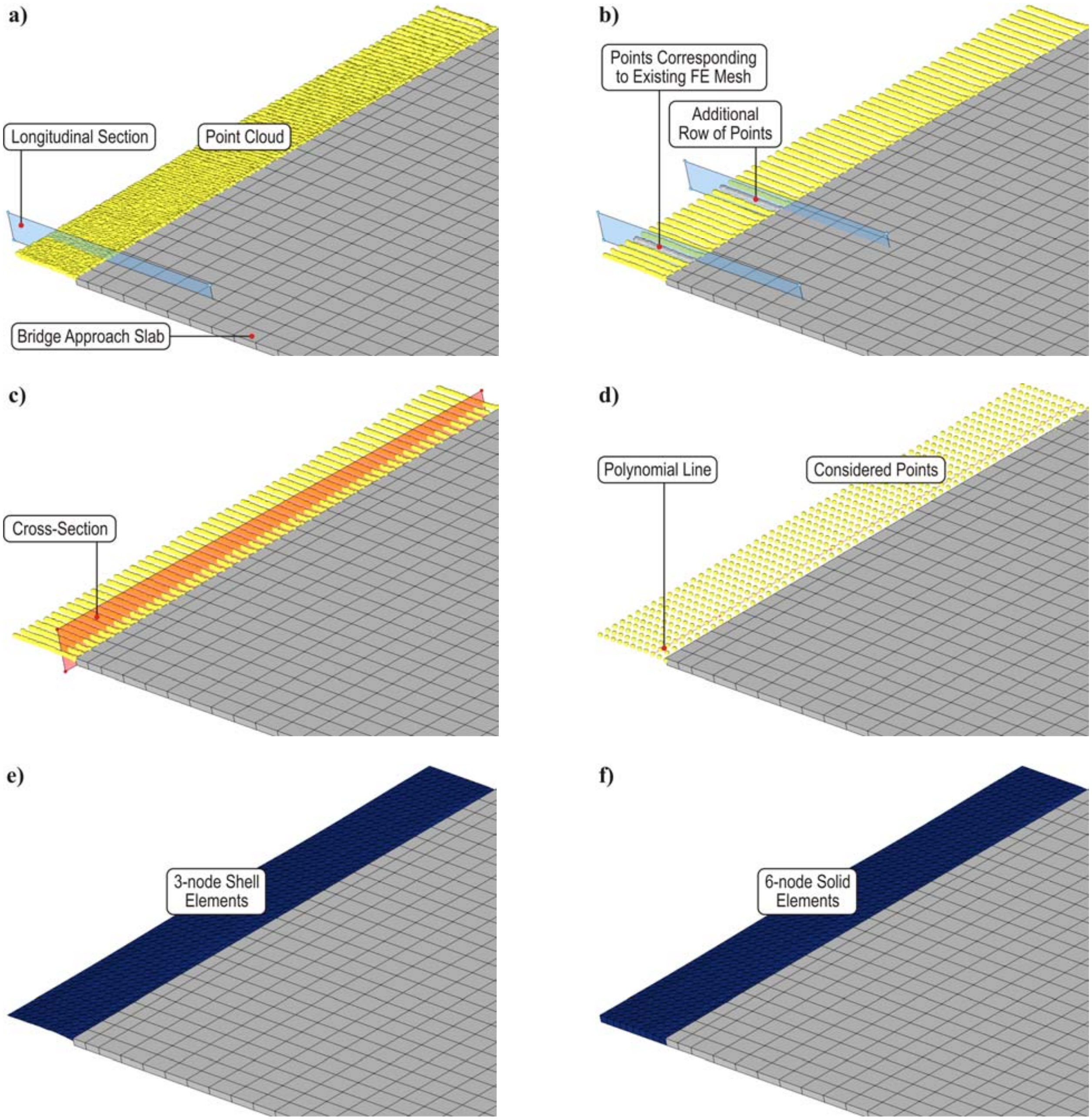

Figure 4.12. The main section of the bridge approach FE model:
a) selection of points in longitudinal direction from the point cloud, b) points corresponding to existing FE mesh and additional rows of points located between mesh, c) selection of points in transverse direction, d) reduced number of points used in FE model development, e) preliminary FE mesh of 3-node shell elements, f) a complete FE model of the main section of the bridge approach consisting of 6-node solid elements

The following procedure was developed and used to convert the scanned point cloud into the FE approach model. First, several rows of points which coincided with the longitudinal gridlines of the existing FE model of the bridge approach slab were selected from the point cloud (Figure 4.12a). An additional mid-point row was included to make the FE mesh twice denser and more accurate (Figure 4.12b). Resulting data points were subsequently processed along the transverse direction in the next step. Several cross-sections were considered (Figure 4.12c) and polynomial trend lines were established based on all points pertinent to each section (Figure 4.12d).

Two distinct ruts were observed on each lane of the asphalt approach on the testing site. They were deeper and more significant for the cross-sections located closer to the bridge slab. One of the selected cross-sections, close to the bridge slab, is presented in Figure 4.13. Both ruts were modeled using a 4-th order polynomial with two concavities (valleys) to reflect actual rut pattern. The last step was to project selected points on the polynomial curve and to create an FE mesh using 3-node shell elements (Figure 4.12e), which were subsequently converted to three dimensional 6-node solid elements (Figure 4.12f).

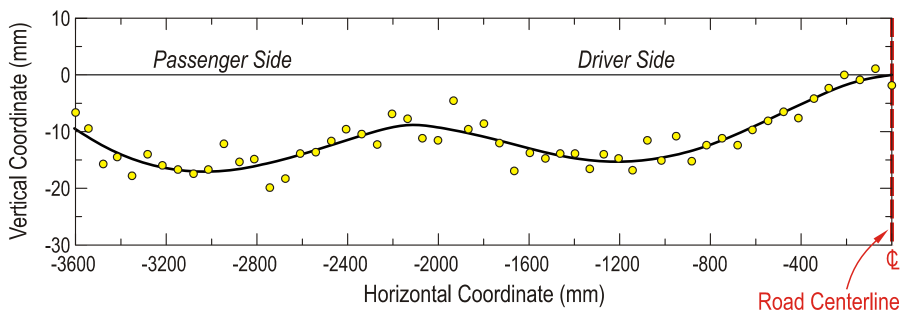

Figure 4.13. Data points in the cross-section of the bridge approach on the westbound lane.
The slope of the pavement is not included.
The road and the bridge axis is shown on the right with a horizontal coordinate = 0 mm

The transient section was modeled using 6-node solid elements. Its surface geometry is presented in Figure 4.14. Both sections of the bridge approach FE model were considered as rigid bodies in the LS-DYNA code. A simple contact model (*CONTACT_SURFACE_TO_SURFACE) was applied to describe an interaction between the FE models of the tire treads and that of the bridge approach. Top faces of the FE elements belonging to the bridge approach FE model were treated as master segment, whereas the slave segment include all treads of the wheel FE models.

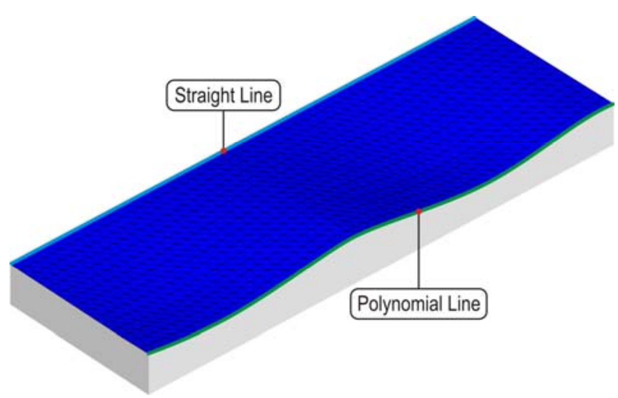

Figure 4.14. Transient section of the bridge approach FE model. Top faces of the elements were presented only.
Note: The vertical scale is magnified ten times as compared with horizontal distances

4.3. Development of a FE model for the Speed Bump

The Optech's ILRIS scanner was also used to capture geometry of an actual speed bump (Figure 4.15). This technique was applied to develop FE models of the speed bump for subsequent FE analyses. The speed bump was used for suspension tests at the Broadmoor Estate site in Tallahassee. The overall width of selected bump was near to 0.3 m (1 foot), whereas the height was 0.06–0.07 m (≈2.5"). An approach and departure of the speed bump was rather soft due to wear and tear caused by long-lasting operation.

The methodology of data processing for the cloud of points is illustrated in Figure 4.16. In the first step, the number of points obtained from the scanner was limited to those surrounding the speed bump. The scanned and selected points are shown in Figure 4.16. The next step was to generate polynomial curves, based on the selected points, which were subsequently used to create surfaces. Finally, the surfaces were meshed using 4-node shell elements resulting in the FE model of the speed bump. Rigid material was applied for the speed bump elements due to their high stiffness as compared with the tires.

Figure 4.15. A speed bump used for the suspension tests for the tractor-trailer and the crane

A simple surface to surface contact model between bumps and tire models was used with a friction coefficient f = 0.65 (Reference Tables, 2008). All tire treads were included in the slave segment whereas the FE model of the speed bump was considered as the master in the tire and road surface contact model. In addition, the road was considered as a flat with no slopes taken into account. It allows modeling the pavement as a rigid wall option available in LS-DYNA code. The element size of the bump FE model was set up to match the size of the tread FE model. A complete FE model of the speed bump consisted of 300 finite elements.

Figure 4.17 presents exemplary snapshots of the FE model of the truck tractor driving over the speed bump for different time instants. Three different lines were drawn in that picture to emphasis behavior of the vehicle model and its suspension during such process. Moreover, they allow assessing a correctness of the developed FE model.

The green line describes a road surface including a shape of the speed bump FE model. The blue one traces out a location of the center of the wheel. The red line presents track of the point on the tractor bodywork.

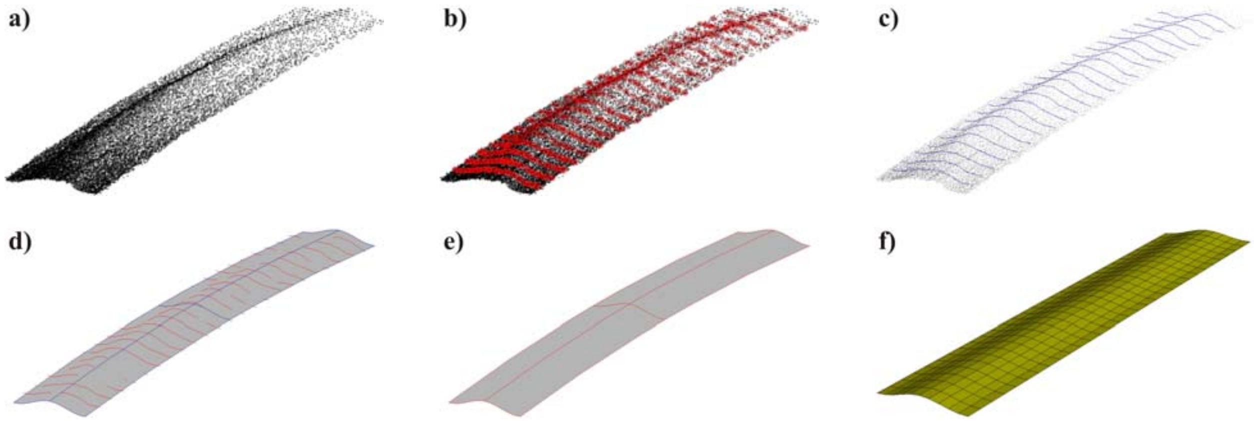

Figure 4.16. Cloud point processing: a) cloud point surrounding the speed bump, b) points selected to draw the polynomial curves, c) polynomial curves used to developing the equivalent surfaces, d, e) equivalent surfaces, f) FE model of the speed bump with no slope of the road taken into account

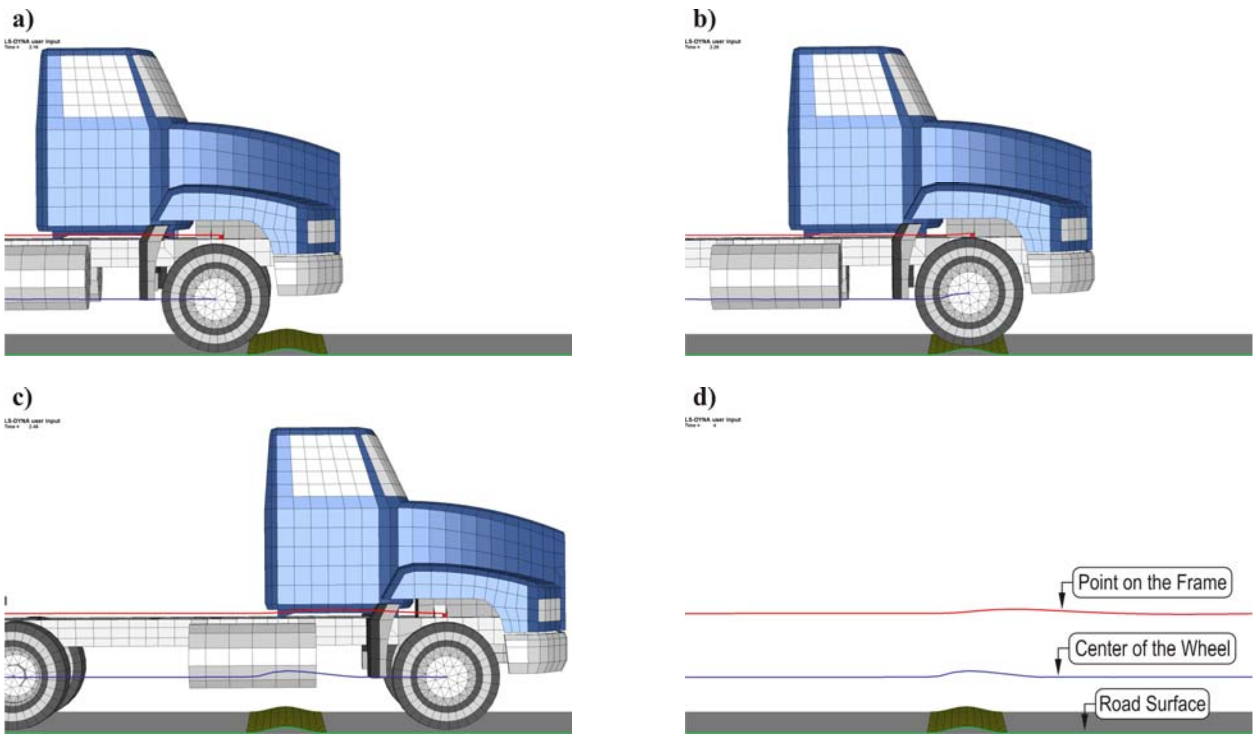

Figure 4.17. Snapshots of the FE model of the truck tractor during driving over the speed bump for different time instants. Trajectories of two selected points are presented

4.4. Development of a FE model for the Tractor-Trailer

The truck tractor Mack CH613 with a three axle single drop lowboy trailer was selected as a representative for this project (see Figure 4.18). A complete FE model of that vehicles consisted of over 25,000 finite elements. This model is presented in Figure 4.19. In-situ measurements, as well as blueprints and data available from the manufacturers' websites were used for the FE model development. Additional load used during the experimental tests was also added in the model. Therefore, a complete FE model of the tractor trailer with the following three options was developed:

- the first, basic configuration, with no additional loads (option I);
- the second configuration with one large cargo located approximately in the middle of the trailer (option II);
- the third configuration with additional load distributed evenly on the load and top deck of the trailer (option III) .

The first two options were used only for the suspension validation analysis, whereas the last one was combined with the bridge FE model.

Summary of the final FE model of the tractor-trailer system for each option is provided in Table 4.3. It includes such information as the number of parts, elements, nodes, and material models. Material properties applied in the FE model of the tractor-trailer were provided in Appendix A.2.

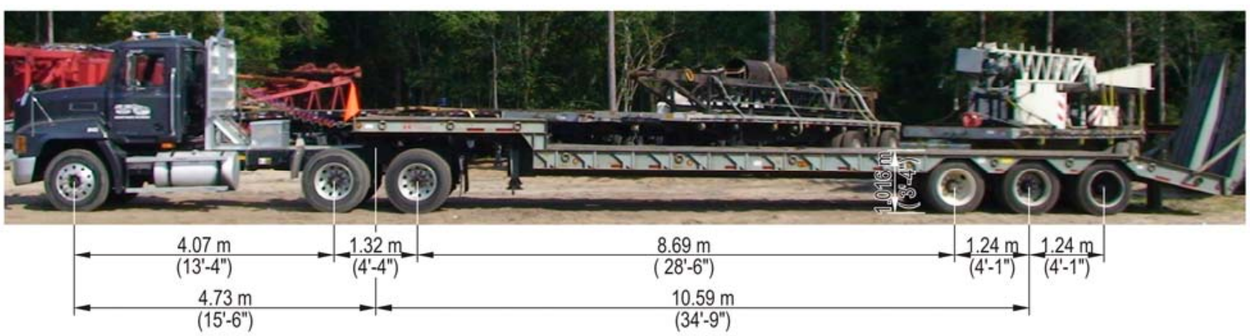

Figure 4.18. Truck tractor and lowboy trailer used in the tests

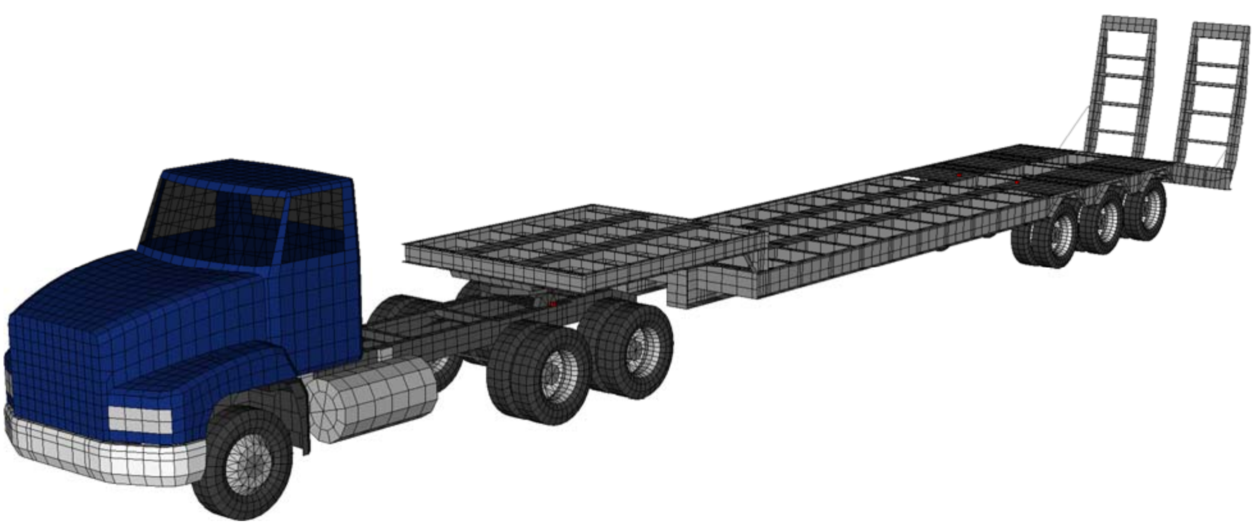

Figure 4.19. FE model of the truck tractor and lowboy trailer in basic configuration without any cargo

Table 4.6. Summary of the complete FE model of the tractor-trailer with three different options

Specification	Option I	Option II	Option III
Number of parts	200	201	204
Number of elements	25674	26130	26194
– solid elements	608	1064	1128
– shell elements	24790	24790	24790
– beam elements	248	248	248
– discrete elements	22	22	22
– mass elements	6	6	6
Number of nodes	18996	19694	19941
Number of material models	34	35	38

Truck Tractor

The selected truck tractor is one of the most popular in the United States. Its wheelbase is 4.73 m (15'-6") long and may vary in a wide range between 3.68 and 6.10 m (12'-1" and 20'-0"). The tandem axle spacing in the rear suspension remains the same for each wheelbase, thus simple modifications of the wheelbase in the FE model—for further projects—are possible and they can be easily applied by adding or removing elements from the longitudinal frame (Figure 4.20).

The FE model of the truck tractor (Figure 4.21) was developed based on available data. Dimensions of the truck and its selected elements were taken from datasheets available on MACK Company website and other companies manufacturing truck components. Material density was adjusted as necessary to ensure that mass of the FE components is close to real objects that they represented. Mass distribution between unsprung and sprung masses was carefully checked when adjusting material density.

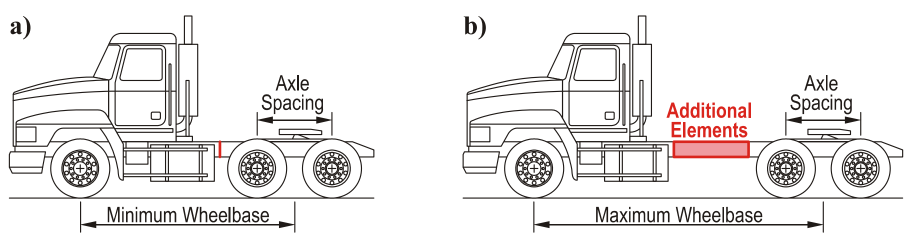

Figure 4.20. A simple method of the wheelbase modifications of the FE models of the selected truck: a) minimum wheelbase, b) maximum wheelbase

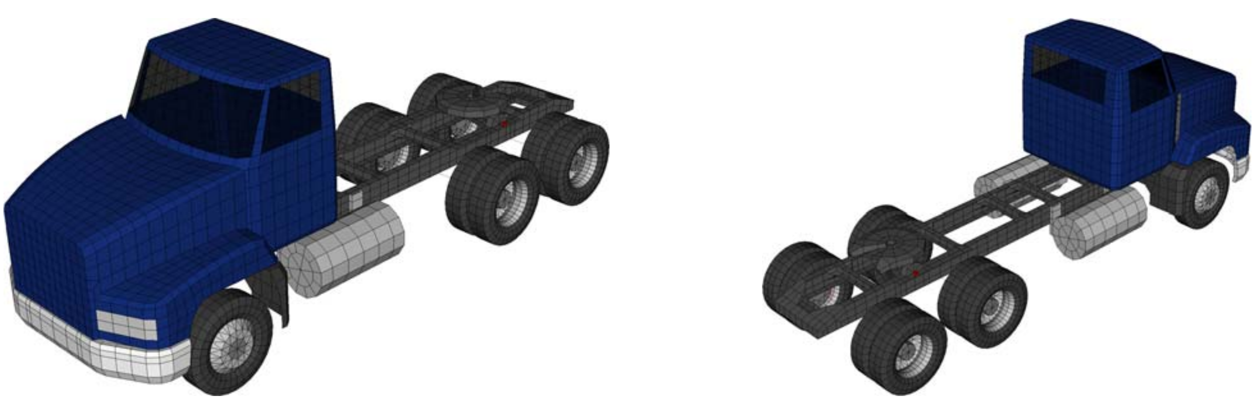

Figure 4.21. FE model of the MACK CH613 truck tractor: front and back view

The following components were included in the FE model of the truck tractor:

- a chassis, including complete wheels with elastic tires, simplified front single axle, rear tandem axles, and suspension systems;
- a complete frame, including longitudinal frame rail and transverse beams, e.g. cross-members, engine support beam, etc.;
- a fifth wheel.

Since the above truck components significantly influence the behavior of its FE model, extensive efforts were made for their FE model development. The suspension systems and the tires received much attention in the modeling process as clearly having a distinct impact on the interaction between the vehicle and the road surface. A complete truck frame was modeled as an elastic part. The fifth wheel system was also very important due to direct connection between two units – the truck tractor and the trailer.

Other components – including driver cab, hood, and engine – were modeled as rigid parts. A few details were added only to improve appearance of the FE model. They included a front bumper, fuel tanks and mudguards. Such modeling strategy resulted in simplifications in the FE model, as well as in reduction in the total number of elements and the CPU time. Methodology of modeling of selected components is described in detail in the following sections.

Truck Tractor Wheels

The selected truck tractor was equipped with aluminum wheels with hub-piloted mounting system 22.5"×8.25" in size, as presented in Figure 4.22. Each wheel had tubeless Goodyear G372LHD 295/75R22.5 tire. Cross-section of the selected wheel and the tire is presented in Figure 4.23 and their dimensions are provided in Table 4.7 and Table 4.8, respectively.

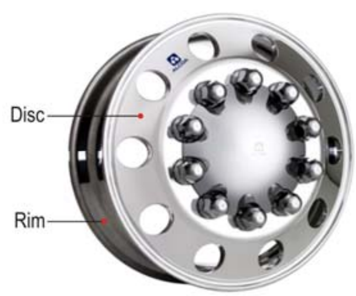

Figure 4.22. Front view of the truck wheel (Alcoa Wheels, 2008)

The FE model of the truck wheel included a disc, a rim, and sidewalls and tread of the tire, as presented in Figure 4.24. Four-node shell elements were used for most components, except for discs that were modeled using 3-node shell elements. The FE model of the tire consists of the sidewalls and the tread parts. Each of these components includes two coincident layers of 4-node shell elements (Figure 4.25). The first layer represents a rubber-like material with average properties for rubber, whereas the second layer (representing the cord) uses a material model for fabrics, with stiffness for tension only. A simple pressure volume airbag model was used for the FE pneumatic models of the tires. The values of pressure inside the airbags were set up according to data provided by the tire manufacturer (see Table 4.8) and can be easily changed in the FE model, if needed. The thicknesses of the shell elements used for wheels and tires was based on data available from manufacturer websites; however some of them were modified in order to obtain mass similar to that in actual wheels. Thickness of elements for each part is provided in Table 4.9. Dimensions of the FE model of the complete wheel are shown in Figure 4.26.

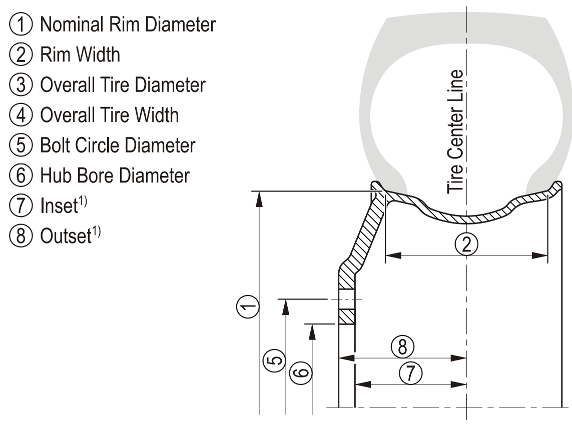

Figure 4.23. Cross-sections of the selected wheel and tire – dimensions are provided in Table 4.7 and Table 4.8.
[1)] inset and outset are the distances from the rim/tire centerline to the mounting face of the wheel

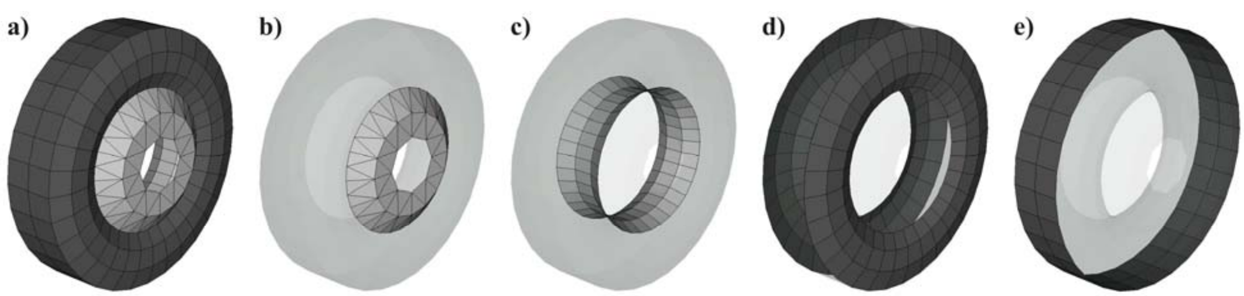

Figure 4.24. FE model of the wheel: a) complete wheel, b) disc, c) rim, d) sidewalls, e) tread.
Sidewalls and tread include two layers of elements for rubber and fabric materials (see Figure 4.25)

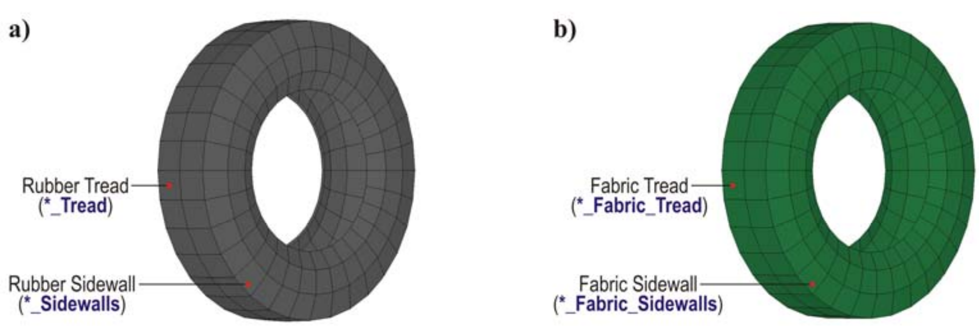

Figure 4.25. FE model of the tire and respective layers of elements simulated:
a) rubber component, b) fabric component

Table 4.7. Dimensions of the truck wheels (Alcoa Wheels, 2008)

Specification	Unit	Value	Comments
Size	—	22.5"×8.25"	Part No. 88364
Nominal rim diameter (1)	(mm) / (in)	571.5 / 22.5	
Rim width (2)	(mm) / (in)	210 / 8.25	
Bolt circle diameter (5)	(mm) / (in)	285.75 / 11.25	
Hub bore diameter (6)	(mm) / (in)	220.1 / 8.669	
Inset (7)	(mm) / (in)	147.6 / 5.81	
Outset (8)	(mm) / (in)	169.2 / 6.66	
Disc thickness	(mm) / (in)	21.6 / 0.85	outset – inset
Wheel mass	(kg) / (lb)	21.8 / 48	

Table 4.8. Dimensions of the truck tires (Goodyear Tires, 2008)

Specification	Unit	Value	Comments
Size	—	295/75R22.5	
Rim width (2)	(mm) / (in)	210 / 8.25	
Overall diameter (3)	(mm) / (in)	1,044 / 41.1	
Overall width (4)	(mm) / (in)	282 / 11.1	
Static loaded radius	(mm) / (in)	488 / 19.2	
Tire mass	(kg) / (lb)	60 / 132	
Single max load	(kg) / (lb)	2,800 / 6,175	front axle only
Dual max load	(kg) / (lb)	2,575 / 5,675	rear axles only
Single inflation	(kPa) / (psi)	760 / 110	front axle only
Dual inflation	(kPa) / (psi)	690 / 100	rear axles only

Table 4.9. Thickness of elements used for the truck wheel FE model

Wheel	Part name	Number of elements	Thickness (mm)
Disc	*_Discs	2 × 72	21.6
Rim	*_Rim	96	7.7
Tire			
Fabric sidewalls	*_Fabric_Sidewalls	192	2.0
Fabric tread	*_Fabric_Tread	64	3.0
Rubber sidewalls	*_Sidewalls	192	16.0
Rubber tread	*_Tread	64	40.0

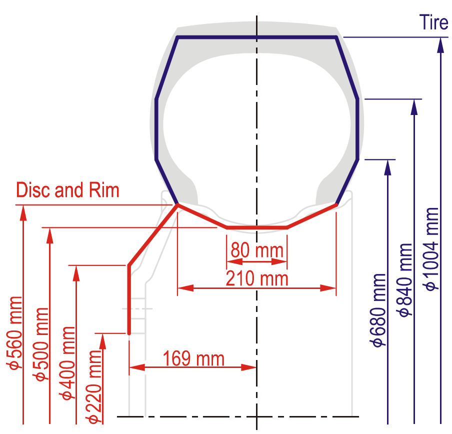

Figure 4.26. Dimensions of the cross-section of the truck wheel FE model

Both wheel discs – right and left – were grouped into one part in FE model, while other components were treated separately due to requirements of the applied airbag model. The rim, rubber sidewalls and rubber tread are formed as a closed control volume filled by the pressure, therefore each of them can be a part of one wheel only. In addition, normal vectors for each FE element of these parts must be oriented outwards from the control volume (LS-DYNA Keyword User's Manual, 2007), as presented in Figure 4.27.

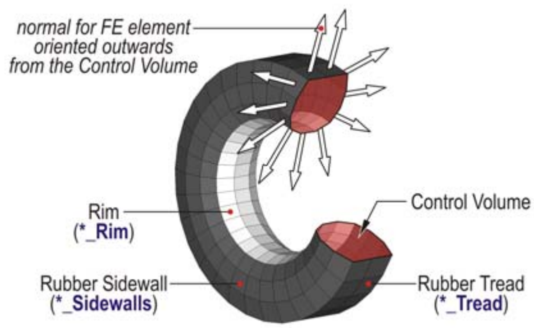

Figure 4.27. Parts of the FE wheel model used in the airbag model

The following abbreviations for each wheel in the truck FE model was used (Table 4.10). It was depended on the axle number, side of the model and location wheel location. Passenger side was treated as the right side and the driver side – as the left side.

Table 4.10. Description and abbreviations of the wheels in the truck FE model

Axle		Wheel	
Front axle	F1_	WR	**R**ight
		WL	**L**eft
Rear tandem axles: **1**st and **2**nd	R1_ R2_	WRO	**R**ight **O**uter
		WLO	**L**eft **O**uter
		WRI	**R**ight **I**nner
		WLI	**L**eft **I**nner

Assumed properties of aluminum, rubber and fabric used for all parts in the wheel FE model are provided in Appendix A.2. Calculated mass of the complete wheel FE model was compared with the actual wheel in Table 4.11.

Table 4.11. Comparison between calculated mass of the complete tractor wheel FE model and the manufacturer data for the actual wheel (Alcoa Wheels, 2008), (Goodyear Tires, 2008)

FE model part name	Calculated mass		Actual component	Mass
*_Discs (one disc only)	14.218 kg	21.800 kg	Wheel	21.800 kg
*_Rim	7.582 kg			
*_Fabric_Sidewalls	2.270 kg	60.021 kg	Tire	60.000 kg
*_Fabric_Tread	1.984 kg			
*_Sidewalls	22.701 kg			
*_Tread	33.066 kg			

Truck Tractor Suspension Systems

Front suspension of the selected truck tractor is presented in Figure 4.70. It includes three main components: the steer axle, two Mack Taperleaf leaf springs, and two shock absorbers, which were included in the FE model.

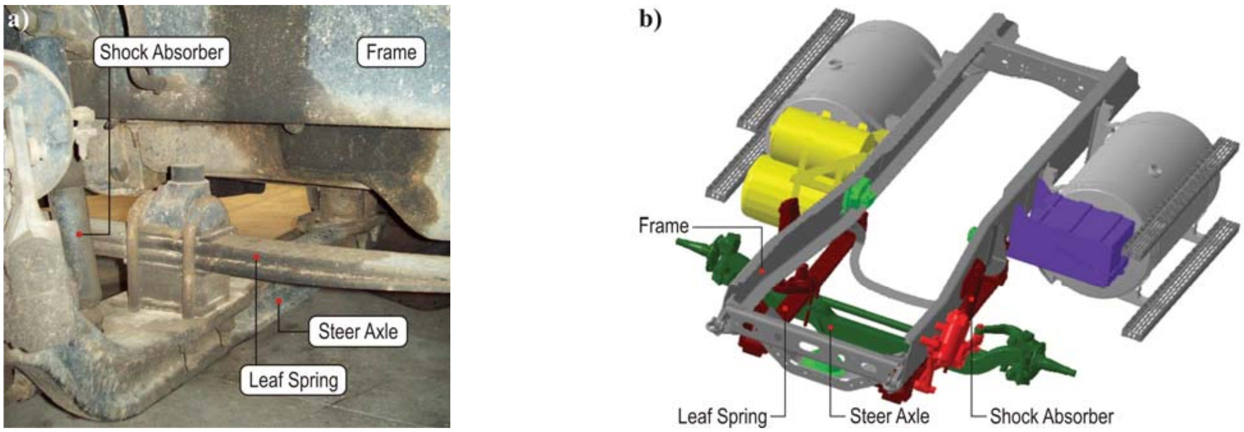

Figure 4.28. Front suspension system of the truck tractor: a) detail of the actual suspension, b) overall front part of the frame with suspension (Mack Products, 2004)

Total mass of the front suspension was estimated based on available data. It was assumed as 123.4 kg (272 lb) for the complete front suspension system, including frame hangers, main springs, bushings, height control system, shocks, upper shock brackets and axle attachment hardware (Hendrickson Products, 2008). Only three main components mentioned, as mentioned before, were included in the FE suspension model. Other components were lumped together as a sprung mass connected with the bodywork. The total mass of these components was lumped up into an equivalent part (F1_Vertical_Cylindrical_Joint), which was rigidly connected with the frame. Density of a rigid material used for modeling this part was recalculated to obtain its appropriate mass.

Mass of the front axle of the truck was determined as 142.4 kg (314 lb). It included: an axle beam, knuckle/steering arm assemblies, and tie rod assemblies (Roadranger Products, 2004). They were represented in the FE model by two parts: F1_Axle_Rigid_Rotating and F1_Axle_Rigid_Non_Rotating, as shown in Figure 4.29. Both parts were connected using the *CONSTRAINED_JOINT option in the LS-DYNA code. It allows modeling of several distinct joints as: spherical, cylindrical, revolute, planar, universal between two rigid bodies (LS-DYNA Keyword User's Manual, 2007). The vertical motion of the axle set was achieved by using the cylindrical joints and the special purpose discrete elements which simulate springs and shock absorbers, as presented in Figure 4.30. One dimensional beam elements with tubular cross-sections were used for the FE axle model.

The following discrete elements: linear elastic for springs, and linear viscous for dampers were used for suspension modeling. These elements are massless and they have the simplest force-displacement and force-velocity relations, respectively. Spring constants and dumping coefficients were determined from experimental suspension testing. Their values are provided in following chapters of this report.

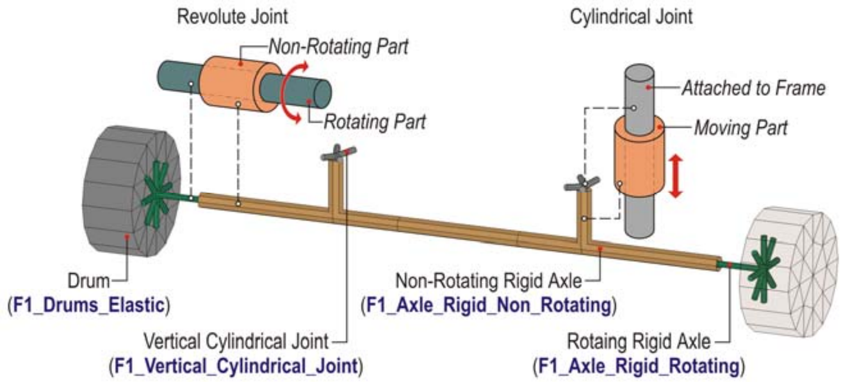

Figure 4.29. Constrained joints used in the FE model of the truck tractor front suspension

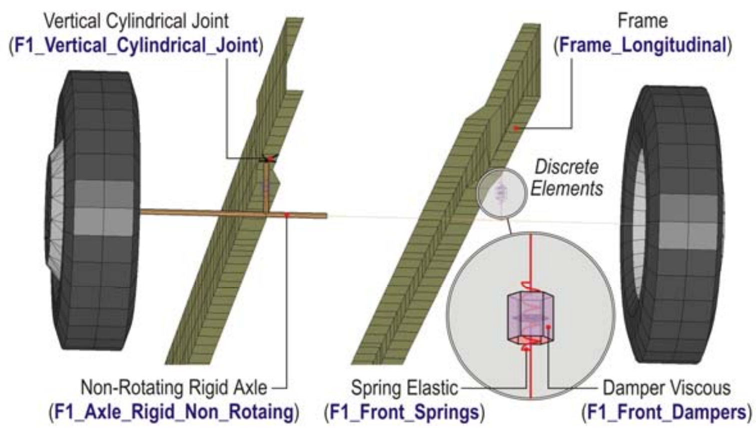

Figure 4.30. FE model of the truck tractor front suspension with discrete elements

An air suspension system for the drive tandem axles was used in the selected truck (Figure 4.31a). A similar HAS Series air suspension, manufactured by Hendrickson, is shown in Figure 4.31b. The complete suspension system includes: air springs, shock absorbers, cross channels, main support members, ultra rods, torque rods, axle and frame brackets (Hendrickson Products, 2008) with total mass of 417 kg (920 lb). That mass was distributed to equivalent elements similar to those used in the front suspension system in the FE model.

Tandem drive axles with 44,000 lb capacity, as presented in Figure 4.32, were used in the selected truck. Manufacturer datasheets (Arvin Meritor Rear Axles, 2008) were used to provide information on total mass of the first/forward and second/rear axle as 428 kg (944 lb) and 345 kg (760 lb), respectively. Oil, brakes, hubs, drums or rotors, bearing cones, seals, wipers, suspension brackets, yokes and other options were not included in this mass. Both axles were modeled using rigid beam elements as it was done for the front axle FE model. The FE model of the complete rear suspension system is presented in Figure 4.33.

Truck Tractor Frame

The truck had a steel frame made of channel sections C 10.74"×3.54"×0.24". In-situ measurements of the frame were used to develop an FE model of the frame, as presented in Figure 4.34. It includes: two single channel frame rails, cross members and transverse beams, fifth wheel plate, and additional connections between the frame and the engine FE. All parts of the FE frame model are shown in Figure 4.35. The elastic material model was applied for all parts of the tractor frame. Two dimensional 4-node shell elements were used for the frame model with appropriate thickness, based on the actual measurements.

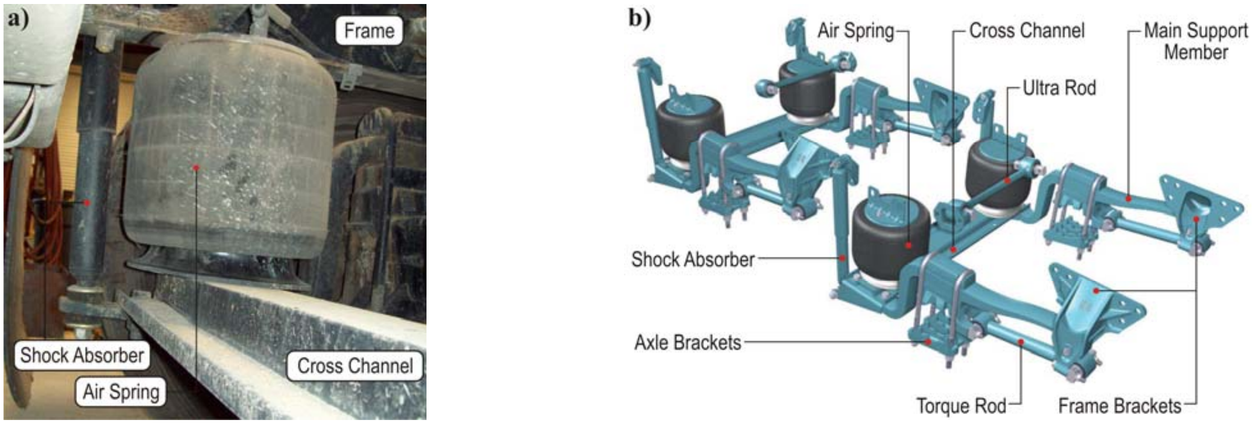

Figure 4.31. Rear suspension system of the selected truck tractor:
a) the actual truck suspension, b) Hendrickson HAS Series air suspension (Hendrickson Products, 2008)

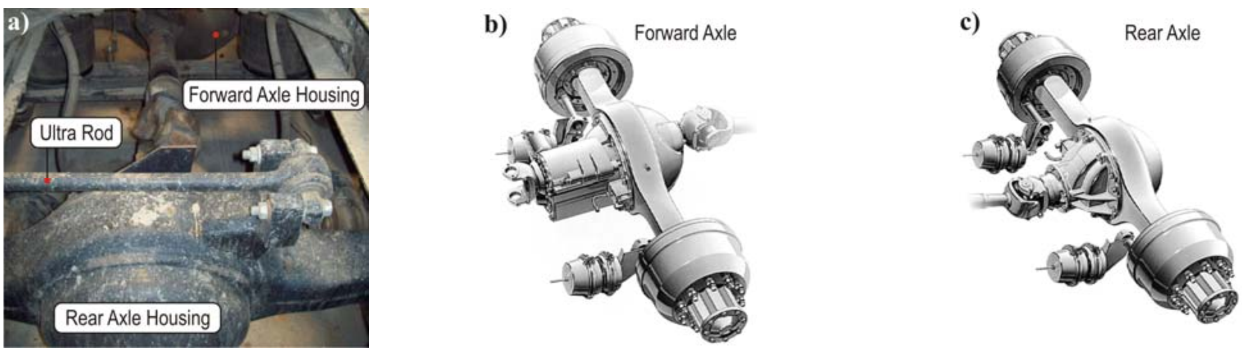

Figure 4.32. Rear tandem axles of the selected truck: a) the actual axle,
b) the forward axle, and c) the rear axle (Arvin Meritor Rear Axles, 2008)

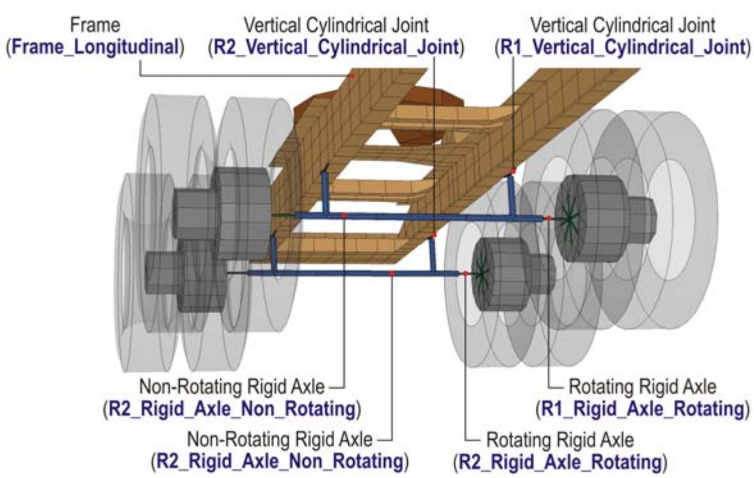

Figure 4.33. FE model of the rear suspension system

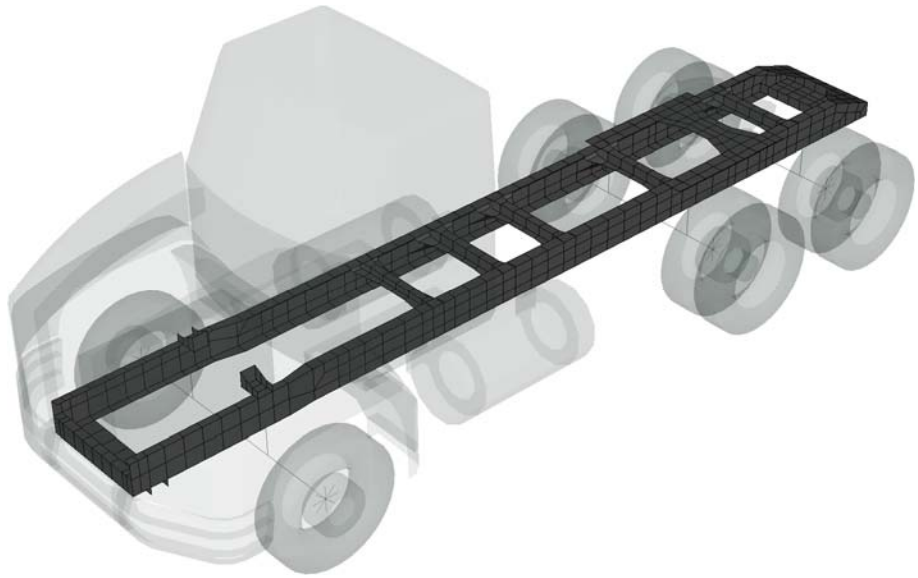

Figure 4.34. The FE model of the complete frame of the truck

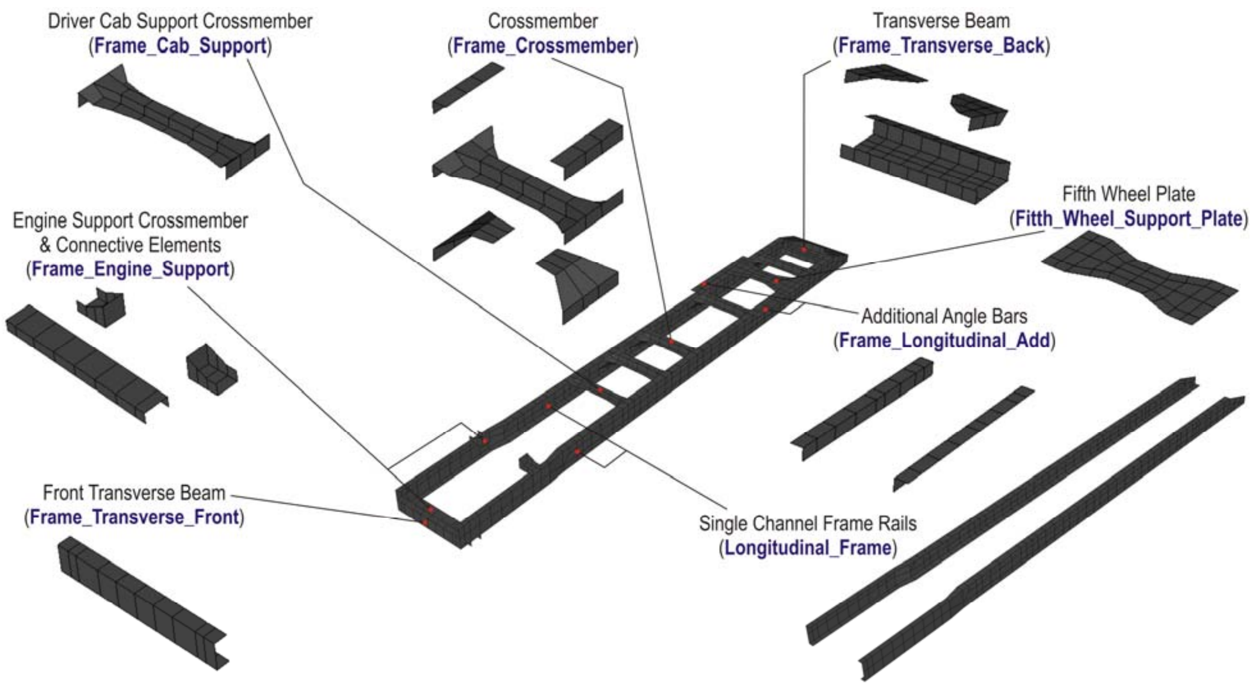

Figure 4.35. An exploded view of the frame components in the FE model

Fifth Wheel Coupling

A fifth wheel coupling is commonly used for longer and heavier vehicles. It provides a connection between a lowboy trailer and the towing truck. It consists of two main components: a fifth wheel located on the frame of the tractor (Figure 4.36a) and a king pin attached to a skid plate at the bottom front of the trailer (Figure 4.36b).

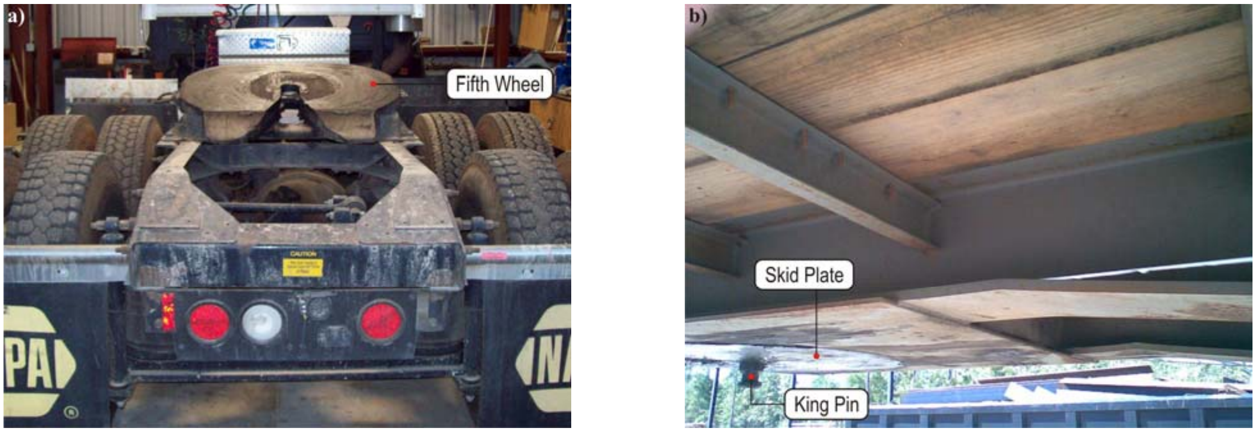

Figure 4.36. Fifth wheel coupling of the selected tractor-trailer system:
a) fifth wheel on the truck tractor, b) king pin and the skid plate of the lowboy trailer

The fifth wheel on the vehicle was modeled with 8-node 3D solid elements, as presented in Figure 4.37a. The corresponding FE model includes two rigid parts: the fifth wheel and its bearing, which are connected using two revolute joints. They allow for the relative motion of the tractor and the trailer in their vertical plane. Since all analysis under this study were limited to straight runs of the vehicle on a bridge (with no turns), the FE model was restricted to the straight direction and any movements of the trailer in the horizontal plane were not allowed. Hence, the fifth wheel and the skid plate of the trailer were rigidly connected by merging coincident nodes (Figure 4.37b). Fifty millimeter (2") offset for the fifth wheel was applied.

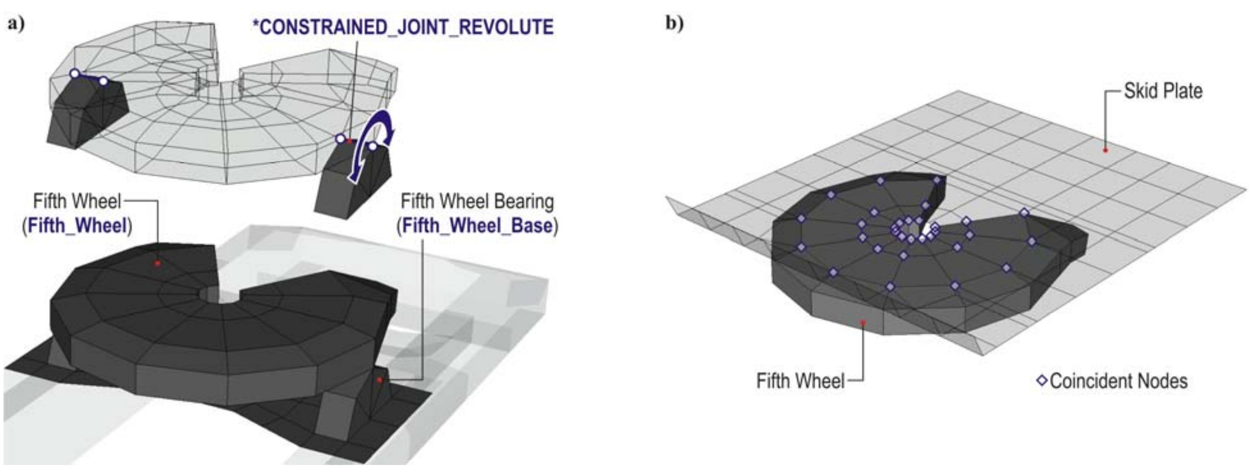

Figure 4.37. a) FE model of the fifth wheel, b) connection between fifth wheel and the skid plate

Truck Tractor Engine

An engine was the last actual component of the truck tractor, which mass was well-known. The selected vehicle was equipped with the MACK MP8 Series Diesel engine (Mack Products, 2004). Total mass of the dry engine is 1,161 kg (2,560 lb). It includes air compressor but does not include fluids, a fan, a starter, an alternator and a clutch (Mack Powertrain, 2008). Therefore, the total mass of the engine FE model was increased by a few kilograms, which was distributed evenly through one 3D rigid part attached to the frame.

Other Components

The rest of the truck tractor components such as a driver cab, a hood, a front bumper, mudflaps and fuel tanks, were simulated as rigid bodies. Their mass was closely estimated, in proportion to their dimensions. All rigid parts of the truck tractor, included in the FE model, are shown in Figure 4.38.

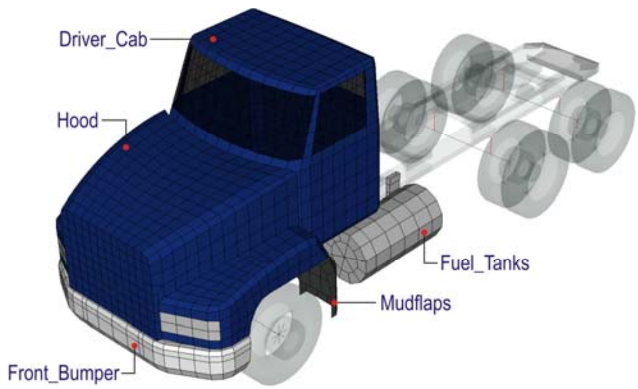

Figure 4.38. Rigid parts in the truck tractor FE model

Lowboy Trailer

The selected single drop lowboy trailer was manufactured by Wallace Trailers. It was made of two groups of components which were included in the FE model. The first group comprises of: a chassis with wheels, three axles, and a suspension system. Other components, as: longitudinal and transverse beams, side beams, steel plates on the load deck, and the fifth wheel skid plate were included in the second group – the trailer frame.

Trailer Wheels

The selected trailer had twelve 2-hand hole wheels 22.5"×7.50" in size, with hub-piloted mounting system (Figure 4.39a). Each wheel was equipped with a tubeless Dunlop SP 160 tire 255/70R22.5 in size. A cross-section of the wheel and the tire are presented in Figure 4.39b and their dimensions are provided in Table 4.12 and Table 4.13, respectively.

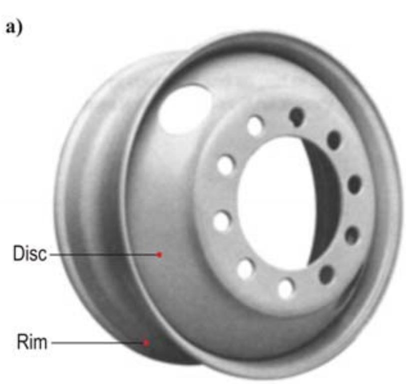

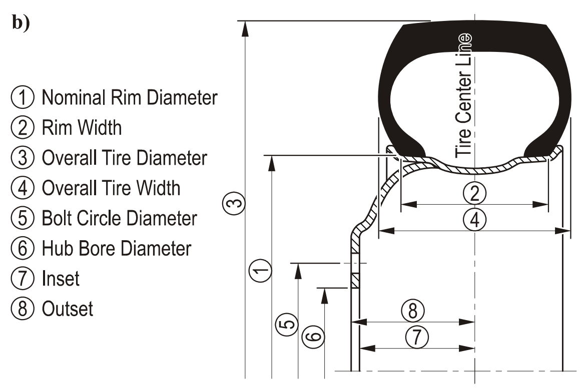

Figure 4.39. The trailer wheel: a) front view of the actual wheel (Accu-Lite Steel Wheels, 2007), b) cross-sections of the wheel and tire – dimensions are provided in Table 4.12 and Table 4.13

Table 4.12. Dimensions of the trailer wheels (Accu-Lite Steel Wheels, 2007)

Specification	Unit	Value	Comments
Size	—	22.5"×7.50"	
Nominal rim diameter (1)	(mm) / (in)	571.5 / 22.5	
Rim width (2)	(mm) / (in)	191 / 7.50	
Bolt circle diameter (5)	(mm) / (in)	285.75 / 11.25	
Hub bore diameter (6)	(mm) / (in)	220.1 / 8.669	
Inset (7)	(mm) / (in)	152.5 / 6.003	
Outset (8)	(mm) / (in)	163.6 / 6.440	
Disc thickness	(mm) / (in)	11.1 / 0.437	
Wheel mass	(kg) / (lb)	31.8 / 70	

Table 4.13. Dimensions of the truck tires (Dunlop Truck Tires, 2008)

Specification	Unit	Value	Comments
Size	—	255/70R22.5	
Rim width (2)	(mm) / (in)	191 / 7.50	
Overall diameter (3)	(mm) / (in)	928 / 36.5	
Overall width (4)	(mm) / (in)	254 / 10.0	
Static loaded radius	(mm) / (in)	435 / 17.1	
Tire mass	(kg) / (lb)	39 / 86	
Single max load	(kg) / (lb)	2,500 / 5,510	
Dual max load	(kg) / (lb)	2,300 / 5,070	rear axles
Single inflation	(kPa) / (psi)	830 / 120	
Dual inflation	(kPa) / (psi)	830 / 120	rear axles

Modeling strategy used for the development of the FE model of the trailer wheels was exactly the same as for the tractor wheels and tires. Abbreviations used for each wheel in the trailer FE model are listed in Table 4.14. The FE model of the complete wheel and its dimensions is shown in Figure 4.40, while thickness of each component is provided in Table 4.15.

Table 4.14. Abbreviations used for the wheels in the trailer FE model

Axle		Wheel	
Trailer axles: **1**st, **2**nd and **3**rd	T1_ T2_ T3_	WRO	**R**ight **O**uter
		WLO	**L**eft **O**uter
		WRI	**R**ight **I**nner
		WLI	**L**eft **I**nner

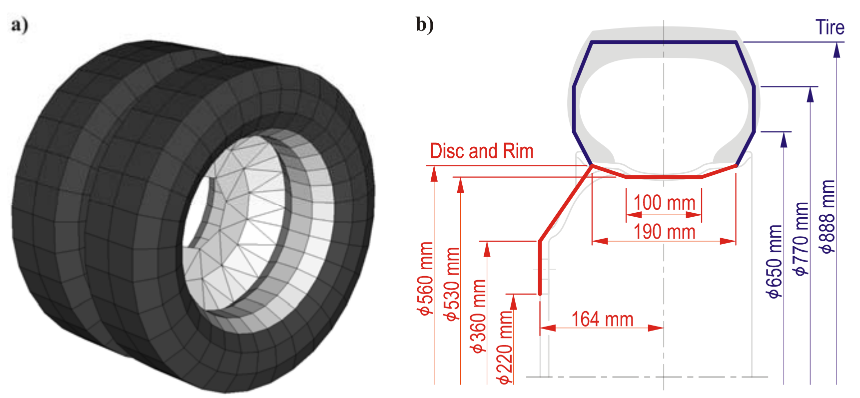

Figure 4.40. FE model of the trailer wheel: a) dual wheel FE model, b) dimensions of the cross-section

Table 4.15. Thickness of elements used for the FE model of the trailer wheel

Wheel	Part name	Number of elements	Thickness (mm)
Disc	T*_Discs	2 × 72	11.1
Rim	T*_Rim	96	4.7
Tire			
Fabric sidewalls	T*_Fabric_Sidewalls	192	2.0
Fabric tread	T*_Fabric_Tread	64	3.0
Rubber sidewalls	T*_Sidewalls	192	9.4
Rubber tread	T*_Tread	64	40.0

Properties of steel, rubber and fabric used for the FE model of the trailer wheel are provided in Appendix A.2. Calculated mass of the complete FE model of the wheel was compared with the actual object in Table 4.16.

Table 4.16. Comparison between calculated mass of the complete trailer wheel FE model and the manufacturer data for the actual wheel (Accu-Lite Steel Wheels, 2007), (Dunlop Truck Tires, 2008)

FE model part name	Calculated mass		Actual component	Mass
T*_Discs (one disc only)	21.243 kg	31.768 kg	Wheel	31.800 kg
T*_Rim	10.525 kg			
T*_Fabric_Sidewalls	1.601 kg	39.007 kg	Tire	39.000 kg
T*_Fabric_Tread	1.588 kg			
T*_Sidewalls	9.358 kg			
T*_Tread	26.460 kg			

Trailer Suspension

The trailer selected was equipped with three 127 mm (5") round axles supported by two high arch 3-leaf springs (Figure 4.41a, b) without shock absorbers. The load vs. deflection curve for the spring was adopted from the manufacturer's specification and is presented in Figure 4.41c. The axles were mounted in underslung configuration to reduce the suspension height, which is a standard feature of all lowboy trailers. Mass of an axle assembly for 102" trailer with standard configuration (excluding hubs, bearings, brake drums) is 167 kg (369 lb). The fully dressed axle – (Arvin Meritor Trailer Axles, 1997) has mass of 333 kg (735 lb).

Methodology of the trailer axle and suspension modeling was the same as for the two suspension systems already described. The FE model of the complete trailer chassis is presented in Figure 4.42. An elastic material with non-linear load – deflection curve as depicted in Figure 4.43, was used for the trailer springs in the FE model.

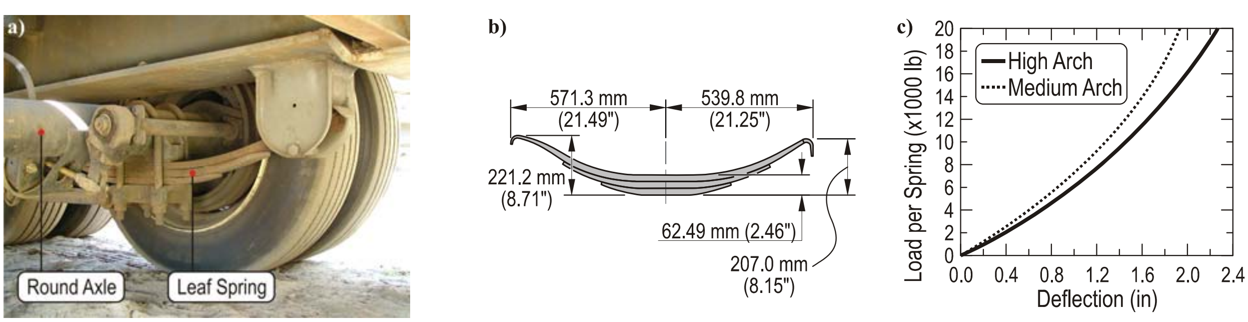

Figure 4.41. Trailer suspension system: a) actual suspension, b) major dimensions of the high arch 3-leaf spring, c) load vs. deflection curve for the selected spring (Spring Appendix, 2004)

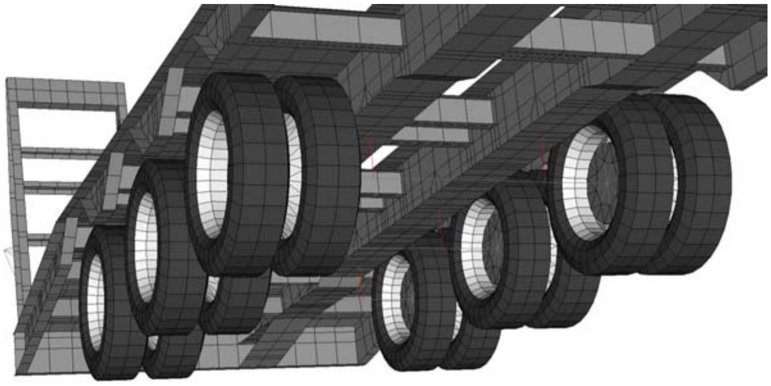

Figure 4.42. FE model of the trailer suspension system

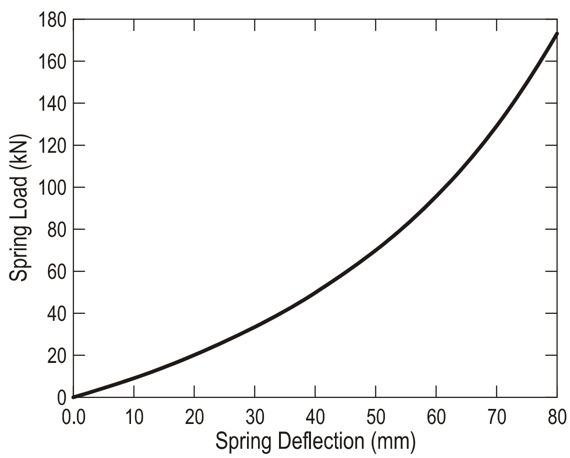

Figure 4.43. Non-linear load vs. deflection curve for the selected leaf spring, which was applied in the FE model

Trailer Frame

Two major parts were distinguished in the trailer structure: the load deck and the top deck. It was assumed that entire structure was made of standard U.S. structural steel profiles including: C-channels, S-flanges and wide flanges. Dimensions obtained from in-situ measurements of the actual object were compared with values for available standardized shapes and the closest profiles were chosen for FE model development. The selected profiles are listed in Table 4.17. All components of the load and top deck of the trailer FE model with their equivalent cross-sections are presented in Figure 4.44 through Figure 4.52.

Table 4.17. Standard profiles selected for the trailer structure (Structural Shapes, 2008)

	Structure components	Profile type	Designation
Load deck	Longitudinal main beams	Wide flange	W18×86
	Side beams	C-channel	C12×20.7
	Transverse beams	S-flange	S6×12.5
	Additional transverse beams	C-channel	C6×8.2
Top deck	Longitudinal main beams	Wide flange	W18×86
	Side beams	C-channel	C8×13.75
	Transverse beams	C-channel	C4×5.4

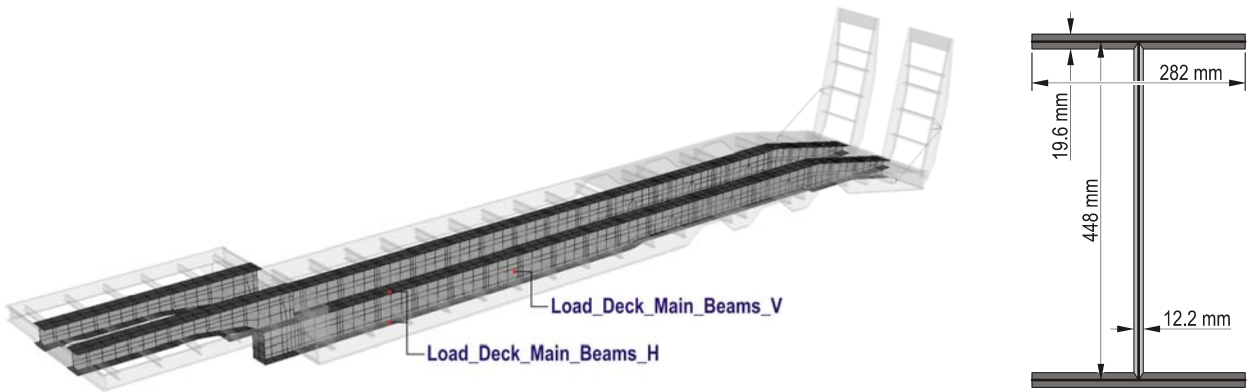

Figure 4.44. FE model of the longitudinal main beams and their cross-section

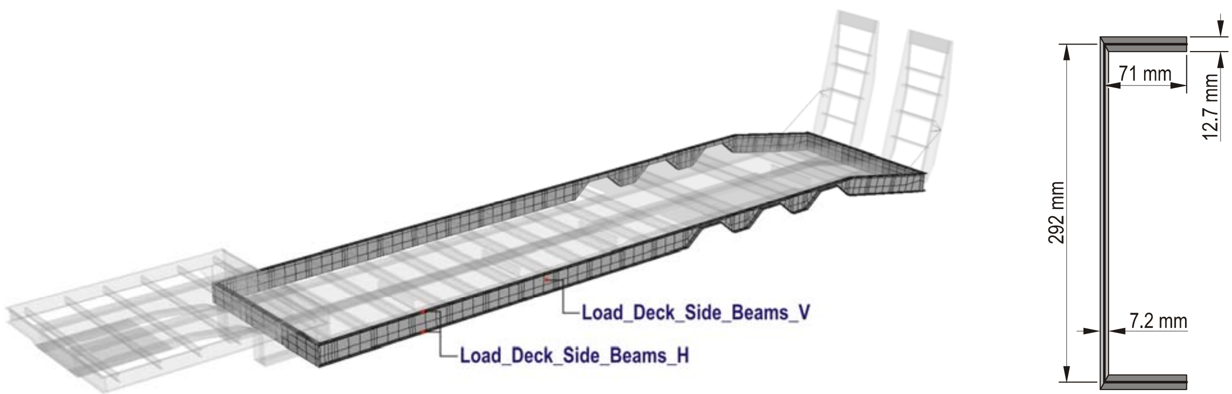

Figure 4.45. FE model of the side beams and their cross-section

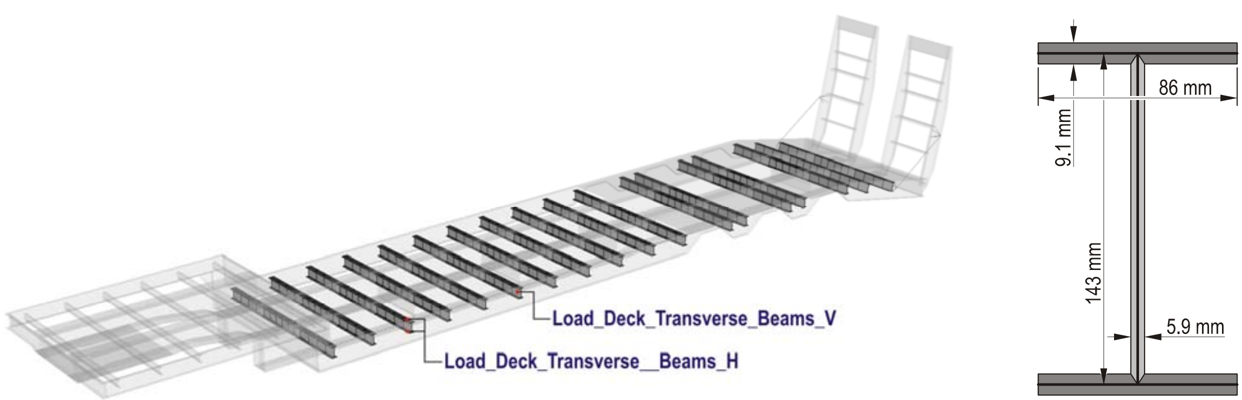

Figure 4.46. FE model of the transverse beams and their cross-section

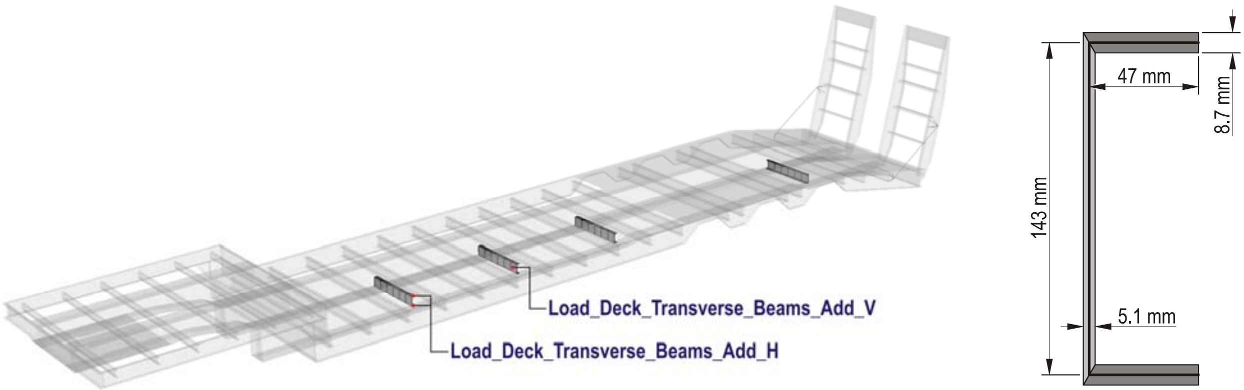

Figure 4.47. FE model of the additional transverse beams and their cross-section

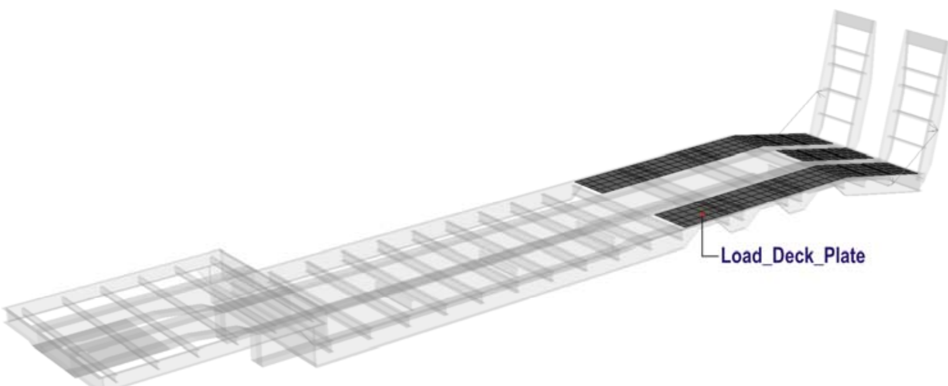

Figure 4.48. FE model of the load deck steel plate

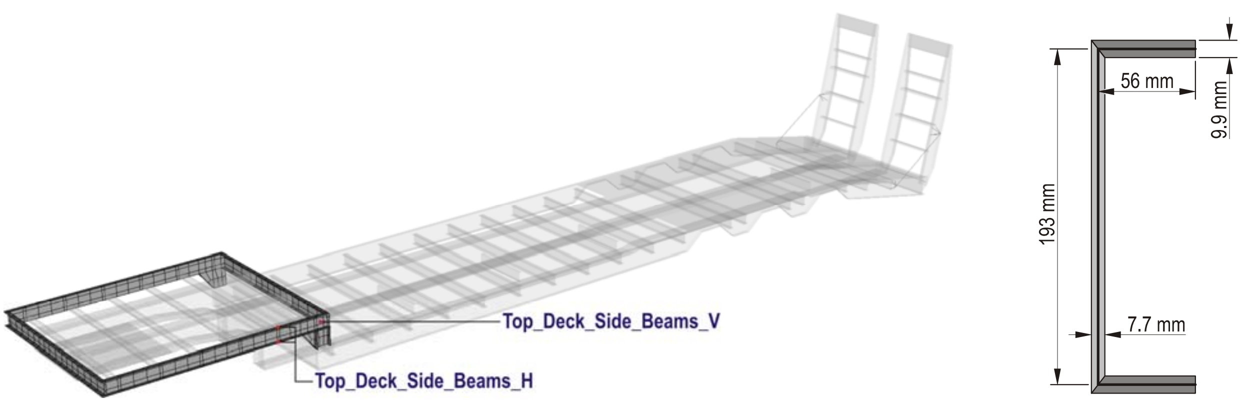

Figure 4.49. FE model of the top deck side beams and their cross-section

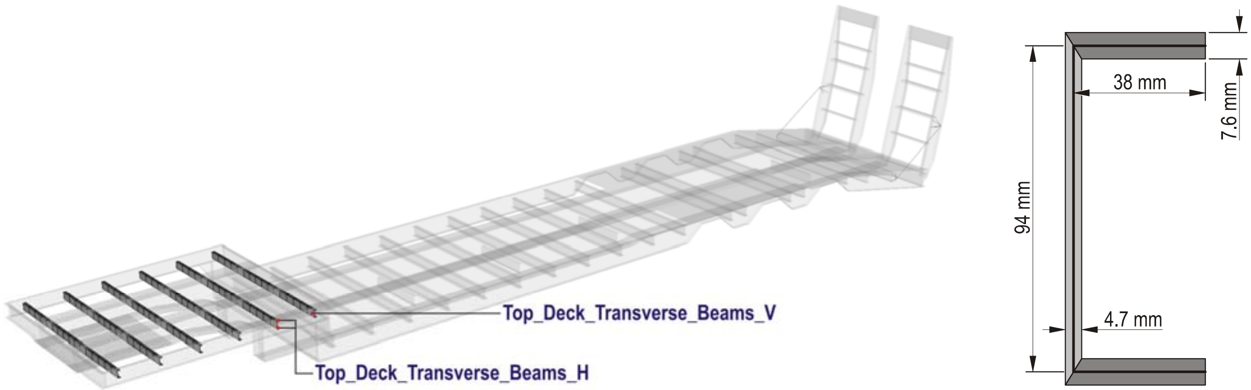

Figure 4.50. FE model of the top deck transverse beams and their cross-section

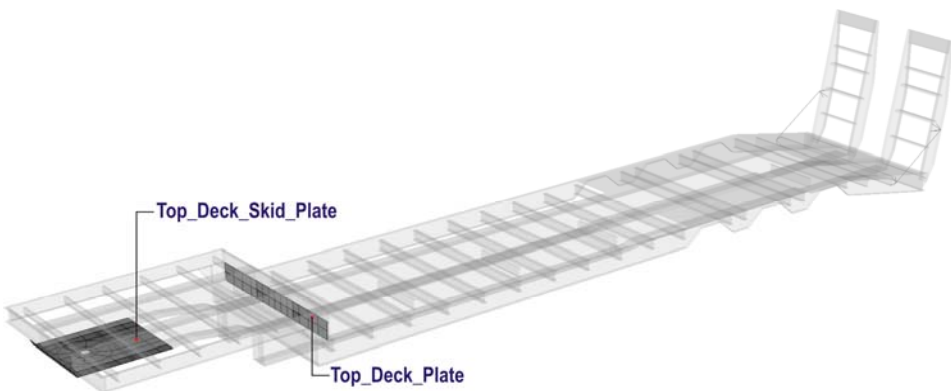

Figure 4.51. FE model of the top deck plate and skid plate

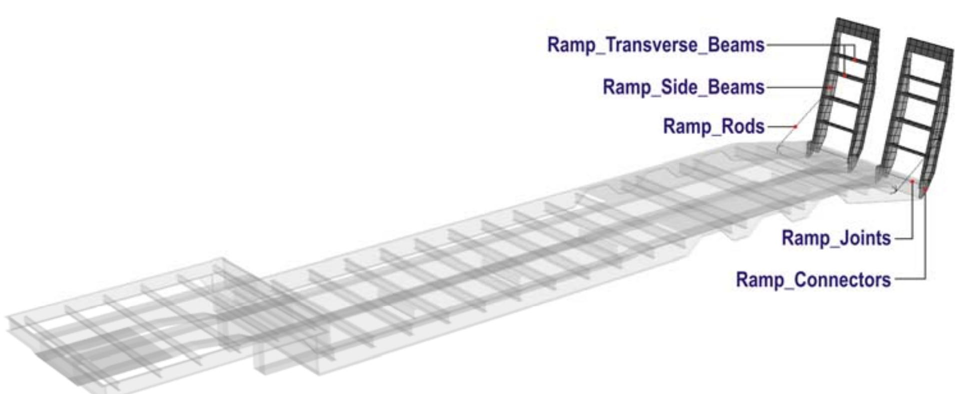

Figure 4.52. FE model of the trailer ramps and the rest components

4.5. Development of a FE model for the Terex T-340 Crane

Cranes are not as popular and usually not as heavy as tractor trailers. However, their footprints are shorter with all axle load concentrated on a smaller area of the bridge. Such load configuration can result in larger moments and higher dynamic impact factors. A mid-size Terex T-340 crane was selected as a representative crane for this project. Its complete FE model, presented in Figure 4.53, consists of over 17,400 finite elements. In-situ measurements, blueprints, and data available from the manufacturers' websites were used for the FE model development. The FE model of the crane is more detailed than those of the other two heavy vehicles described in this report. Most components of the T-340 crane were modeled as rigid bodies. A summary of the complete crane FE model is provided in Table 4.18. Material properties and information regarding the crane FE model are provided in Appendix A.3 in detail.

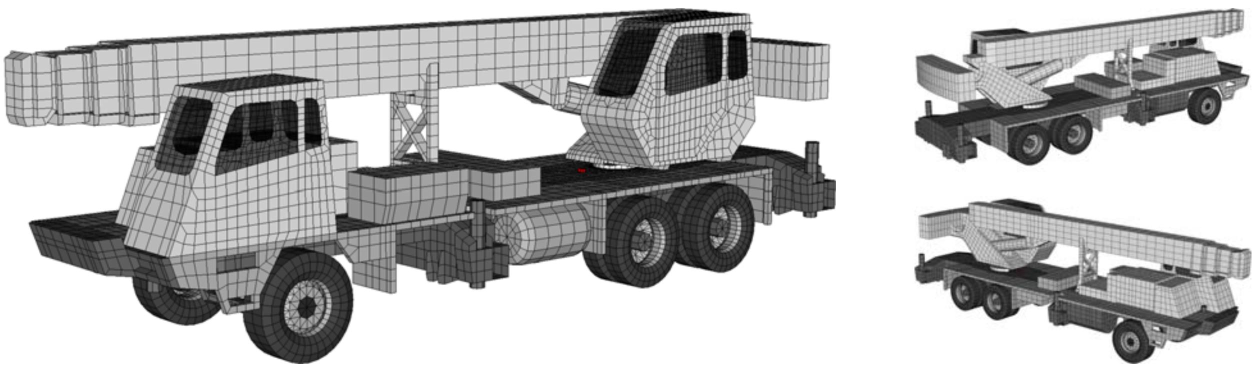

Figure 4.53. The FE model of the Terex T-340 crane

Table 4.18. Summary of the complete FE model of the Terex T-340 crane

Specification		Specification	
Number of parts	153	Number of elements	20,837
Number of nodes	17,401	– solid elements	1,338
Number of material models	29	– shell elements	19,323
		– beam elements	142
		– discrete elements	28
		– mass elements	6

Crane Wheels

The selected crane was equipped with aluminum wheels with hub-piloted mounting system 22.5"×12.25" in size (front axle) and 22.5"×8.25" in size (rear tandem axles). Front wheels had tubeless Goodyear G286A 425/65R22.5 tire, whereas the rear wheels – Dunlop SP 453 11R22.5. Cross-sections of the selected wheels and the tires are presented in Figure 4.54 and their dimensions are provided in Table 4.19 through Table 4.22.

Modeling strategy used for the development of the FE model of the crane wheels was the same as that for the tractor-trailer wheels and tires described in previous sub-chapter. The FE model of the wheel includes: a disc, a rim, and sidewalls and tread of the tire, as presented in Figure 4.55. Thicknesses of shell elements used for the wheels and the tires was based on data available from manufacturer websites; however it was slightly adjusted in some cases to obtain mass similar to that of the actual wheels. Thickness of elements for each part is provided in Table 4.23 and Table 4.24. Dimensions of the FE models of the complete wheel are shown in Figure 4.56.

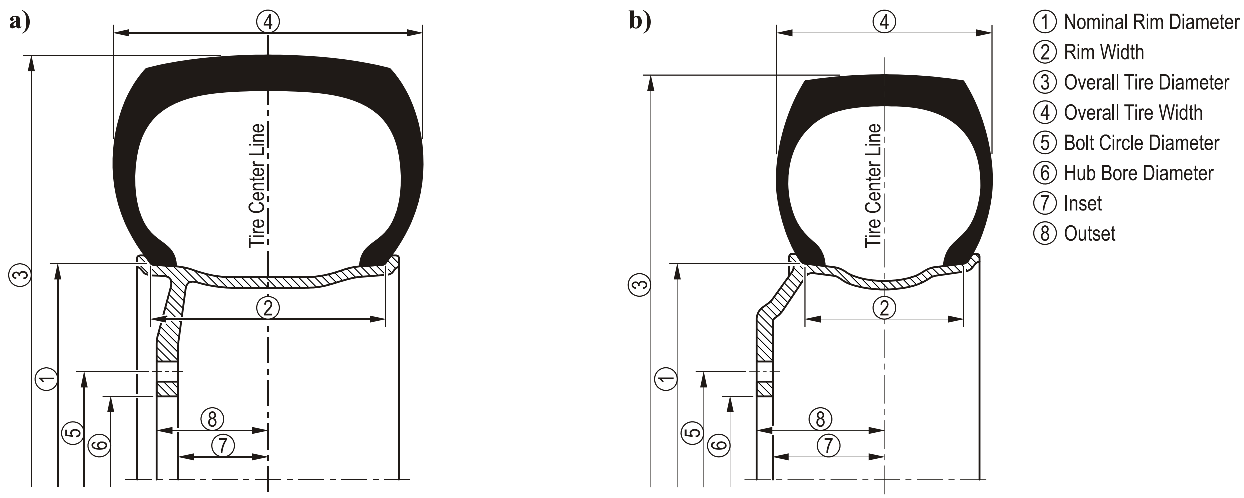

Figure 4.54. Cross-sections of the crane wheel and tire: a) front wheel, b) rear wheel. Dimensions are provided in Table 4.19 through Table 4.22

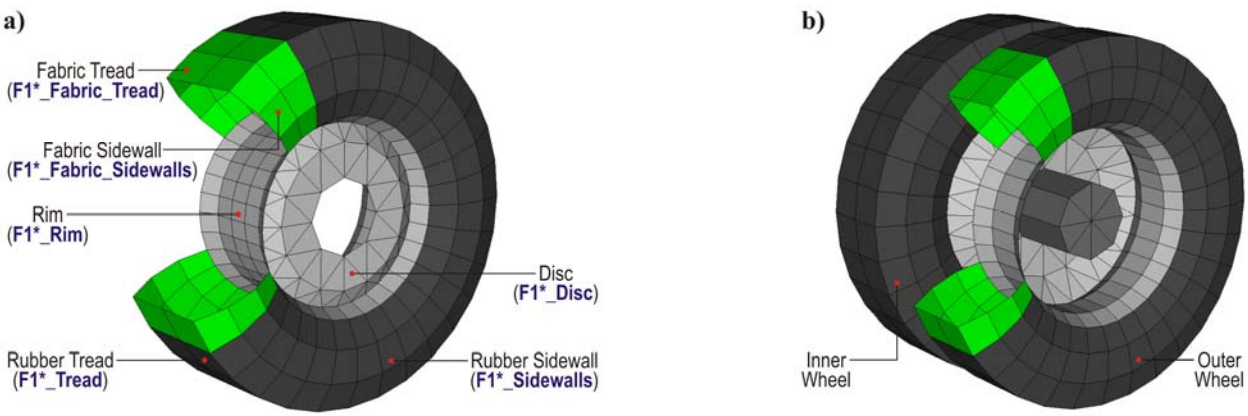

Figure 4.55. FE model of the crane wheel: a) a complete front wheel, b) complete rear dual wheels

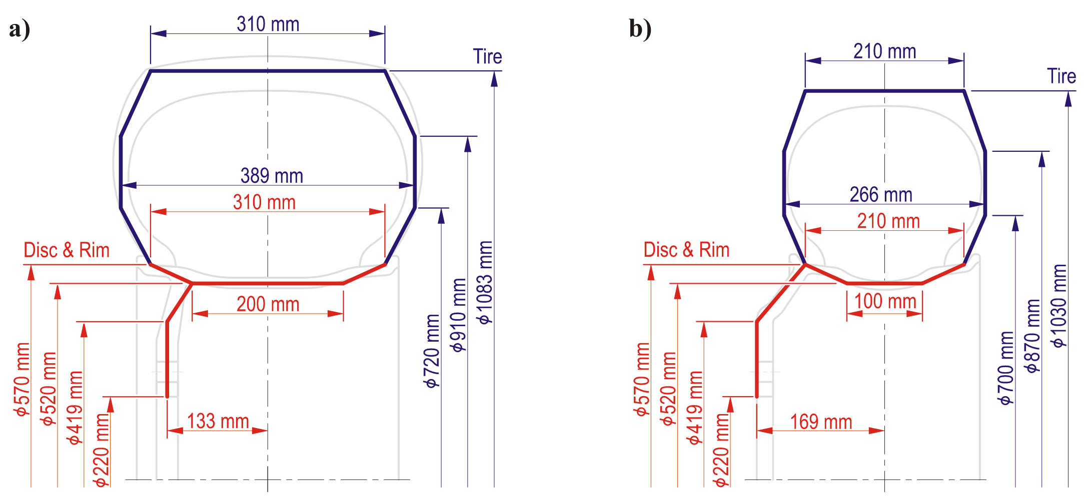

Figure 4.56. Dimensions of the cross-section of the crane wheel FE model: a) front wheel, b) rear wheel

Table 4.19. Dimensions of the Terex T-340 crane front wheels (Alcoa Wheels, 2008)

Specification	Unit	Value	Comments
Size	—	22.5"×12.25"	Alcoa Part No. 82364
Nominal rim diameter (1)	(mm) / (in)	571.5 / 22.5	
Rim width (2)	(mm) / (in)	311 / 12.25	
Bolt circle diameter (5)	(mm) / (in)	285.75 / 11.25	
Hub bore diameter (6)	(mm) / (in)	220.1 / 8.669	
Inset (7)	(mm) / (in)	60.45 / 2.380	
Outset (8)	(mm) / (in)	88.9 / 3.500	
Disc thickness	(mm) / (in)	28.45 / 1.120	
Wheel mass	(kg) / (lb)	32.2 / 71	

Table 4.20. Dimensions of the Terex T-340 crane rear wheels (Alcoa Wheels, 2008)

Specification	Unit	Value	Comments
Size	—	22.5"×8.25"	Alcoa Part No. 88364
Nominal rim diameter (1)	(mm) / (in)	571.5 / 22.5	
Rim width (2)	(mm) / (in)	210 / 8.25	
Bolt circle diameter (5)	(mm) / (in)	285.75 / 11.25	
Hub bore diameter (6)	(mm) / (in)	220.1 / 8.669	
Inset (7)	(mm) / (in)	147.6 / 5.81	
Outset (8)	(mm) / (in)	169.2 / 6.66	
Disc thickness	(mm) / (in)	21.6 / 0.85	
Wheel mass	(kg) / (lb)	21.8 / 48	

Table 4.21. Dimensions of the Terex T-340 crane front tires (Goodyear Tires, 2008)

Specification	Unit	Value	Comments
Size	—	425/65 R 22.5	
Rim width (2)	(mm) / (in)	311 / 12.25	
Overall diameter (3)	(mm) / (in)	1,123 / 44.2	
Overall width (4)	(mm) / (in)	409 / 16.1	
Static loaded radius	(mm) / (in)	516 / 20.3	
Tire mass	(kg) / (lb)	92 / 202	
Single max load	(kg) / (lb)	5,150 / 11,400	
Single inflation	(kPa) / (psi)	830 / 120	

Table 4.22. Dimensions of the Terex T-340 crane rear tires (Dunlop Truck Tires, 2008)

Specification	Unit	Value	Comments
Size	—	11 R 22.5	
Rim width (2)	(mm) / (in)	210 / 8.25	
Overall diameter (3)	(mm) / (in)	1,070 / 42.1	
Overall width (4)	(mm) / (in)	285 / 11.2	
Static loaded radius	(mm) / (in)	501 / 19.7	
Tire mass	(kg) / (lb)	54 / 119	
Single max load	(kg) / (lb)	3,000 / 6,610	
Dual max load	(kg) / (lb)	2,325 / 6,005	
Single inflation	(kPa) / (psi)	830 / 120	
Dual inflation	(kPa) / (psi)	830 / 120	

Table 4.23. Thickness of elements used for the crane front wheel FE model

Wheel	Part name	Number of elements	Thickness (mm)
Disc	F1*_Disc	72	28.5
Rim	F1*_Rim	160	12.2
Tire			
Fabric sidewalls	F1*_Fabric_Sidewalls	192	2.0
Fabric tread	F1*_Fabric_Tread	64	3.0
Rubber sidewalls	F1*_Sidewalls	192	18.8
Rubber tread	F1*_Tread	64	40.0

Table 4.24. Thickness of elements used for the crane rear wheel FE model

Wheel	Part name	Number of elements	Thickness (mm)
Disc	R*_Disc	72	21.6
Rim	R*_Rim	96	6.9
Tire			
Fabric sidewalls	R*_Fabric_Sidewalls	192	2.0
Fabric tread	R*_Fabric_Tread	64	3.0
Rubber sidewalls	R*_Sidewalls	192	10.4
Rubber tread	R*_Tread	64	40.0

Properties of aluminum, rubber and fabric used for the FE model of the crane wheel are provided in Appendix A.3. Calculated mass of the complete FE model of the wheel was compared with the actual object in Table 4.25 and Table 4.26.

Table 4.25. Comparison between calculated mass of the complete crane front wheel FE model and the manufacturer data for the actual wheel (Alcoa Wheels, 2008), (Goodyear Tires, 2008)

FE model part name	Calculated mass		Actual component	Mass
F1*_Disc	14.660 kg	32.198 kg	Wheel	32.200 kg
F1*_Rim	17.538 kg			
F1*_Fabric_Sidewalls	2.834 kg	92.000 kg	Tire	92.000 kg
F1*_Fabric_Tread	3.159 kg			
F1*_Sidewalls	33.355 kg			
F1*_Tread	52.652 kg			

Table 4.26. Comparison between calculated mass of the complete crane rear wheel FE model and the manufacturer data for the actual wheel (Alcoa Wheels, 2008), (Dunlop Truck Tires, 2008)

FE model part name	Calculated mass		Actual component	Mass
R*_Disc	14.879 kg	21.800 kg	Wheel	21.800 kg
R*_Rim	6.921 kg			
R*_Fabric_Sidewalls	2.401 kg	54.001 kg	Tire	54.000 kg
R*_Fabric_Tread	2.035 kg			
R*_Sidewalls	15.643 kg			
R*_Tread	33.922 kg			

Crane Suspension

Selected crane was equipped with heavy duty front steer axle. It was a deep drop I-beam type axle suspended on two 14-leaf springs with two shock absorbers, as depicted in Figure 4.57a. Total mass of the similar Meritor FL-943 Easy Steer axle is 218 kg (480 lb) including steering arm and both hubs but no brakes (Arvin Meritor Products, 2003). That mass was distributed between corresponded parts in FE model. The I-beam axle was modeled using 4-node shell elements, as presented in Figure 4.57b. Several 1-D beam elements were located at the ends of I-beam model. They were connected with drum FE model using revolute joints allowing drum to rotate about axle. All mentioned components were modeled as rigid bodies.

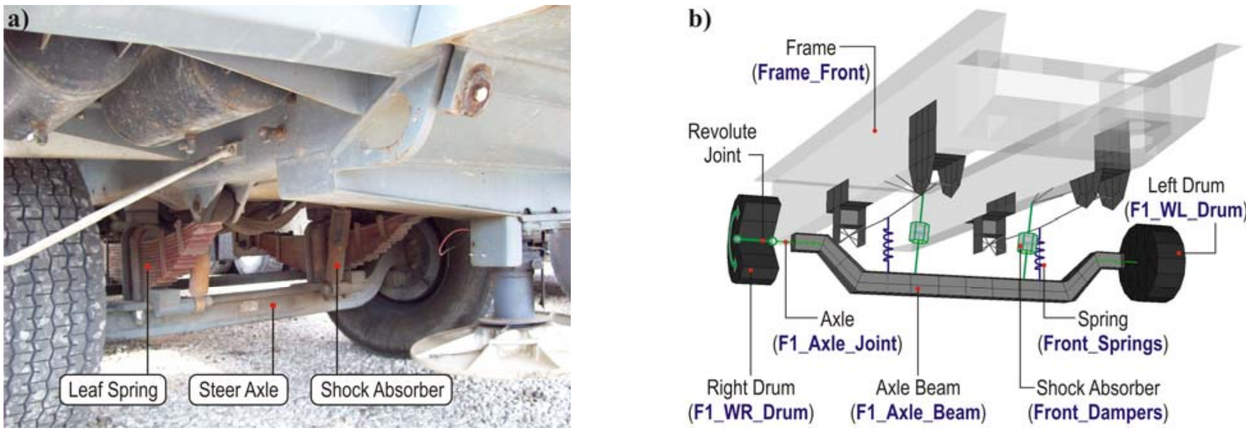

Figure 4.57. Front suspension system of the Terex T-340 crane:
a) actual object, b) FE model

Vertical movements of the front axle FE model were possible due to cylindrical joints (Figure 4.58) similar to ones used in the tractor-trailer suspension FE model. In addition, two types of discrete elements were applied in FE model of the crane suspension – a linear spring and linear damper. The spring elements were located exactly over the I-beam FE model, however forces transmitted by them were distributed through additional beam elements to the points corresponded to the leaf spring brackets in the actual object. The damper elements were not vertically positioned. There was a tilt angle close to one in the tested vehicle.

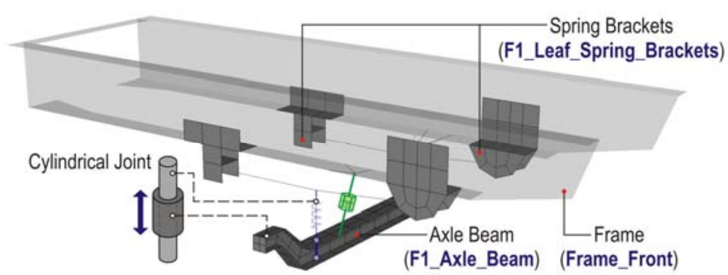

Figure 4.58. Cylindrical joint in the crane front suspension FE model

Rear suspension of the selected crane was quite simple and easy for modeling. The crane was equipped with 40,000 lb capacity tandem drive axles mounted on equalizer beams to distribute weight evenly (Truck Cranes Specifications, 1997), as presented in Figure 4.59a. In addition, the torque rods were installed between axle housings and frame to ensure an appropriate kinematics of the complete system Figure 4.59b. All main components were reflected in FE model of the suspension system, as depicted in Figure 4.60.

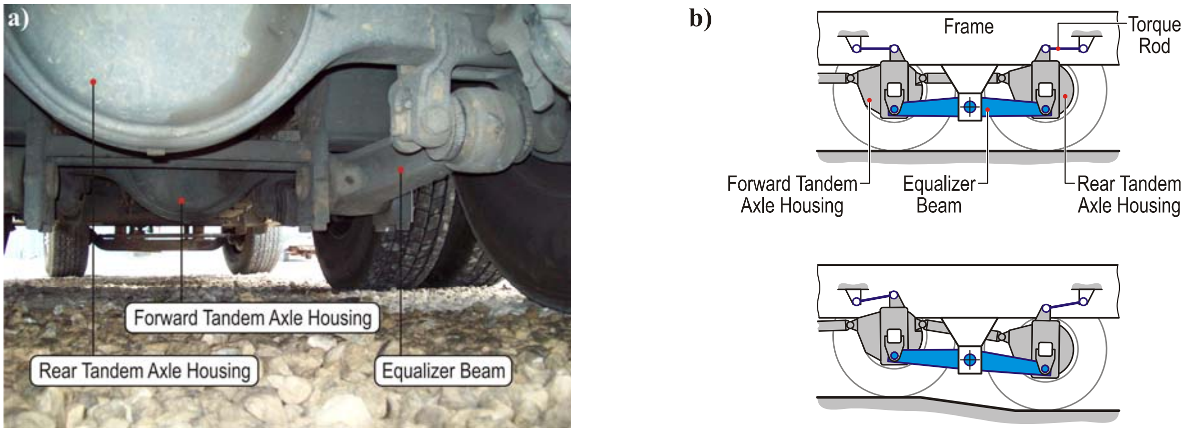

Figure 4.59. Rear suspension system of the Terex T-340 crane:
a) actual object, b) kinematic scheme of the suspension with equalizer beams

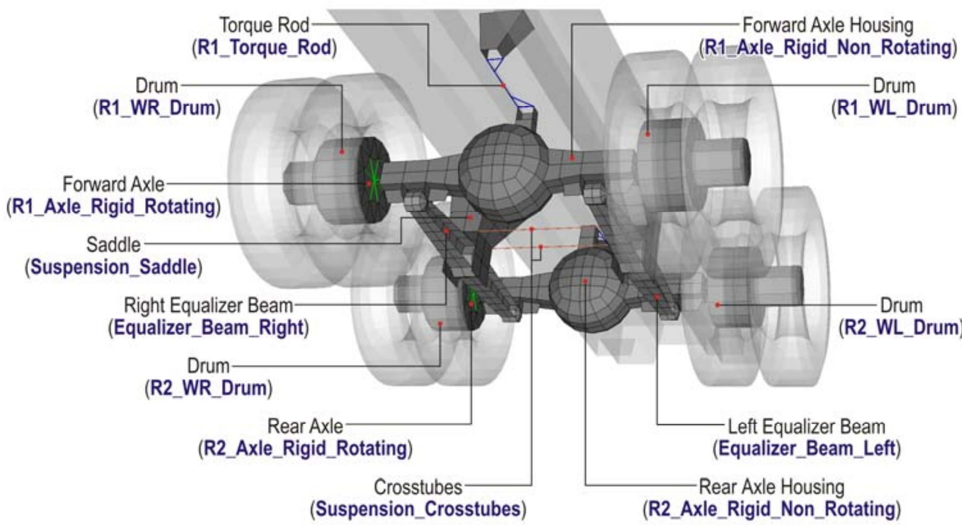

Figure 4.60. FE model of the rear suspension system of the Terex T-340 crane

The masses of each component were based on available data of similar ones as follows: 751 kg (1658 lb) for Eaton D40-170 tandem axles (Roadranger Specification Guide, 2008) and 408 kg (900 lb) for R-Series Hendrickson solid mount suspension (Truck Suspension Systems, 2008). These masses were distributed between appropriate parts in the FE model.

Axle housings, equalizer beams and suspension saddle assembly were modeled as rigid bodies using 2-D shell elements. Rotating rigid axles modeled using 1-D beam elements were located inside the non-rotating ones – axle housing FE models. Beam elements were also used for torque rod modeling. Total of 12 revolute joints (LS-DYNA Keyword User's Manual, 2007) were applied in the rear suspension FE model, as presented in Figure 4.61. They allowed each parts to move in the same way as corresponded components in the actual object.

Several rubber bushing were applied in the actual suspension system to absorb shock and reduce vibration. These components were not straight reflected in FE model to make it less complicated. However, it was decided to used additional discrete spring and damper elements between each parts (Figure 4.62) to achieve similar effect. The values of the spring stiffnesses and damping coefficients were relatively low and determined using trial and error method.

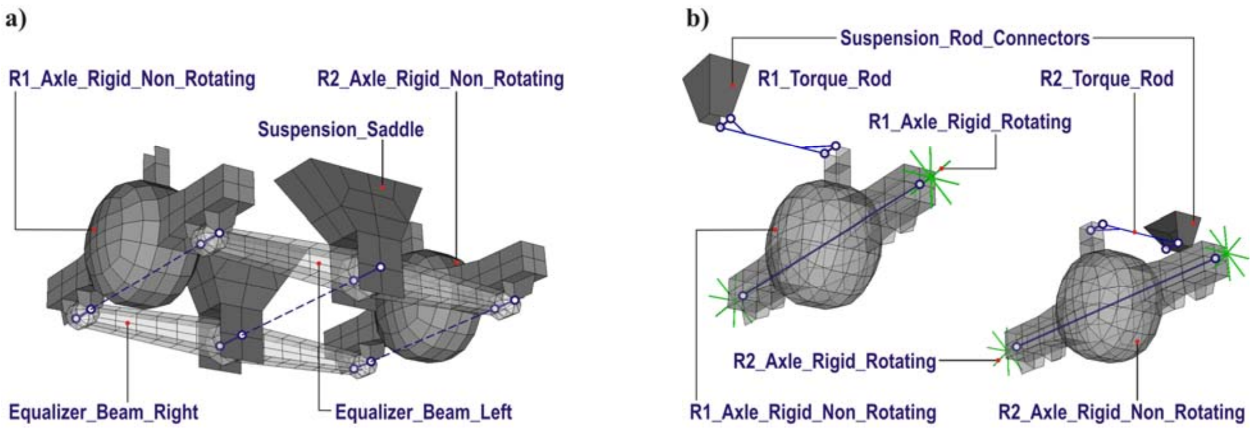

Figure 4.61. Constrained revolute joints in FE model of the crane rear suspension system

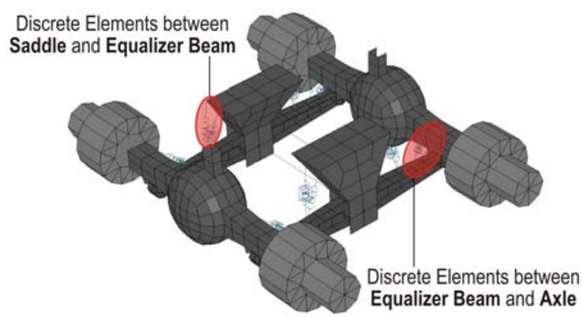

Figure 4.62. Discrete elements – linear springs and viscous dampers – applied in the FE model of the crane rear suspension system

Crane Frame and Carrier Components

Selected crane was equipped in triple box construction frame made from high strength alloy steel (Truck Cranes Specifications, 1997). FE model of the crane frame consisted of two sections: the front and the main one, as depicted in Figure 4.63. Both were modeled as using 2-D shell elements. The middle part of the main section under the turntable connection included additional reinforcement in the form of steel plates which were also modeled as extra layers of finite elements (see Figure 4.63). Full aluminum deck was modeled using 2-D shell elements. All above-mentioned components were considered as the elastic parts in the FE model.

Selected crane had four independent hydraulic outriggers extended on left and right side and one additional in the front next to the driver cab. All components of each outrigger set (Figure 4.64) were modeled using 2-D shell elements except for horizontal and vertical hydraulic cylinders which were modeled by 3-D solid elements. The rest of the crane carrier components, including driver cab, hood, front bumper, tanks and hand tool boxes (Figure 4.64), were modeled using 2-D shell elements. Most of them were considered as rigid parts.

It is worth to say that the crane carrier was not positioned horizontally in its travel configuration, as depicted in Figure 4.65. It was caused by differences in the wheel diameters in the front and back as well as a chassis structure itself.

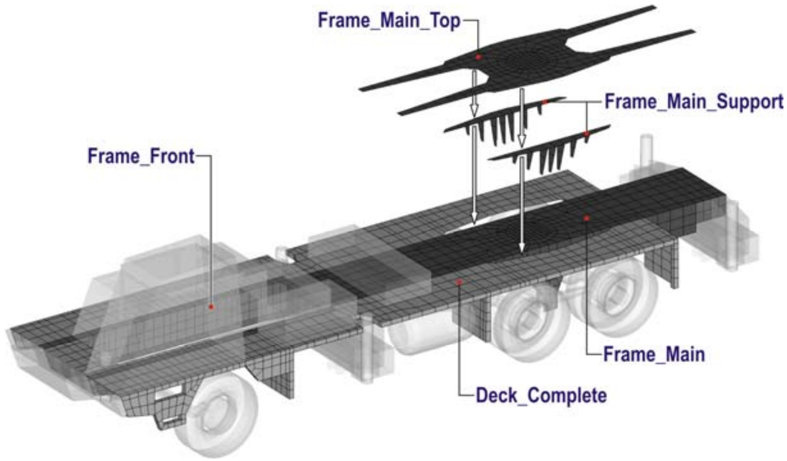

Figure 4.63. FE model of the crane frame and deck

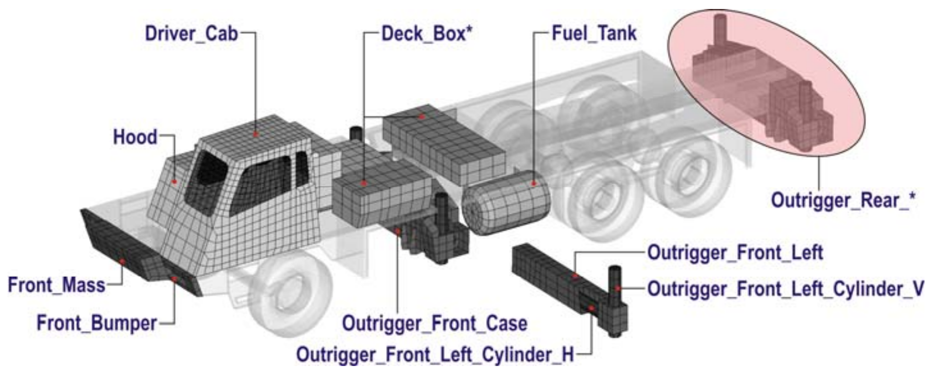

Figure 4.64. FE models of the outriggers and additional components of the crane carrier

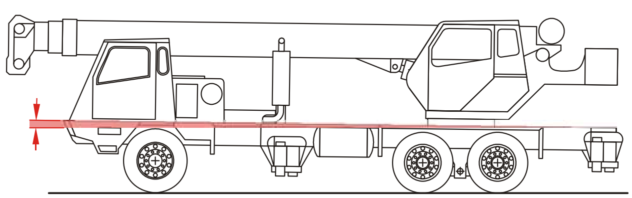

Figure 4.65. Scheme of the Terex T-340 crane in travel configuration

Boom and Upperstructure Equipment

In standard configuration, the Terex T-340 crane was equipped with four section boom, a single boom hoist cylinder, and a counterweight bolted to the turntable frame. All main boom components were modeled, as presented in Figure 4.66. Two-dimensional 4-node shell elements were used for modeling of the boom sections, turntable structure, counterweight case and operator cab. Thicknesses of FE elements were corresponded to the thicknesses of the actual objects. The boom hoist cylinder as well as a telescope cylinder inside the boom were modeled using 3-D solid elements. All upperstructure components were considered as rigid bodies. They were connected together using revolute joint elements, as depicted in Figure 4.67.

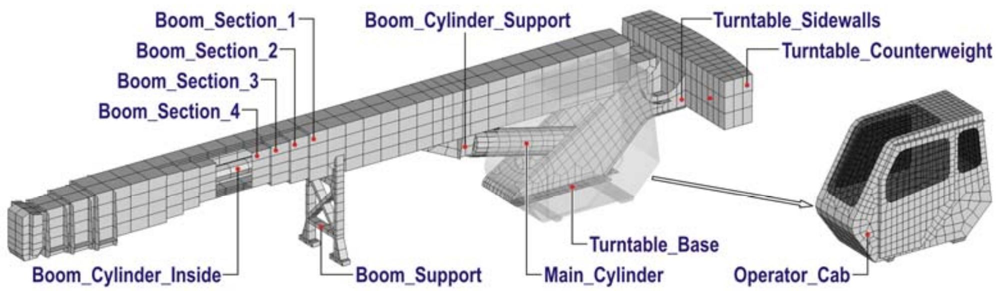

Figure 4.66. FE model of the crane boom and upperstructure

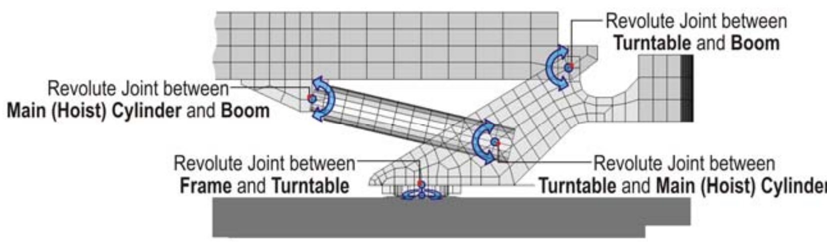

Figure 4.67. Revolute joints applied in FE model of the crane upperstructure

4.6. Development of FE model for the FDOT Truck

FDOT truck was utilized in the earlier research titled: *Analytical and Experimental Evaluation of Existing Florida DOT Bridges* – FDOT Project No. BD493 (Wekezer, Li, Kwasniewski, & Malachowski, 2004). It was used for dynamic testing of the bridge #500133 on US90 to the east of Chattahoochee over Mosquito Creek. Since all data from experimental testing of that bridge was still available it was decided to investigate the effect of time (between 2004 and 2008) on dynamic response of the same bridge under dynamic loading triggered by the same truck. A few minor modifications were introduced in the original FDOT truck model. They included: wheels, a driver cab, a fifth wheel coupling, and suspension systems.

The new model, as presented in Figure 4.68, was developed based on data available from manufacturers' websites and in-situ measurements of the actual vehicle. A complete and improved FE model of consists of over 18,500 finite elements. A summary of the complete FDOT truck FE model is provided in Table 4.27. Material properties and information regarding the FDOT truck FE model are provided in Appendix A.4 in detail.

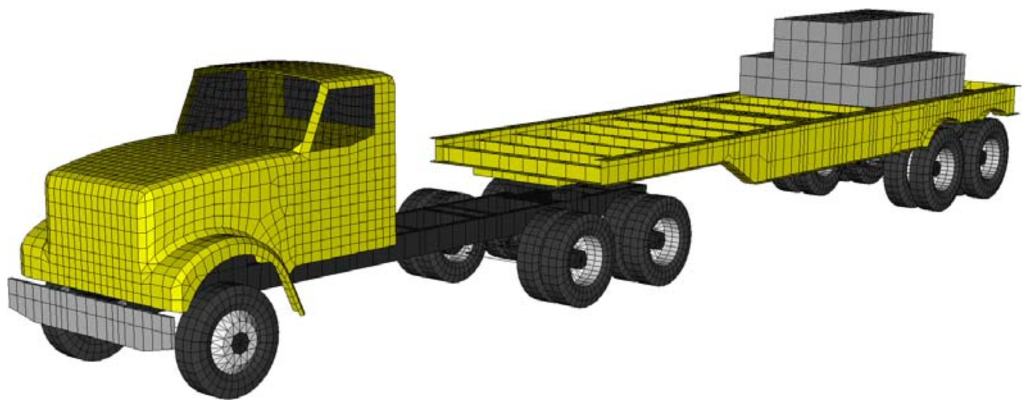

Figure 4.68. The improved FE model of the FDOT truck

Table 4.27. Summary of the complete FE model of the FDOT truck

Specification		Specification	
Number of parts	181	Number of elements	18,569
Number of nodes	13,031	– solid elements	926
Number of material models	25	– shell elements	17,137
		– beam elements	440
		– discrete elements	58
		– mass elements	8

Truck Tractor

The FE model of the FDOT truck tractor was based on the International 5000*i* Series model. It is a three axle tractor with a wheelbase of 5.55 m (218") and tandem axle spacing of 1.42 m (56") in tested configuration. It is equipped with two leaf springs in a front suspension system, and equalizer beams in the back. The FE model of the truck tractor is presented in Figure 4.69. Methodology of modeling was exactly the same as for the truck tractor FE model described earlier in section 4.4.

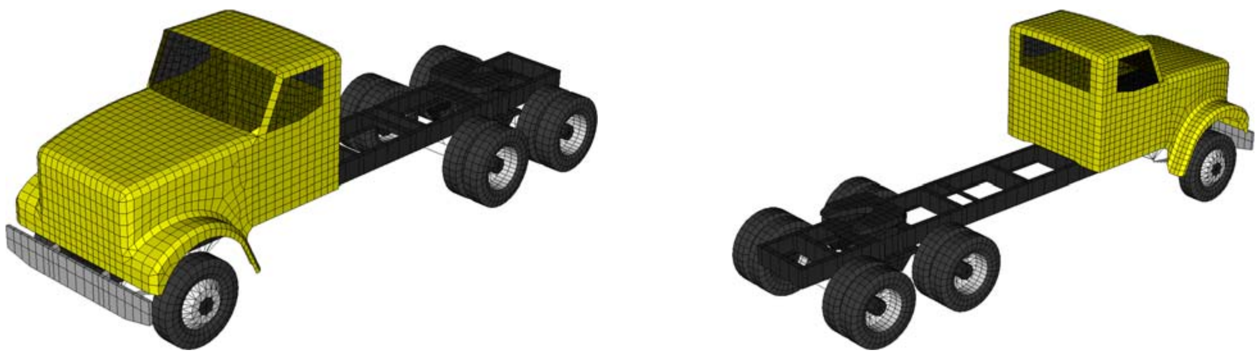

Figure 4.69. FE model of the FDOT truck tractor: front and rear views

Tractor Wheels

The selected truck tractor was equipped with steel 5-hand hole wheels with hub-piloted mounting system 22.5"×8.25" in size, as shown in Figure 4.70a. Each wheel had tubeless Goodyear G149 RSA 11R22.5 tire. Cross-section of the selected wheel and the tire is presented in Figure 4.70b. Their dimensions are listed in Table 4.28 and Table 4.29, respectively.

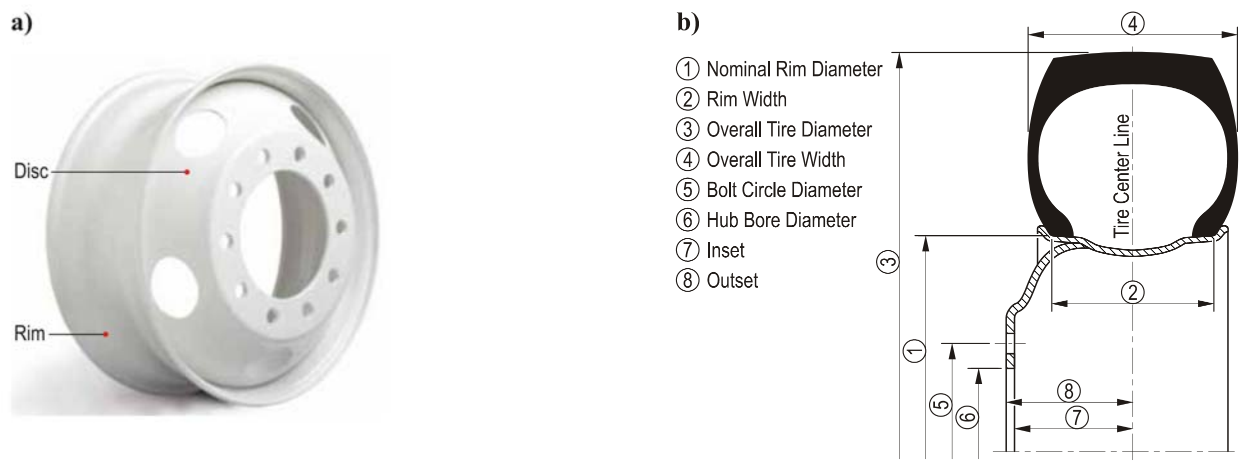

Figure 4.70. The FDOT truck tractor wheel: a) front view of the wheel, b) cross-sections of the wheel and tire – dimensions are provided in Table 4.28 and Table 4.29

Table 4.28. Dimensions of the FDOT tractor wheels (Accu-Lite Steel Wheels, 2007)

Specification	Unit	Value	Comments
Size	—	22.5"×8.25"	
Nominal rim diameter (1)	(mm) / (in)	571.5 / 22.5	
Rim width (2)	(mm) / (in)	210 / 8.25	
Bolt circle diameter (5)	(mm) / (in)	285.75 / 11.25	
Hub bore diameter (6)	(mm) / (in)	220.1 / 8.669	
Inset (7)	(mm) / (in)	156.5 / 6.163	
Outset (8)	(mm) / (in)	167.6 / 6.600	
Disc thickness	(mm) / (in)	11.1 / 0.437	
Wheel mass	(kg) / (lb)	30.8 / 68	

Table 4.29. Dimensions of the FDOT truck tractor tires (Goodyear Tires, 2008)

Specification	Unit	Value	Comments
Size	—	11R22.5	
Rim width (2)	(mm) / (in)	210 / 8.25	
Overall diameter (3)	(mm) / (in)	1,057 / 41.6	
Overall width (4)	(mm) / (in)	277 / 10.9	
Static loaded radius	(mm) / (in)	493 / 19.4	
Tire mass	(kg) / (lb)	57 / 126	
Single max load	(kg) / (lb)	3,000 / 6,610	front axle only
Dual max load	(kg) / (lb)	2,725 / 6,005	rear axles only
Single inflation	(kPa) / (psi)	830 / 120	front axle only
Dual inflation	(kPa) / (psi)	830 / 120	rear axles only

The FE model of the wheel, including: a disc, a rim, and sidewalls and tread of the tire, is presented in Figure 4.71. Four-node shell elements were used for most components, except for discs, which were modeled using three-node elements. The FE model of the tire consists of the sidewalls and the tread parts. Each of these components includes two coinciding layers of four-node shell elements, which represent rubber-like material and fabrics. A simple pressure volume airbag model was used for the FE pneumatic models of the tires. The values of pressure inside the airbags were set up according to data provided in Table 4.29. Thickness of the shell FE elements used for wheels and tires (see Table 4.30) were based on the data from manufacturer websites. Density of some materials was adjusted to obtain total mass similar to the actual wheel, as presented in Table 4.31.

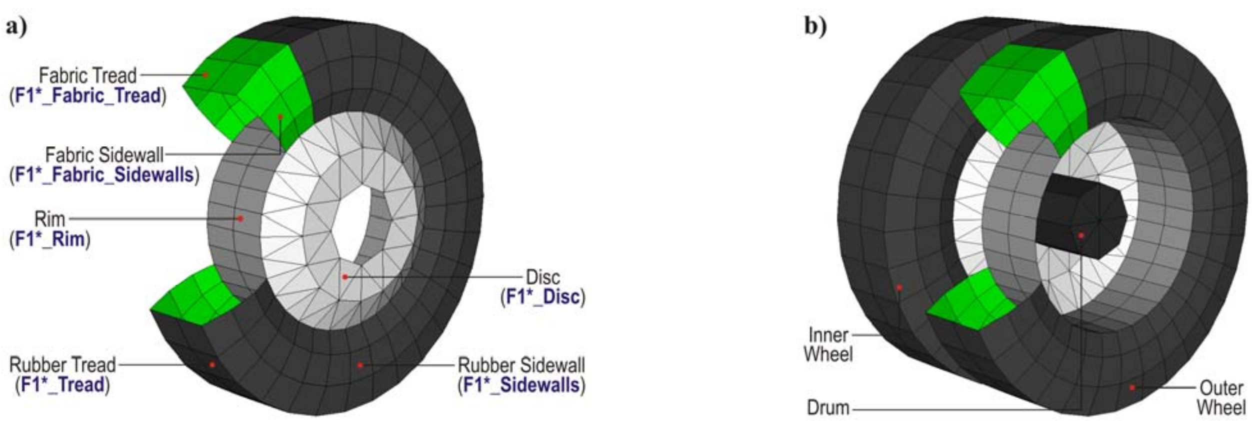

Figure 4.71. FE models of the complete FDOT truck tractor wheels: a) front wheel, b) rear dual wheels

Table 4.30. Thicknesses of elements used for the FDOT truck tractor wheel FE model

Wheel	Part name	Number of elements	Thickness (mm)
Disc	*_Discs	72	11.1
Rim	*_Rim	64	11.1
Tire			
Fabric sidewalls	*_Fabric_Sidewalls	192	2.0
Fabric tread	*_Fabric_Tread	64	3.0
Rubber sidewalls	*_Sidewalls	192	16.0
Rubber tread	*_Tread	64	40.0

Table 4.31. Comparison between calculated mass of the complete wheel FE model and the actual wheel (Accu-Lite Steel Wheels, 2007), (Goodyear Tires, 2008)

FE model part name	Calculated mass		Actual wheel component	Mass
*_Disc	12.369 kg	30.840 kg	Wheel	30.800 kg
*_Rim	18.471 kg			
*_Fabric_Sidewalls	2.263 kg	56.996 kg	Tire	57.000 kg
*_Fabric_Tread	2.010 kg			
*_Sidewalls	21.258 kg			
*_Tread	31.465 kg			

Tractor Suspension

Selected truck tractor was equipped with two leaf springs in the front. Due to complex suspension system It was decided to apply structural elements such as beam elements instead of shell or solid elements. A complete FE model of the front suspension system is presented in Figure 4.72.

The leaf springs were modeled using 2-D beam elements with a rectangular cross-section and dimensions corresponded to the actual object. Each leaves were connected together using the rivet elements (LS-DYNA Keyword User's Manual, 2007). In addition, two discrete dampers were applied in the suspension FE model. Spring dimensions as well as their material properties were similar to ones used previously.

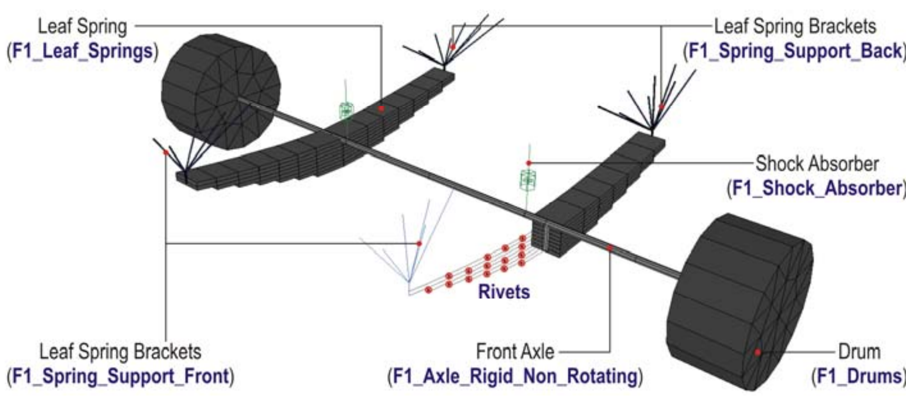

Figure 4.72. FE model of front suspension system of the FDOT truck tractor

The FDOT truck tractor was equipped with the RS Series suspension system (Hendrickson Products, 2008) in the back, as presented in Figure 4.73a. It was a two equalizer beam suspension with additional rubber load cushions between saddle and the tractor frame. Methodology of modeling was similar to one described in sub-chapter 4.5 for the Terex crane, however the FE model was not as detailed as previously. One dimensional beam elements were used for the most parts (Figure 4.73b). Each parts were connected using revolute joints. In addition, several discrete springs and dampers were applied in the FE model (Figure 4.74) to reflect the rubber bushings in the actual object.

Rubber load cushions were modeled using 3-D solid elements and viscoelastic material model. An accurate vertical motion of the suspension saddle FE model was achieved by additional constrains—called cylindrical joints—which prevent displacements in horizontal plane, as shown in Figure 4.75.

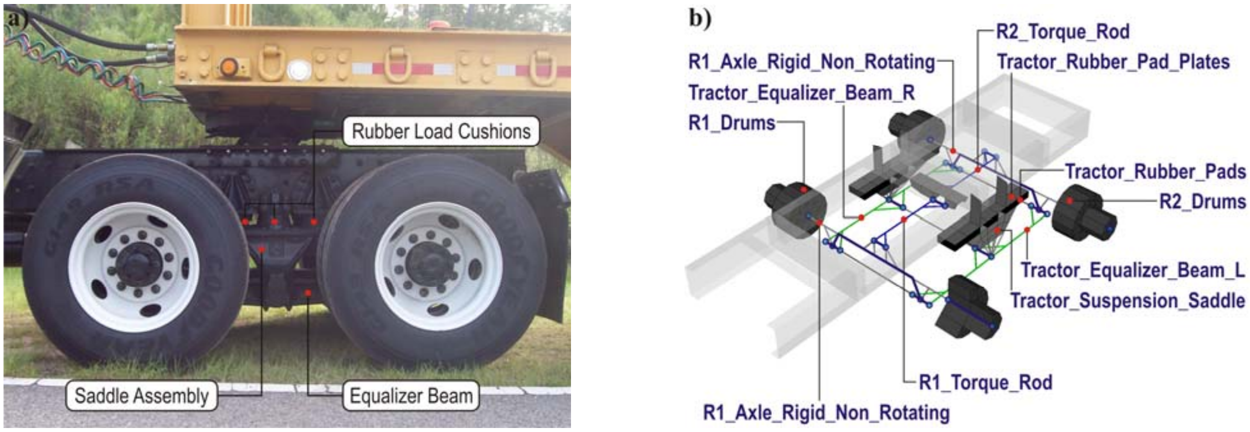

Figure 4.73. Rear suspension system of the FDOT truck tractor: a) actual object, b) FE model

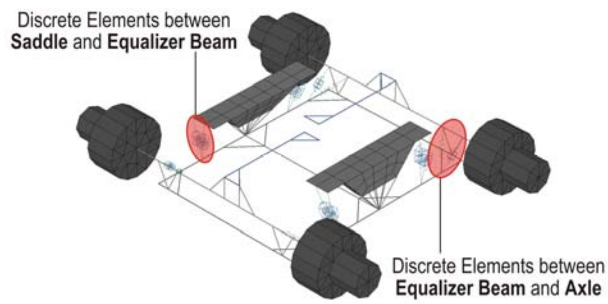

Figure 4.74. Discrete elements – linear springs and viscous dampers – applied in the FE model of the truck tractor rear suspension system

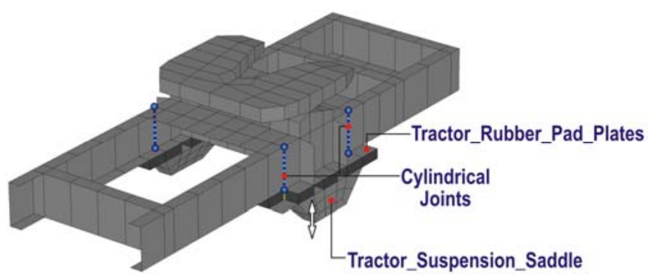

Figure 4.75. Additional cylindrical joints applied in the rear suspension FE model

Tractor Bodywork

Bodywork components of the FDOT truck tractor such as a frame, a bumper and a driver cab were modeled using 2-D shell elements. FE model of the frame consisted of two longitudinal C-channel rails and several transverse beams, as presented in Figure 4.76. Complete frame was characterized by an elastic material model.

A tractor engine and fifth wheel were modeled using 3-D solid elements and considered as rigid bodies. FE model of the engine was attached to the frame. Connection between FE models of the tractor and the trailer was similar to one described in sub-chapter 4.4. The FE model of the FDOT truck was restricted to the straight direction and any movements of the trailer in the horizontal plane were not allowed. Therefore, the fifth wheel and the skid plate of the trailer were rigidly connected by merging coincident nodes.

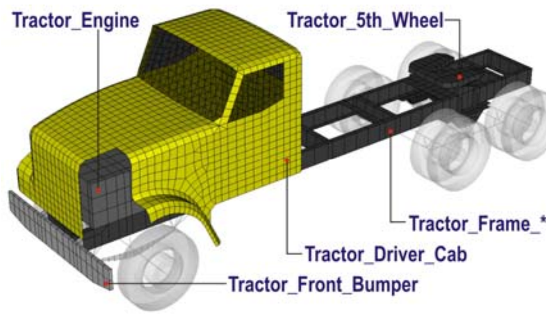

Figure 4.76. FE model of the FDOT truck tractor bodywork

Trailer Wheels

The selected FDOT trailer was equipped with steel 5-hand hole wheels with hub-piloted mounting system 24"×8" in size, similar to those used in the truck tractor. Each wheel had tube-type Goodyear G286 11.00R24 tire. Cross-section of the selected wheel and the tire is presented in Figure 4.77a. Their dimensions are listed in and, respectively.

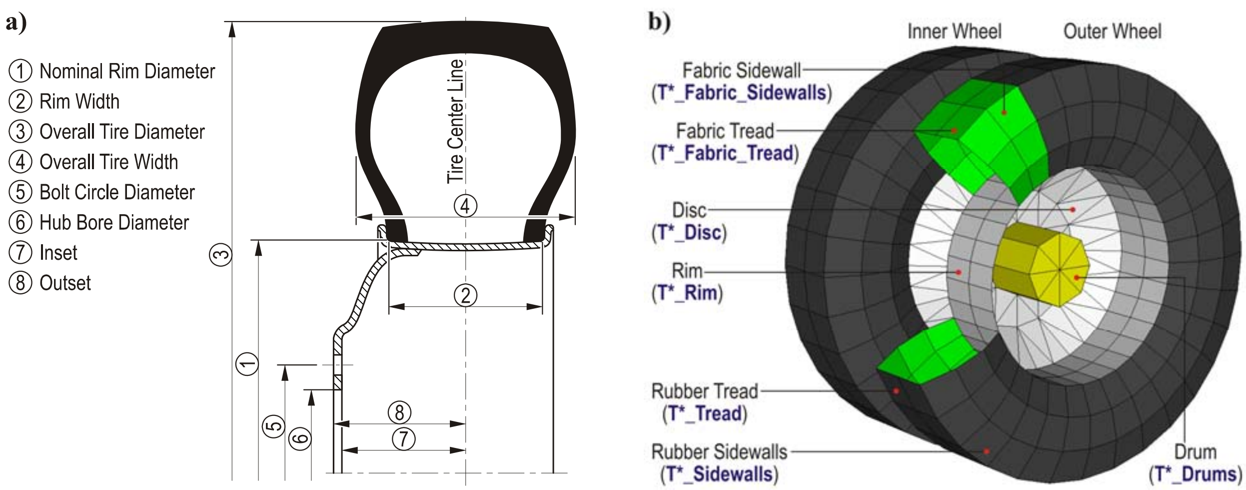

Figure 4.77. The FDOT trailer wheel: a) cross-sections of the wheel and tire – dimensions are provided in Table 4.32 and Table 4.33, b) FE model

Table 4.32. Dimensions of the FDOT trailer wheels (Accu-Lite Steel Wheels, 2007)

Specification	Unit	Value	Comments
Size	—	24"×8"	
Nominal rim diameter (1)	(mm) / (in)	610 / 24.0	
Rim width (2)	(mm) / (in)	203 / 8.00	
Bolt circle diameter (5)	(mm) / (in)	285.75 / 11.25	
Hub bore diameter (6)	(mm) / (in)	220.1 / 8.669	
Inset (7)	(mm) / (in)	164.1 / 6.163	
Outset (8)	(mm) / (in)	174.8 / 6.880	
Disc thickness	(mm) / (in)	10.7 / 0.420	
Wheel mass	(kg) / (lb)	39.0 / 86	

Table 4.33. Dimensions of the FDOT trailer tires (Goodyear Tires, 2008)

Specification	Unit	Value	Comments
Size	—	11.00R24	
Rim width (2)	(mm) / (in)	203 / 8.00	
Overall diameter (3)	(mm) / (in)	1,194 / 47.0	
Overall width (4)	(mm) / (in)	290 / 11.4	
Static loaded radius	(mm) / (in)	559 / 22.0	
Tire mass	(kg) / (lb)	73 / 160	
Single max load	(kg) / (lb)	3,750 / 8,270	
Dual max load	(kg) / (lb)	3,450 / 7,610	
Single inflation	(kPa) / (psi)	830 / 120	
Dual inflation	(kPa) / (psi)	830 / 120	

The FE model of the trailer wheel, including: a disc, a rim, and sidewalls and tread of the tire, is presented in Figure 4.77b. Modeling strategy used for the development of the FE model of the trailer wheels was exactly the same as for the tractor wheels and tires. Four-node shell elements were used for most components, except for discs, which were modeled using three-node elements. The FE model of the tire consists of the sidewalls and the tread parts. Each of these components includes two coinciding layers of four-node shell elements, which represent rubber-like material and fabrics. A simple pressure volume airbag model was used for the FE pneumatic models of the tires. The values of pressure inside the airbags were set up according to data provided in Table 4.33. Thickness of the shell FE elements used for wheels and tires (see Table 4.34) were based on the data from manufacturer websites. Density of some materials was adjusted to obtain total mass similar to the actual wheel, as presented in Table 4.35.

Table 4.34. Thicknesses of elements used for the truck tractor wheel FE model

Wheel	Part name	Number of elements	Thickness (mm)
Disc	T*_Discs	72	10.7
Rim	T*_Rim	64	10.7
Tire			
Fabric sidewalls	T*_Fabric_Sidewalls	192	2.0
Fabric tread	T*_Fabric_Tread	64	3.0
Rubber sidewalls	T*_Sidewalls	192	18.0
Rubber tread	T*_Tread	64	40.0

Table 4.35. Comparison between calculated mass of the complete wheel FE model and the actual wheel (Accu-Lite Steel Wheels, 2007), (Goodyear Tires, 2008)

FE model part name	Calculated mass		Actual wheel component	Mass
T*_Disc	17.513 kg	39.000 kg	Wheel	39.000 kg
T*_Rim	21.487 kg			
T*_Fabric_Sidewalls	3.141 kg	72.996 kg	Tire	73.000 kg
T*_Fabric_Tread	2.204 kg			
T*_Sidewalls	33.137 kg			
T*_Tread	34.514 kg			

Trailer Suspension

The FDOT trailer had very stiff suspension in the form of two equalizer beams without any additional rubber cushions (Figure 4.78a). Modeling strategy used for the development of the suspension FE model was exactly the same as for the FDOT truck tractor rear suspension. One dimensional beam elements were used for the most parts (Figure 4.78b). Each parts were connected using revolute joints. Several discrete springs and dampers were also applied similarly to the tractor suspension FE model.

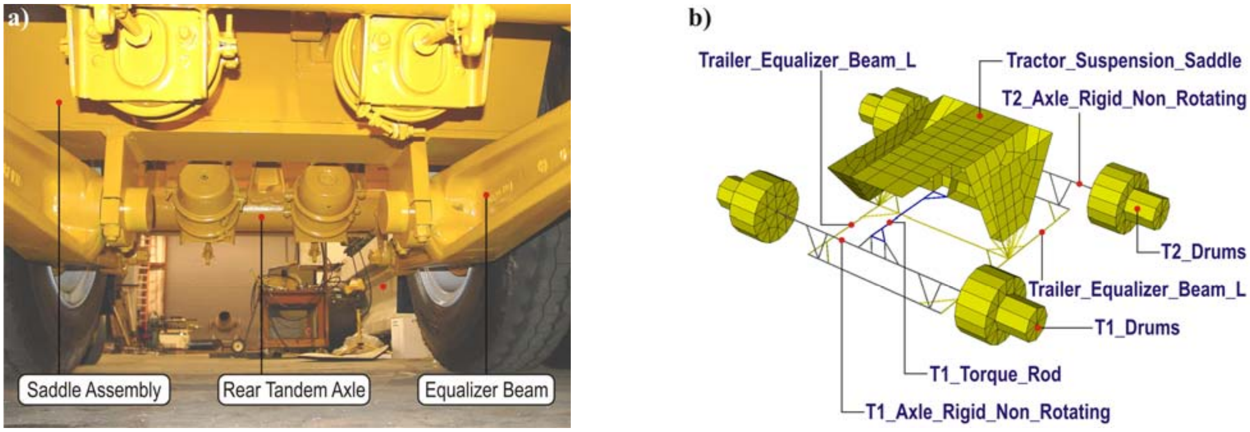

Figure 4.78. Suspension of the FDOT trailer: a) actual object, b) FE model

Trailer Frame

The trailer FE model was slightly modified in comparison to the original model developed for the previous project. Modification were related to the fifth wheel coupling and suspension saddle. In addition, several parts of existing FE model were re-meshed. Original FE model of the trailer was developed based on the drawings provided by the FDOT Structures Lab, along with in situ measurements (Wekezer, Li, Kwasniewski, & Malachowski, 2004). 2-D shell elements were applied to create three dimensional structure of the trailer frame, as depicted in Figure 4.79.

The trailer frame included two main longitudinal I-beams on both sides and several transverse C-channels (front section) and I-beams (middle and back section). Two additional longitudinal I-beams were located in the rear section above the suspension saddle. Concrete blocks applied as a cargo during the experimental tests were modeled as rigid body using 3-D solid elements.

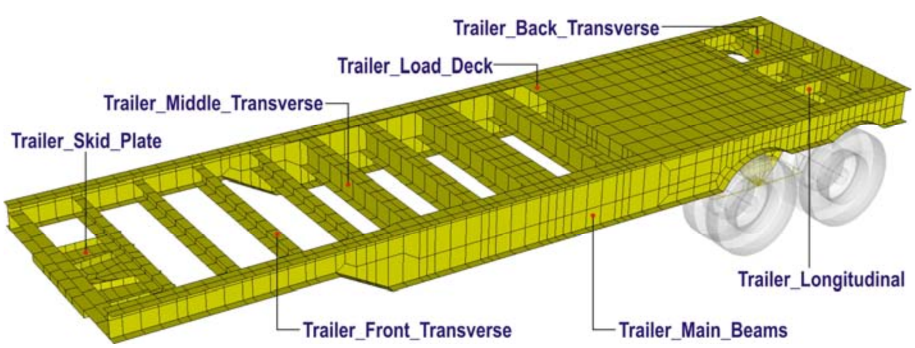

Figure 4.79. FE model of the FDOT trailer

4.7. Motion of the Vehicle FE Models

FE model of the vehicles presented in sub-chapter 4.4 through 4.6 were used in static as well as dynamic analysis. The first case included axle load measurements but also the static analysis on the bridge FE model. During such analysis the vehicle models were dropped on rigid walls or the bridge slab FE model, respectively. Dynamic analysis required a motion of the vehicle FE model with a constant velocity. It was executed by a coupling of two commands available in LS-DYNA code – *INITIAL_VELOCITY_GENERATION and *BOUNDARY_PRESCRIBED_MOTION_SET (LS-DYNA Keyword User's Manual, 2007). The first one was active only at the beginning of analysis. It was attributed to all nodes of the FE model which had to move with a translational velocity (Figure 4.80). In the next and following time steps the motion of the vehicle FE model was achieved by rotation of wheels.

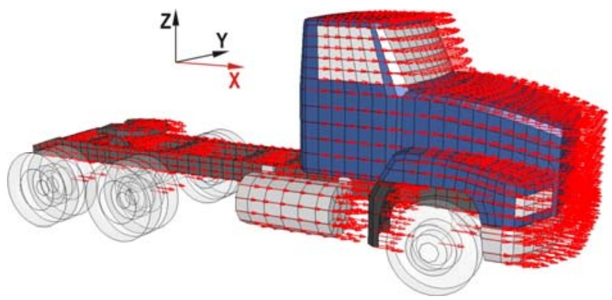

Figure 4.80. Translational initial velocity vectors attributed to appropriate nodes of the truck tractor FE model

The second command *BOUNDARY_PRESCRIBED_MOTION_SET was attributed to all nodes belonging to the treads, sidewalls and rims of the wheels for each axle separately. Rotational motion was executed about a vector parallel to suitably defined base vector. All base vectors were oriented according to *Y*-axis and their tails were located in the center of each axle, as presented in Figure 4.81.

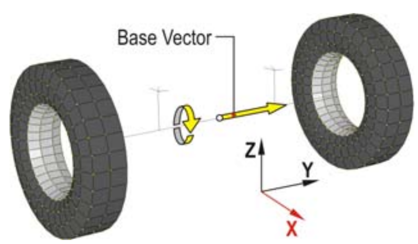

Figure 4.81. Orientation of an exemplary base vector and corresponded node set

Figure 4.82 shows an exemplary cycloid generated by the rolling front wheel that confirms a correctness of an applied strategy for the rotation of wheels.

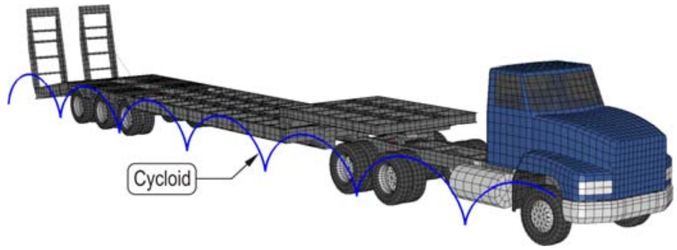

Figure 4.82. A cycloid generated by the rolling front wheel of the truck tractor

5. SUSPENSION TESTING FOR SELECTED VEHICLES

Suspension testing was carried out at the Broadmoor Estate in Tallahassee. The most desirable characteristics of the selected track included:

- a gated property to ensure safety during testing with heavy truck,
- close proximity to Tallahassee to save money and time,
- a long, straight and flat section of road, which would allow for developing desirable vehicle speeds.

The heavy vehicle was driven over a speed bump, called "a half-round", during the experimental tests. A standard speed bump made of asphalt was used for the tests. Their shapes and dimensions allowed for obtaining the measurable range of vibration for representative points.

The vehicle velocities were varied between 5 and 20 mph. That range was the most common among the tests described in the literature. Lower velocity ensured the driver safety and preserved testing equipment and sensors. However, in some cases the obtained data were not completed due to signal failures or a damage of the gauges.

Accelerations of selected points as well as changes in distance between axles and frame were measured. Identical tests were carried out using numerical simulation in LS-DYNA software and results obtained from both methods were compared. The suspension parameters in the FE model were adjusted until simulation data were matched with experimental results.

The plan for the suspension tests was developed in cooperation with the FDOT Structures Lab. The field tests were based on similar ones reported in the literature (Valášek, Stejskal, Šika, Vaculín, & Kovanda, 1998), (Letherwood & Gunter, 2001), (Lehtonen, 2005), (Gáspár & Kuti, 2006).

5.1. Suspension Tests of the Tractor-Trailer

Suspension tests of the tractor-trailer included 15 runs with different velocities. The vehicle was driven over a speed bump with the speeds of 16, 24 and 32 km/h (10, 15 and 20 mph) without load, and with the speed of 8 and 16 km/h (5 and 10 mph) loaded. Three runs were conducted for each speed to check the validity of obtained results. All considered cases are provided in Table 5.1.

Five displacement gauges were used during the tractor-trailer tests. Three of them with a larger stroke of 150 mm (6") were attached to the shock absorbers in the truck tractor – one per each axle, as presented in Figure 5.1. Two sensors with a stroke of 100 mm (4") were applied in the trailer for the first and the third axle, as shown in Figure 5.2. Characteristics of the gauges used for the tests are provided in Table 5.2.

Fourteen accelerometers were used for the tests (see Figure 5.3). Their characteristics are provided in Table 5.3. Those with a range of ±10g were glued primarily to the axles, whereas ones with a range of ±5g were attached to the frame and load deck of the trailer. Location of the accelerometers was based on the expected range of obtained accelerations – higher for the axles than for the bodywork.

Positions of all displacement gauges and accelerometers are summarized in Table 5.4 and Table 5.5, respectively.

Table 5.1. Summary of all considered cases for the suspension tests of the tractor-trailer

Run #	Pass #	Velocity	Vehicle configuration
01	1	16 km/h (10 mph)	unloaded
02	2		
03	3		
04	1	24 km/h (15 mph)	unloaded
05	2		
06	3		
07	1	32 km/h (20 mph)	unloaded
08	2		
09	3		
10	1	8 km/h (5 mph)	loaded
11	2		
12	3		
13	1	16 km/h (10 mph)	loaded
14	2		
15	3		

Table 5.2. Characteristics of the displacement gauges used for spring deflection measurement during the test

Manufacturer	Penny+Giles	Mechanical Stroke	(mm) / (in)	104 / 4 154 / 6
Model Number	MLS130/100/R/N MLS130/150/R/N	Weight	(g) / (lb)	101 / 0.223 115 / 0.254

Table 5.3. Characteristics of the accelerometers located on the vehicles during the test

Manufacturer	Summit Instruments, Inc.	Rated Output	(mV/g's)	450
Model Number	13200B 13203B	Range	(g's)	±10 ±5
Weight (g) / (lb)	38 / 0.084	Frequency Response / Natural	(Hz)	N.A. / N.A.
Non-Linearity	0.2% Full Scale Reading	Excitation Voltage Used	(V)	10

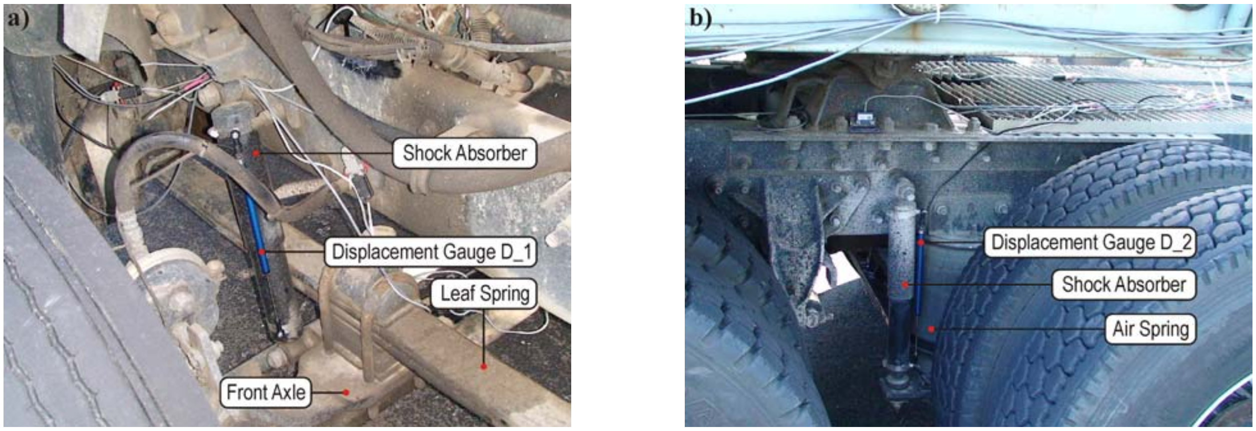

Figure 5.1. Location of the displacement gauges for the truck tractor:
a) front steer axle; b) forward drive tandem axle

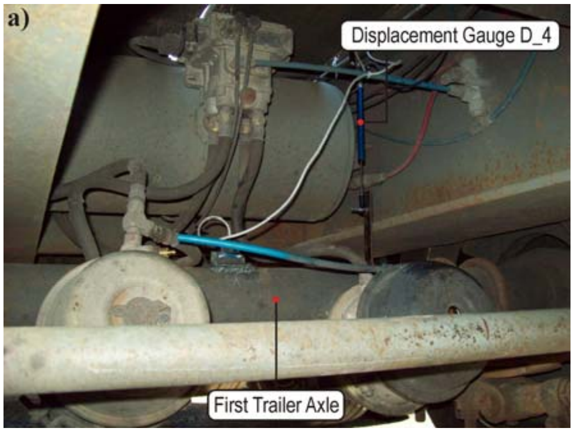

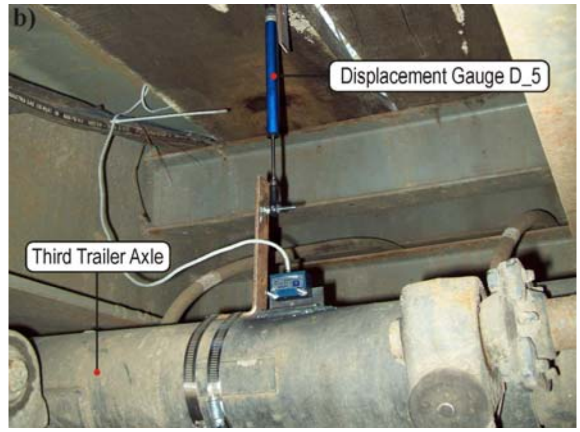

Figure 5.2. Location of the displacement gauges for the trailer:
a) first triadem axle; b) third triadem axle

Table 5.4. Displacement gauge locations for the suspension test of the tractor-trailer

Sensor type	Sensor No.	Stroke	Mounting location
Displacement gauge	D_1	150 mm (6")	Shock absorber of the front suspension system on the passenger side
	D_2	150 mm (6")	Shock absorber of the rear suspension system on the passenger side – forward tandem drive axle
	D_3	150 mm (6")	Shock absorber of the rear suspension system on the passenger side – rear tandem drive axle
	D_4	100 mm (4")	Center of the first trailer triadem axle – between a round axle and the load deck
	D_5	100 mm (4")	Center of the third trailer triadem axle – between a round axle and the load deck

Table 5.5. Accelerometer locations for the suspension test of the tractor-trailer

Sensor type	Sensor No.	Range	Mounting location
Accelerometer	A_01 A_02	±10g	152 mm (6") from the inside edge of the leaf spring mounting block toward the center of the steer axle on the driver/passenger side
	A_03 A_04	±10g	203 mm (8") from the centerline on the driver/passenger side on the forward tandem drive axle channel
	A_05 A_06	±5g	203 mm (8") from the centerline on the driver/passenger side on the rear tandem drive axle channel
	A_07	±10g	On top of the center of the first triadem trailer axle
	A_08	±5g	On top of the center of the third triadem trailer axle
	A_09 A_10	±5g	Directly above the steer axle on the top of the frame on the driver/passenger side
	A_11 A_12	±5g	To the right/left of the center bolt on the fifth wheel mounting plate
	A_13 A_14	±5g	On top of the trailer I-beam directly over the first trailer triadem axle on the driver/passenger side

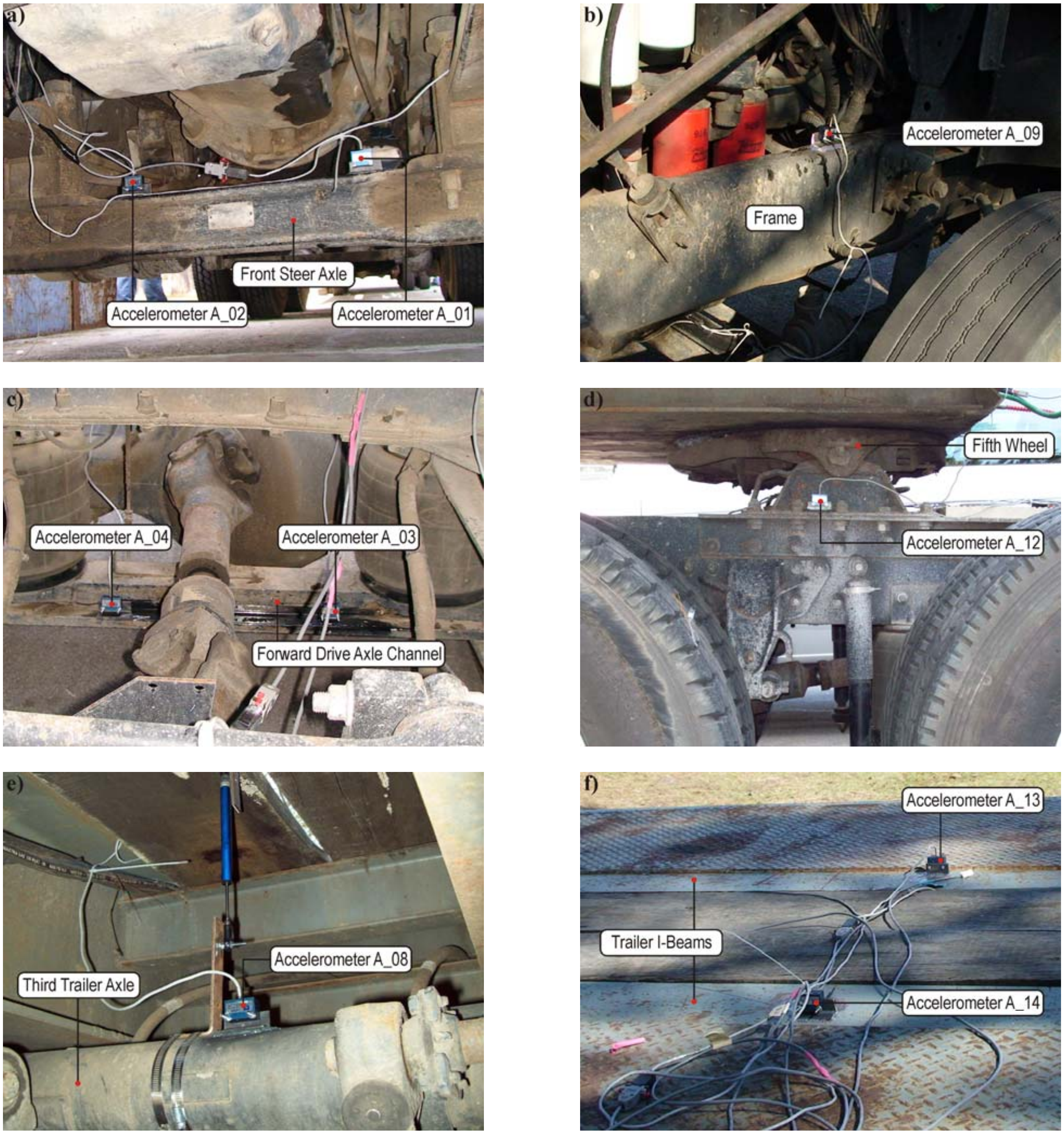

Figure 5.3. Location of the accelerometers for the tractor-trailer:
a) on the front steer axle; b) above the steer axle on the top of the frame on the driver side;
c) on the forward tandem drive axle channel; d) above the rear suspension system;
e) on the top of the trailer axle; f) on the trailer I-beams

Exemplary results of the suspension tests of the tractor-trailer in the form of time histories for the velocity of 24 km/h (15 mph) are presented in Figure 5.4 through Figure 5.6. Time histories of accelerations and the changes in distance were limited to five-second periods – one second before the speed bump and four seconds after it for each suspension system.

Complete results for all cases are presented in Appendix B.1 and B.2.

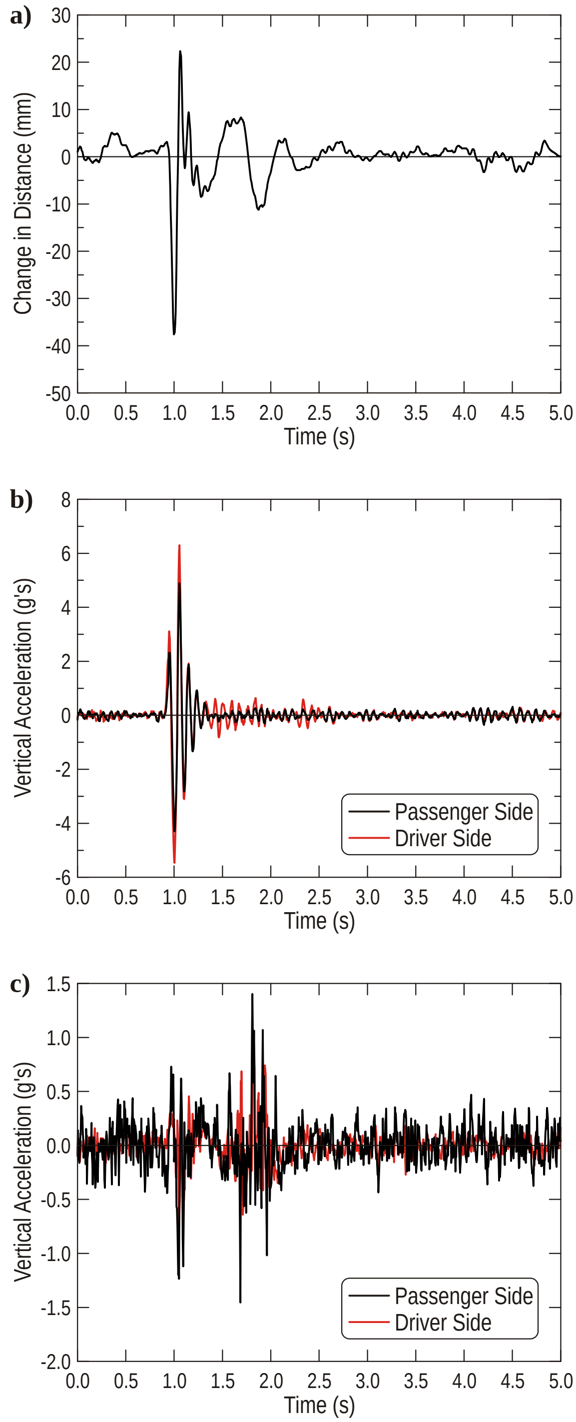

Figure 5.4. Time histories for the front suspension system for run #04 – velocity of 24 km/h (15 mph): a) change in distance between frame and the front axle; b) vertical acceleration of the axle; c) vertical acceleration of the points located on the frame above the axle

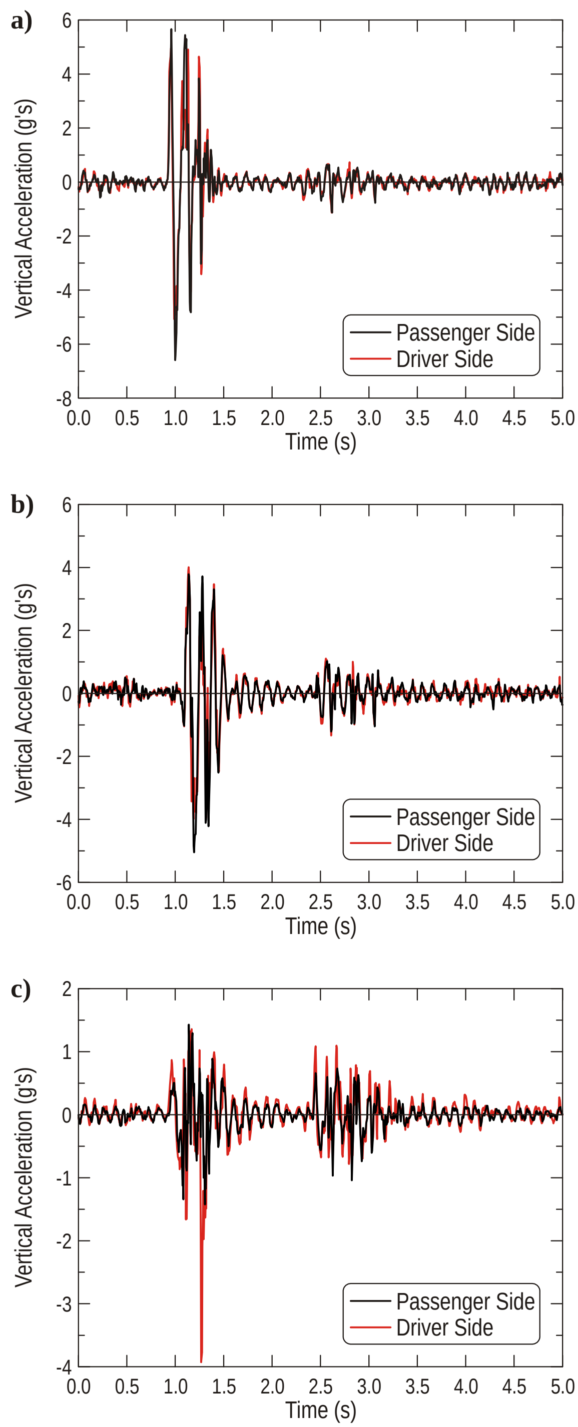

Figure 5.5. Time histories for the rear suspension system for run #04 – velocity of 24 km/h (15 mph): a) vertical acceleration of the forward tandem drive axle; b) vertical acceleration of the rear tandem drive axle; c) vertical acceleration of the points located on the frame above the rear tandem axles

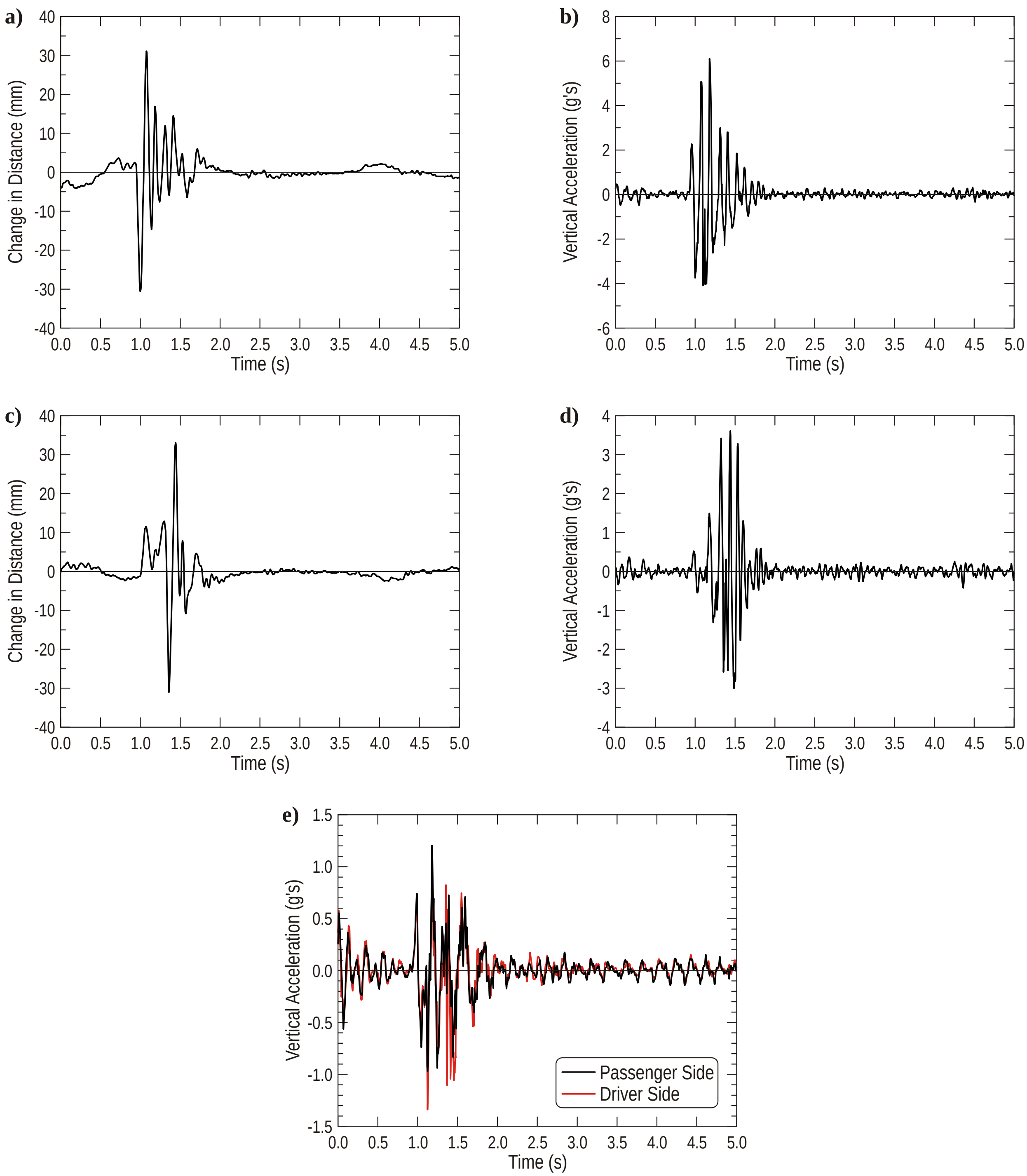

Figure 5.6. Time histories for the trailer suspension system for run #04 – velocity of 24 km/h (15 mph): a) change in distance between load deck and the first trailer axle; b) vertical acceleration of the first trailer axle; c) change in distance between load deck and the third trailer axle; d) vertical acceleration of the third trailer axle; e) vertical acceleration of the points located on the load deck above the first trailer axle

5.2. Suspension Tests of the Terex Crane

Suspension tests of the Terex crane included 12 runs with four different velocities – 8, 16, 24, and 32 km/h (5, 10, 15, and 20 mph). All considered cases are provided in Table 5.6. The strategy of the conducted tests was similar to the one for the tractor-trailer.

Table 5.6. Summary of all considered cases for the suspension tests of the Terex crane

Run #	Pass #	Velocity	Run #	Pass #	Velocity
01	1	8 km/h (5 mph)	07	1	24 km/h (15 mph)
02	2		08	2	
03	3		09	3	
04	1	16 km/h (10 mph)	10	1	32 km/h (20 mph)
05	2		11	2	
06	3		12	3	

The selected crane was not equipped in any components like springs or dampers in its rear suspension system. Therefore, the displacement gauge was attached only for the front axle; spring stiffness and damping coefficient were determined only for that axle.

Additionally, six accelerometers with a range of ±5g were attached in selected points. Positions of accelerometers are presented in Figure 5.7 and summarized in Table 5.7.

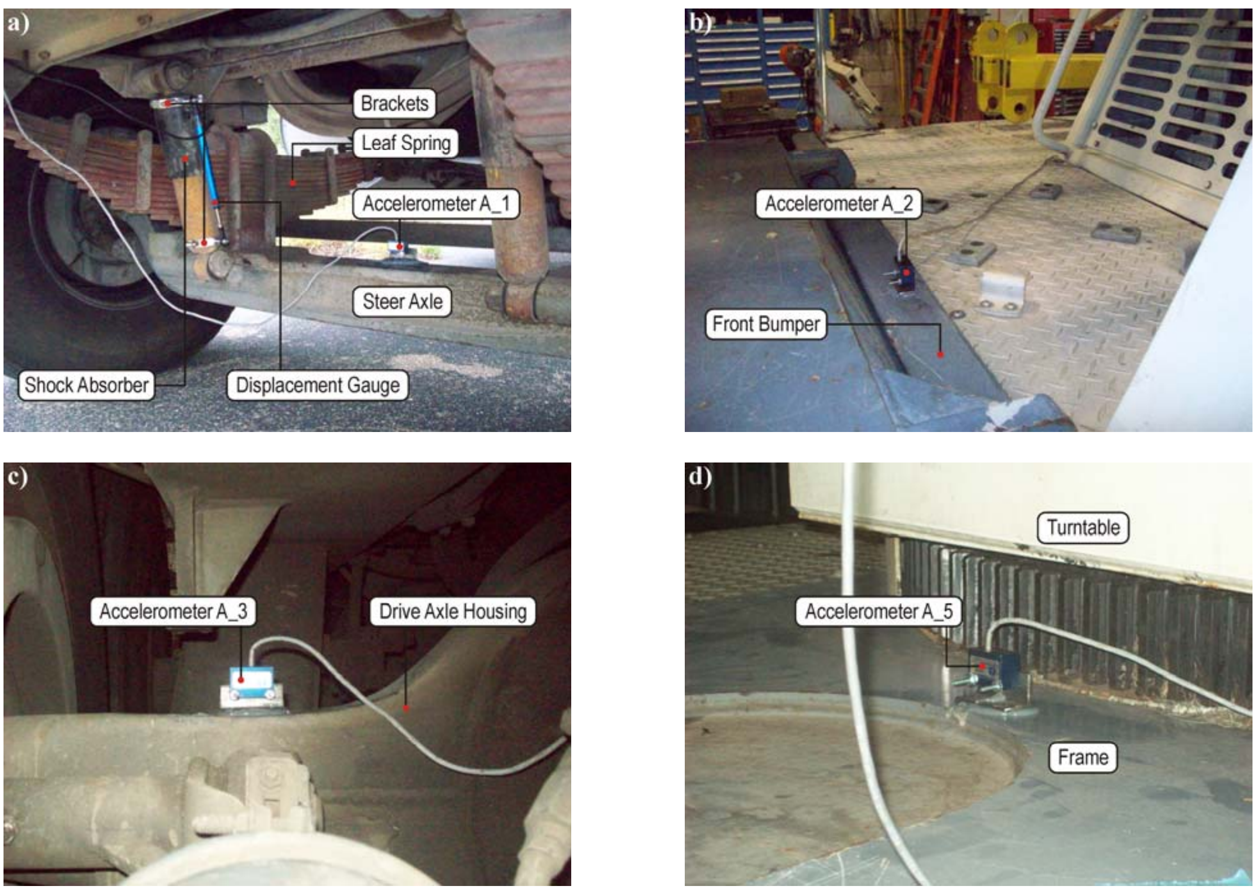

Figure 5.7. Location of the accelerometers on the Terex crane: a) on the front steer axle, b) on the front bumper, c) on the forward drive axle housing, d) on the frame next to the turntable

Table 5.7. Accelerometer locations for the suspension test of the Terex crane

Sensor type	Sensor No.	Range	Mounting location
Accelerometer	A_1	±5g	Center of the front steer axle
	A_2	±5g	Center of the front bumper
	A_3	±5g	Passenger side of the forward tandem drive axle
	A_4	±5g	Passenger side of the rear tandem drive axle
	A_5	±5g	Center of the frame near operator's cab
	A_6	±5g	Boom above the front axle

Time histories of accelerations and the changes in distance were limited to five-second periods – one second before the front axle was driven over the speed bump and four seconds after it. Exemplary results of the suspension tests of the Terex crane for the velocity of 24 km/h (15 mph) are presented in Figure 5.8 through Figure 5.11. Complete results for all cases are presented in Appendix B.3.

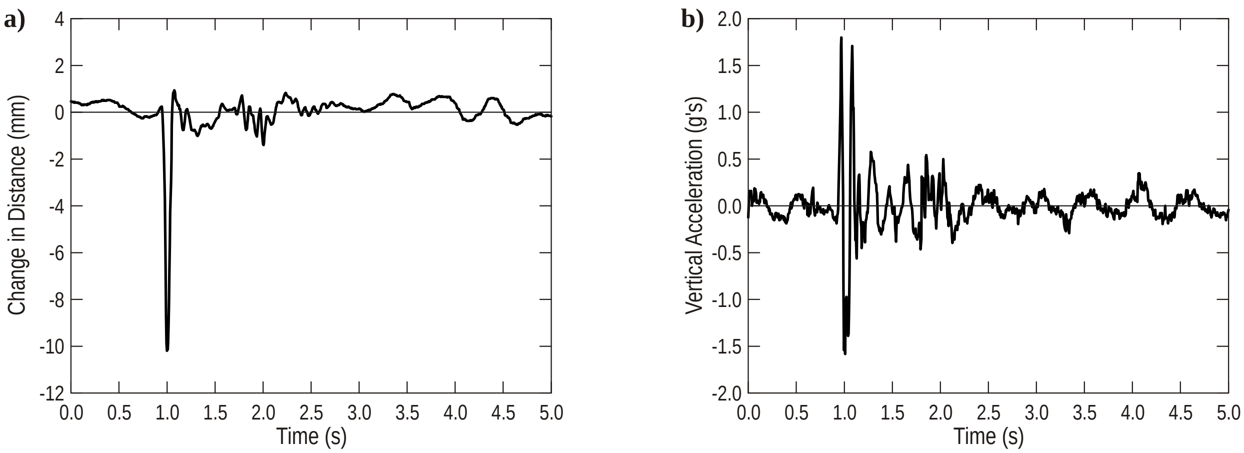

Figure 5.8. Time histories for the front axle – velocity of 24 km/h (15 mph), run #07: a) change in distance between the axle and frame, b) vertical acceleration of the axle

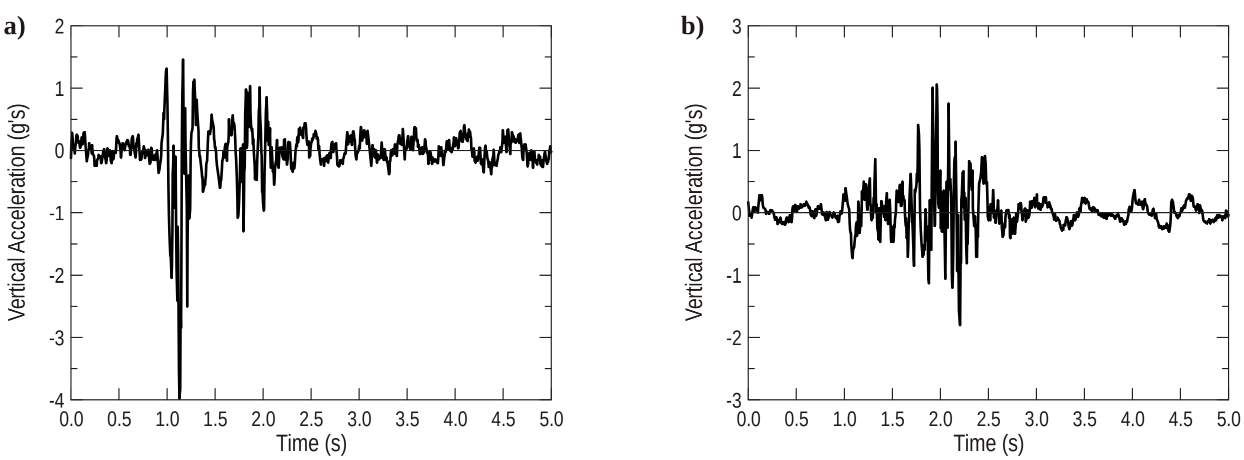

Figure 5.9. Time histories for the points located in front of the crane – velocity of 24 km/h (15 mph), run #07: a) point on the front bumper, b) point on the boom above the front axle

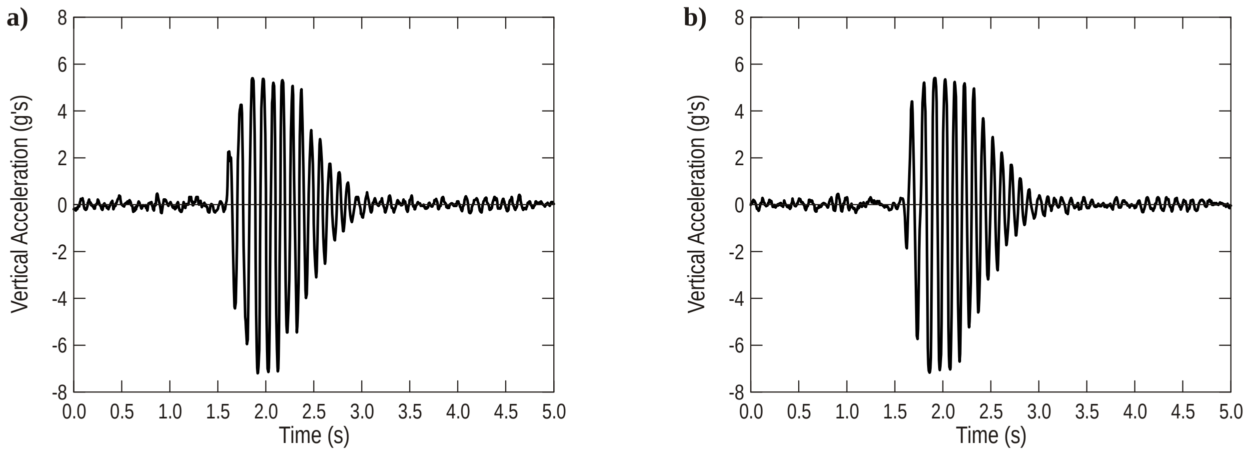

Figure 5.10. Time histories for the points located on the rear tandem axles – velocity of 24 km/h (15 mph), run #07: a) forward axle, b) rear axle

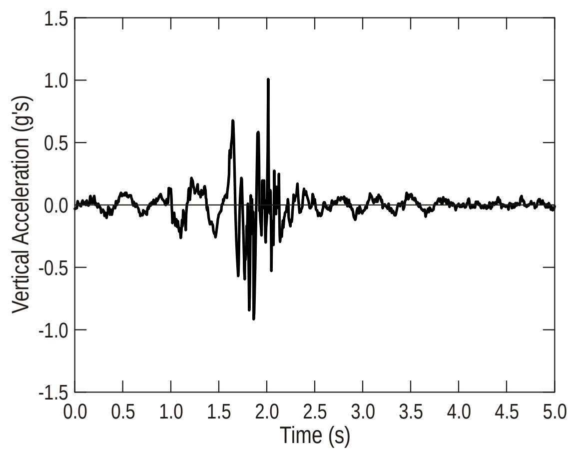

Figure 5.11. Time histories for the point located on the frame above the rear tandem axles – velocity of 24 km/h (15 mph), run #07

6. VALIDATION OF THE VEHICLE FE MODELS

Validation is the process of determining the degree to which a model is an accurate representation of the real world from the perspective of the intended uses of the model (Schwer, 2006).

Two criteria were used for validation of the new vehicle FE models. Validation began with checking the mass distribution in FE models on the basis of axle loads. Results obtained for FE models were compared with values taken from measurements of the actual objects.

A new strategy of the axle load measurement for FE models was proposed in the current project. Previously, the reaction forces were calculated for the two (left most and right most) nodes of each axle which were constrained in the vertical displacement. After applying gravity, the FE model was considered as the load supported on selected nodes. Hence, the axle loads were calculated based on the node reaction. There is one significant disadvantage of such method. It takes into consideration only the suspension deflection. However, the FE model of the vehicle is not able to affect the appropriate configuration because the tire deflection was not enabled. Therefore, during the current analysis, the FE model was dropped on planar rigid wall elements (*RIGIDWALL_PLANAR_FINITE_FORCES) which were located under each axle, as presented in Figure 6.1. This type of element allows determination of the load exerted on it. In addition, nodes can be welded to that element after contact with or without sliding (LS-DYNA Keyword User's Manual, 2007). Global damping with a high damping factor was used to damp vibrations of the FE model in an initial phase. The analysis was 5 seconds long but the results were averaged after the final 2-second range.

Complete FE models were usually lighter than the actual objects due to some simplification. Therefore, their calculated masses had to be increased by changing densities of some materials as well as applying mass nodes in several points of bodywork, mostly in proximity of the axles. No additional changes in the FE models were performed, neither for axle nor wheel models. This allowed keeping an appropriate ratio between sprung and unsprung mass of the vehicles.

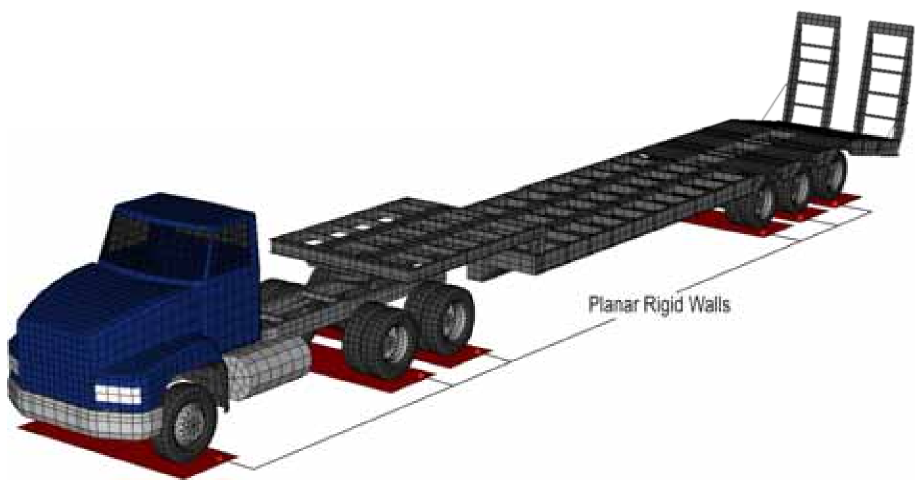

Figure 6.1. FE model of the tractor-trailer dropped on rigid wall elements

Finding a leaf spring stiffness and damping coefficient for each suspension system was the second step in the FE models validation. Experimental test described in chapter 5 were simulated using the LS-DYNA code. This analysis allowed for validation of each suspension system as well as the complete FE. During this analysis the vehicle FE model was driven over the speed bump FE model. Velocities of the vehicle FE model corresponded with the speeds of actual objects. The vertical accelerations of selected nodes and the change in length of the discrete spring elements were recorded as a function of time and compared with the time histories obtained from the experimental tests. The spring and damping coefficients at all axles were adjusted as necessary until the performance of the FE model closely matched that of the actual vehicle. A determinant used in this matching process was a correlation coefficient between two considered variables, experimental and numerical ones. It can be defined as follows:

$$r_{xy} = \frac{\Sigma(x-\bar{x})(y-\bar{y})}{\sqrt{\Sigma(x-\bar{x})^2 \Sigma(y-\bar{y})^2}} \tag{6.1}$$

where:

x, y	=	variables
$\bar{x}, \bar{y}$	=	means of x and y.

If the correlation coefficient ranges between 0.5 and 1.0, it can be assumed that the correlation between the two considered variables is large (Cohen, 1988).

Before the proper analysis, we tried to identify the leaf spring stiffness. For some cases this was not necessary due to available spring characteristics on manufacturers' websites. This data was applied directly to the material model in appropriate units. In other cases, the leaf spring stiffness k was estimated according to following equation:

$$k = \frac{8E\,n\,b\,t^3}{3L^3} \tag{6.2}$$

where:

E	=	Young's modulus (MPa);
n	=	number of leaves;
b	=	width of main leaf (mm);
t	=	thickness of main leaf (mm);
L	=	length of main leaf (mm).

Some preliminary analyses were performed for each vehicle FE model with the estimated spring stiffness. The results were compared with time histories from the experimental test. Change in length of the discrete spring element was the primary variable taken into account. It was compared with the axle displacement of the actual vehicle. However, this method could not be used for all suspension systems because some displacement gauges were broken during the test due to small strokes. Therefore, acceleration histories were considered in those cases.

6.1. Validation of the Tractor-Trailer FE Model

The truck tractor and trailer FE model was the most difficult for validation due to the large number of axles and three different configurations used during the tests (see sub-chapter 4.4). The selected vehicle had 6 fully suspended axles and each of them had to be considered separately. There was not any direct connection between axles as in the case of equalizer beams described in sub-chapter 4.5. We tried to obtain the least possible relative error between axle loads from FE analysis and measurements for each axle, not for the set of axles. This made the validation process for this vehicle much longer than for the two other ones.

It was assumed that springs and dampers belonging to each suspension system (the rear tandem in the truck tractor and a triadem in the trailer) have the same properties. During the validation process, the modifications were not related to spring stiffness only. An offset of the discrete elements (LS-DYNA Keyword User's Manual, 2007) applied for the spring was modified also. It allowed us to obtain the correct position of the vehicle FE model and to satisfy values of the axle loads.

It is worth noting that the validation of the tractor-trailer FE model was a complex and long-lasting process. It was related to an assumption that any modification of the mass in the FE models could be performed neither for axle models nor the wheel ones. Even slight modification in spring stiffness influenced the position of the vehicle FE model and axle loads.

Mass distribution

As mentioned above, mass distribution was achieved by simultaneous modifications of the following three parameters: additional mass elements, spring stiffness resulting from suspension testing, and the offsets of the spring discrete elements.

Additional mass elements were attached to several nodes belonging to the tractor frame and trailer longitudinal beams. These elements were attached above axles, two of them were placed on each axle, one on the left and right side. Their masses were dependent on the results from the previous analysis; if the obtained axle load was lower than one from experimental test, the mass of corresponded elements were raised. To reduce the number of analyses, additional mass elements were attached above the axles No. 1 (front axle), No. 3 (rear tandem axle), and No. 6 (third trailer axle) only. Changing the mass of each point element had strong influence on the configuration of the complete FE model and loads of any of six axles. Therefore, finding correct values of mass for the additional elements was quite difficult.

Spring stiffness was determined on the basis of the experimental tests. It was modified until the conformity between time histories from FE analysis and from field testing was sufficient. Successive axle load calculation was necessary after every single modification of the spring stiffness.

Offsets for the discrete spring elements were also modified. The offset allows changing the spring length without any additional changes in the FE model. Changing the offset influences the length of the spring in static configuration as well as the position of the FE model in the vertical plane and on the axle loads, as presented in Figure 6.2 for a simple FE model of the tractor trailer.

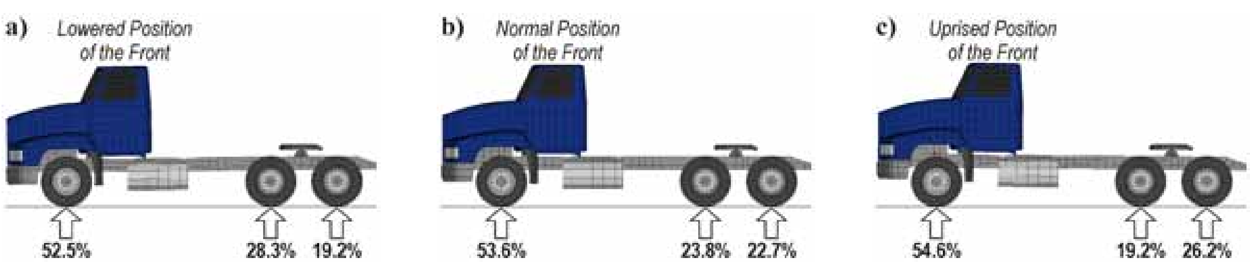

Figure 6.2. An influence of the offset in the spring elements on vehicle position and axle loads: a) without offset; b) offset equals to 50 mm; c) offset equals to 100 mm

Results of axle load measurements of the FE models for all three configurations are compared with values for the actual objects in Table 6.1 through Table 6.3. Time histories of the axle load are presented in Figure 6.3 for the basic configuration of the tractor-trailer without cargo.

Table 6.1. Comparison of the axle loads from FE analysis and measurements for the unloaded tractor-trailer (option I – basic configuration with no cargo)

Axle No.	Axle type	Axle load (kN)		Relative error
		Measurements	FE model	(%)
1	Front steer axle	38.802	38.093	–1.83
2	Forward tandem drive axle	26.253	26.373	0.46
3	Rear tandem drive axle	29.546	30.319	2.61
4	First trailer axle	29.635	29.516	–0.40
5	Second trailer axle	33.818	33.866	0.14
6	Third trailer axle	38.713	38.633	–0.21
TOTAL		196.767	196.800	0.02

Table 6.2. Comparison of the axle loads from FE analysis and measurements for the loaded tractor-trailer (option II – one cargo located in the middle of the trailer)

Axle No.	Axle type	Axle load (kN)		Relative error
		Measurements	FE model	(%)
1	Front steer axle	39.959	39.845	–0.29
2	Forward tandem drive axle	108.574	108.573	0.00
3	Rear tandem drive axle	115.604	115.303	–0.26
4	First trailer axle	119.787	119.499	–0.24
5	Second trailer axle	112.044	112.742	0.62
6	Third trailer axle	105.815	105.835	0.02
TOTAL		601.783	601.797	0.002

Table 6.3. Comparison of the axle loads from FE analysis and measurements for the loaded tractor-trailer (option III – four cargos distributed evenly on the trailer)

Axle No.	Axle type	Axle load (kN)		Relative error
		Measurements	FE model	(%)
1	Front steer axle	42.184	42.291	0.25
2	Forward tandem drive axle	89.440	89.439	0.00
3	Rear tandem drive axle	94.957	95.008	0.05
4	First trailer axle	94.601	93.946	–0.69
5	Second trailer axle	98.517	97.908	–0.62
6	Third trailer axle	100.831	101.754	0.92
TOTAL		520.530	520.346	–0.04

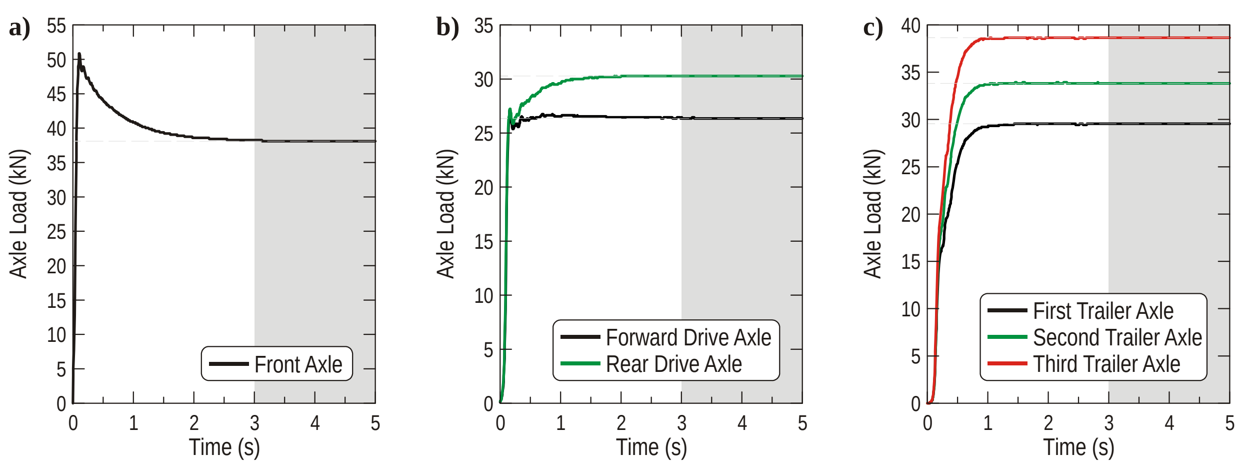

Figure 6.3. Time histories of the axle loads: a) front axle; b) rear tandem axles; c) trailer triadem axles

Suspension Parameters

As mentioned in sub-chapter 5, numerical analyses reflecting conducted experimental tests were performed using the LS-Dyna code. Results obtained from both methods were compared. The suspension parameters in the FE model were adjusted until simulation data was matched with experimental results.

Validation of the suspension parameters was not done independently for all three configurations of the FE model. Therefore, for some cases the differences between results obtained from numerical analysis and experimental tests are higher than for other ones. We chose to select the most optimal solution for all considered cases and to not "calibrate" the FE model in every single case.

The most satisfying correlation of the result between FE analysis and experimental tests was obtained for the front suspension system. The front suspension was fully loaded during the experimental tests and data collection data was completed. Hence, up to 3 parameters could be taken into consideration in the validation process: change in distance between the front axle and the frame, as well as accelerations of the axle and a point on the frame. The one and only disadvantage related with this suspension was a high range of noise recorded by the accelerometers located on the frame due to close proximity of a running engine. In spite of this inconvenience, we managed to obtain a correlation coefficient of 0.80–0.85. Comparison between results from the tests and numerical analysis are presented in Figure 6.4 and Figure 6.5.

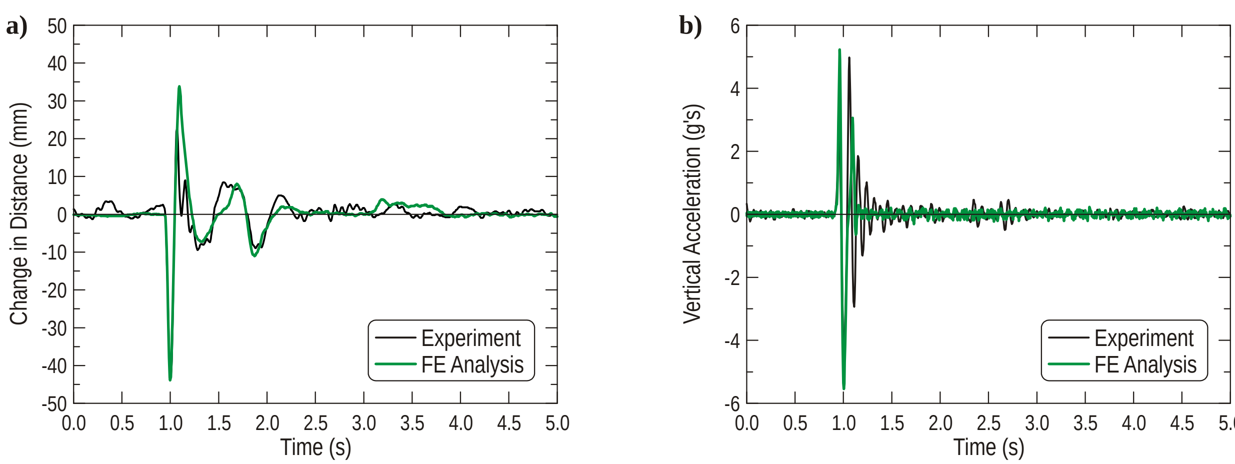

Figure 6.4. Comparison between time histories obtained from the experimental tests and FE analysis for the front axle – velocity of 24 km/h (15 mph), run #05:
a) change in distance between axle and frame, b) vertical acceleration of the axle

As depicted in Figure 6.4, the shapes of both curves, experimental and numerical one, are similar, although some slight differences are also visible. They could be the result of simplification of the suspension FE model which did not include any buffers, whereas the actual object did. A stroke of the front suspension in the actual vehicle was bounded during compression by additional rubber buffers on the leaf spring; the stroke of the spring was also limited during expansion. However, such high deflections of the suspension will not take place during the experimental tests conducted on the bridge; therefore the developed FE model can be used for further analysis.

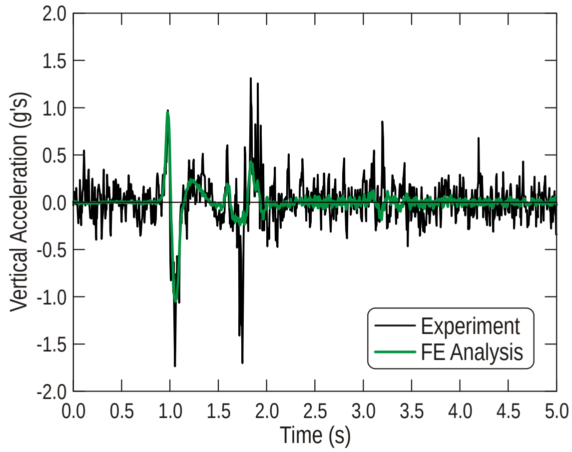

Figure 6.5. Comparison between time histories of vertical acceleration obtained from the experimental tests and FE analysis for points located on the frame above the front axle – velocity of 24 km/h (15 mph), run #05

A slightly worse correlation was obtained for the rear suspension system. Accelerations of the tandem axles and a point located on the frame next to the fifth wheel were the only recorded data since both displacement gauges used for the tests were broken due to its insufficient stroke. Comparison of the results from the experiment and the FE analysis are shown in Figure 6.6 and Figure 6.7. Correlation coefficients did not exceed 0.70. It is worth noting that the selected tractor was equipped with air springs in the rear suspension system allowing adjustment of its height depending on the actual axle load. This type of suspension is more complicated for modeling due to its nonlinearity. However, in a short operating range, such as took place during the bridge tests where deflections were much lower than for the suspension tests, it might be simulated as a linear one. The offsets of the discrete spring elements were modified for the second and third configuration of the FE model including additional load placed on the trailer due to very large deflections of the suspension.

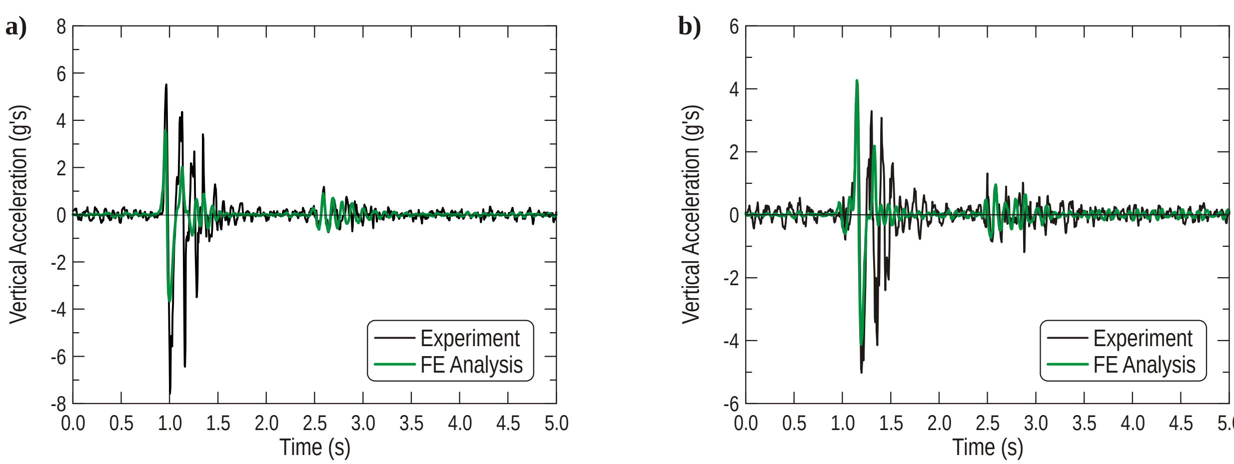

Figure 6.6. Comparison between time histories of the vertical accelerations obtained from the experimental tests and FE analysis for the rear tandem axles – velocity of 24 km/h (15 mph), run #06: a) forward axle, b) rear axle

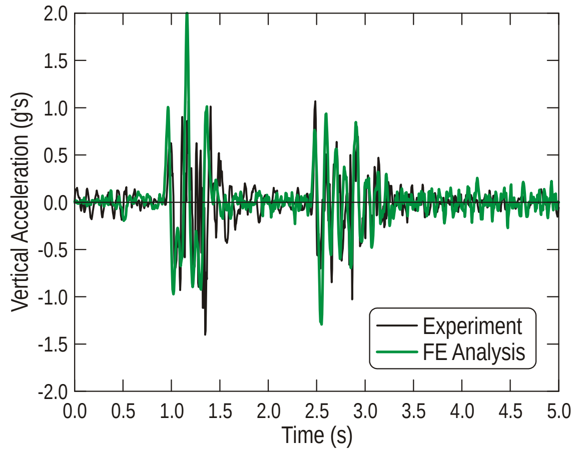

Figure 6.7. Comparison between time histories of the vertical acceleration obtained from the experimental tests and FE analysis for point located on the frame above the rear tandem axles – velocity of 24 km/h (15 mph), run #06

The results obtained for the trailer suspension were characterized by correlation coefficients close to 0.85 for distances and 0.65 for accelerations. The most difficulty in this case was to estimate an appropriate value of the damping coefficient. The selected trailer was equipped with very stiff leaf springs without any dampers. However, additional discrete damping elements had to be applied in the FE model to reduce a high range of vibrations generated when driving over the speed bump. Time histories for the trailer suspension system are presented in Figure 6.8 through Figure 6.10.

During the validation process most time was spent on finding the appropriate spring and damping parameters. However, properties of the wheel FE model also have a strong influence on behavior of the vehicle FE model. Material properties of the rubber material model were similar to ones used in the previous project, as well as a mass weighted damping factor used in the airbag model applied in the tire FE model. No additional experimental tests of the tire were conducted.

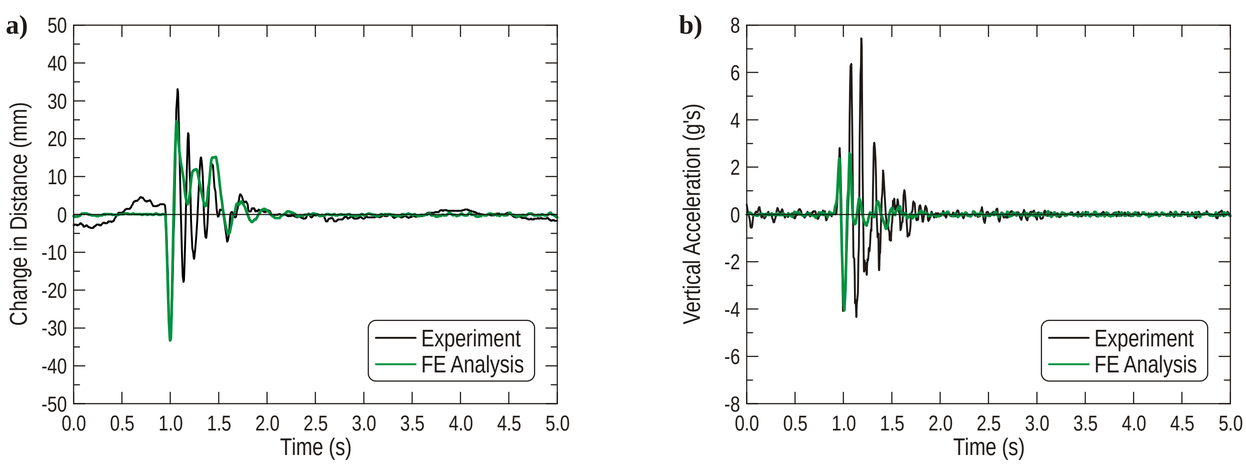

Figure 6.8. Comparison between time histories obtained from the experimental tests and FE analysis for the first trailer axle – velocity of 24 km/h (15 mph), run #06:
a) change in distance between axle and the load deck, b) vertical acceleration of the axle

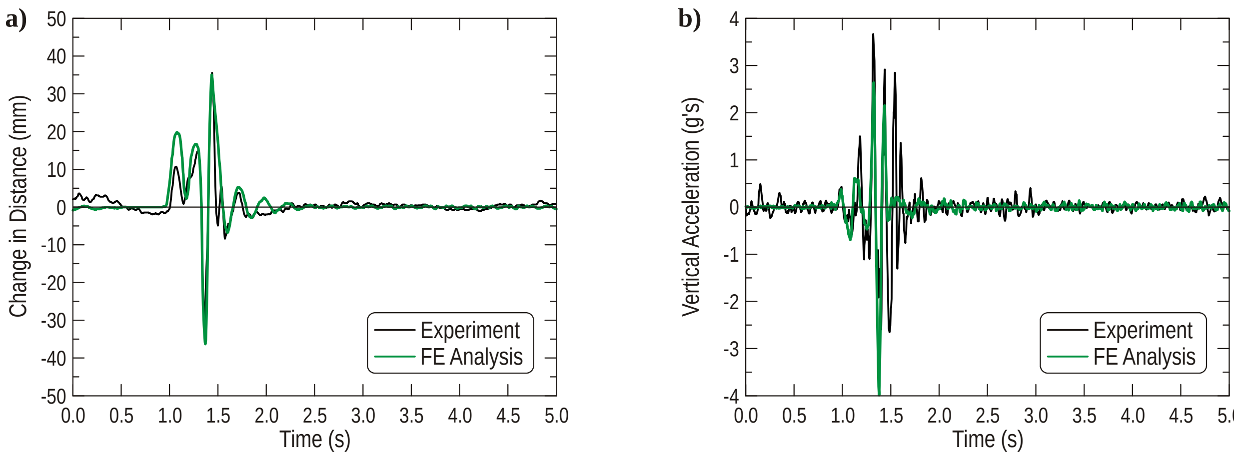

Figure 6.9. Comparison between time histories obtained from the experimental tests and FE analysis for the third trailer axle – velocity of 24 km/h (15 mph), run #06: a) change in distance between axle and the load deck, b) vertical acceleration of the axle

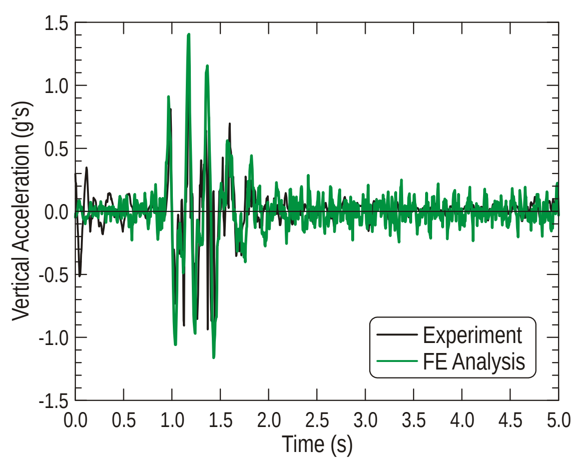

Figure 6.10. Comparison between time histories of vertical acceleration obtained from the experimental tests and FE analysis for point located on the trailer deck above the first trailer axle – velocity of 24 km/h (15 mph), run #06

Conclusion

Since the complete FE model of the heavy vehicle presented in this sub-chapter includes two units joined together, it is supposed to be considered as a complex kinematic system. The analyses show that the speed bump has not only a direct influence on the axle/suspension, but also indirectly on the complete structure of the vehicle and remaining suspension systems.

Time histories presented in the current sub-chapter are characterized by a relatively large correlation when the considered axle is crossing over the speed bump. Some discrepancies between results appear in a later phase. Therefore, the most correct strategy for the suspension FE model validation and/or finding out its properties would be to separate the considered suspension system from the other ones. Unfortunately, that method is possible to simulate in FE analysis but it is more difficult to carry out on the actual object.

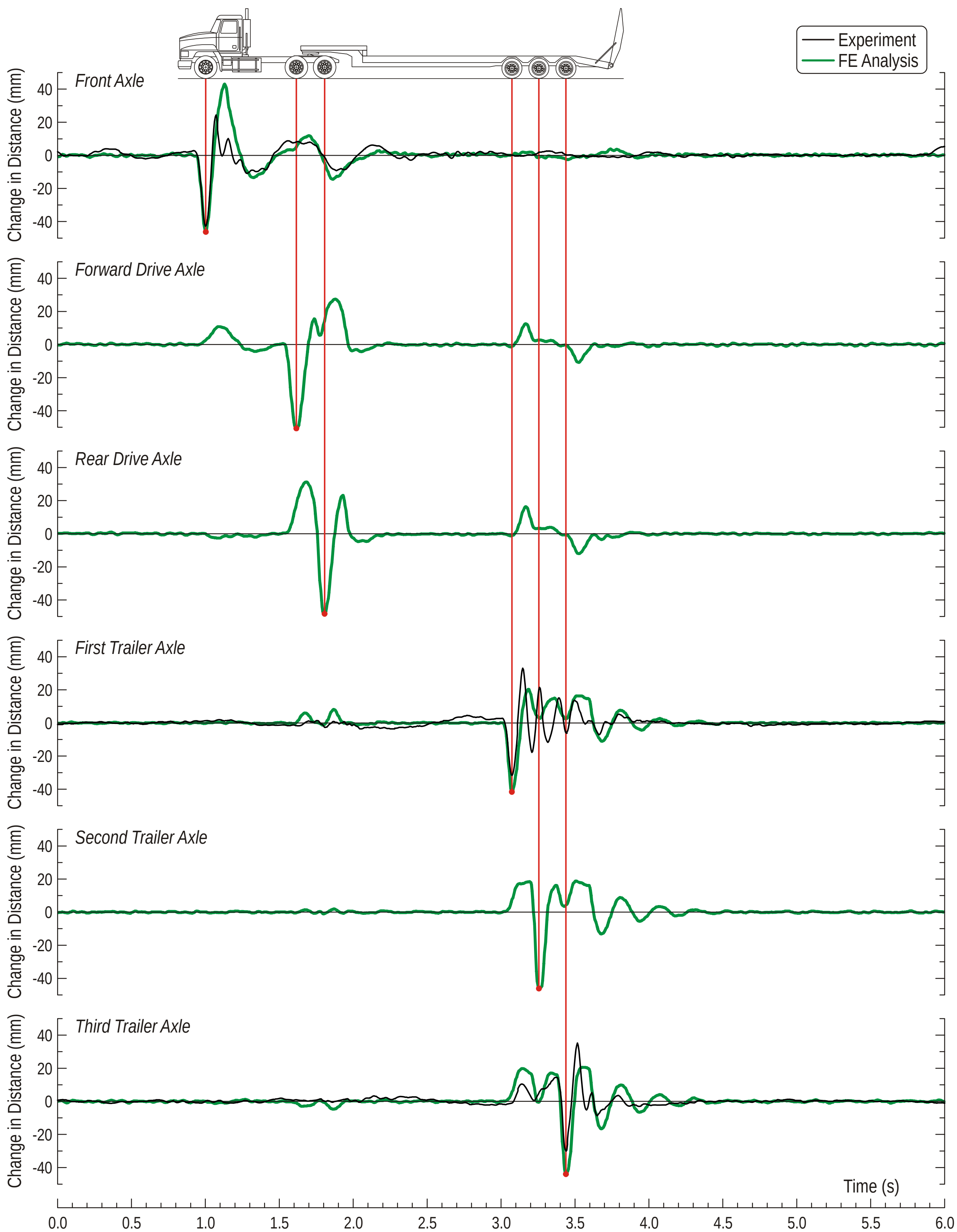

Figure 6.11. Time histories of change in distance between axles and the frame/load deck for the complete FE model of the tractor-trailer

6.2. Validation of the Terex Crane FE Model

Mass Distribution

Strategy of validation process for the Terex Crane FE model was exactly the same as one described in the previous sub-chapter for the tractor-trailer. Validation began with checking the mass distribution in the FE model on the basis of axle loads. Four additional mass elements, two in the front and two in the back, were attached in the FE model to obtain its total mass and axle loads close to the actual object. This procedure was much easier than one for the previous vehicle due to fewer axles and a very simple rear suspension system allowing for distributing the load on each axle evenly. Results of axle load measurements of the FE models are compared with values for the actual objects in Table 6.4.

Table 6.4. Comparison of the axle loads from FE analysis and measurements for the Terex crane

Axle No.	Axle type	Axle load (kN)		Relative error (%)
		Measurements	FE model	
1	Front steer axle	85.257	85.249	–0.01
2	Forward tandem drive axle	93.714	93.715	0.00
3	Rear tandem drive axle	92.466	92.479	0.01
TOTAL		271.437	271.443	0.002

Suspension Parameters

Comparisons between selected time histories from the experimental test and FE analysis for the Terex crane are presented in Figure 6.12 through Figure 6.13. The correlation is not as large as for the tractor-trailer, about 0.60–0.70 for the front suspension and less than 0.50 for the rear one. Differences between deflections of the front axle obtained from both sources can be related with a simplification of the FE model of the suspension. It does not include any additional buffers which were applied to the actual object. Therefore, change in distance between axle and the frame rejected during the tests is less than one from the FE analysis. Furthermore, the maximum displacement of the front axle coming up to 11–12 millimeters was the same for the highest velocities of the vehicle. It confirms that deflection of the front leaf spring was bounded by an additional component.

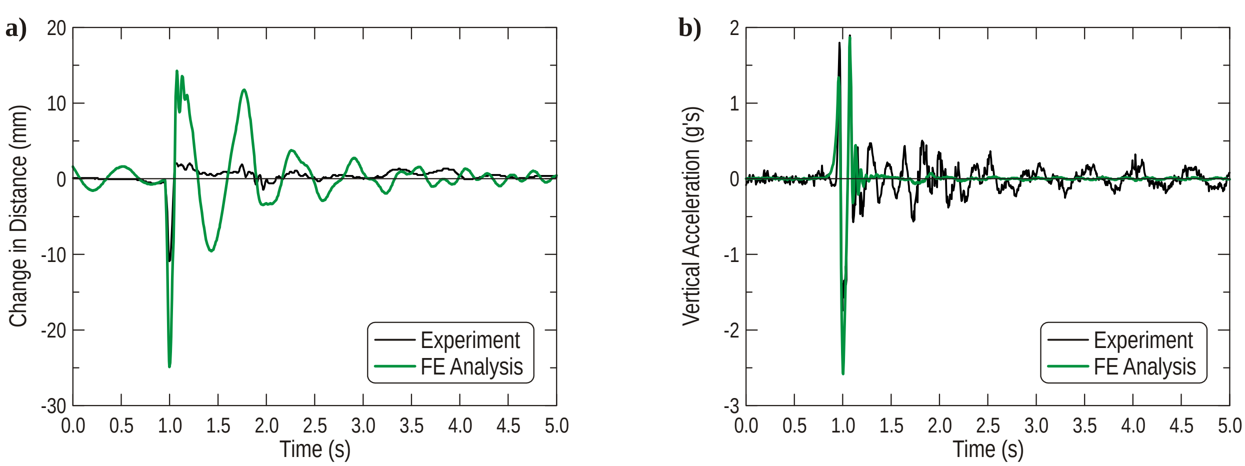

Figure 6.12. Comparison between results obtained from the experimental tests and FE analysis for the front axle – velocity of 24 km/h (15 mph): a) change in distance between axle and the frame, b) vertical acceleration of the axle

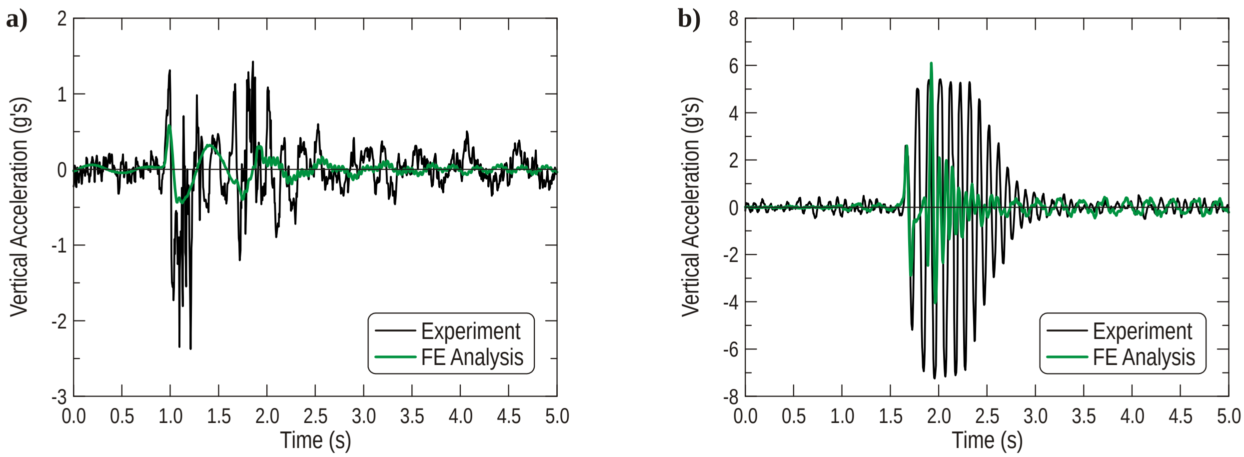

Figure 6.13. Comparison between results obtained from the experimental tests and FE analysis – velocity of 24 km/h (15 mph): a) vertical acceleration of the point located on the front bumper, b) vertical acceleration of the forward drive tandem axle

6.3. Validation of the FDOT Truck FE Model

In this case, additional experimental tests were not conducted. An FDOT truck was tested for the purpose of comparing obtained results with those from previous projects. Therefore, validation of this model is based on the mass distribution only. The FDOT truck and trailer has very simple suspension systems and there was no problem with validation of their FE models. Both tandems were equipped with equalizer beams allowing them to distribute loads per axle evenly, providing that there are no any mechanical damages in the suspension system and both axles are the same.

Several FE analyses were carried out to achieve acceptable correlation of results, close to the data provided by the FDOT. Densities of some materials used for bodywork elements were recalculated and additional point mass elements were attached to selected nodes. We did not try to change masses of the axles or wheels, and attached any mass element right there. This allowed us to keep an appropriate ratio between sprung and unsprung mass of the truck. Final results are provided in Table 6.5, whereas the time histories of axle loads are presented in Figure 6.14. Correctness of the obtained results is very good due to above-mentioned advantage of the equalizer beams applied in the suspension systems of the tested vehicle.

Table 6.5. Comparison of the axle weights from FE analysis and measurements for the FDOT truck

Axle No.	Axle type	Axle load (kN)		Relative error (%)
		Measurements	FE model	
1	Front steer axle	50.104	50.104	0.00
2	Forward tandem drive axle	48.057	48.069	0.02
3	Rear tandem drive axle	48.057	48.046	–0.02
4	Forward tandem trailer axle	84.501	84.508	0.01
5	Rear tandem trailer axle	84.501	84.502	0.00
TOTAL		315.220	315.229	0.003

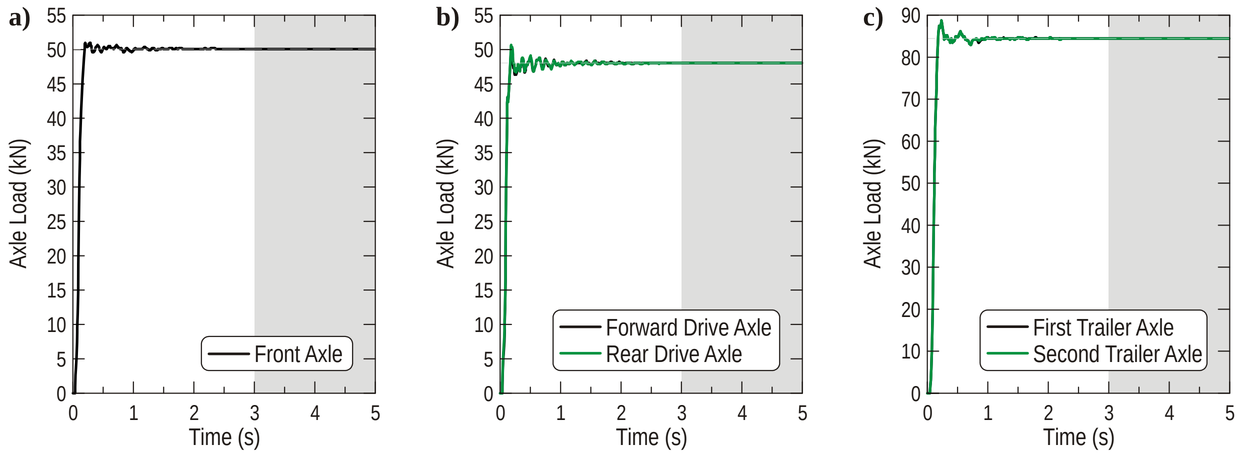

Figure 6.14. Time histories of the axle loads: a) front axle, b) rear tandem axles, c) trailer tandem axles

7. BRIDGE TESTS

The main aim of the conducted experimental tests was to assess an actual dynamic load allowance, also known as the impact factor, for a selected bridge. Moreover, the field tests were used to confirm the correctness of the existing FE model and performed FE analyses. The considered bridge #500133 was described in detail in sub-chapter 3.1.

7.1. Experimental Tests Procedure

Experimental tests consisted of 37 runs including dynamic as well as static cases. All considered configurations are provided in Table 7.1. Most of the runs were repeated to check the validity of readings. Three different heavy vehicles were used during the tests. Their schemes and configurations were presented in sub-chapter 3.2. Each vehicle was weighed before the tests (see Figure 7.1) to find the axle load.

Table 7.1. All configurations of the static and dynamic tests for bridge #500133

Run #	Pass #	Test Type	Vehicle position	Velocity	Vehicle
01	1	Static	Center of Westbound Lane	N/A	Tractor-Trailer
02	1	Static	Center of Roadway	N/A	
03	1	Static	Center of Eastbound Lane	N/A	
04	1	Dynamic	Center of Westbound Lane	30 mph	
05	2	Dynamic	Center of Westbound Lane	30 mph	
06	1	Dynamic	Center of Roadway	30 mph	
07	2	Dynamic	Center of Roadway	30 mph	
08	1	Dynamic	Center of Westbound Lane	50 mph	
09	2	Dynamic	Center of Westbound Lane	50 mph	
10	1	Dynamic	Center of Roadway	50 mph	
11	2	Dynamic	Center of Roadway	50 mph	
12	1	Static	Center of Westbound Lane	N/A	
13	1	Static	Center of Roadway	N/A	
14	1	Static	Center of Eastbound Lane	N/A	
15	1	Static	Center of Westbound Lane	N/A	FDOT Truck
16	1	Static	Center of Roadway	N/A	
17	1	Static	Center of Eastbound Lane	N/A	
18	1	Dynamic	Center of Westbound Lane	50 mph	
19	2	Dynamic	Center of Westbound Lane	50 mph	
20	1	Dynamic	Center of Roadway	50 mph	
21	2	Dynamic	Center of Roadway	50 mph	
22	1	Static	Center of Westbound Lane	N/A	Terex T-340 Crane
23	1	Static	Center of Roadway	N/A	
24	1	Static	Center of Eastbound Lane	N/A	
25	1	Dynamic	Center of Westbound Lane	30 mph	
26	2	Dynamic	Center of Westbound Lane	30 mph	
27	1	Dynamic	Center of Roadway	30 mph	
28	2	Dynamic	Center of Roadway	30 mph	
29	1	Dynamic	Center of Westbound Lane	50 mph	
30	2	Dynamic	Center of Westbound Lane	50 mph	
31	1	Dynamic	Center of Roadway	50 mph	
32	2	Dynamic	Center of Roadway	50 mph	
33	1	Static	Center of Westbound Lane	N/A	
34	1	Static	Center of Roadway	N/A	
35	1	Static	Center of Eastbound Lane	N/A	

Figure 7.1. Axle load measurement: a) two portable scales,
b) forward axle of the rear tandem of the truck tractor during the measurement

The testing plan for experiments conducted in the current project was discussed and developed with the Florida Department of Transportation (FDOT) Structures Lab. All tests were based on similar ones carried out in the previous project (Wekezer, Li, Kwasniewski, & Malachowski, 2004), (Kwasniewski, Wekezer, Roufa, Li, Ducher, & Malachowski, 2006) and presented in the literature (Baumgaertner, 1998), (Brady, Gonzalez, Znidaric, & O'Brien, 2002), (Brownjohn, Lee, & Cheong, 1999), (Chan, Law, & Yung, 2000), (Chowdhury & Ray, 2003), (Green & Cebon, 1994).

7.2. Bridge Instrumentation

There were three cross-sections in the first span of the bridge taken into consideration in the current project, depicted in Figure 7.2. It was assumed that only the first span near the east bank would be fully instrumented due to more convenient access under the bridge, as mentioned at the beginning. The location of the selected point was made on the basis of the previous project that allows us to compare the results obtained in both tests. Moreover, the selection of the measure points on the bridge was performed based on the mesh of the FE model of the bridge.

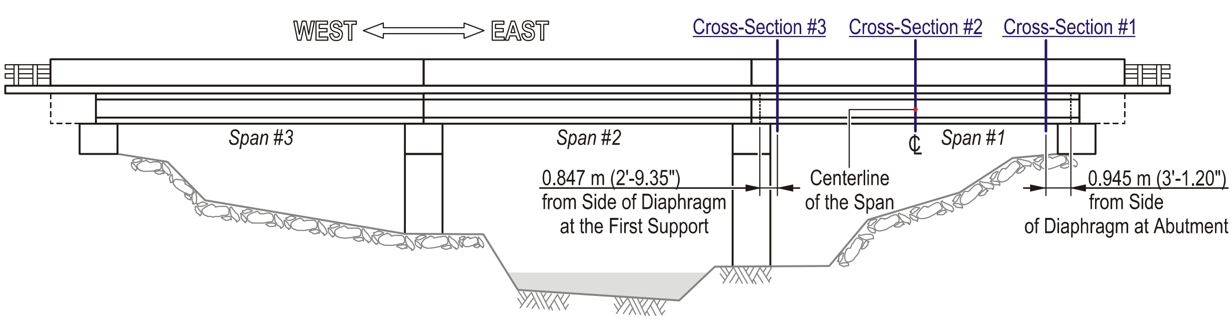

Figure 7.2. Location of the instrumented cross-sections for the tested bridge

Strains were measured using 38 strain gauges. The position of the strain gauges corresponds with the midpoints of the appropriate elements in the FE model of the bridge. All strain gauges were oriented to measure the longitudinal component of strains. Deflection of the bridge span was measured in the middle section using two Linear Variable Displacement Transformer (LVDT) devices. Moreover, the accelerations for selected points at the bridge slab were registered during the dynamic tests. A total of 14 accelerometers were used and their location was determined by the coordinates of the nodes in FE model.

Data was sampled at 200 samples per second and recording duration was approximately 10-12 seconds depending on the test type. Files were recorded to a LabVIEW measurement file which is an ASCII tab delimited file.

Characteristics of all gauges used for the tests and attached to the bridge are provided in Table 7.2 to Table 7.4. Detailed description of the instrumentation of the tested bridge is presented in the next parts.

Table 7.2. Characteristics of the strain gages used for the bridge testing

Manufacturer	TML	Gauge Length	(mm) / (in)	60 / 2.36
Model Number	MFL-60-350-1L	Gauge Resistance	(Ω)	350
Gauge Factor	2.03	Excitation Voltage Used	(V)	2.5

Table 7.3. Characteristics of the LVDS devices used for the bridge testing

Manufacturer	TML	Gauge Length	(mm) / (in)	200 / 7.87
Model Number	SDP-200R	Rated Output	(mV/V)	5
Non-Linearity	0.3% Rated Output	Excitation Voltage Used	(V)	5.0

Table 7.4. Characteristics of the accelerometers used for the bridge testing

Manufacturer	TML	Range	(G)	±5
Model Number	ARF-50A	Rated Output	(mV/V)	0.5
Weight (g) / (lb)	13 / 0.029	Frequency Response / Natural	(Hz)	130 / 240
Non-Linearity	1.0% Rated Output	Excitation Voltage Used	(V)	2.0

Cross-Section #1

This cross-section was located at a distance of 0.945 m (3'-1.20") from the side of the diaphragm at the abutment. A total of 12 gauges were attached in this section (Figure 7.3) with one gauge at the bottom of each girder (Figure 7.4a) and one at the side of each girder in the middle of its web (Figure 7.4b). The location of gauges #07 to #12 was determined by the position of the neutral axis for the complete cross-section of the bridge span. In the previous project (Wekezer, Li, Kwasniewski, & Malachowski, 2004), the corresponding strain gauges were attached at the side of each girder close to the deck. Thereupon, the registered values of strains were relatively low, because of too short distance between the strain gauges and the neutral axis. It was decided to attach gauges in the middle of the girder's web to obtain measureable values of strains higher than previously.

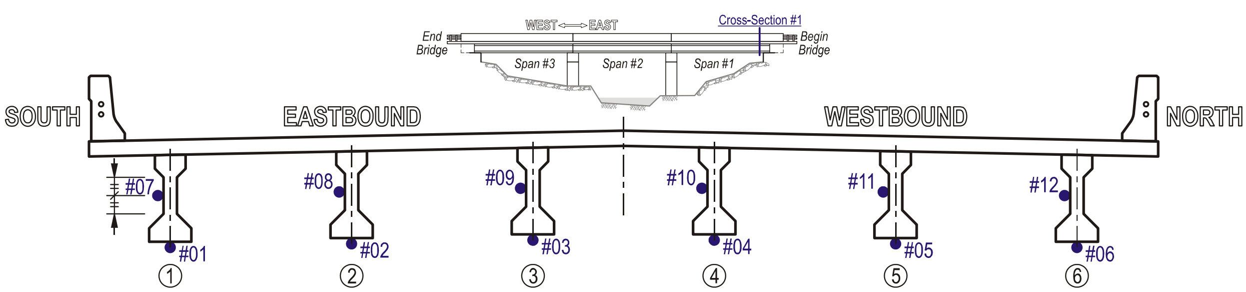

Figure 7.3. Location of the strain gages in the cross-section #1 for the tested bridge

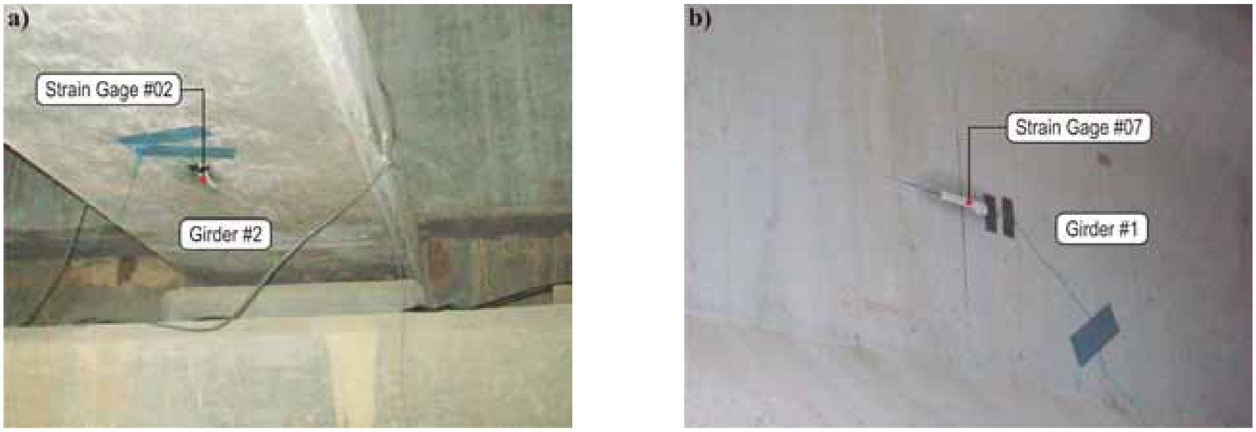

Figure 7.4. Strain gages: a) #02 attached at the bottom of the girder #2, b) #07 attached at the side of the girder #1 in the middle of its web

Cross-Section #2

The second cross-section was located in the middle of the first span. It was coincident with the centerline ℄ of that span. This cross-section was the most representative for the strain and displacement readings. It was assumed that obtained values of strains would be measureable enough and would be close to the highest possible values. Moreover, the absolute maximum bending moment for the single span was achieved close to that section for each of the three tested vehicles. Selection of cross-section #2 allows us to compare results with those obtained from the previous project. A total of 12 strains gauges were attached in this section (see Figure 7.5) and their positions were analogues to those in the cross-section #1, except for two additional gauges (#19 and # 26) glued to the top surface of the railing barrier (see Figure 7.6a).

Two displacement transducers, as presented in Figure 7.6b, were used to measure the deflection of the bridge span in the considered cross-section. These were installed under girder #3 and #4 (see Figure 7.7), in the middle distance between bearings.

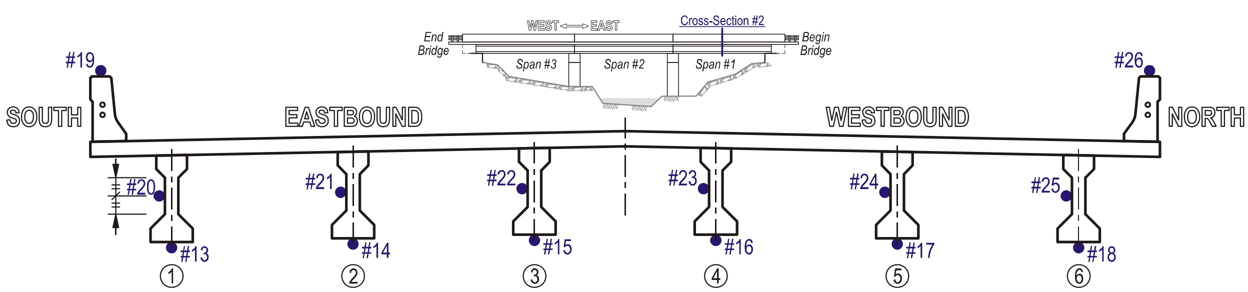

Figure 7.5. Location of the strain gages in the cross-section #2 for the tested bridge

Cross-Section #3

This cross-section was located at the distance of 0.847 m (2'-9.35") from the side of the diaphragm at the first support. A total of 12 gauges was attached in this section (Figure 7.3) similarly to those in the cross-section #1.

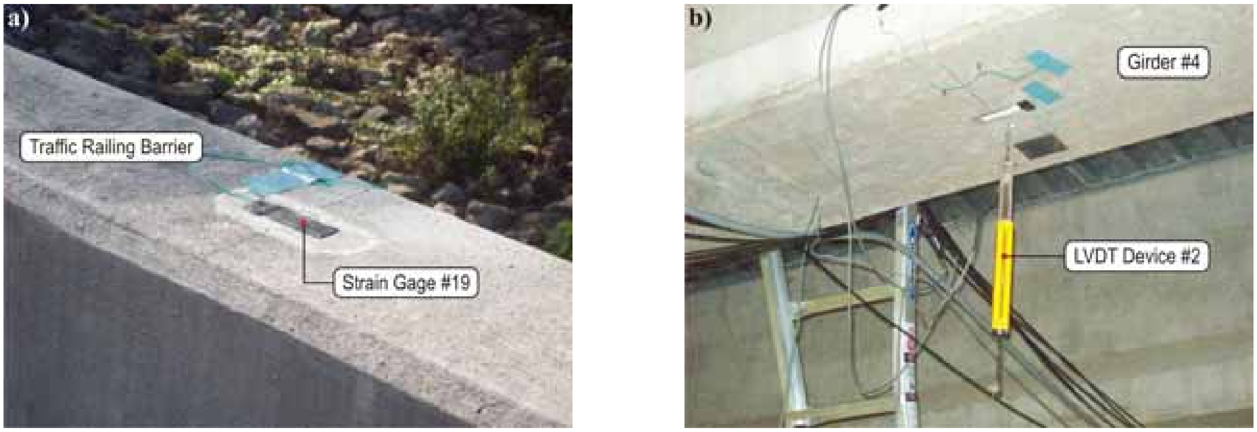

Figure 7.6. a) strain gage #19 attached to the top surface of the railing barrier, b) the displacement transducer located under the girder # 4

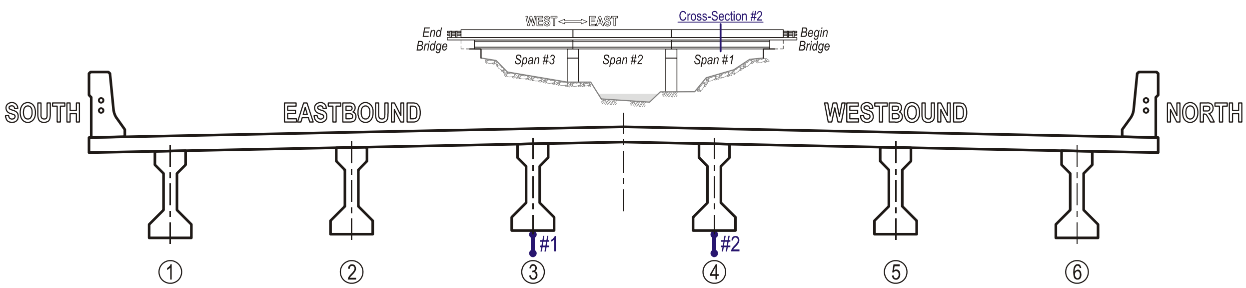

Figure 7.7. Location of the LVDS devices in the cross-section #2 for the tested bridge

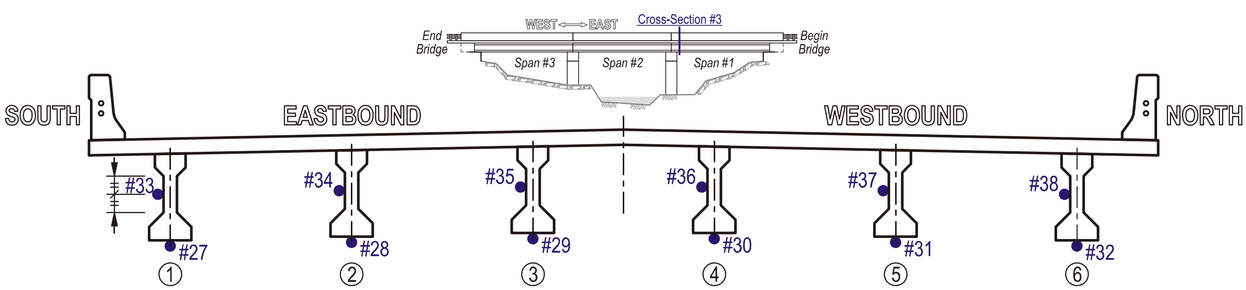

Figure 7.8. Location of the strain gages in the cross-section #3 for the tested bridge

Accelerometers on the Bridge Slab

A total of 14 accelerometers were used during the test. They were glued to the bridge slab and located symmetrically on each side of the slab, close to the railing barriers (see Figure 7.9). A selected accelerometer is presented as an example in Figure 7.10.

7.3. Vehicles Instrumentation

Two of the selected heavy vehicles—the truck tractor with the lowboy trailer and the Terex crane—were instrumented for the tests. Accelerometers were located mostly on the axles and on the frame or deck close to the corresponded axle. Moreover, the linear displacement sensor was used to measure the deflection of the front leaf spring for the Terex crane.

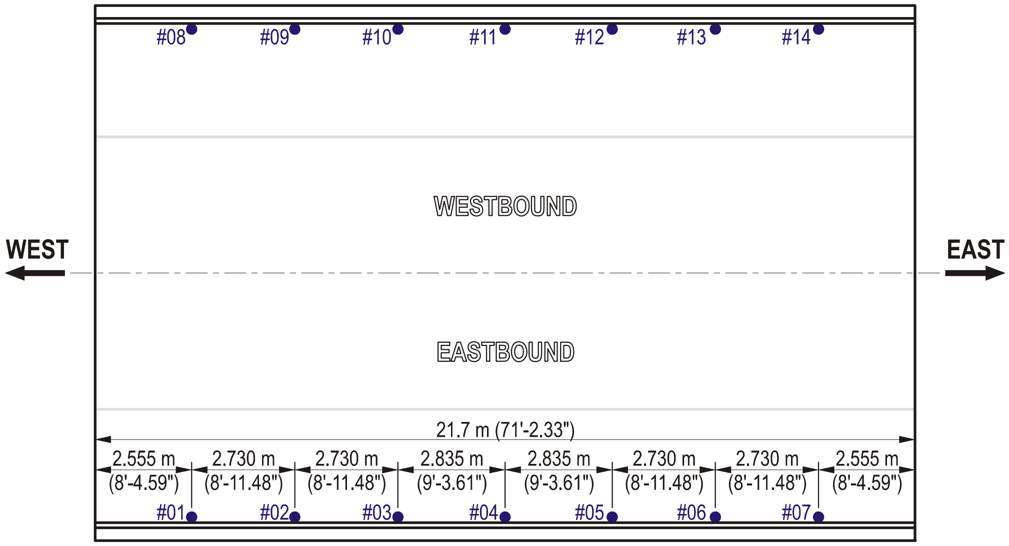

Figure 7.9. Location of the accelerometers on the bridge slab

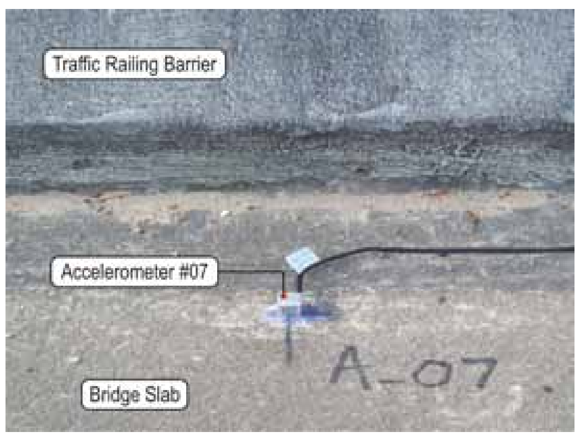

Figure 7.10. Accelerometer #07 glued to the bridge slab

Characteristics of the gauges used for the test were provided in Table 7.5 and Table 7.6. Detailed description of the instrumentation of the vehicles is presented in the next parts.

Table 7.5. Characteristics of the accelerometers located on the vehicles during the test

Manufacturer	Summit Instruments, Inc.	Range	(G)	±5
Model Number	13203B	Rated Output	(mV/G)	450
Weight (g) / (lb)	38 / 0.084	Frequency Response / Natural	(Hz)	N.A. / N.A.
Non-Linearity	0.2% Full Scale Reading	Excitation Voltage Used	(V)	10

Table 7.6. Characteristics of the displacement gauge used for spring deflection measurement during the test

Manufacturer	Penny+Giles	Mechanical Stroke	(mm) / (in)	104 / 4.1
Model Number	MLS130/100/R/N	Weight	(g) / (lb)	101 / 0.223

Tractor-Trailer

A total of 8 accelerometers were installed on this vehicle. Five of them were glued to the axles whereas the rest were attached to the tractor frame (two) and the load deck of the trailer (one). The mounting location of all accelerometers is provided in Table 7.7. Selected gauges installed on the tractor-trailer system are presented in Figure 7.11.

Table 7.7. Mounting location of the accelerometers for the truck tractor with the single drop lowboy trailer

No.	Mounting Location	No.	Mounting Location
A_1	Center of the Axle No. 1 – Steer Axle	A_5	Center of the Axle No. 4
A_2	Center of the Axle No. 2 – Cross Channel	A_6	Center of the Axle No. 6
A_3	Center of the Axle No. 3 – Cross Channel	A_7	Trailer Load Deck Above the Axle No. 4
A_4	Center of the 5th Wheel Plate	A_8	Passenger Side of the Tractor Frame Near the Engine

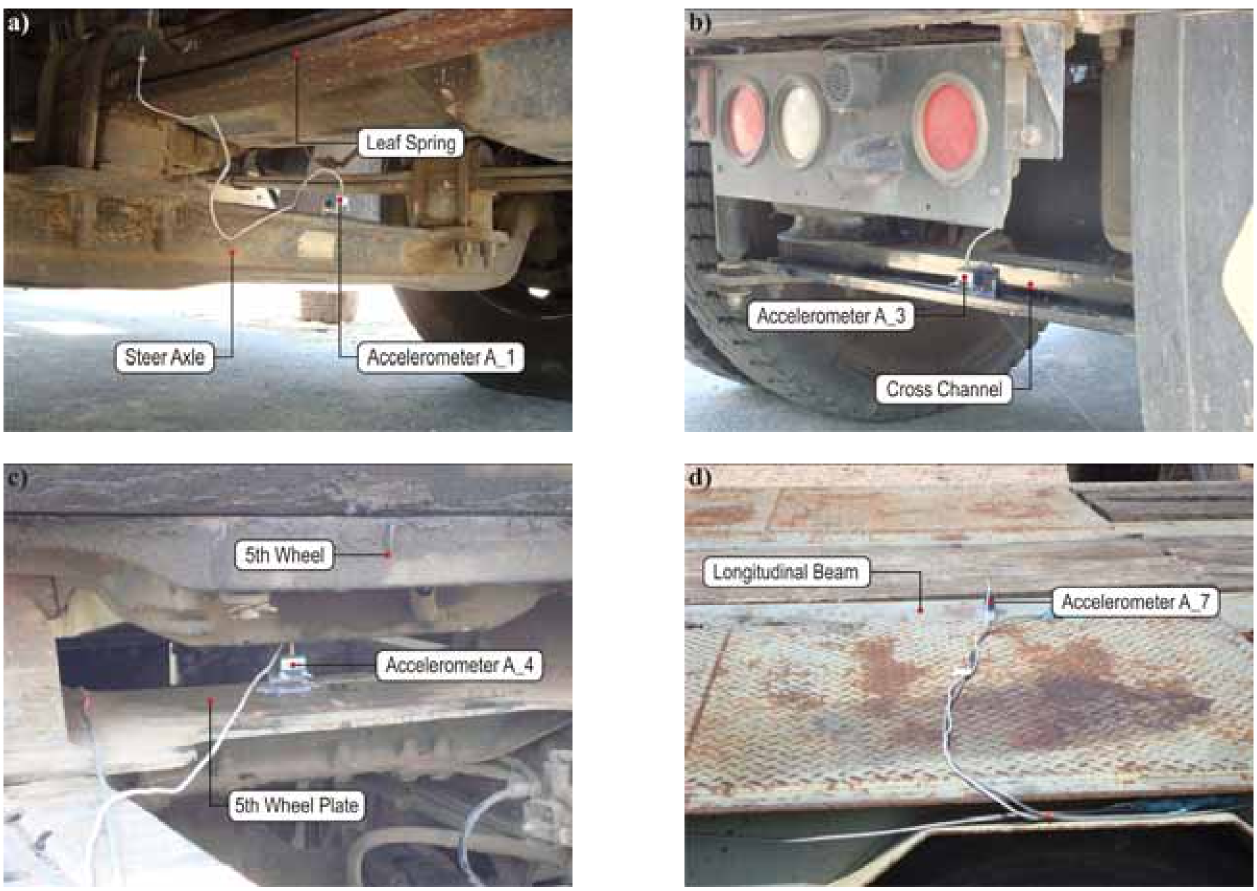

Figure 7.11. Selected accelerometers located on the truck tractor and lowboy trailer:
a) accelerometer A_1 – front steer axle, b) accelerometer A_3 – cross channel of the rear suspension,
c) accelerometer A_4 – fifth wheel plate, d) accelerometer A_7 – longitudinal beam of the trailer

Terex T-340 Crane

A total of 6 accelerometers were installed on this vehicle – one on each axle, two on the frame and one on the boom. Mounting location of all accelerometers is provided in Table 7.8. A linear displacement sensor used for the spring deflection measurement was mounted to the front shock absorber using special brackets. Selected gauges installed on the Terex crane are presented in Figure 7.12.

Table 7.8. Mounting location of the accelerometers for the Terex T-340 crane

No.	Mounting Location	No.	Mounting Location
A_1	Center of the Axle No. 1 – Steer Axle	A_4	Passenger Side of the Axle No. 3 – Axle Housing
A_2	Center of the Front Bumper	A_5	Center of the Frame Near the Turntable
A_3	Passenger Side of the Axle No. 2 – Axle Housing	A_6	Boom Above the Axle No. 1

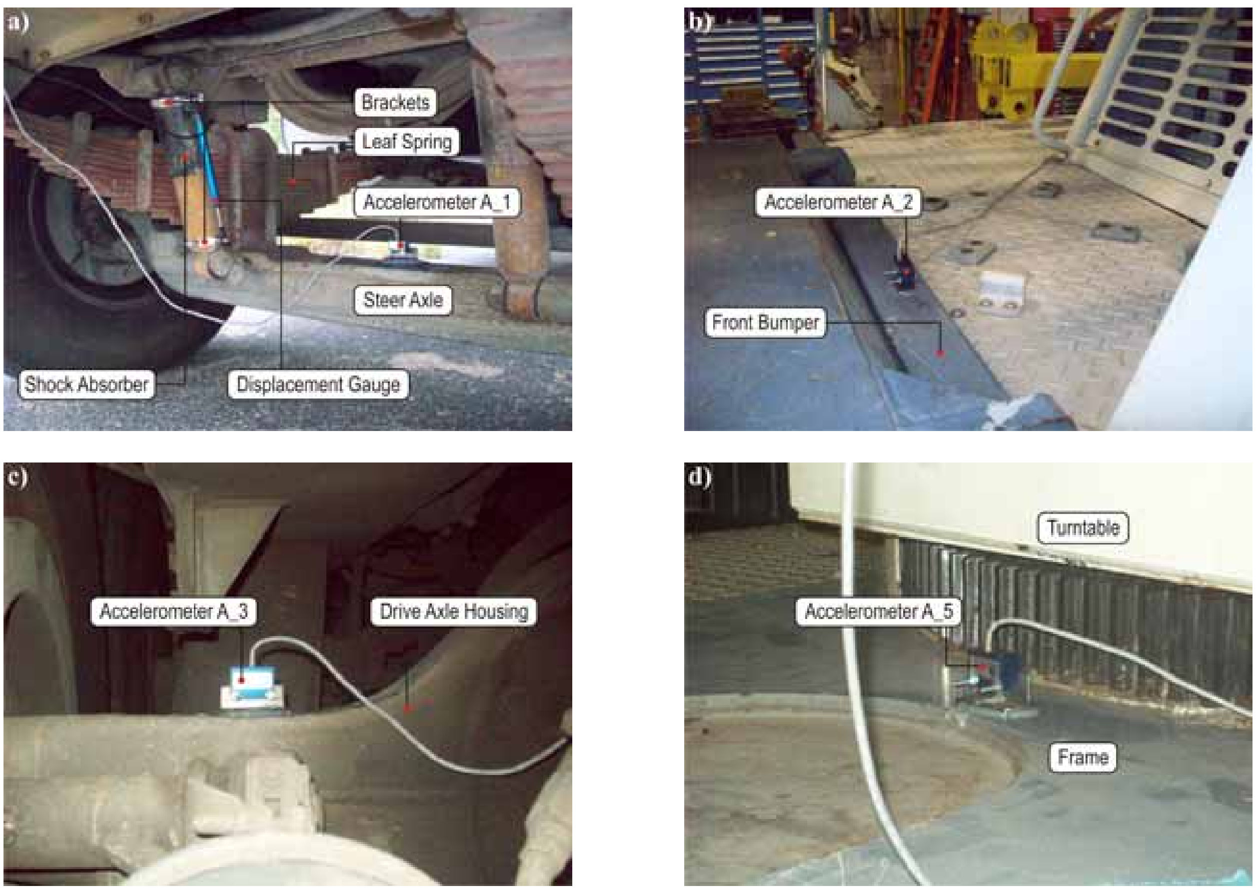

Figure 7.12. Selected gauges located on the Terex crane:
a) accelerometer A_1 and displacement gauge – front steer axle, b) accelerometer A_2 – front bumper,
c) accelerometer A_3 – forward drive axle housing, d) accelerometer A_5 – frame next to the turntable

7.4. Loading Configurations for the Static Tests

Calculations of the appropriate position for each vehicle are described in this sub-chapter. Static tests were carried out for the longitudinal position of the vehicle that causes the maximum bending moment in the middle of the bridge span. Therefore, all tested vehicles were weighed before the tests to find out the axle load. The results are provided in Table 7.9 to Table 7.11. Moreover, three different transverse positions of vehicle were taken into consideration, as presented in Figure 7.13. In each static test strains and displacements in the middle section of the bridge span were measured.

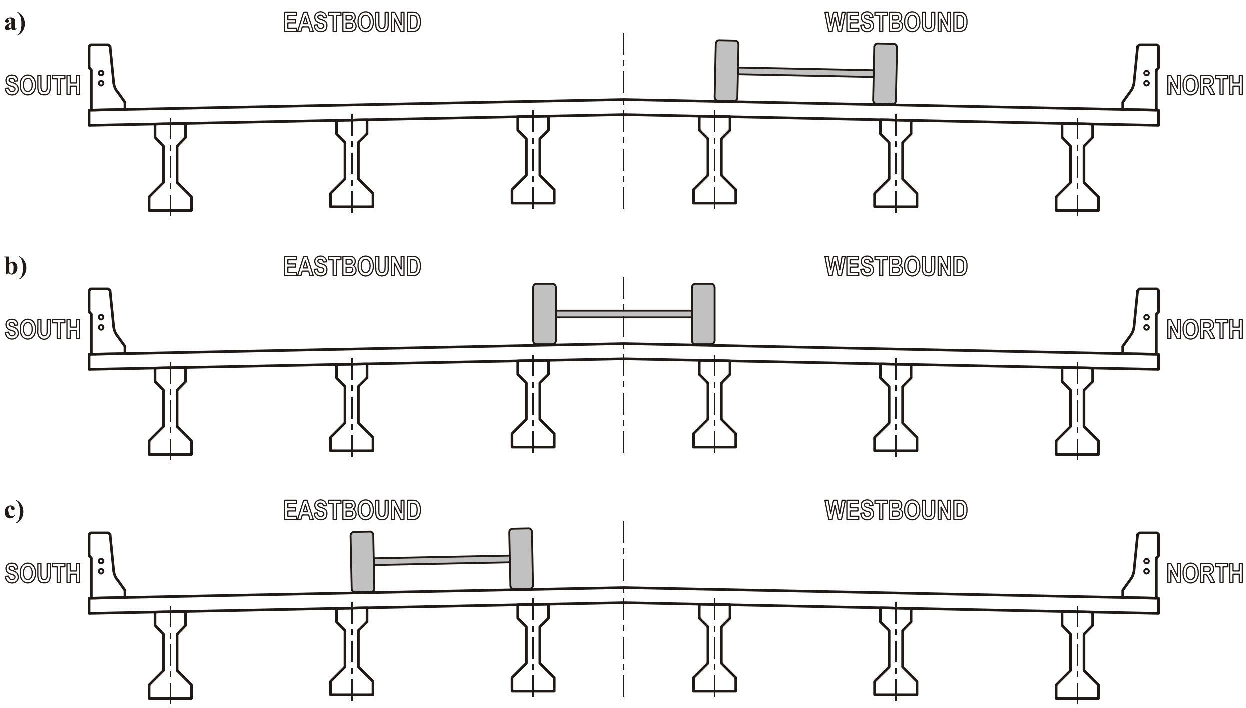

Figure 7.13. Transverse positions of the vehicles for the static tests:
a) vehicle in the center of the westbound traffic lane, b) vehicle at the center of the roadway,
c) vehicle in the in the center of the eastbound traffic lane.
In each configuration vehicle was heading west

Table 7.9. Axle load for the truck tractor and loaded lowboy trailer

Axle No.		1	2	3	4	5	6	Total
Weight	(kg)	4,300	9,117	9,680	9,643	10,043	10,278	53,061
	(lb)	9,480	20,100	21,340	21,260	22,140	22,600	116,980
Load	(kN)	42.184	89.440	94.958	94.602	98.517	100.831	520.532

Table 7.10. Axle load for the Terex T-340 crane

Axle No.		1	2	3	Total
Weight	(kg)	8,691	9,553	9,426	27,670
	(lb)	19,160	21,060	20,780	61,000
Load	(kN)	85.257	93.711	92.466	271.434

Table 7.11. Axle load for the FDOT truck tractor and trailer

Axle No.		1	2	3	4	5	Total
Weight	(kg)	5,108	4,898	4,898	8,614	8,614	32,132
	(lb)	11,260	10,800	10,800	18,990	18,990	72,840
Load	(kN)	50.104	48.057	48.057	84.501	84.501	315.220

Longitudinal Position of the Tractor-Trailer

Finding out the critical position of the vehicle which gives maximum bending moment in the middle of the span is based on the theory of the influence lines for statically determinate structures (Hibbeler, 1998). If we look upon the bridge as a simple supported beam, the maximum moment in the middle of that beam occurs if the major of the concentrated forces lying nearest the resultant force of the system is located at the centerline of the beam.

For the tractor-trailer system maximum moment in the middle of the span occurs if the fourth axle is situated at the centerline of the span, as presented in Figure 7.14a.

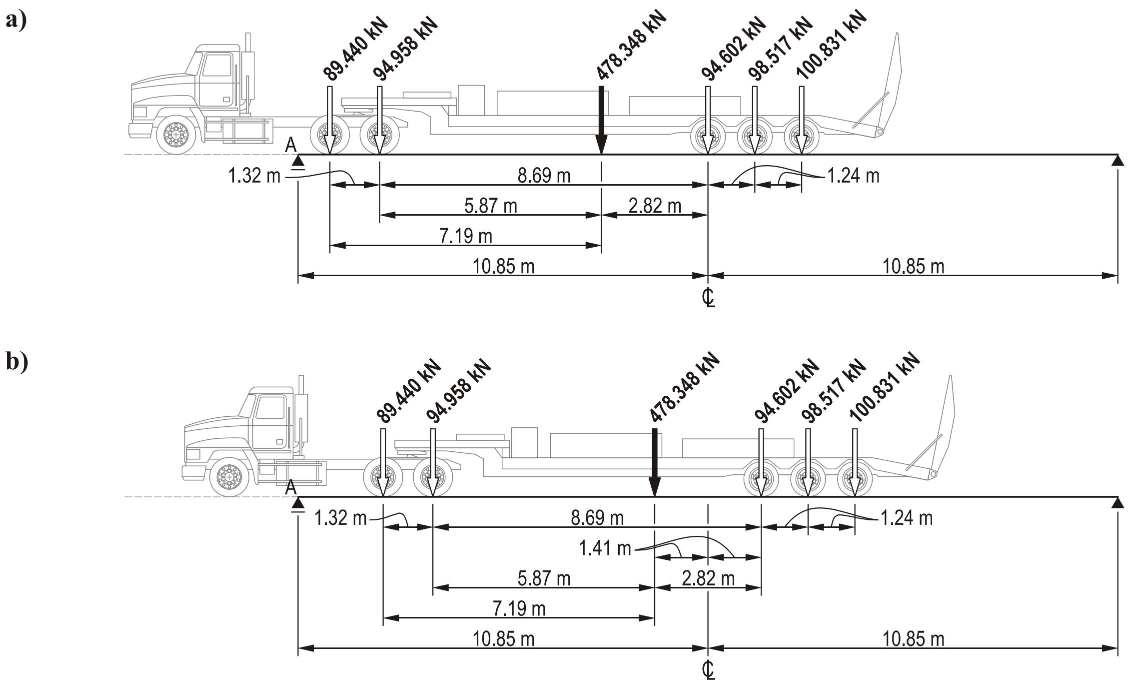

Figure 7.14. Position of the tractor-trailer system which results:
a) the maximum moment in the middle of the span, b) the absolute maximum moment

The resultant force for the following configuration is

$$F_R = 89.440 + 94.958 + 94.602 + 98.517 + 100.831 = 478.348 \text{ kN}$$

and its location is defined as the distance from the second axle

$$d = \frac{94.958 \cdot (1.32) + 94.602 \cdot (10.01) + 98.517 \cdot (11.25) + 100.831 \cdot (12.49)}{478.348} = 7.19 \text{ m}$$

The reaction force in point A is

$$A_y = \frac{478.348 \cdot (10.85 + 2.82)}{21.7} = 301.337 \text{ kN}$$

and the maximum moment in the middle of the span is

$$M = 301.337 \cdot (10.85) - 89.440 \cdot (1.32 + 8.69) - 94.958 \cdot (8.69) = 1549.027 \text{ kN} \cdot \text{m}$$

The absolute maximum moment for the considered system occurs under the fourth axle in position depicted in Figure 7.14b.

The reaction force in point A is

$$A_y = \frac{478.348 \cdot (10.85 + 1.41)}{21.7} = 270.256 \text{ kN}$$

and the absolute maximum moment is

$$M_{\max} = 270.256 \cdot (10.85 + 1.41) - 89.440 \cdot (1.32 + 8.69) - 94.958 \cdot (8.69) = 1592.859 \text{ kN} \cdot \text{m}$$

Longitudinal Position of the Terex Crane

For the Terex T-340 crane maximum moment in the middle of the span occurs if the second axle is situated at the centerline of the span, as presented in Figure 7.15a.

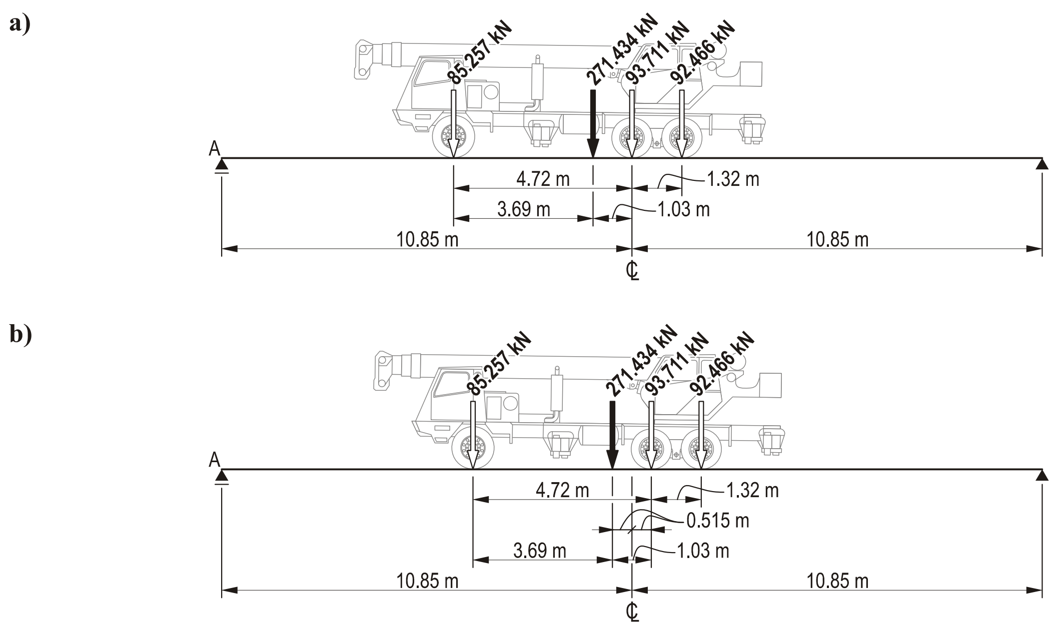

Figure 7.15. Position of the Terex T-340 crane which results:
a) the maximum moment in the middle of the span, b) the absolute maximum moment

The resultant force for the following configuration is

$$F_R = 85.257 + 93.711 + 92.466 = 271.434 \text{ kN}$$

and its distance from the first axle

$$d = \frac{93.711 \cdot (4.72) + 92.466 \cdot (6.04)}{271.434} = 3.69 \text{ m}$$

The reaction force in point A is

$$A_y = \frac{271.434 \cdot (10.85 + 1.03)}{21.7} = 148.601 \text{ kN}$$

and the maximum moment in the middle of the span is

$$M = 148.601 \cdot (10.85) - 85.257 \cdot (4.72) = 1209.908\,\text{kN} \cdot \text{m}$$

The absolute maximum moment for the considered system occurs under the second axle in position depicted in Figure 7.15b.

The reaction force in point A is

$$A_y = \frac{271.434 \cdot (10.85 + 0.515)}{21.7} = 142.159\,\text{kN}$$

and the absolute maximum moment is

$$M_{\max} = 142.159 \cdot (10.85 + 0.515) - 85.257 \cdot (4.72) = 1213.224\,\text{kN} \cdot \text{m}$$

Longitudinal Position of the FDOT Truck

For the FDOT truck maximum moment in the middle of the span occurs if the fourth axle is situated at the centerline of the span, as presented in Figure 7.16a.

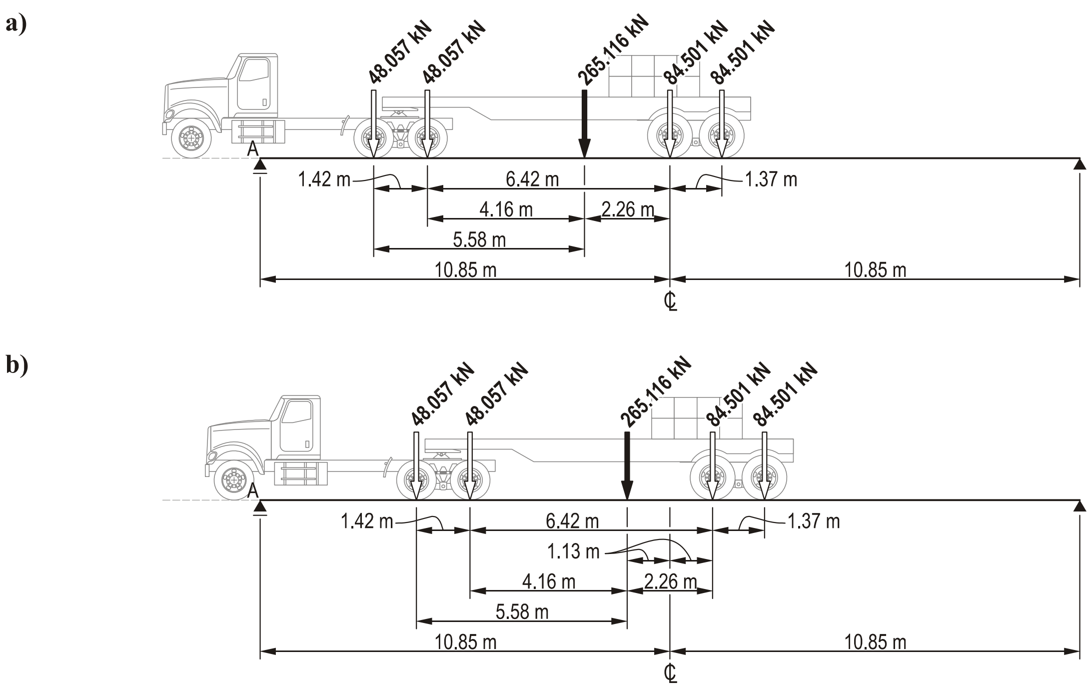

Figure 7.16. Position of the FDOT truck which results:
a) the maximum moment in the middle of the span, b) the absolute maximum moment

The resultant force for the following configuration is

$$F_R = 48.057 + 48.057 + 84.501 + 84.501 = 265.116\,\text{kN}$$

and its distance from the second axle

$$d = \frac{48.057 \cdot (1.42) + 84.501 \cdot (7.66) + 84.501 \cdot (9.03)}{265.116} = 5.58\,\text{m}$$

The reaction force in point A is

$$A_y = \frac{265.116 \cdot (10.85 + 2.26)}{21.7} = 160.169\,\text{kN}$$

and the maximum moment in the middle of the span is

$$M = 160.169 \cdot (10.85) - 48.057 \cdot (1.42 + 6.42) - 48.057 \cdot (6.42) = 1052.541\,\text{kN} \cdot \text{m}$$

The absolute maximum moment for the considered system occurs under the fourth axle in position depicted in Figure 7.16b.

The reaction force in point A is

$$A_y = \frac{265.116 \cdot (10.85 + 1.13)}{21.7} = 146.364\,\text{kN}$$

and the absolute maximum moment is

$$M_{\max} = 146.364 \cdot (10.85 + 1.13) - 48.057 \cdot (1.42 + 6.42) - 48.057 \cdot (6.42) = 1068.148\ \text{kN} \cdot \text{m}$$

Values of the maximum moment in the middle of the bridge span and the absolute maximum moment for all tested vehicles are compared in Table 7.12.

Table 7.12. Maximum bending moments in the bridge span for different vehicles used for the tests

Vehicle		Truck-Tractor	Terex T-340 Crane	FDOT Truck
Total Weight of the Tested Vehicle	(kg) (lb)	53,061 116,980	27,670 61,000	32,132 70,840
Maximum Bending Moment in the Middle of the Bridge Span	(kN·m) (ft·k)	1549.027 1142.504	1209.908 892.382	1052.541 776.314
Absolute Maximum Bending Moment in the Bridge Span	(kN·m) (ft·k)	1592.859 1147.833	1213.224 894.828	1068.148 787.826
Distance of the Maximum Moment from the Centerline of the Span	(m) (in)	1.41 55.51	0.515 20.58	1.13 44.49

Based on results provided in Table 7.12, it can be claimed that the value of the bending moment does not depend on the total weight of the vehicle only. Axle spacing as well as their number has influence on the load distribution on the bridge span and on the maximum moment. The crane used for the tests had lower weight than the FDOT truck, but it caused relatively higher load on the bridge span due to small wheelbase and less number of the axles.

7.5. Loading Configurations for the Dynamic Tests

Dynamic tests included runs of each vehicle on the westbound lane and on the center of the roadway (see Figure 7.17) at two different speeds – 30 mph (48 km/h) and 50 mph (80 km/h). During the tests, the vehicles were entering bridge from east and heading west, according to regular traffic direction.

In each dynamic test, strains, displacements and accelerations in selected points for the bridge were recorded as well as accelerations in a few points located on the vehicles.

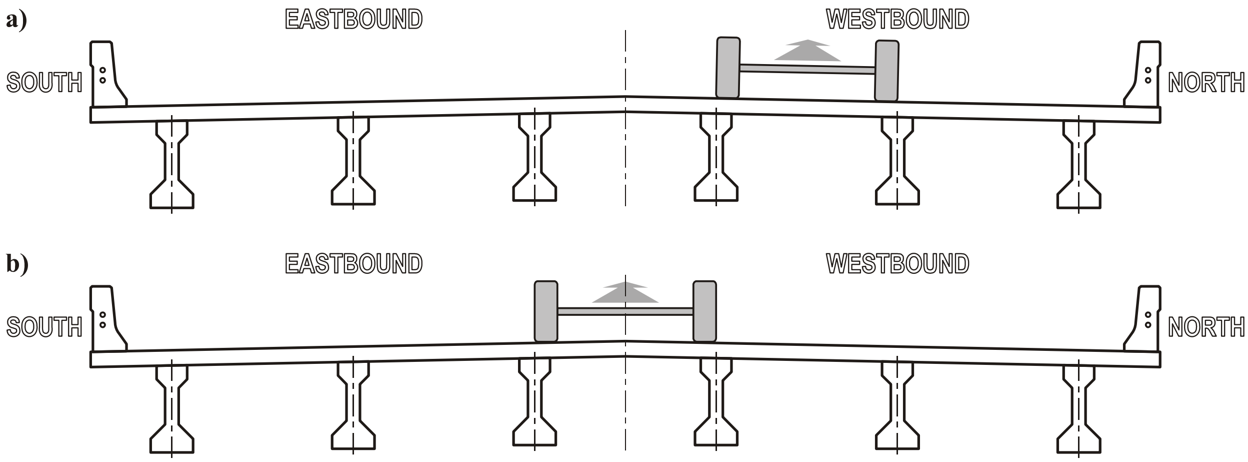

Figure 7.17. Transverse positions of the vehicles for the dynamic tests:
a) vehicle in the center of the westbound traffic lane, b) vehicle at the center of the roadway.
In each configuration vehicle was heading west

7.6. Results of the Static Tests

Results of the conducted static tests are presented for the middle section (No. 2) since obtained values were the most significant and reliable. Moreover, deflection of the span as well as strains achieves maximum range in this section. The results are shown separately for three different vehicles and for each of the three transverse positions depicted in Figure 7.13.

The results from the strain gages located at the bottom of each girder are presented in the Final Report only. The obtained strains are the maximum ones and they were taken into consideration for the impact factor calculation. Their values will be also compared with the results of the FE analysis in Chapter 8.

Results obtained for the strain gages attached to the railing barriers were not presented since they were characterized by a high scatter of values.

Static Tests for the Tractor-Trailer

Static tests for the truck tractor and the lowboy trailer included runs No. 1–3 (Attempt 1) and No. 12–14 (Attempt 2). Deflections of the bridge span measured using two independent LVDT devices located under the girders No. 3 and No. 4 are provided in Table 7.13.

Table 7.13. Deflection of the bridge span for the tractor-trailer

	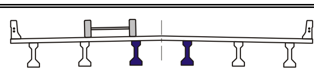		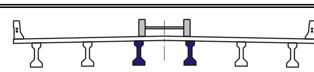		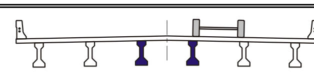	
	Girder #3	Girder #4	Girder #3	Girder #4	Girder #3	Girder #4
Attempt 1	–1.71	–0.49	–1.77	–1.22	–0.88	–1.02
Attempt 2	–1.96	–0.75	–1.96	–1.29	–0.98	–1.19
Average Value	**–1.84**	**–0.62**	**–1.86**	**–1.25**	**–0.93**	**–1.11**

The obtained results show that there is no symmetry in the considered case. It might be related with the fact that calibration of the displacement devices was not performed every single time before each run; it was done before a group of three runs.

Results of the static test from the strain gages located at the bottom of each girder are depicted in the form of column charts in Figure 7.18. The results of the tests carried out in two attempts, one before the dynamic test and one after it, show relatively good repeatability. The highest values of the strains (about 50 micro strains) were observed always for the girders located directly under the vehicle. Symmetry of the results is noticeable – its axis corresponded to the vertical axis of symmetry of the vehicle.

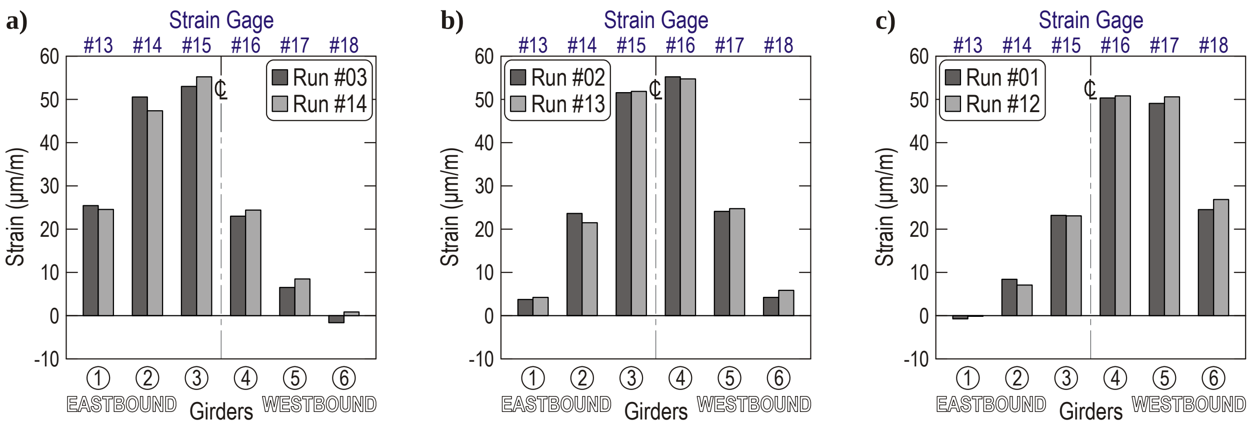

Figure 7.18. Longitudinal strains at the bottom of the girder for the tractor-trailer: a) vehicle in the center of the eastbound traffic lane, b) vehicle at the center of the roadway, c) vehicle in the in the center of the westbound traffic lane

Static Tests for the Terex Crane

Static tests for the Terex crane tractor included runs No. 22–24 (Attempt 1) and No. 33–35 (Attempt 2). Deflections of the bridge span measured under the girders No. 3 and No. 4 are provided in Table 7.14.

Table 7.14. Deflection of the bridge span for the Terex crane

	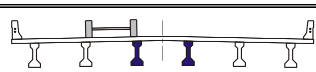		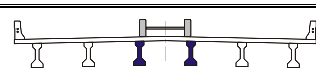		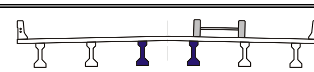	
	Girder #3	Girder #4	Girder #3	Girder #4	Girder #3	Girder #4
Attempt 1	–1.27	–0.69	–1.27	–1.48	–0.54	–1.38
Attempt 2	–1.37	–0.64	–1.37	–1.48	–0.56	–1.39
Average Value	**–1.32**	**–0.67**	**–1.32**	**–1.48**	**–0.55**	**–1.38**

Results of the static test from the strain gages located at the bottom of each girder are depicted in Figure 7.19. The results show relatively good repeatability. However, some of them were not considered due to their significantly higher values in comparison to the other ones. Maximum strains are about 5 micro strains less than values obtained for the tractor-trailer which was almost twice heavier. It is caused by the small outer bridge length of the crane and the load distributed on a shorter distance.

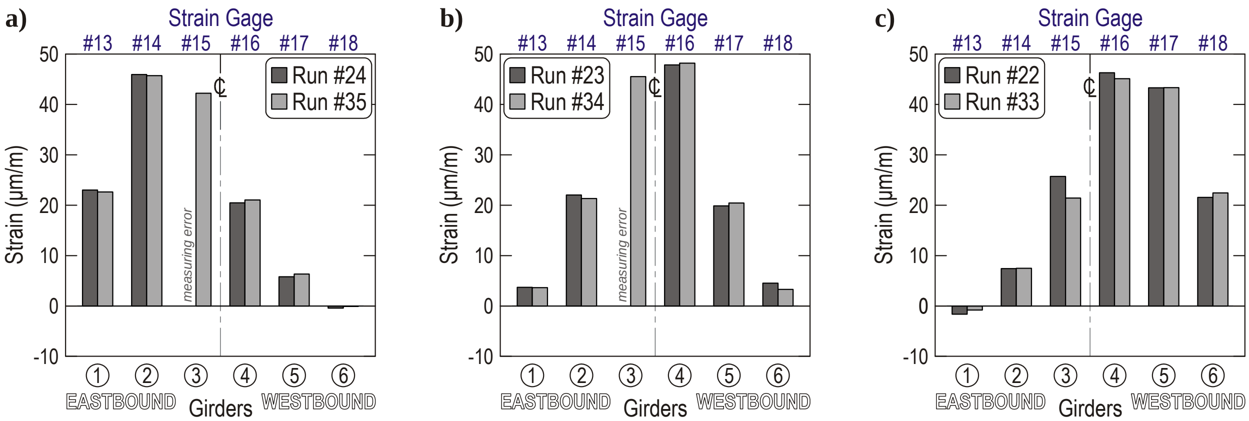

Figure 7.19. Longitudinal strains at the bottom of the girder for the Terex crane:
a) vehicle in the center of the eastbound traffic lane, b) vehicle at the center of the roadway,
c) vehicle in the in the center of the westbound traffic lane

Static Tests for the FDOT Truck

Static tests for the Terex crane tractor included runs No. 15–17 (Attempt 1). Deflections of the bridge span measured under girders No. 3 and No. 4 are provided in Table 7.15. Strain values from the strain gages located at the bottom of each girder are depicted in Figure 7.20.

Table 7.15. Deflection of the bridge span for the FDOT truck

	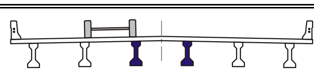		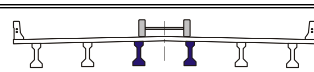		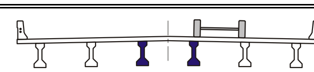	
	Girder #3	Girder #4	Girder #3	Girder #4	Girder #3	Girder #4
Attempt 1	–1.47	–0.39	–1.57	–0.93	–0.73	–0.65

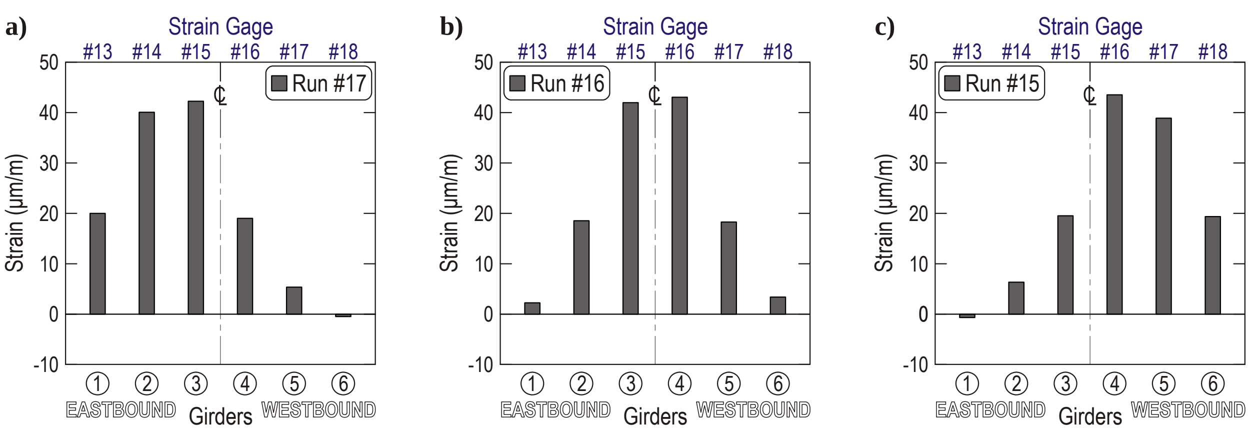

Figure 7.20. Longitudinal strains at the bottom of the girder for the FDOT truck:
a) vehicle in the center of the eastbound traffic lane, b) vehicle at the center of the roadway,
c) vehicle in the in the center of the westbound traffic lane

7.7. Results of the Dynamic Tests

Results of the conducted dynamic tests are presented, as previously, for the middle section only. They are shown separately for three different vehicles and for each of the two transverse positions depicted in Figure 7.17. A velocity of 80 km/h (50 mph) was taken into account in the current Final Report since all three vehicles were tested at that velocity. The range of values on the ordinate axes, bridge deflection or strain, remains the same for all considered cases. This approach allows easy comparison of the obtained results.

Time histories of the deflection of the span and the longitudinal strains at the bottom surface of each girder are presented for the selected cases provided in Table 7.1. It was decided to omit the acceleration histories of selected points located on the bridge deck. A range of data recorded for the tractor-trailer and the FDOT truck was too low to consider it and, consequently, useless for current research. Data from the strain gages located at the bottom of each girder are presented in the Final Report only.

The time histories were presented for five-second long time periods. All data were filtered during processing using cosine filters available in the LS-PrePost software. Frequencies as well as number of average points were the same for all corresponding cases. It allows eliminating divergences between presented results.

Dynamic Tests for the Tractor-Trailer

Dynamic tests for the truck tractor and the lowboy trailer at a velocity of 80 km/h (50 mph) included runs No. 8–11. Deflection of the bridge span was measured using LVDT devices located under girders No. 3 and No. 4. The obtained results are depicted in Figure 7.21.

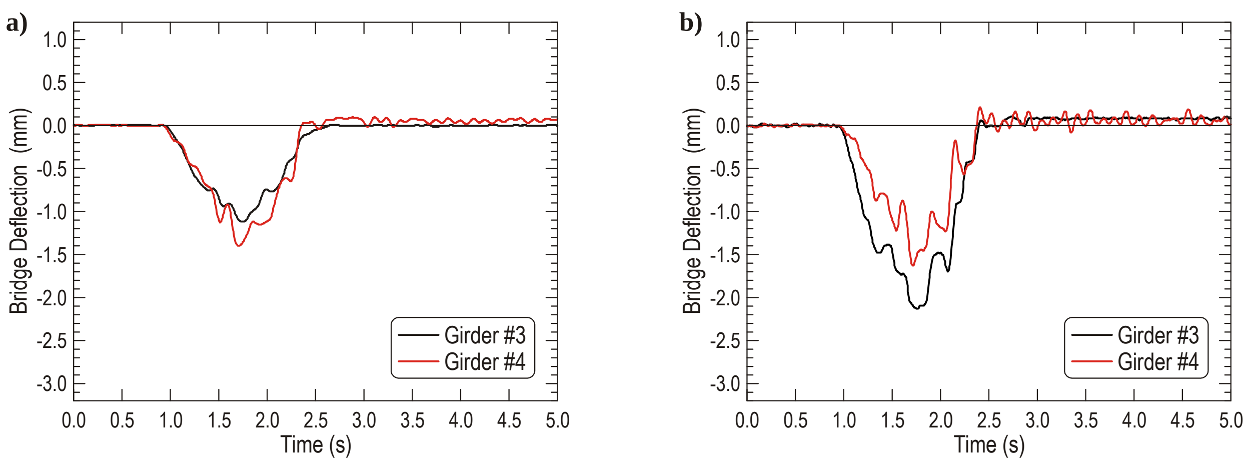

Figure 7.21. Deflection of the bridge for the tractor-trailer:
a) vehicle in the center of the westbound traffic lane – run #08,
b) vehicle at the center of the roadway – run #10

Maximum deflection of the bridge span is about 2 millimeters. The obtained curves are smooth and any additional vibration of the span was not be observed. In the final phase of crossing over the bridge it can be seen that the bridge does not return to its initial position – deflection does not equal to 0 mm. It is caused by the LVDT sensors used for the test. Therefore it should be assumed that final configuration of the bridge is exactly the same as the initial one in spite of the obtained results.

Strain histories measured at the girders for the considered vehicle are presented in Figure 7.22 and Figure 7.23. Maximum strains reach values of about 50 to 55 micro strains depending on the considered case. These values are similar to ones obtained during the static tests. Therefore, expected values of the impact factor will be close to zero – the differences between static and dynamic response of the bridge are slight.

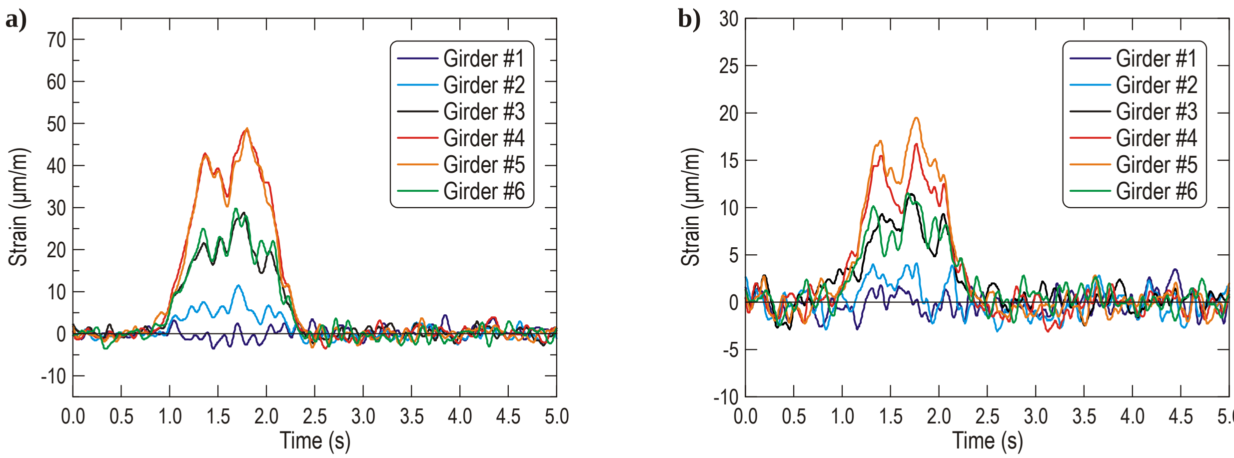

Figure 7.22. Strain histories for the tractor-trailer positioned in the center of the westbound traffic lane – run #08: a) measured at the bottom of the girders; b) measured at the side of the girder's web

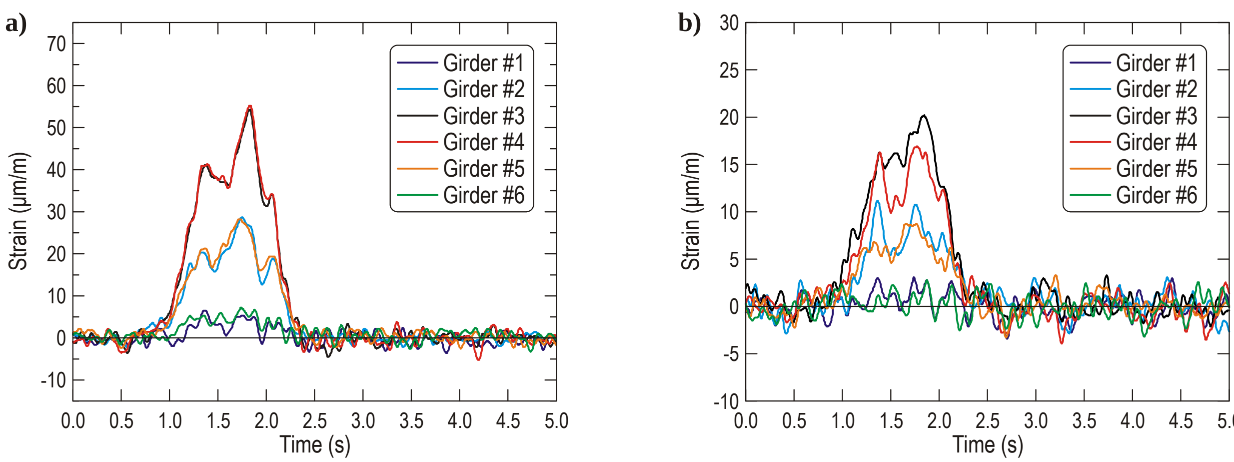

Figure 7.23. Strain histories for the tractor-trailer positioned at the center of the roadway – run #10: a) measured at the bottom of the girders; b) measured at the side of the girder's web

Dynamic Tests for the Terex Crane

Dynamic tests for the Terex crane at a velocity of 80 km/h (50 mph) included runs No. 29–32. Histories of the deflection of the bridge span are shown in Figure 7.24. Maximum deflection is about 2 millimeters and it is close to one rejected for the tractor-trailer. The obtained curves are smooth without any additional vibration.

Strain histories measured at the girders for the Terex crane are presented in Figure 7.25 and Figure 7.26. Maximum strains reach values of about 55 to 65 micro strains depending on the transverse position of the vehicle. Therefore, the differences between static and dynamic response of the bridge are more significant than for the previous vehicle. It is strictly related to the very stiff suspension of the crane.

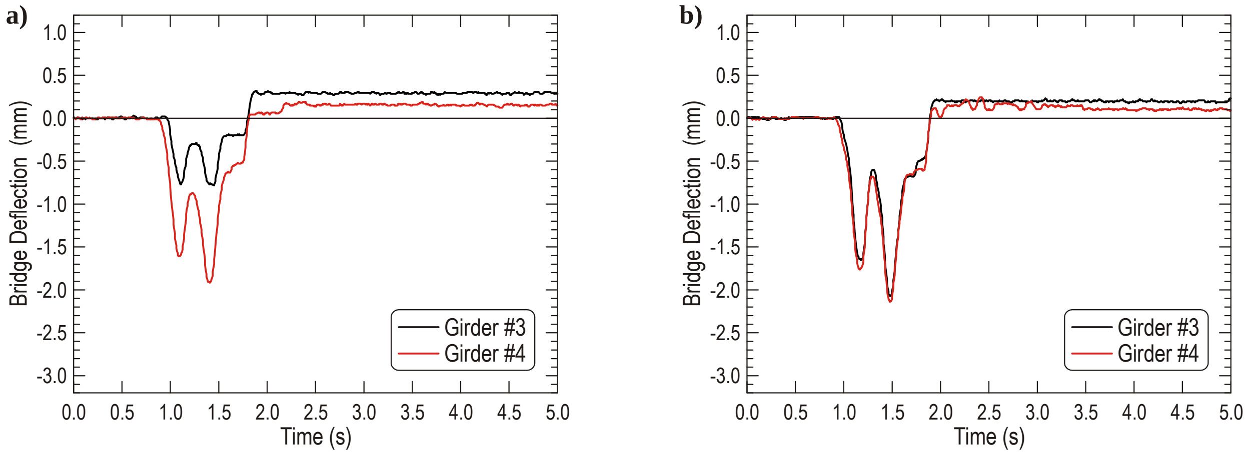

Figure 7.24. Deflection of the bridge for the Terex crane:
a) vehicle in the center of the westbound traffic lane – run #29,
b) vehicle at the center of the roadway – run #31

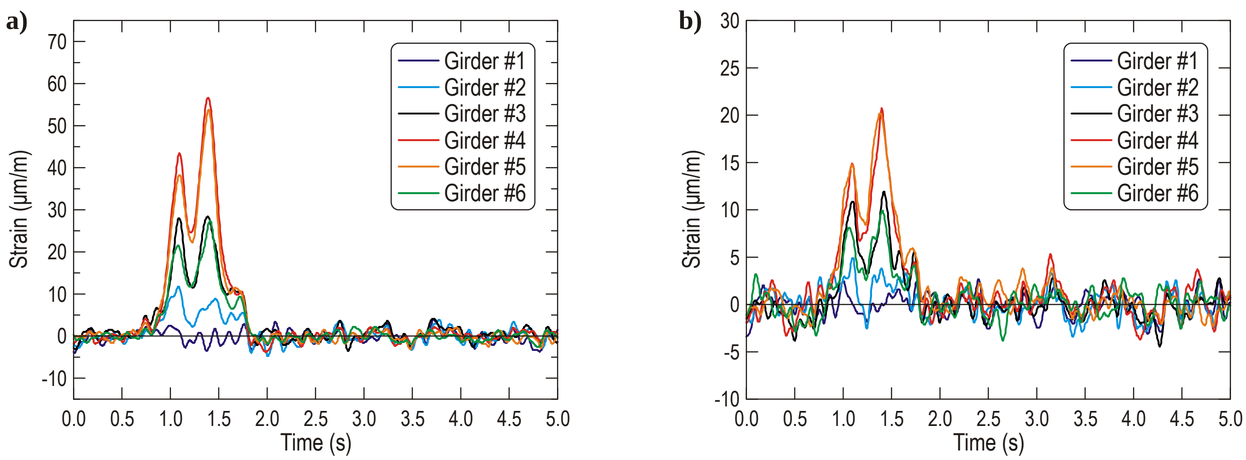

Figure 7.25. Strain histories for the Terex crane positioned in the center of the westbound traffic lane – run #29:
a) measured at the bottom of the girders; b) measured at the side of the girder's web

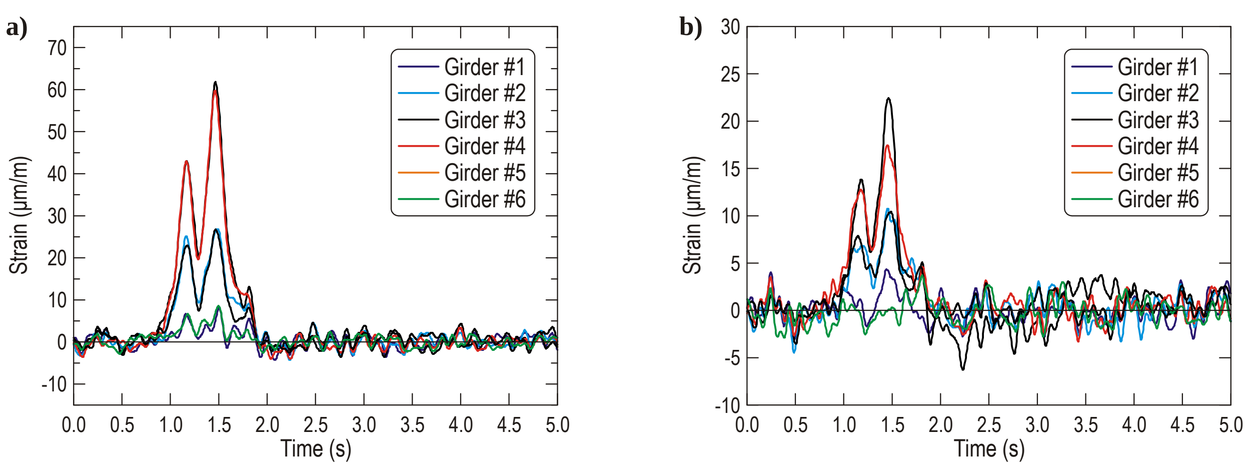

Figure 7.26. Strain histories for the Terex crane positioned at the center of the roadway – run #31:
a) measured at the bottom of the girders; b) measured at the side of the girder's web

Dynamic Tests for the FDOT Truck

Dynamic tests for the FDOT truck at a velocity of 80 km/h (50 mph) included runs No. 18–21. Histories of the deflection of the bridge span are depicted in Figure 7.27. Maximum obtained deflection of 3 millimeters is the highest one for all the considered vehicles.

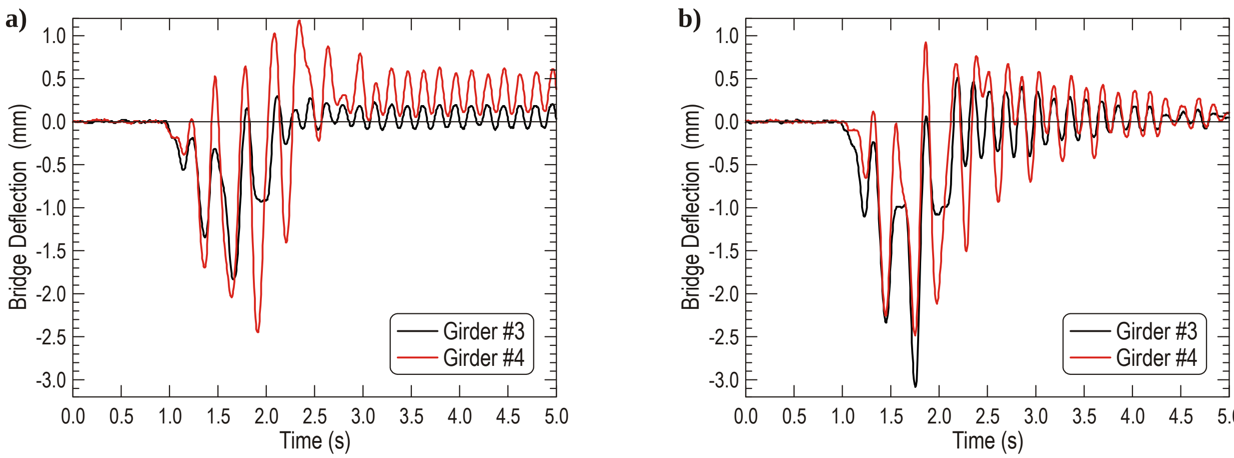

Figure 7.27. Deflection of the bridge for the FDOT truck:
a) vehicle in the center of the westbound traffic lane – run #18,
b) vehicle at the center of the roadway – run #20

Shapes of presented curves are completely different in comparison to one obtained for the two previous vehicles. Additional vibrations occur while the crane is crossing over the considered span. These oscillations do not disappear until the vehicle drives off the bridge. That phenomenon was the result of a hammering effect. Cargo located on the trailer consisted of twelve concrete blocks fastened to the load deck using chains. This type of binding is characterized by slight backlashes allowing for bounce of the cargo while driving on an uneven surface. This circumstance, in conjunction with very stiff suspension of the trailer, causes additional vibration generated while the vehicle runs over a threshold before the bridge. In addition, those vibrations are still detectable even though the vehicle is on the second or the third span. Oscillations are transmitted to other spans by the bridge slab which is continuous and common for all three spans.

Strain histories measured at the girders for the FDOT truck are presented Figure 7.28 and Figure 7.29. Maximum strains reach values close to 70 micro strains, the highest one for all tested vehicles.

7.8. Calculation of the Impact Factor

The impact factor *IM* is calculated based on the dynamic and static responses (deflections and/or strains) of the bridge structure. It is defined as:

$$IM = \frac{R_{dyn} - R_{st}}{R_{st}} \cdot 100\% \tag{7.1}$$

where:

R_{dyn} — maximum dynamic response (deflection, strain);

R_{st} — maximum static response (deflection, strain).

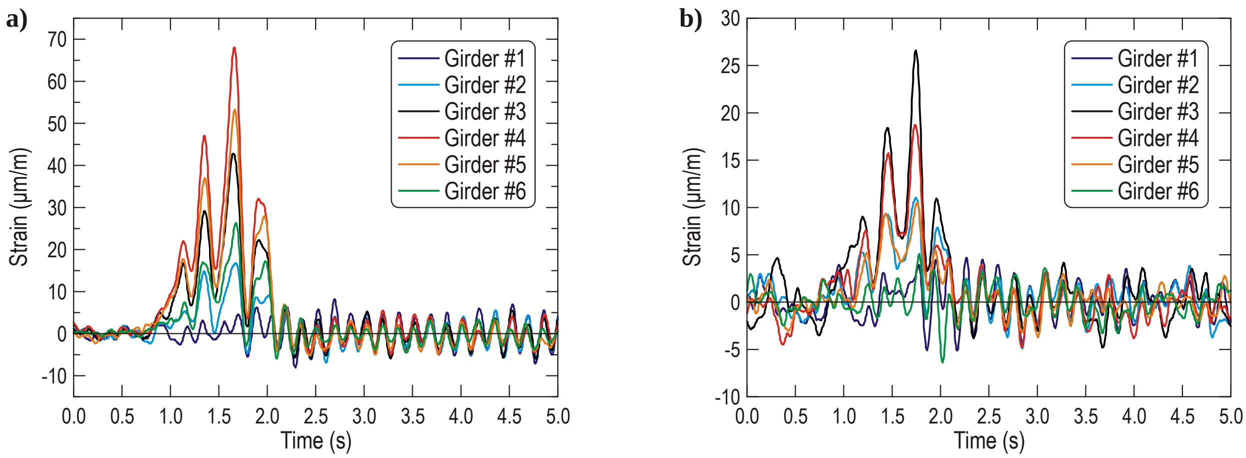

Figure 7.28. Strain histories for the FDOT truck positioned in the center of the westbound traffic lane – run #18: a) measured at the bottom of the girders; b) measured at the side of the girder's web

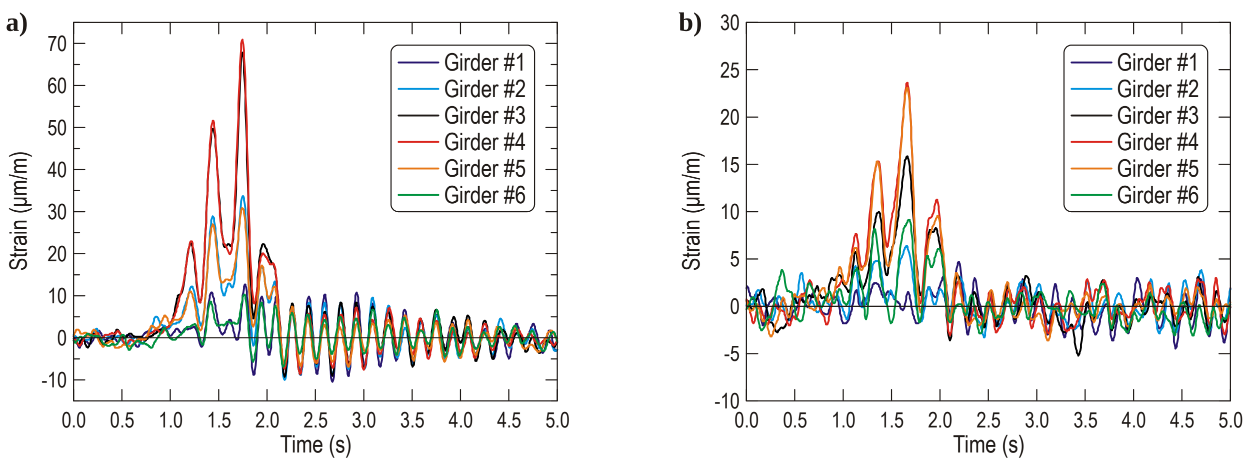

Figure 7.29. Strain histories for the FDOT truck positioned at the center of the roadway – run #20: a) measured at the bottom of the girders; b) measured at the side of the girder's web

The maximum values of deflections and strains, interpreted as the maximum static and dynamic responses, were taken into consideration in the impact factor calculation. Average values from two runs for each case are provided in Table 7.16 through Table 7.19. In addition, we decided to estimate the impact factor for the most loaded girders – those located exactly under the vehicle. This strategy allows us to eliminate obtaining extremely high values of the impact factor for cases calculated on the basis of very small values of strain, especially for the far left or the far right girders.

Table 7.16. Maximum deflections of the bridge span and values of the impact factor for vehicles positioned in the center of the westbound lane

	Girder	Tractor-Trailer	Terex Crane	FDOT Truck
Maximum Deflection (mm) Static	#3	–0.93	–0.55	–0.73
	#4	–1.11	–1.38	–0.65
Maximum Deflection (mm) Dynamic	#3	–1.08	–0.97	–1.92
	#4	–1.41	–2.07	–2.58
Impact Factor (%)	**#3**	**16.13**	**76.36**	**163.01**
	#4	**27.03**	**50.00**	**296.92**

Table 7.17. Maximum deflections of the bridge span and values of the impact factor for vehicles positioned at the center of the roadway

	Girder	Tractor-Trailer	Terex Crane	FDOT Truck
Maximum Deflection (mm) Static	#3	–1.86	–1.32	–1.57
	#4	–1.25	–1.48	–0.93
Maximum Deflection (mm) Dynamic	#3	–2.11	–2.05	–2.97
	#4	–1.52	–2.15	–2.35
Impact Factor (%)	**#3**	**13.44**	**55.30**	**89.17**
	#4	**21.60**	**45.27**	**152.69**

Table 7.18. Maximum strains at the bottom of the girder and values of the impact factor for the vehicles positioned in the center of the westbound lane

	Girder	Tractor-Trailer	Terex Crane	FDOT Truck
Maximum Strain (μm/m) Static	#4	50.59	45.69	43.52
	#5	49.84	43.32	38.98
Maximum Strain (μm/m) Dynamic	#4	49.36	59.78	70.10
	#5	48.30	54.26	55.41
Impact Factor (%)	**#4**	**–2.43**	**30.84**	**61.08**
	#5	**–3.09**	**25.23**	**42.15**

Table 7.19. Maximum strains at the bottom of the girder and values of the impact factor for the vehicles positioned at the center of the roadway

	Girder	Tractor-Trailer	Terex Crane	FDOT Truck
Maximum Strain (μm/m) Static	#3	51.72	45.53	41.98
	#4	55.00	48.18	43.06
Maximum Strain (μm/m) Dynamic	#3	54.54	60.17	66.14
	#4	55.94	58.74	67.66
Impact Factor (%)	**#3**	**5.45**	**32.15**	**57.55**
	#4	**1.71**	**21.92**	**57.13**

7.9. Conclusions

The impact factor was calculated based on responses, deflection and strains. The obtained results are presented in Figure 7.30. All rejected data were relatively small (2–3 millimeters for deflection and 50–70 micro strains for strain) and they were enclosed in the range of a measuring error. Therefore, the obtained values of the impact factor are should be considered in a qualitative respect instead of the quantitative one.

The worst case takes place for the FDOT truck due to its very stiff suspension. Equalizer beams applied in the FDOT trailer are not equipped with any additional rubber pads or cushions. Moreover, the bounced concrete blocks on the load deck increase the vibrations of the trailer and dynamic response of the bridge. Very high dynamic responses and a relatively small static load for this case results in extreme values of the impact factor.

The impact factor for the Terex crane, also equipped with equalizer beams, is much lower than the one for the FDOT truck. It confirms an assumed thesis about additional influence of the bounced load on the dynamic behavior of the driving vehicle.

The lowest values of the impact factor were obtained for the tractor-trailer, even though it was the heaviest vehicle used in the test. It is strictly related to the full suspension of that vehicle. Moreover, cargo placed on the deck of the trailer was fastened more carefully. Additional wooden planks were placed between the load components and the load deck. This allowed for partial damping of vibrations generated while the vehicle is crossing over the threshold before the bridge.

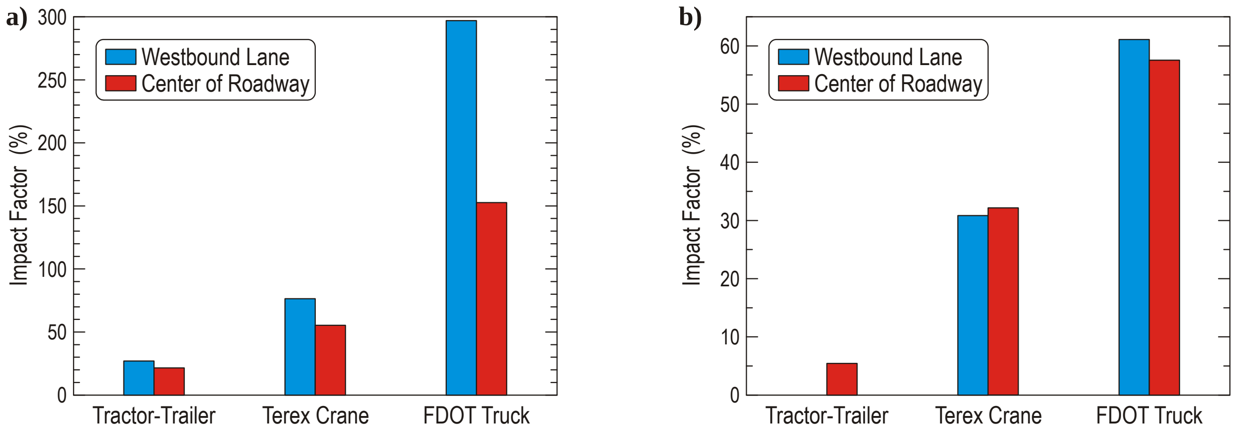

Figure 7.30. Comparison of the impact factor for different heavy vehicles calculated based on: a) deflections of the bridge span; b) strains at the bottom of the girder

8. FE ANALYSIS OF THE VEHICLE-BRIDGE INTERACTION

FE analyses were performed to check the correctness of vehicle FE models as well as their interaction with the bridge FE model. As mentioned in sub-chapter 4.1, the bridge FE model was already validated in a previous project (Wekezer, Li, Kwasniewski, & Malachowski, 2004) and it was applied in the current analyses without any additional modifications. FE analyses presented in the Final Report reflected an experimental test carried out on bridge #500133. Time histories obtained from the tests were compared with those from the simulations for each selected heavy vehicle. Cases for a maximum velocity of 80 km/h (50 mph) were considered in the current project. In addition, it was decided to assess the influence of railing barriers on the bridge strength and its behavior under dynamic interaction with the crossing vehicle.

8.1. FE Analysis for the Tractor-Trailer

FE analysis of the interaction between the tractor-trailer and the bridge included quasi-static and dynamic ones. In the first case, the experimental static tests were reflected. They allowed for measurement of deflection of the bridge FE model. Three different transverse positions of the vehicle were considered. Results are provided in Table 8.1. Values obtained from the FE analysis are significantly higher (about twice higher in some cases) than those from the experiment. It is hard to explain such differences but it is highly probable that they are related to the experimental test conducted on the bridge. Longitudinal strains recorded during the test and those from an FE analysis do not draw such discrepancies.

Longitudinal strains, as depicted in Figure 8.1, were rejected. Two dimensional shell elements were attached to the girder FE model in the locations corresponding to the strain gage position on the actual bridge.

Table 8.1. Comparison of the deflection (mm) of the bridge span and its FE model for the tractor-trailer

	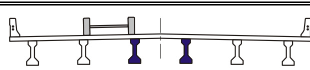		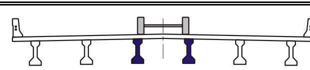		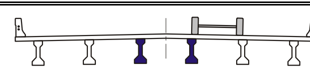	
	Girder #3	Girder #4	Girder #3	Girder #4	Girder #3	Girder #4
Attempt 1	–1.71	–0.49	–1.77	–1.22	–0.88	–1.02
Attempt 2	–1.96	–0.75	–1.96	–1.29	–0.98	–1.19
FE analysis	–2.93	–1.72	–3.01	–3.01	–1.72	–2.93

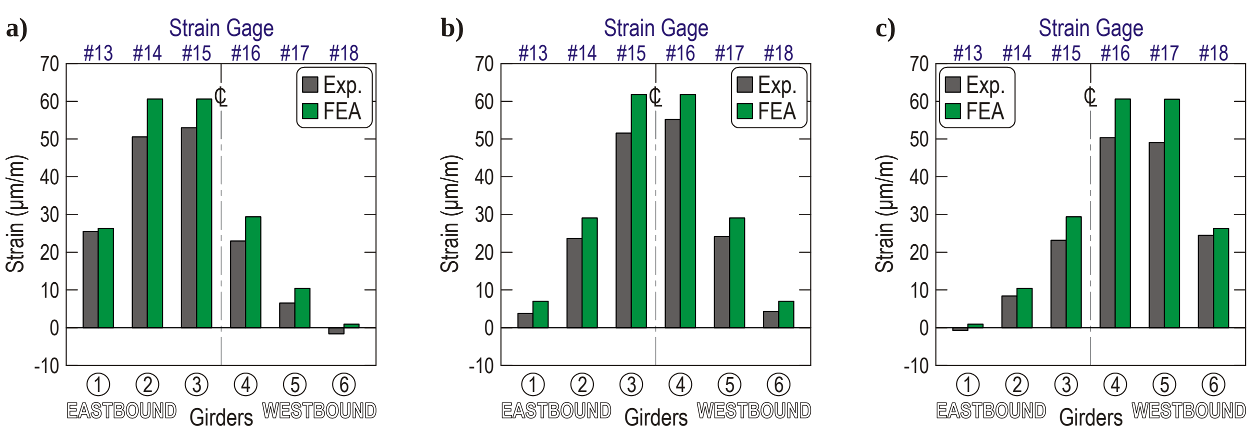

Figure 8.1. Longitudinal strain from the experimental testing and FE analysis at the bottom of the girder for the tractor-trailer: a) vehicle in the center of the eastbound traffic lane (run #03), b) vehicle at the center of the roadway (run #02), c) vehicle in the in the center of the westbound traffic lane (run #01)

Dynamic analyses included two runs at a velocity of 80 km/h (50 mph) for the vehicle FE model located in the center of the eastbound traffic lane and at the center of the roadway, as presented in Figure 8.2 through Figure 8.5. Just as previously, the significant differences in time histories of the bridge deflection are visible. It suggests that "zero" adjustments are supposed to be conducted before each dynamic and static run. In the tests carried out in this project, zeroing was done once, at the beginning of the tests for each vehicle.

In addition, three more FE analyses at velocities 32, 48, and 64 km/h (20, 30, and 40 mph) were performed for the tractor-trailer located in the center of the eastbound traffic lane. They allowed estimation of the influence of the velocity on the impact factor. The maximum deflection of girder No. 4 was taken into consideration only. It was decided to consider this girder due to its maximum load for selected transverse position of the vehicle. The results are shown in Table 8.1 and in Figure 8.6. Differences between maximum deflections for considered velocities are relatively small. In practice, they enclose within the bound of measurement error. However, even these slight differences influence the value of the impact factor.

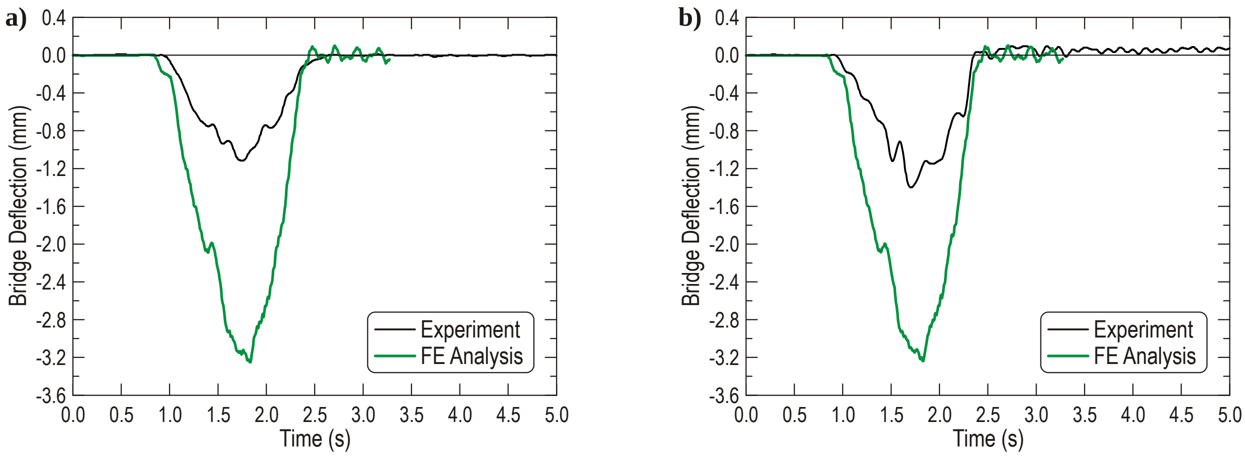

Figure 8.2. Deflection of the bridge span from the experimental testing and FE analysis for the tractor-trailer in the center of the westbound traffic lane (run #08): a) girder #3, b) girder #4

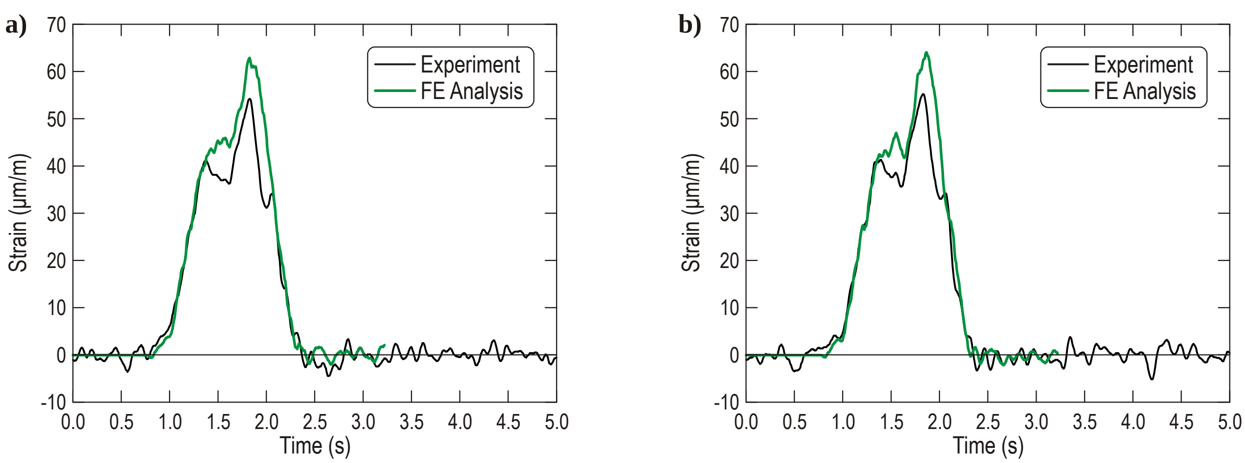

Figure 8.3. Longitudinal strain at the bottom of the girder from the experimental testing and FE analysis for the tractor-trailer in the center of the westbound traffic lane (run #08): a) girder #4, b) girder #5

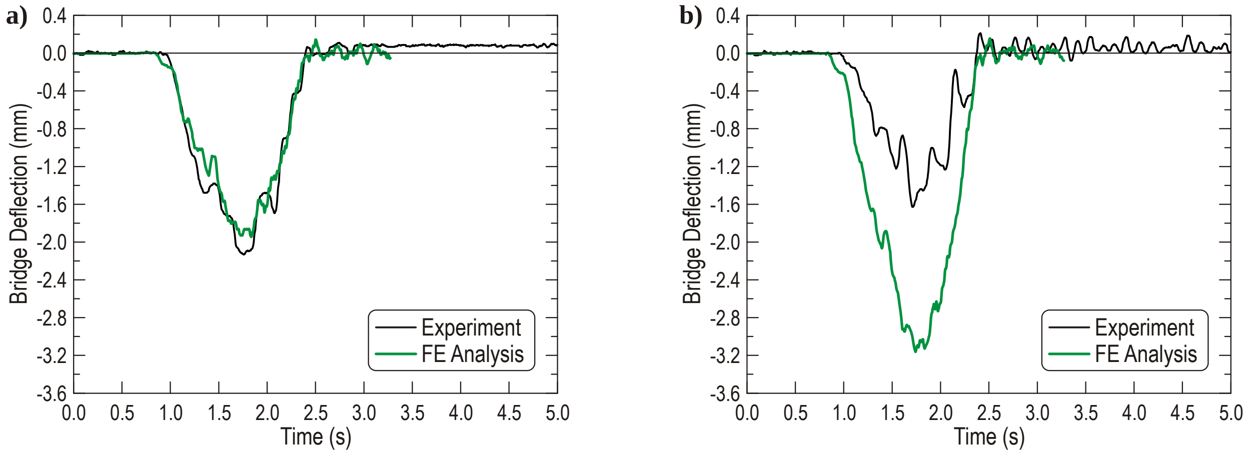

Figure 8.4. Deflection of the bridge span from the experimental testing and FE analysis for the tractor-trailer at the center of the roadway (run #10): a) girder #3, b) girder #4

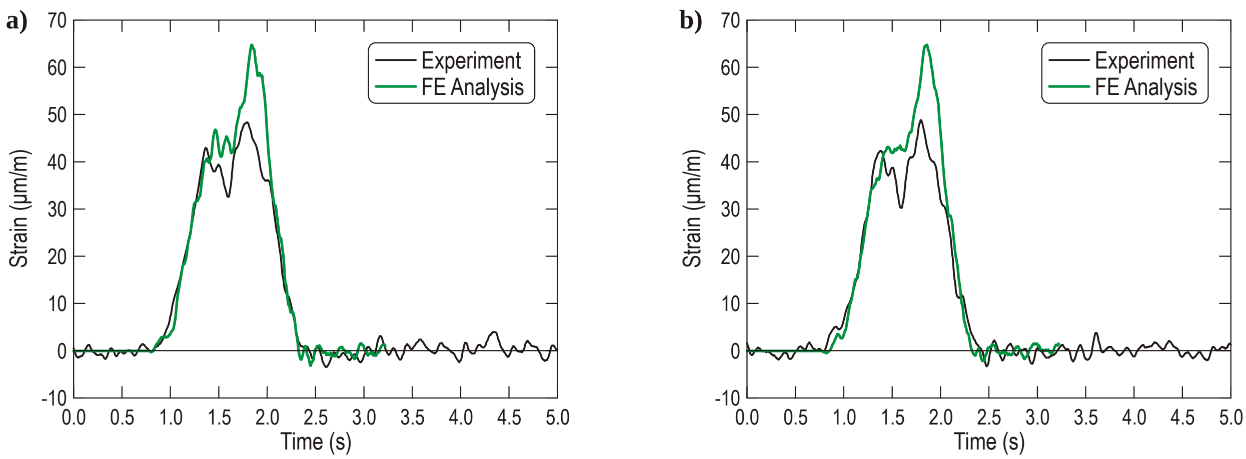

Figure 8.5. Longitudinal strain at the bottom of the girder from the experimental testing and FE analysis for the tractor-trailer at the center of the roadway (run #10): a) girder #3, b) girder #4

Table 8.2. The influence of the vehicle velocity on the impact factor for the girder #4

Vehicle velocity (km/h)	Girder deflection (mm)	Impact factor (%)
0	–2.93	—
32	–3.06	4.44
48	–3.07	4.78
64	–3.15	7.51
80	–3.16	7.85

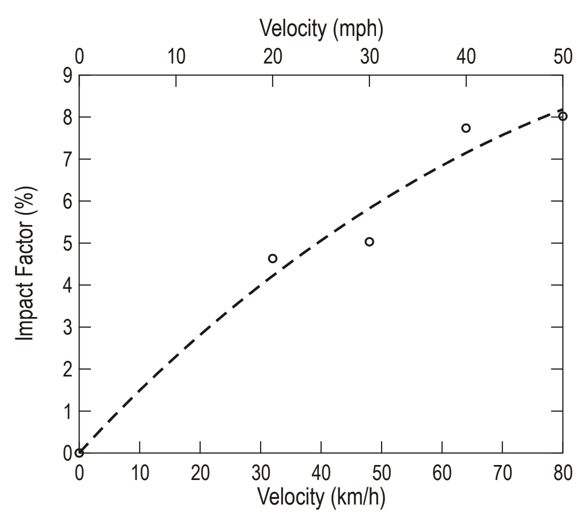

Figure 8.6. The influence of the vehicle velocity on the impact factor for the girder #4

Exemplary acceleration histories obtained for the selected points from the experimental test (run #08) and the FE analysis are compared in Figure 8.7.

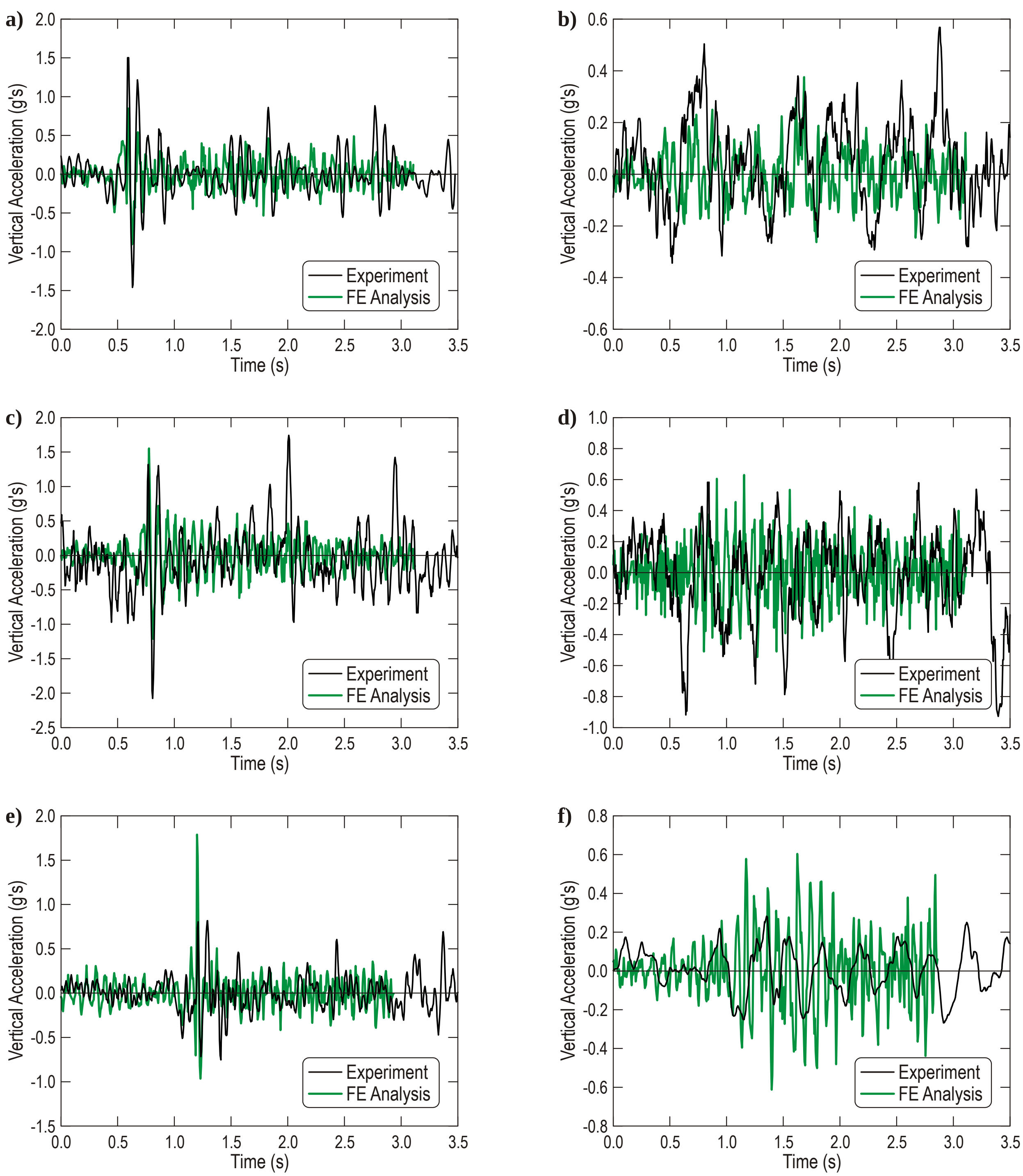

Figure 8.7. Comparison of the acceleration histories for the tractor-trailer (run #08):
a) front axle, b) point above the front axle, c) forward tandem drive axle,
d) point located on the fifth wheel plate above the rear tandem drive axles,
e) first trailer axle, f) point located on the load deck of the trailer

The last issue was to estimate the influence of railing barriers on the bridge strength and its behavior under dynamic interaction with the crossing vehicle. Two analyses were performed at a velocity of 80 km/h (50 mph). In the first case, the complete FE model of the bridge was used, whereas in the second one, the railing barriers together with their reinforcing bars were removed from the FE model, as presented in Figure 8.8.

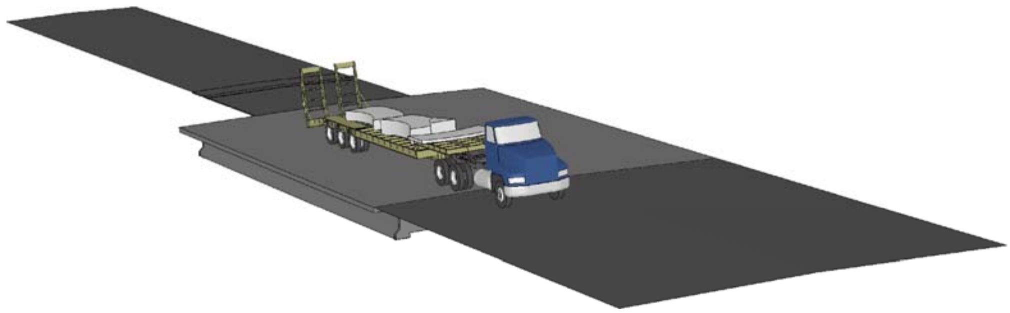

Figure 8.8. FE model of the bridge without railing barriers used for simulations

Deflection of girder #4 for both FE models (with and without railing barriers) is presented in Figure 8.9. The results are similar without any significant differences. However, in the final stage when the vehicle left the bridge a slight phase shift in vibrations of the bridge span can be seen. It might be the result of changing the stiffness of the bridge caused by removing the railing barriers.

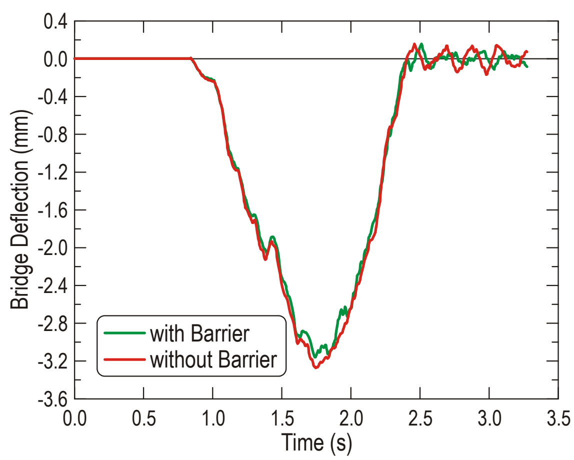

Figure 8.9. Deflection of the bridge FE model with and without railing barrier

Time histories for longitudinal strains at the bottom of the girders #3 through #6 are shown in Figure 8.10. The most significant dissimilarity of the results is observed for the far right girder next to the originally located barrier.

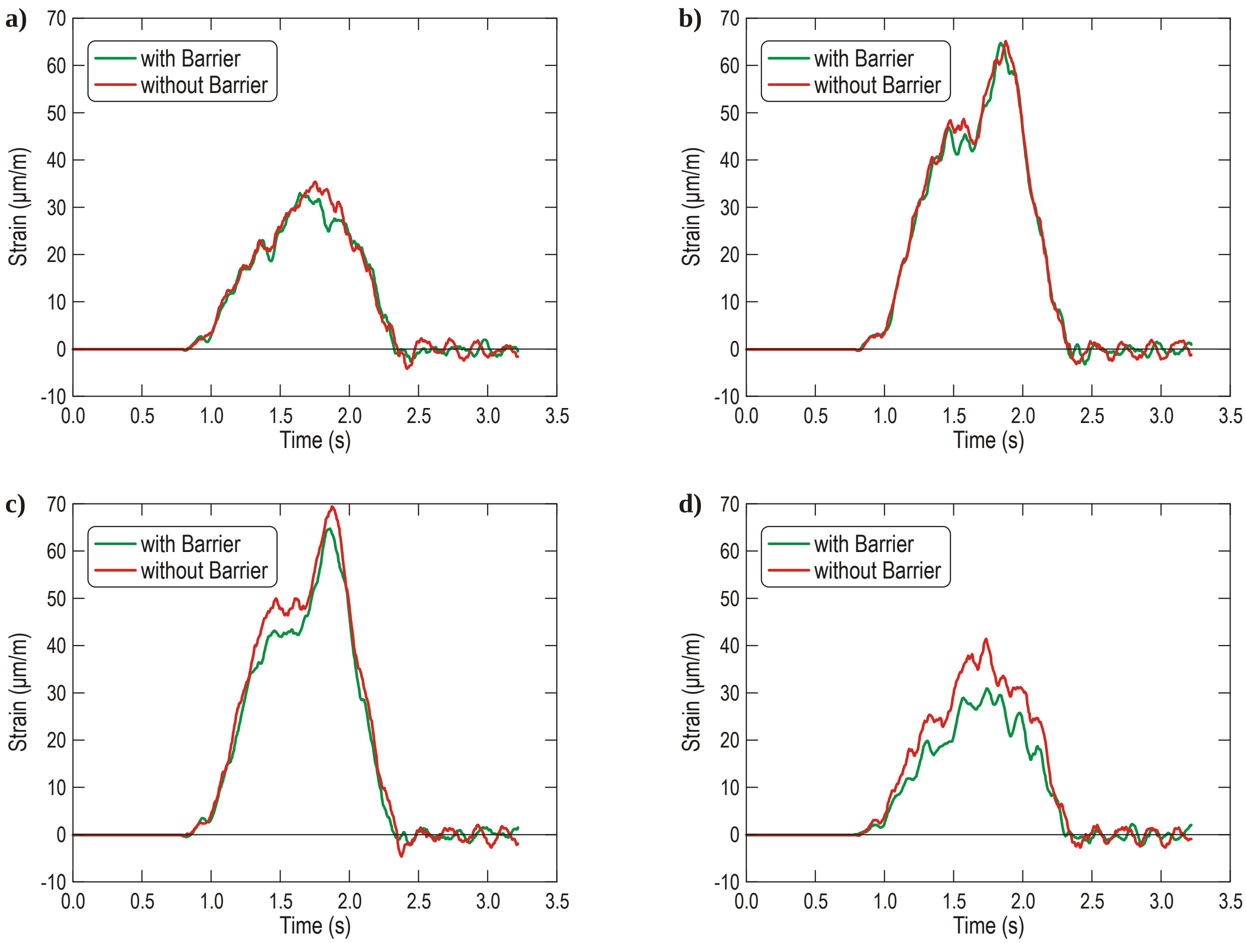

Figure 8.10. Longitudinal strains at the bottom of the girders for FE model of the bridge with and without railing barrier: a) girder #3, b) girder #4, c) girder #5, d) girder #6

8.2. FE Analysis for the Terex Crane

FE analysis reflected the experimental tests carried out on the bridge. Deflections obtained for the static tests are provided in Table 8.3. Longitudinal strains on the bottom of each girder are presented in Figure 8.11.

Table 8.3. Comparison of the deflection (mm) of the bridge span and its FE model for the Terex crane

	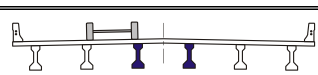		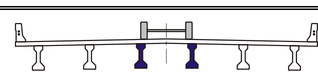		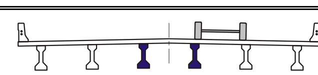	
	Girder #3	Girder #4	Girder #3	Girder #4	Girder #3	Girder #4
Attempt 1	–1.27	–0.69	–1.27	–1.48	–0.54	–1.38
Attempt 2	–1.37	–0.64	–1.37	–1.48	–0.56	–1.39
FE analysis	–2.21	–1.28	–2.29	–2.28	–1.30	–2.22

Results of dynamic analyses were compared with ones form the experimental tests in Figure 8.12 and Figure 8.13 for the crane located in the center of the westbound traffic lane, and in Figure 8.14 and Figure 8.15 for the crane at the center of the roadway.

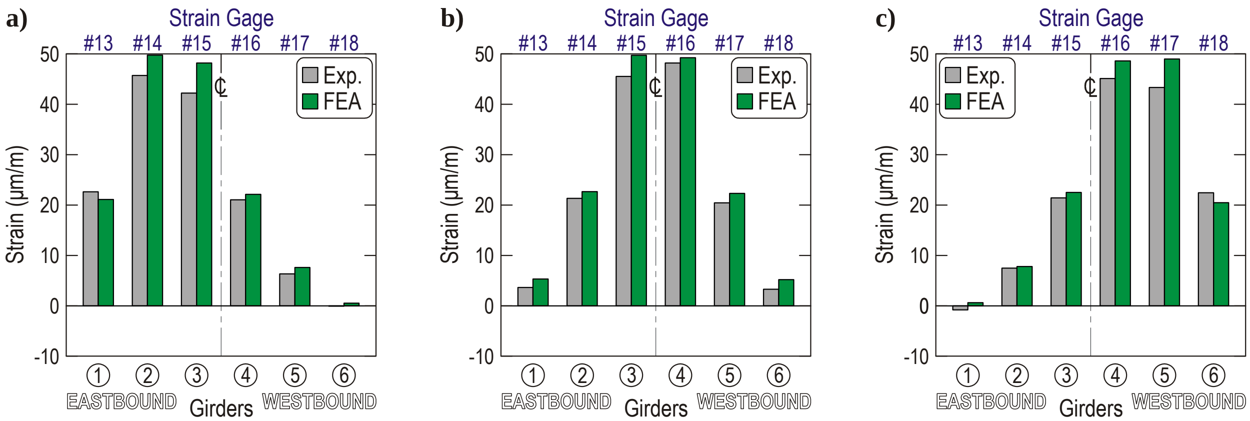

Figure 8.11. Longitudinal strain from the experimental testing and FE analysis at the bottom of the girder for the Terex crane: a) vehicle in the center of the eastbound traffic lane (run #03), b) vehicle at the center of the roadway (run #02), c) vehicle in the in the center of the westbound traffic lane (run #01)

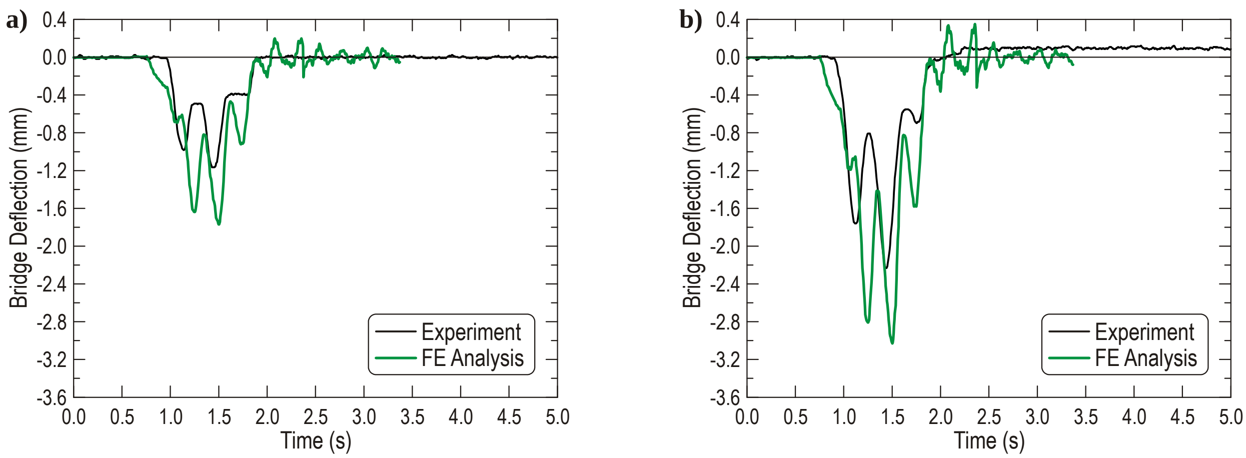

Figure 8.12. Deflection of the bridge span from the experimental testing and FE analysis for the Terex crane in the center of the westbound traffic lane (run #30): a) girder #3, b) girder #4

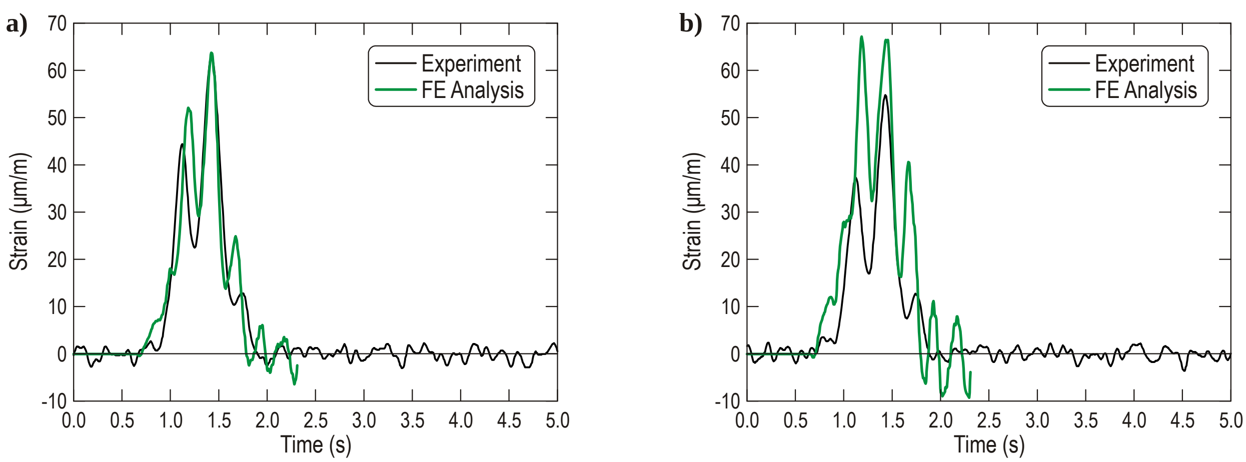

Figure 8.13. Longitudinal strain at the bottom of the girder from the experimental testing and FE analysis for the Terex crane in the center of the westbound traffic lane (run #30): a) girder #4, b) girder #5

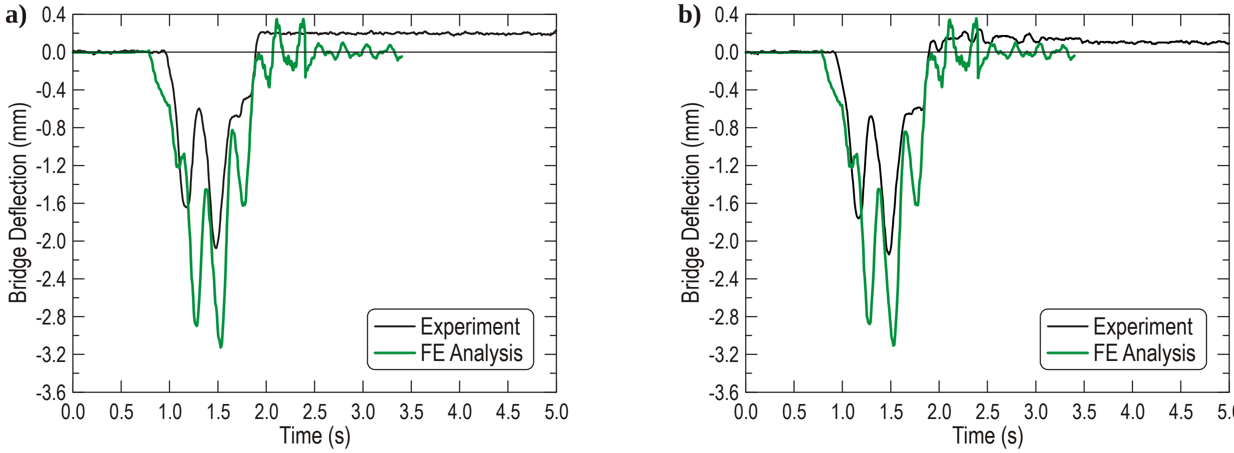

Figure 8.14. Deflection of the bridge span from the experimental testing and FE analysis for the Terex crane at the center of the roadway (run #31): a) girder #3, b) girder #4

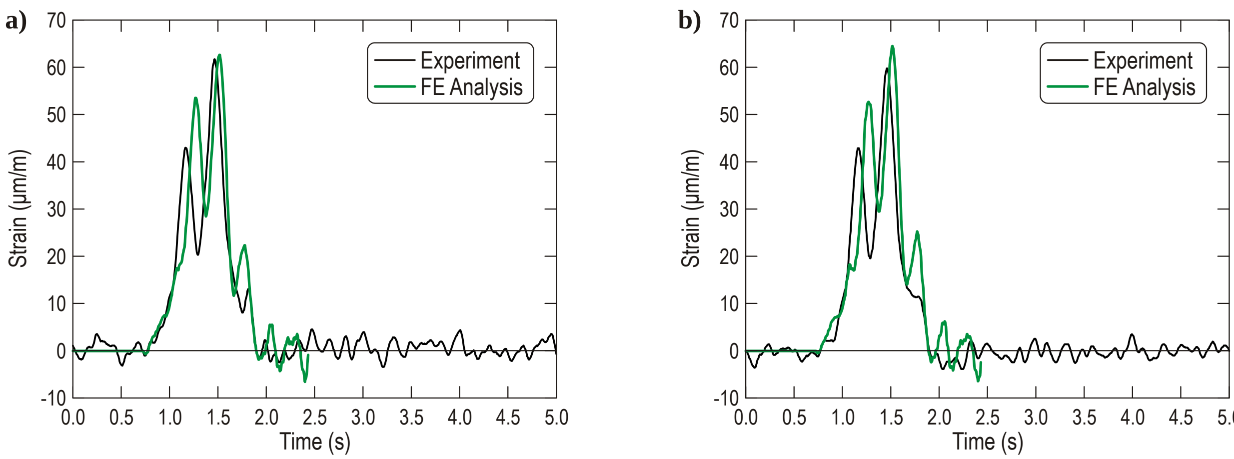

Figure 8.15. Longitudinal strain at the bottom of the girder from the experimental testing and FE analysis for the Terex crane at the center of the roadway (run #31): a) girder #3, b) girder #4

The results obtained from the FE analysis are characterized by a high conformity in qualitative respect for strains, in particular. Three specific peaks appear in time histories, more noticeable in the FE analysis. They may be interpreted as a low-frequency vibration generated by the crane driven over the bridge. A slight phase shift of the vibrations is visible, but the maximum values from the FE analysis are similar to ones obtained from the test.

8.3. FE Analysis for the FDOT Truck

Deflections of the bridge span obtained from the FE analysis for the static case are provided in Table 8.4. Longitudinal strains on the bottom of each girder are presented in Figure 8.16.

Table 8.4. Comparison of the deflection (mm) of the bridge span and its FE model for the FDOT truck

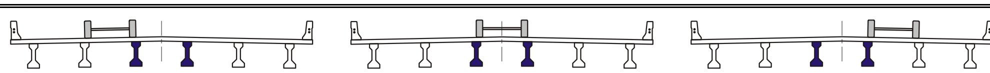

	Girder #3	Girder #4	Girder #3	Girder #4	Girder #3	Girder #4
Experiment	–1.47	–0.39	–1.57	–0.93	–0.73	–0.65
FE analysis	–1.92	–1.13	–1.98	–1.98	–1.23	–1.91

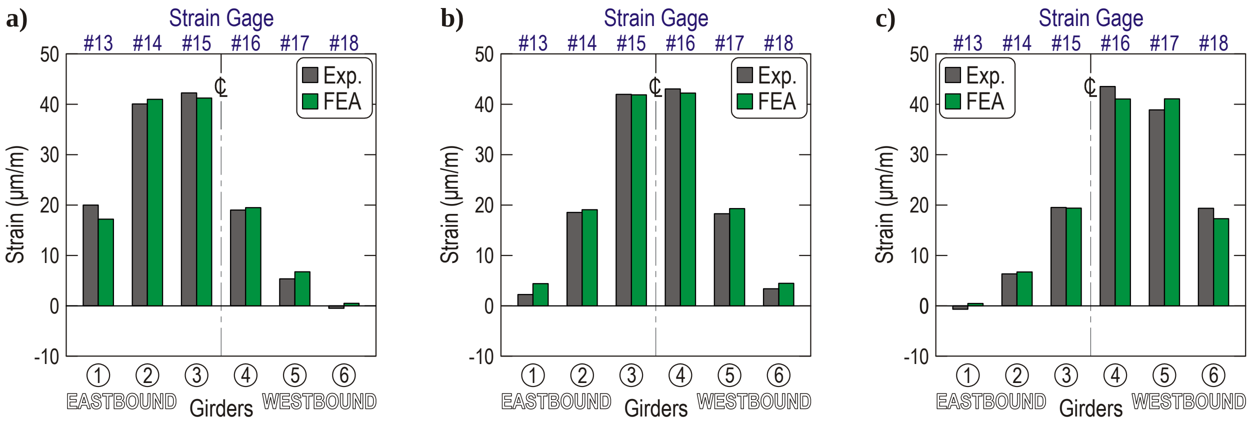

Figure 8.16. Longitudinal strain from the experimental testing and FE analysis at the bottom of the girder for the FDOT truck: a) vehicle in the center of the eastbound traffic lane (run #17), b) vehicle at the center of the roadway (run #16), c) vehicle in the in the center of the westbound traffic lane (run #15)

Results of FE analysis of the dynamic tests are presented in Figure 8.17 through Figure 8.20.

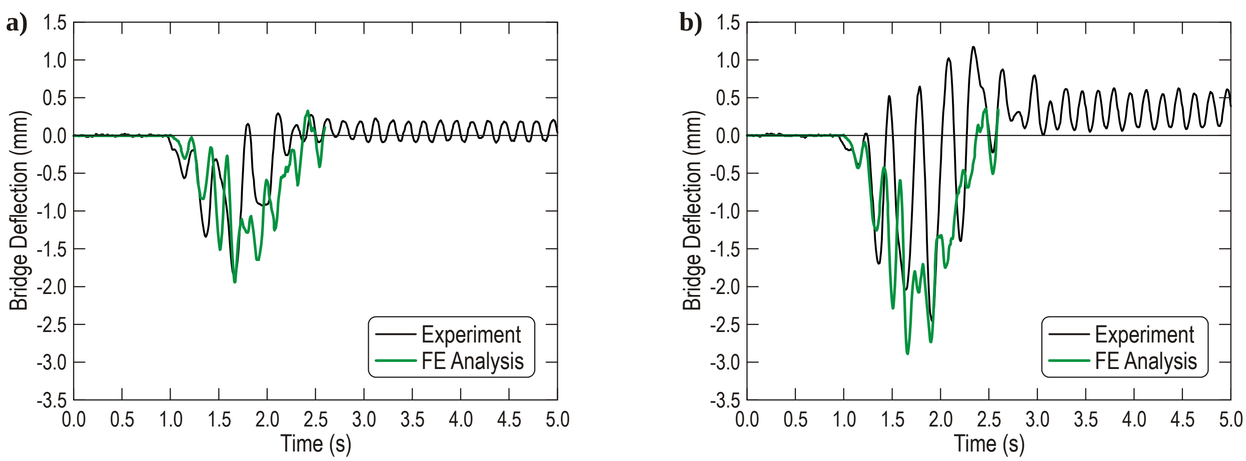

Figure 8.17. Deflection of the bridge span from the experimental testing and FE analysis for the FDOT truck in the center of the westbound traffic lane (run #18): a) girder #3, b) girder #4

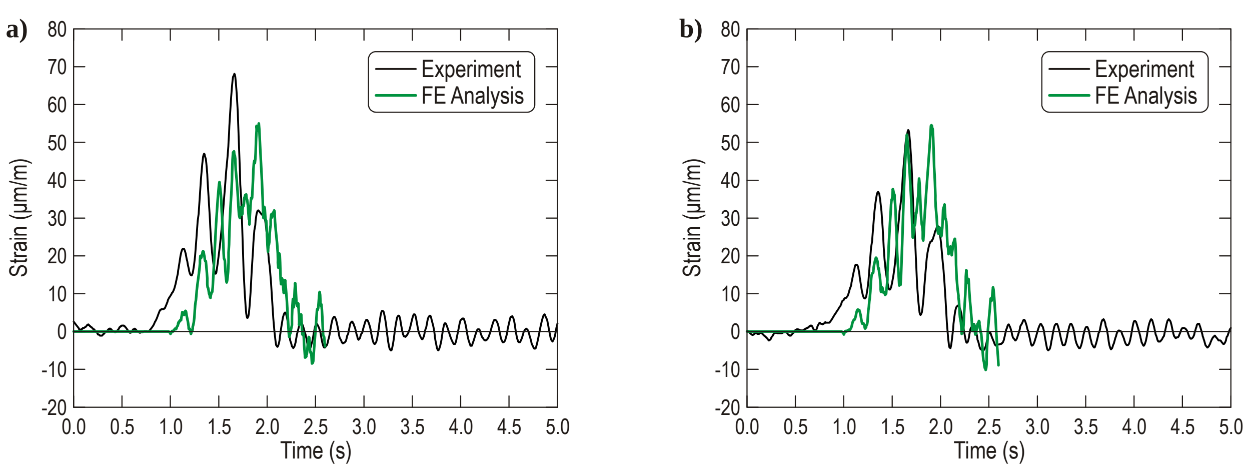

Figure 8.18. Longitudinal strain at the bottom of the girder from the experimental testing and FE analysis for the FDOT truck in the center of the westbound traffic lane (run #18): a) girder #4, b) girder #5

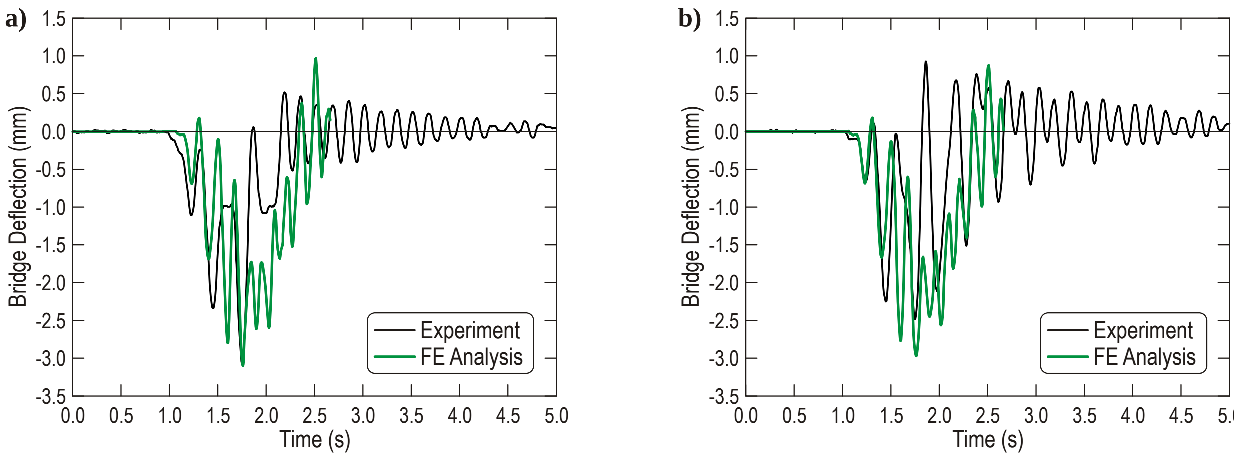

Figure 8.19. Deflection of the bridge span from the experimental testing and FE analysis for the FDOT truck at the center of the roadway (run #20): a) girder #3, b) girder #4

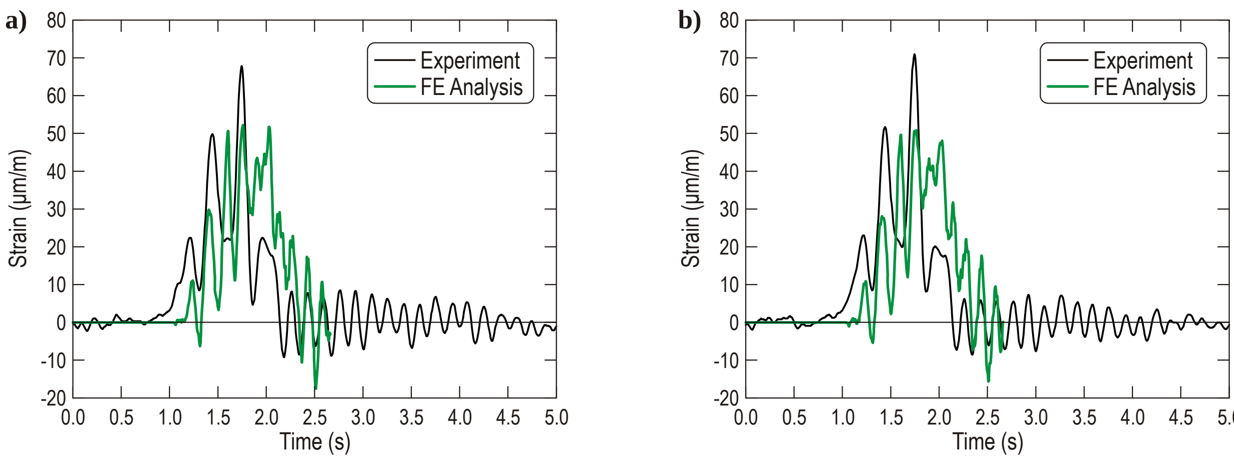

Figure 8.20. Longitudinal strain at the bottom of the girder from the experimental testing and FE analysis for the FDOT truck at the center of the roadway (run #20): a) girder #3, b) girder #4

The results obtained from the FE analysis are characterized by a high conformity in qualitative as well as quantitative respects. The frequency of noticeable oscillations is higher than the one obtained for the crane FE model due to the hammering effect which intensifies vibration. An FE model of the trailer took into account a possibility of the load bouncing on the trailer deck.

8.4. Impact Factor on the Basis of FE Analysis

The obtained results allow calculating the impact factor based on deflections of the bridge span and strains at the bottom of the girder. Values of the impact factor for three selected vehicles driven at a velocity of 80 km/h (50 mph) and positioned in the center of the westbound traffic lane (location encountered in reality) are provided in Table 8.5 and presented in Figure 8.21. Two girders, No. 4 and No. 5, were taken into consideration as those located directly under the vehicle and maximal loaded.

The lowest values of the impact factor were obtained for the tractor-trailer FE model. Values calculated by both methods (on the basis of deflections and strains) do not draw significant differences in this case.

Higher values of the impact factor (about 4 times higher in comparison with the tractor-trailer FE model) were obtained for the Terex crane FE model. In this case, values of the calculated impact factor based on the deflections and strains are comparable. The most disadvantageous case is the FDOT truck. The impact factor calculated on the basis of deflection of the span reaches a value over 50%.

Table 8.5. Deflections, strains and values on the impact factor obtained from FE analysis for the selected vehicles

		Deflection (mm)		Impact	Strains (μm/m)		Impact
		Static	Dynamic	Factor (%)	Static	Dynamic	Factor (%)
Tractor-Trailer	Girder #4	–2.93	–3.16	7.85	60.614	64.710	6.76
	Girder #5	—	—	—	60.540	64.701	6.87
Terex Crane	Girder #4	–2.22	–3.03	36.49	48.612	63.681	31.00
	Girder #5	—	—	—	48.987	67.149	37.08
FDOT Truck	Girder #4	–1.91	–2.89	51.31	41.058	55.026	34.02
	Girder #5	—	—	—	41.077	54.558	32.82

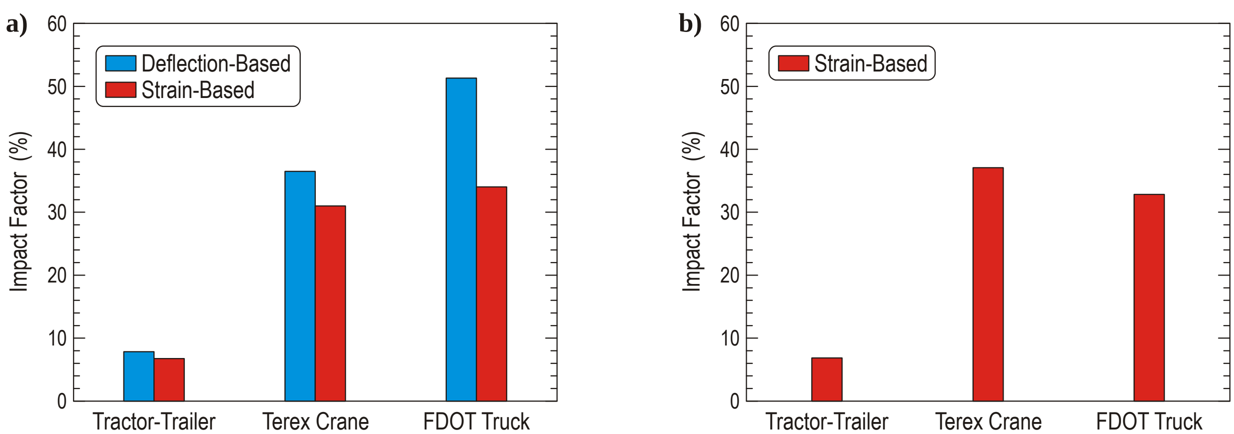

Figure 8.21. Impact factor obtained from FE analysis for selected vehicle FE models positioned in the center of the westbound traffic lane: a) girder #4, b) girder #5

9. SUMMARY AND CONCLUSIONS

The main purpose of this project was to develop numerical models of the heavy vehicle applicable for transient analysis of dynamic vehicle-bridge interaction. Two completely new FE models of a tractor-trailer and a crane were developed and validated. Validation included checking the mass distribution and determining a spring constant and a damping coefficient of the suspension systems. The results obtained of the validation process are satisfactory for most cases. However, some differences between results obtained from numerical analysis and experimental tests are also apparent. We chose to select the most optimal solution for all considered cases (different velocities, loads, etc.) and to not "calibrate" the FE model every time.

An FE model of heavy vehicles was used for analysis of their dynamic interaction with the bridge FE model. This analysis reflected a full scale experimental test carried out on the actual #500133 bridge on US90 over Mosquito Creek. Results obtained by both methods were compared; their conformity is quite good for most cases. Therefore, existing FE models of the vehicle and the bridge can be successfully used in further multi-variant analysis instead of using expensive and time consuming experimental tests.

In addition, we decided to assess the influence of railing barriers on bridge strength and its behavior under dynamic interaction with the crossing vehicle using FE analysis. The results obtained for the FE model of the bridge without the railing barriers and reinforcing bars do not differ by much. However, in the final stage when the vehicle left the bridge, a slight phase shift in vibrations of the bridge span can be seen. This might be the result of changing stiffness of the bridge caused by removing the railing barriers. The most significant dissimilarity of the results is observed for the external girders next to the originally located barriers.

Conclusions and practical recommendations regarding individual aspects of this project are presented in following parts.

Experimental Tests on the Bridge

Bridge testing was carried out correctly and the results provided valuable data. However, some inaccuracies appeared during the test. For some dynamic cases, in the final phase of crossing over the bridge it can be seen that the bridge does not return to its initial position; i.e., deflection does not equal 0 mm. This was probably caused by the LVDT sensors used for the tests. We suggest using another type of measurement device based on laser technology and locating them under each girder, if possible, for further work. In addition, we recommended that "zero" adjustments should be conducted before each static run. In the tests carried out in this project, zeroing was done once before every three static runs. Such an approach allows for rejecting reliable data, especially for strains. Cross-sections close to the end and the beginning of the span can be omitted due to small values obtained there.

Impact Factor

At the beginning, it should be emphasized that most data rejected during the tests on the bridge and from this FE analysis were relatively small. Deflection of the bridge did not exceed 3 millimeters, whereas longitudinal strains at the bottom of the girder reached up to 70 micro strains. Very often, they were within the range of measurement error. Therefore, the impact factor, calculated on the basis of the obtained data, is supposed to be considered in a qualitative respect instead of a quantitative one. In addition, we recommend calculating the impact factor for the most loaded girders only. In such cases, the obtained values of both static and dynamic responses (deflections, strain) are relatively high and differences between them allow for the most reliable determination of the impact factor. The external girders are not as loaded as ones located directly under the crossing vehicle, and the strain and deflection of the bridge responses are much lower. However, for such small values, the difference between static and dynamic cases is very high and results in extreme values of the impact factor that cannot be taken into account.

The conducted tests and FE analyses provided significant information about determinants that influence the impact factor. The first one is undoubtedly related to the suspension parameters of the vehicle. In practice, the difference between dynamic and static response of the bridge for a fully suspended vehicle is not so large. Heavy vehicles with very stiff suspension systems have much more effect on the bridge. Differences between static and dynamic responses are higher, consequently increasing the impact factor. The dynamic response for such vehicles can be further intensified by the "bounced" cargo located on the load deck. Vibration of the vehicle caused by road surface imperfections (e.g. thresholds, crack, potholes etc.) can generate additional oscillations of the load and intensify the dynamic influence on the bridge span.

Suspension Modeling

Experimental tests were carried out to determine a spring constant and a damping coefficient of the suspension systems of the selected vehicle. Time histories of accelerations of selected points and the axles' deflection underlie the validation procedure for the suspension system FE models. Identical tests were reflected in numerical simulation in LS-DYNA software and results obtained from both methods were compared. Validation of the vehicle suspension was based primarily on axle deflection. Accelerations of the axle and bodywork were considered as an additional data source. The suspension parameters in the FE model were adjusted until simulation data was matched with experimental results.

Values obtained from the experimental tests were satisfied and allowed for finding out most of the unknown parameters. However, in some cases data was not completed due to signal failures or damage to the displacement gauge due to its too short stroke. Therefore, we recommend applying laser sensors which have a much higher operating range.

Time histories obtained from the numerical analysis are characterized by a relatively large correlation when the considered axle is crossing over the speed bump. Some discrepancies between results appear in a later phase. Therefore, the most correct strategy for the suspension FE model validation and/or finding out its properties would be to separate the considered suspension system from the other ones. Unfortunately, that method is possible to simulate in FE analysis but it is more difficult to carry out on the actual object.

Wheel Modeling

The suspension systems and the tires, which received much attention in the modeling process, clearly have a distinct influence on the interaction between vehicle and the bridge. Finding all the necessary data for suspension development took a significant amount of time during this project. Results obtained from the FE analysis are satisfying but some modifications in the FE model are necessary. We strongly recommend modifying the existing FE model of the wheel and retesting it at least twice. The current mesh of finite elements in the tire tread FE model is strictly determined by the size of elements in the bridge FE model. Their sizes are supposed to be similar to ensure correctness of the performed analysis with respect to contact between the tire tread and the bridge slab. The new wheel FE model entails additional modification in the bridge slab.

We also recommend conducting additional experimental tests to provide necessary parameters for the rubber material model used for the tire. At least one tire taken from the heavy vehicle should be tested to determine its radial stiffness and damping factor.

REFERENCES

AASHTOO Standard Specifications for Highway Bridges (17 ed.). (2002).

Alcoa Wheels. (2008). Retrieved October 20, 2008, from Alcoa: http://www.alcoa.com/alcoawheels/north_america/en/hdtt/product.asp?prod_id=3875

Alcoa Wheels. (2008). Retrieved October 3, 2008, from Alcoa: http://www.alcoa.com/alcoawheels/north_america/en/hdtt/product.asp?prod_id=3897

All Terain Cranes. (2008). Retrieved September 13, 2008, from Terex-Demag: http://www.demag24.com/r_en/products/d/AC140_US.B1.200808.pdf

Arvin Meritor Products. (2003). Retrieved October 23, 2008, from Arvin Meritor: http://www.meritorhvs.com/MeritorHVS_Documents/SP0225.pdf

Arvin Meritor Rear Axles. (2008). Retrieved October 5, 2008, from Arvin Meritor: http://www.meritorhvs.com/MeritorHVS_Documents/TP9391.pdf

Arvin Meritor Trailer Axles. (1997). Retrieved October 5, 2008, from Arvin Meritor: http://www.meritorhvs.com/MeritorHVS_Documents/tp97127.pdf

Baumgaertner, W. (1998). Bridge-Truck Interaction: Simulation, Measurements and Load Identification. *5th International Symposium on Heavy Vehicle Weights and Dimensions*, (pp. 114-131). Maroochydore, Australia.

Brady, S. P., Gonzalez, A., Znidaric, A., & O'Brien, E. J. (2002). Impact Factors on Medium Span Bridges due to Multiple Vehicle Presence. *7th International Symposium on Heavy Vehicle Weight and Dimensions*, (pp. 1-10). Delft, The Nederlands.

Brownjohn, J. M., Lee, J., & Cheong, B. (1999). Dynamic Performance of a Curved Cable-Stayed Bridge. *Engineering Structures , 21*, 1015-1027.

Chan, T. H., Law, S. S., & Yung, T. H. (2000). Moving Force Identification Using an Existing Prestressed Concrete Bridge. *Engineering Structures , 22*, 1261-1270.

Chowdhury, M. R., & Ray, J. C. (2003). Accelerometers for Bridge Load Testing. *NDT&E International , 36*, 237-244.

Clemente, P., Marulo, F., Lecce, L., & Bifulco, A. (1998). Experimental Modal Analysis of the Garigliano Cable-Stayed Bridge. *Soil Dynamics and Earthquake Engineering , 17*, 485-493.

Cohen, J. (1988). *Statistical Power Analysis for the Behavioral Sciences.* Hillsdale, NJ: Lawrence Erlbaum Associates, Inc.

Das, A., Dutta, A., & Talukdar, S. (2004). Efficient Dynamic Analysis of Cable-Stayed Bridges under Verticular Movement using Space and Time Adaptivity. *Finite Elements in Analysis nad Design , 40* (4), 407-424.

Dunlop Truck Tires. (2008). Retrieved October 20, 2008, from Dunlop Commercial Truck Tires: https://www.dunloptires.com/truck/tires/sp453measures.html

Dunlop Truck Tires. (2008). Retrieved October 5, 2008, from Dunlop Commercial Truck Tires: http://www.dunloptires.com/truck/tires/sp160measures.html

Edara, R., Shih, S., Tamini, N., Palmer, T., & Tang, A. (2008). 18 Wheel Truck Dynamic and Durability Analysis using Virtual Proving Ground. *10th International LS-DYNA Users Conference* (pp. 13.25-13.38). Dearborn: Livermore Software Technology Corporation.

Finite Element Model Archive. (2008). Retrieved December 16, 2008, from National Crash Analysis Center: http://www.ncac.gwu.edu/vml/models.html

Gáspár, P., & Kuti, I. (2006). The Dynamic Modelling of Road Vehicle for the Numerical Verification of Active Suspensions. *International Journal of Vehicle Design , 40* (1-3), 36-51.

Goodyear Tires. (2008). Retrieved October 20, 2008, from Goodyear Commercial Tire Systems: http://www.goodyear.com/cfmx/web/truck/line.cfm?prodline=160904

Goodyear Tires. (2008). Retrieved October 3, 2008, from Goodyear Commercial Tire Systems: http://www.goodyear.com/cfmx/web/truck/line.cfm?prodline=160615

Goodyear Tires. (2008). Retrieved October 3, 2008, from Goodyear Commercial Tire Systems: http://www.goodyear.com/cfmx/web/truck/line.cfm?prodline=160312

Goodyear Tires. (2008). Retrieved October 3, 2008, from Goodyear Commercial Tire Systems: http://www.goodyear.com/cfmx/web/truck/line.cfm?prodline=160907

Google Maps. (2008). Retrieved October 3, 2008, from http://maps.google.com

Green, M. F., & Cebon, D. (1997). Dynamic Interaction Between Heavy Vehicles and Bridges. *Computers & Structures , 2*, 253-264.

Green, M. F., & Cebon, D. (1994). Dynamic Responses of Highway Bridges to Heavy Vehicle Loads, Theory and Experimental Validation. *Journal of Sound and Vibration , 170*, 51-78.

Henchi, K., Fafard, M., Talbot, M., & Dhatt, G. (1998). An Efficient Algoritm for Dynamic Analysis of Bridges under Moving Vehicles using a Coupled Modal and Physical Components Approach. *Journal of Sound and Vibration , 212* (4), 663-683.

Hendrickson Products. (2008). Retrieved October 22, 2008, from Hendrickson: http://www.hendrickson-intl.com/pdfs/Truck_PDFs/RS/Sp166b.pdf

Hendrickson Products. (2008). Retrieved October 8, 2008, from Hendrickson: http://www.hendrickson-intl.com/pdfs/Truck_PDFs/Has/45745_095c.pdf

Hendrickson Products. (2008). Retrieved October 5, 2008, from Hendrickson: http://www.hendrickson-intl.com/pdfs/Truck_PDFs/Airtek/Tp_243/Sec_1_2_c.pdf

Hibbeler, R. C. (1998). *Structural Analysis* (4th ed.). Upper Saddle River, New Jersey: Prentice-Hall, Inc.

HyperMesh 8.0 User's Guide. (2007). Troy, Michigan: Altair Engineering, Inc.

Kwasniewski, L., Li, H., Wekezer, J. W., & Malachowski, J. (2006). Finite Element Analysis of Vehicle-Bridge Interaction. *Journal of Finite Elements in Analysis and Design , 42* (11), 950-959.

Kwasniewski, L., Wekezer, J. W., Roufa, G., Li, H., Ducher, J., & Malachowski, J. (2006). Experimental Evaluation of Dynamic Effects for a Selected Highway Bridge. *Journal of Performance of Constructed Facilities , 20*, 1-8.

Lehtonen, T. J. (2005). Validation of an Agricultural Tractor MBS Model. *International Journal of Heavy Vehicle System , 12* (1), 16-27.

Letherwood, M. D., & Gunter, D. D. (2001). Ground Vehicle Modeling and Simulation of Military Vehicles Using High Performance Computing. *Parallel Computing , 27*, 109-140.

LS-DYNA Keyword User's Manual (Vol. I). (2007). Livermore, California: Livermore Software Technology Corporation.

LS-DYNA Keyword User's Manual (Vol. II). (2007). Livermore, California: Livermore Software Technology Corporation.

LS-PrePost Online Documentation. (2008). Retrieved October 13, 2008, from Livermore Software Technology Corporation: http://www.lstc.com/lspp/

Mack Powertrain. (2008). Retrieved October 5, 2008, from Mack Trucks: http://www.macktrucks.com/assets/mack/specsheets/MP8040408/1001511_425E.pdf

Mack Products. (2004). Retrieved October 5, 2008, from Mack Trucks: http://www.macktrucks.com/assets/mack/products/MackAdvantageChassis.pdf

Mack Products. (2007). Retrieved October 5, 2008, from Mack Trucks: http://www.macktrucks.com/assets/mack/Datasheets/Chassis%20Sheets/2008C/CHU6030020738_08C.pdf

Marzougui, D., Jin, S., & Livingston, R. A. (2001). Development of an LS-DYNA Nonlinear Finite Element Model for Use in Damage detection and health Monitoring of Highway Bridges. *Health Monitoring and Management of Civil Infrastructural Systems,* (pp. 432-440).

Marzougui, D., Zink, M., Zaouk, A., Kan, C. D., & Bedewi, N. (2004). Development and Validation of a Vehicle Suspension Finite Element Model for use in Crash Simulations. *International Journal of Crashworthiness* , 565-576.

Nawy, E. G. (2005). *Reinforced Concrete: A Fundamental Approach* (6th ed.). Upper Saddle River, New Jersey: Pearson Education, Inc.

Previati, G., Gobb, M., & Mastinu, G. (2007). Farm Tractor Models for Research and Development Purposes. *VEhicle System Dynamics , 45* (1), 37-60.

Reference Tables. (2008). Retrieved October 5, 2008, from Engineer's Handbook: www.engineershandbook.com/Tables/frictioncoefficients.htm

Roadranger Products. (2004). Retrieved October 5, 2008, from Roadranger: http://www.roadranger.com/Roadranger/productssolutions/drive,steer,traileraxles/e-1002-e-202/index.htm

Roadranger Specification Guide. (2008). Retrieved October 22, 2008, from Roadranger Literature Center: http://www.roadranger.com/ecm/groups/public/@pub/@eaton/@roadranger/documents/content/rr_rrsl-0001.pdf

Schwer, L. E. (2006). An Overview of the ASME Guide for Verification and Validation in Computational Solid Mechanics. *5 LS-DYNA Anwenderforum* (p. 12). Ulm: American Society of Mechanical Engineers.

Spring Appendix. (2004). Retrieved October 15, 2008, from Hutchens Industries: http://www.hutch-susp.com/pdfs/8.23.05_library_pdfs/ssLib_SpringAppendix.pdf

Steel Disc Wheels. (2007). Retrieved October 4, 2008, from Accuride Wheels: http://www.accuridewheels.com/pdf/ACC3.0088%20Accu-Lite%20Brochure.pdf

Structural Shapes. (2008). Retrieved October 8, 2008, from Engineers Edge: http://www.engineersedge.com/structural_shapes_menu.shtml

Tan, G. H., Brameld, G. H., & Tambiratnam, D. M. (1998). Development of an Analytical Model for Treating Vehicle-Bridge Interaction. *Engineering Structure , 20* (1-2), 54-61.

Tedesco, J. W., Stallings, J. M., & El-Mihimy, M. (1999). Finite Element Method Analysis of a Concrete Bridge Repaired with Fiber Reinforced Plastic Laminates. *Computers and Structures , 72*, 379-407.

Thacker, B. (2002). Verification and Validation for Computational Solid Mechanics. *AIAA Structures Technical Committee Meeting* . Santa Fe, New Mexico.

Truck Cranes Specifications. (1997). *Terex T-300 Series* . Terex Cranes, Inc.

Truck Suspension Systems. (2008). Retrieved October 22, 2008, from Hendrickson Products: http://www.hendrickson-intl.com/products/product_detail/r_series.asp

Valášek, M., Stejskal, V., Šika, Z., Vaculín, O., & Kovanda, J. (1998). Dynamic Model of Truck for Suspension Control. *Vehicle System Dynamics , 28*, 496-505.

Wang, T. L., Huang, D., Shahawy, M., Huang, K. (1996). Dynamic Response of Highway Girder Bridge. *Computers & Structures, 60* (6), 1021-1027.

Wekezer, J. W., Li, H., Kwasniewski, L., & Malachowski, J. (2004). *Analytical and Experimental Evaluation of Existing Florida DOT Bridges.* Final Report, Florida State University, Department of Civil and Environmental Engineering, Tallahassee.

Yang, Y., & Lin, B. H. (1995). Vehicle-Bridge Interaction Analysis by Dynamic Condensation Method. *Journal of Structural Engineering , 121* (11), 1636-1643.

Yang, Y., Chang, C. H., & Yau, J. D. (1999). An Element for Analyzing Vehicle Bridge Systems Considering Vehicle's Pitching Effect. *International Journal for Numerical Methods in Engineering , 46*, 1031-1047.

Zaman, M., Taheri, M. R., & Khanna, A. (1996). Dynamic Responseof Cable-Stayed Bridges to Moving Vehicles Using the Structural Impedance Method. *Applied Mathematical Modeling , 20*, 876-889.

Appendix A

MATERIAL PROPERTIES AND FE MODELS SUMMARIES IN DETAIL

TABLE OF CONTENTS

A. MATERIAL PROPERTIES AND FE MODEL SUMMARIES IN DETAIL

A.1. FE Model of the Bridge and Approach

The FE model of the selected bridge for dynamic analysis includes also an FE model of the approach. In addition, two rigid walls were applied before the bridge approach and another two behind the bridge (Figure A.1). The first two rigid walls allowed the vehicle FE model to reach an appropriate speed, whereas the two behind allowed the vehicle FE model to leave the bridge. In both cases, two rigid walls were used due to 2% slopes of the road and the bridge slab.

The FE model of the bridge used for static tests includes only two rigid wall elements in the front, as presented in Figure A.2. During the analysis, these two elements supported each wheel of the front axle for the tractor-trailer and FDOT truck FE models.

A detailed summary of the complete FE model of the bridge is listed in Table A.1.

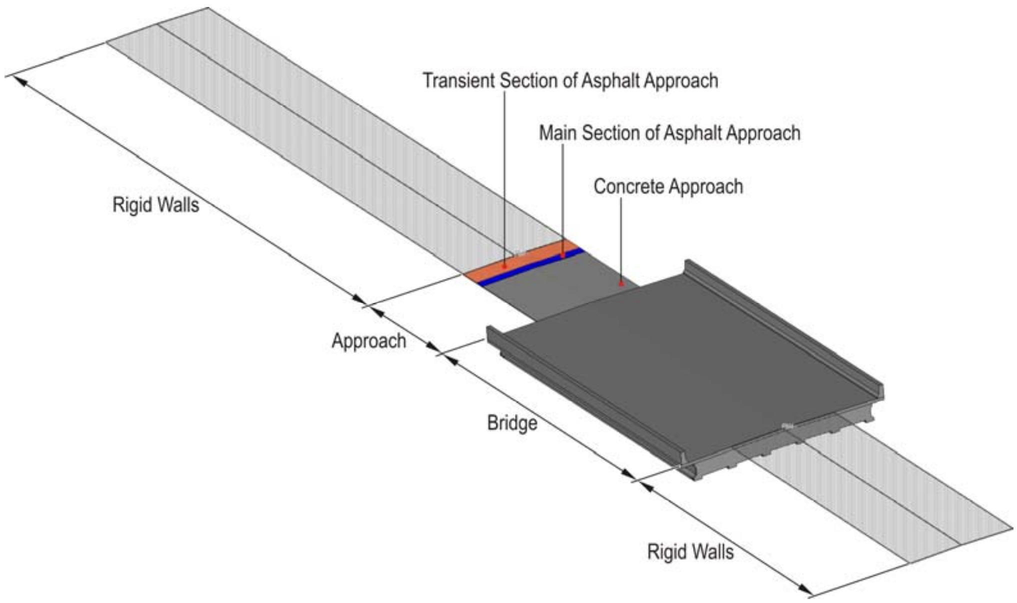

Figure A.1. Complete FE model of the bridge including approach sections and rigid walls used in dynamic analysis

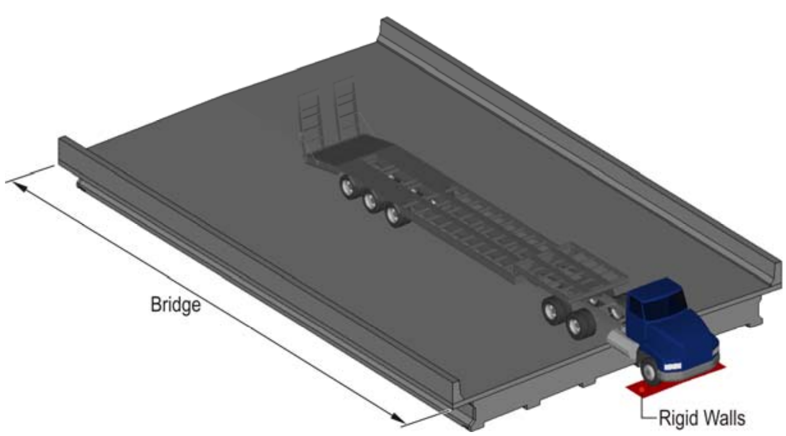

Figure A.2. Complete FE model of the bridge including two rigid walls used in static analysis

Table A.1. Detailed summary of complete FE model of the bridge and approach

Part ID	Part title	Material ID	Element type	Number of elements	Element ID minimum	Element ID maximum
3100	Bridge_Rebars_15M	3101	beam	44,696	**31**00001	**31**44696
3200	Bridge_Rebars_10M	3101	beam	6,790	**32**00001	**32**06790
3300	Bridge_Rebars_20M	3101	beam	312	**33**00001	**33**00312
3400	Bridge_Strand_No13_100	3701	beam	1,818	**34**00001	**34**01818
3500	Bridge_Strand_No13_250	3702	beam	4,248	**35**00001	**35**04248
3600	Bridge_Strand_No13_300	3703	beam	2,424	**36**00001	**36**02424
3700	Bridge_Strand_No09_200	3704	beam	618	**37**00001	**37**00618
3800	Bridge_Concrete_Slab	3103	solid	45,360	**38**00001	**38**45360
3900	Bridge_Concrete_Beams	3102	solid	26,172	**39**00001	**39**26172
4000	Bridge_Concrete_Railing_Barriers	3102	solid	5,670	**40**00001	**40**05670
4100	Bridge_Concrete_Diaphragm	3102	solid	5,732	**41**00001	**41**05732
4200	Bridge_Neoprene_Pads	3601	solid	144	**42**00001	**42**00144
4300	Approach_Concrete	3102	solid	1,620	**43**00001	**43**01620
4400	Approach_Main_Section	3201	solid	2,160	**44**00001	**44**02160
4500	Approach_Transient_Section	3201	solid	3,240	**45**00001	**45**03240
4600	Bridge_Scale	3901	shell	2	**46**00001	**46**00002

Comments:
Parts No. 4300, 4400, 4500 applied in the bridge FE model used in dynamic analysis only.
Part No. 4600 applied in the bridge FE model used in static analysis only.

Five different types of material models were applied in the FE model of the bridge and approach, as listed in Table A.2. Detailed properties of each material model are provided in Table A.3 to Table A.7. The data were presented in accordance with the values declared in the appropriate cards in the LS-DYNA code (LS-DYNA Keyword User's Manual, 2007). In some cases, material models had to be multiplied due to the LS-DYNA code requirements or user conveniences. Therefore, some materials have exactly the same properties but they were referenced by completely different parts in FE model.

Table A.2. Material models used in the FE model of the bridge and approach (LS-DYNA Keyword User's Manual, 2007)

Material number	Material designation in LS-DYNA code	Material model description	Material IDs in FE model (number)
*MAT_001	*MAT_ELASTIC	Isotropic elastic material	3101 to 3103 (3)
*MAT_020	*MAT_RIGID	Rigid material (part made from this material are considered to belong to a rigid body)	3201 (1)
*MAT_006	*MAT_VISCOELASTIC	Viscoelastic material	3601 (1)
*MAT_071	*MAT_CABLE_DISCRETE_BEAM	Elastic material for cables with no force developed in compression	3701 to 3704 (4)
*MAT_009	*MAT_NULL	Null material (equations of state considered without computing deviatoric stresses)	3901 (1)

Comments:
Material model *MAT_020 applied in the bridge FE model used in dynamic analysis only.
Material model *MAT_009 applied in the bridge FE model used in static analysis only.

Table A.3. Properties of the elastic material models used in the FE model of the bridge

Material ID	Material title in FE model	RO (Mg/mm^3)	E (MPa)	PR (–)	Number of referenced parts
3101	Elastic_Bridge_Steel	$7.850 \cdot 10^{-9}$	$2.100 \cdot 10^{5}$	0.30	3
3102	Elastic_Bridge_Concrete	$2.300 \cdot 10^{-9}$	$3.750 \cdot 10^{4}$	0.20	4
3103	Elastic_Bridge_Slab	$2.300 \cdot 10^{-9}$	$4.000 \cdot 10^{4}$	0.20	1

where:
RO — mass density, ρ
E — Young's modulus, E
PR — Poisson's Ratio, ν

Table A.4. Properties of the rigid material model used in the FE model of the bridge

Material ID	Material title in FE model	RO (Mg/mm^3)	E (MPa)	PR (–)	Number of referenced parts
3201	Rigid_Approach	$2.300 \cdot 10^{-9}$	$4.000 \cdot 10^{4}$	0.20	2

where:
RO — mass density, ρ
E — Young's modulus, E
PR — Poisson's Ratio, ν

Table A.5. Properties of the viscoelastic material model used in the FE model of the bridge

Material ID	Material title in FE model	RO (Mg/mm^3)	BULK (MPa)	G0 (MPa)	G1 (MPa)	BETA (–)	Number of referenced parts
3601	Viscoelastic_Neoprene	$2.300 \cdot 10^{-9}$	101	17	16	1	1

where:
RO — mass density, ρ
BULK — elastic bulk modulus, K
G0 — short-time shear modulus, G_0
G1 — long-time (infinite) shear modulus, G_∞
BETA — decay constant, β

Table A.6. Properties of the elastic cable material models used in the FE model of the bridge

Material ID	Material title in FE model	RO (Mg/mm^3)	E (MPa)	F0 (N)	Number of referenced parts
3701	Cable_Strand_No13_100	$7.850 \cdot 10^{-9}$	$2.100 \cdot 10^{5}$	0.0	1
3702	Cable_Strand_No13_250	$7.850 \cdot 10^{-9}$	$2.100 \cdot 10^{5}$	0.0	1
3703	Cable_Strand_No13_300	$7.850 \cdot 10^{-9}$	$2.100 \cdot 10^{5}$	0.0	1
3704	Cable_Strand_No09_200	$7.850 \cdot 10^{-9}$	$2.100 \cdot 10^{5}$	0.0	1

where:
RO — mass density, ρ
E — Young's modulus, E
F0 — initial tensile force, F_0

Table A.7. Properties of the rigid material model used in the FE model of the bridge

Material ID	Material title in FE model	RO (Mg/mm^3)	Number of referenced parts
3901	Null_Scale	$1.000 \cdot 10^{-9}$	1

where:
RO — mass density, ρ

A.2. FE Model of the Tractor-Trailer

Detailed summary of the complete FE model of the tractor-trailer is listed in Table A.8. Three different variants of the complete FE model are presented in Figure A.3. Counterweights (Figure A.4) taken from the Terex AC-140 heavy crane were used as the additional cargo.

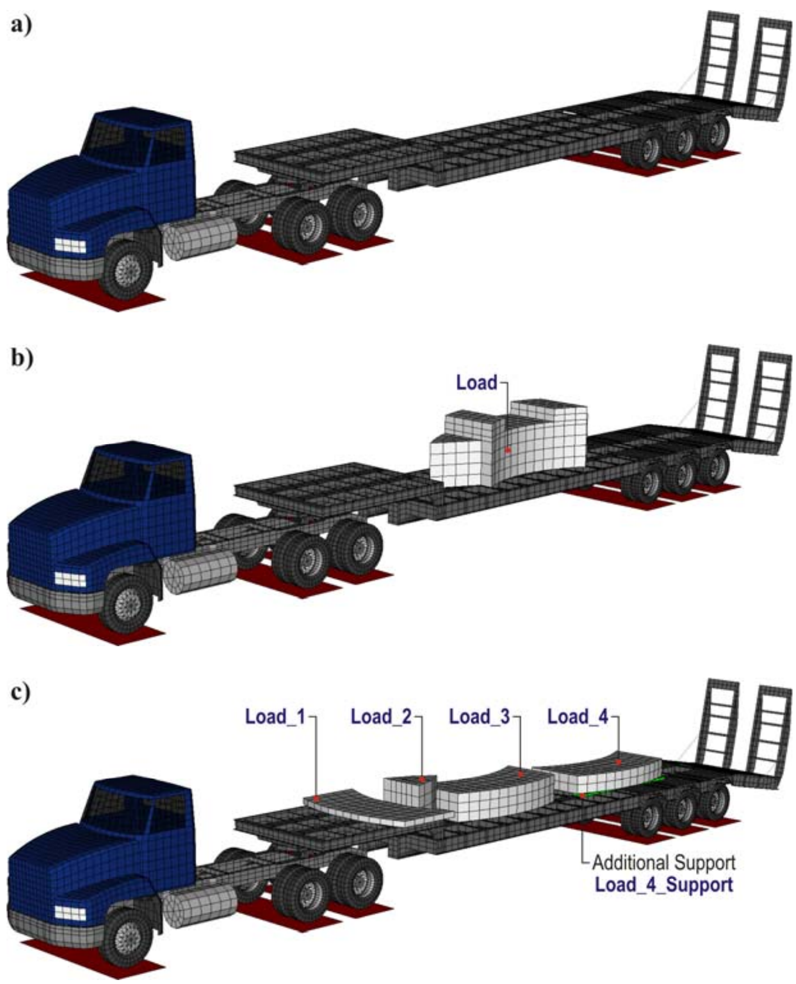

Figure A.3. Three different variants of the complete tractor-trailer FE model:
a) option I – basic configuration without additional load,
b) option II – configuration with one large cargo located approximately in the middle of the trailer,
c) option III – configuration with additional cargos distributed evenly on the load and top deck of the trailer

Figure A.4. Counterweights taken from the Terex AC-140 heavy crane used as the additional cargo during the tests (All Terain Cranes, 2008)

Table A.8. Detailed summary of complete FE model of the tractor-trailer

Part ID	Part title	Material ID	Element type	Number of elements	Element ID minimum	Element ID maximum
11	Front_Springs	11	discrete	2	**11**001	**11**002
12	Front_Dampers	12	discrete	2	**12**001	**12**002
21	Rear_Springs	21	discrete	4	**21**001	**21**004
22	Rear_Dampers	22	discrete	4	**22**001	**22**004
41	Trailer_Springs	41	discrete	6	**41**001	**41**006
42	Trailer_Dampers	41	discrete	6	**42**001	**42**006
100	F1_Vertical_Cylidrical_Joint	209	beam	10	**100**001	**100**010
101	F1_Axle_Rigid_Non_Rotating	212	beam	7	**101**001	**101**007
102	F1_Axle_Rigid_Rotating	201	beam	20	**102**001	**102**020
103	F1_Drums_Elastic	107	solid/penta	64	**103**001	**103**064
104	F1_Discs	102	shell/tria	144	**104**001	**104**144
105	F1_WRO_Rim	102	shell/quad	96	**105**001	**105**096
106	F1_WLO_Rim	102	shell/quad	96	**106**001	**106**096
107	F1_WRO_Fabric_Sidewalls	301	shell/quad	192	**107**001	**107**192
108	F1_WLO_Fabric_Sidewalls	301	shell/quad	192	**108**001	**108**192
109	F1_WRO_Fabric_Tread	301	shell/quad	64	**109**001	**109**064
110	F1_WLO_Fabric_Tread	301	shell/quad	64	**110**001	**110**064
111	F1_WRO_Sidewalls	103	shell/quad	192	**111**001	**111**192
112	F1_WLO_Sidewalls	103	shell/quad	192	**112**001	**112**192
113	F1_WRO_Tread	103	shell/quad	64	**113**001	**113**064
114	F1_WLO_Tread	103	shell/quad	64	**114**001	**114**064
200	R1_Vertical_Cylidrical_Joint	210	beam	6	**200**001	**200**006
201	R1_Axle_Rigid_Non_Rotating	213	beam	7	**201**001	**201**007
202	R1_Axle_Rigid_Rotating	201	beam	20	**202**001	**202**020
203	R1_Drums_Elastic	108	solid/penta	80	**203**001	**203**080
204	R1_Discs_Outer	102	shell/tria	144	**204**001	**204**144
205	R1_WRO_Rim	102	shell/quad	96	**205**001	**205**096
206	R1_WLO_Rim	102	shell/quad	96	**206**001	**206**096
207	R1_WRO_Fabric_Sidewalls	301	shell/quad	192	**207**001	**207**192
208	R1_WLO_Fabric_Sidewalls	301	shell/quad	192	**208**001	**208**192
209	R1_WRO_Fabric_Tread	301	shell/quad	64	**209**001	**209**064
210	R1_WLO_Fabric_Tread	301	shell/quad	64	**210**001	**210**064
211	R1_WRO_Sidewalls	103	shell/quad	192	**211**001	**211**192
212	R1_WLO_Sidewalls	103	shell/quad	192	**212**001	**212**192
213	R1_WRO_Tread	103	shell/quad	64	**213**001	**213**064
214	R1_WLO_Tread	103	shell/quad	64	**214**001	**214**064
254	R1_Discs_Inner	102	shell/tria	144	**254**001	**254**144
255	R1_WRI_Rim	102	shell/quad	96	**255**001	**255**096
256	R1_WLI_Rim	102	shell/quad	96	**256**001	**256**096
257	R1_WRI_Fabric_Sidewalls	301	shell/quad	192	**257**001	**257**192
258	R1_WLI_Fabric_Sidewalls	301	shell/quad	192	**258**001	**258**192
259	R1_WRI_Fabric_Tread	301	shell/quad	64	**259**001	**259**064
260	R1_WLI_Fabric_Tread	301	shell/quad	64	**260**001	**260**064
261	R1_WRI_Sidewalls	103	shell/quad	192	**261**001	**261**192
262	R1_WLI_Sidewalls	103	shell/quad	192	**262**001	**262**192
263	R1_WRI_Tread	103	shell/quad	64	**263**001	**263**064
264	R1_WLI_Tread	103	shell/quad	64	**264**001	**264**064

Table A.8. Detailed summary of complete FE model of the tractor-trailer (cont.)

Part ID	Part title	Material ID	Element type	Number of elements	Element ID minimum	Element ID maximum
300	R2_Vertical_Cylidrical_Joint	210	beam	6	**300**001	**300**006
301	R2_Axle_Rigid_Non_Rotating	214	beam	7	**301**001	**301**007
302	R2_Axle_Rigid_Rotating	201	beam	20	**302**001	**302**020
303	R2_Drums_Elastic	108	solid/penta	80	**303**001	**303**080
304	R2_Discs_Outer	102	shell/tria	144	**304**001	**304**144
305	R2_WRO_Rim	102	shell/quad	96	**305**001	**305**096
306	R2_WLO_Rim	102	shell/quad	96	**306**001	**306**096
307	R2_WRO_Fabric_Sidewalls	301	shell/quad	192	**307**001	**307**192
308	R2_WLO_Fabric_Sidewalls	301	shell/quad	192	**308**001	**308**192
309	R2_WRO_Fabric_Tread	301	shell/quad	64	**309**001	**309**064
310	R2_WLO_Fabric_Tread	301	shell/quad	64	**310**001	**310**064
311	R2_WRO_Sidewalls	103	shell/quad	192	**311**001	**311**192
312	R2_WLO_Sidewalls	103	shell/quad	192	**312**001	**312**192
313	R2_WRO_Tread	103	shell/quad	64	**313**001	**313**064
314	R2_WLO_Tread	103	shell/quad	64	**314**001	**314**064
354	R2_Discs_Inner	102	shell/tria	144	**354**001	**354**144
355	R2_WRI_Rim	102	shell/quad	96	**355**001	**355**096
356	R2_WLI_Rim	102	shell/quad	96	**356**001	**356**096
357	R2_WRI_Fabric_Sidewalls	301	shell/quad	192	**357**001	**357**192
358	R2_WLI_Fabric_Sidewalls	301	shell/quad	192	**358**001	**358**192
359	R2_WRI_Fabric_Tread	301	shell/quad	64	**359**001	**359**064
360	R2_WLI_Fabric_Tread	301	shell/quad	64	**360**001	**360**064
361	R2_WRI_Sidewalls	103	shell/quad	192	**361**001	**361**192
362	R2_WLI_Sidewalls	103	shell/quad	192	**362**001	**362**192
363	R2_WRI_Tread	103	shell/quad	64	**363**001	**363**064
364	R2_WLI_Tread	103	shell/quad	64	**364**001	**364**064
400	T1_Vertical_Cylidrical_Joint	211	beam	6	**400**001	**400**006
401	T1_Axle_Rigid_Non_Rotating	215	beam	6	**401**001	**401**006
402	T1_Axle_Rigid_Rotating	201	beam	21	**402**001	**402**021
403	T1_Drums_Elastic	109	solid/penta	80	**403**001	**403**080
404	T1_Discs_Outer	101	shell/tria	144	**404**001	**404**144
405	T1_WRO_Rim	101	shell/quad	96	**405**001	**405**096
406	T1_WLO_Rim	101	shell/quad	96	**406**001	**406**096
407	T1_WRO_Fabric_Sidewalls	301	shell/quad	192	**407**001	**407**192
408	T1_WLO_Fabric_Sidewalls	301	shell/quad	192	**408**001	**408**192
409	T1_WRO_Fabric_Tread	301	shell/quad	64	**409**001	**409**064
410	T1_WLO_Fabric_Tread	301	shell/quad	64	**410**001	**410**064
411	T1_WRO_Sidewalls	103	shell/quad	192	**411**001	**411**192
412	T1_WLO_Sidewalls	103	shell/quad	192	**412**001	**412**192
413	T1_WRO_Tread	103	shell/quad	64	**413**001	**413**064
414	T1_WLO_Tread	103	shell/quad	64	**414**001	**414**064
454	T1_Discs_Inner	101	shell/tria	144	**454**001	**454**144
455	T1_WRI_Rim	101	shell/quad	96	**455**001	**455**096
456	T1_WLI_Rim	101	shell/quad	96	**456**001	**456**096
457	T1_WRI_Fabric_Sidewalls	301	shell/quad	192	**457**001	**457**192
458	T1_WLI_Fabric_Sidewalls	301	shell/quad	192	**458**001	**458**192
459	T1_WRI_Fabric_Tread	301	shell/quad	64	**459**001	**459**064

Table A.8. Detailed summary of complete FE model of the tractor-trailer (cont.)

Part ID	Part title	Material ID	Element type	Number of elements	Element ID minimum	Element ID maximum
460	T1_WLI_Fabric_Tread	301	shell/quad	64	**460**001	**460**064
461	T1_WRI_Sidewalls	103	shell/quad	192	**461**001	**461**192
462	T1_WLI_Sidewalls	103	shell/quad	192	**462**001	**462**192
463	T1_WRI_Tread	103	shell/quad	64	**463**001	**463**064
464	T1_WLI_Tread	103	shell/quad	64	**464**001	**464**064
500	T2_Vertical_Cylidrical_Joint	211	beam	6	**500**001	**500**006
501	T2_Axle_Rigid_Non_Rotating	216	beam	6	**501**001	**501**006
502	T2_Axle_Rigid_Rotating	201	beam	21	**502**001	**502**021
503	T2_Drums_Elastic	109	solid/penta	80	**503**001	**503**080
504	T2_Discs_Outer	101	shell/tria	144	**504**001	**504**144
505	T2_WRO_Rim	101	shell/quad	96	**505**001	**505**096
506	T2_WLO_Rim	101	shell/quad	96	**506**001	**506**096
507	T2_WRO_Fabric_Sidewalls	301	shell/quad	192	**507**001	**507**192
508	T2_WLO_Fabric_Sidewalls	301	shell/quad	192	**508**001	**508**192
509	T2_WRO_Fabric_Tread	301	shell/quad	64	**509**001	**509**064
510	T2_WLO_Fabric_Tread	301	shell/quad	64	**510**001	**510**064
511	T2_WRO_Sidewalls	103	shell/quad	192	**511**001	**511**192
512	T2_WLO_Sidewalls	103	shell/quad	192	**512**001	**512**192
513	T2_WRO_Tread	103	shell/quad	64	**513**001	**513**064
514	T2_WLO_Tread	103	shell/quad	64	**514**001	**514**064
554	T2_Discs_Inner	101	shell/tria	144	**554**001	**554**144
555	T2_WRI_Rim	101	shell/quad	96	**555**001	**555**096
556	T2_WLI_Rim	101	shell/quad	96	**556**001	**556**096
557	T2_WRI_Fabric_Sidewalls	301	shell/quad	192	**557**001	**557**192
558	T2_WLI_Fabric_Sidewalls	301	shell/quad	192	**558**001	**558**192
559	T2_WRI_Fabric_Tread	301	shell/quad	64	**559**001	**559**064
560	T2_WLI_Fabric_Tread	301	shell/quad	64	**560**001	**560**064
561	T2_WRI_Sidewalls	103	shell/quad	192	**561**001	**561**192
562	T2_WLI_Sidewalls	103	shell/quad	192	**562**001	**562**192
563	T2_WRI_Tread	103	shell/quad	64	**563**001	**563**064
564	T2_WLI_Tread	103	shell/quad	64	**564**001	**564**064
600	T3_Vertical_Cylidrical_Joint	211	beam	6	**600**001	**600**006
601	T3_Axle_Rigid_Non_Rotating	217	beam	6	**601**001	**601**006
602	T3_Axle_Rigid_Rotating	201	beam	21	**602**001	**602**021
603	T3_Drums_Elastic	109	solid/penta	80	**603**001	**603**080
604	T3_Discs_Outer	101	shell/tria	144	**604**001	**604**144
605	T3_WRO_Rim	101	shell/quad	96	**605**001	**605**096
606	T3_WLO_Rim	101	shell/quad	96	**606**001	**606**096
607	T3_WRO_Fabric_Sidewalls	301	shell/quad	192	**607**001	**607**192
608	T3_WLO_Fabric_Sidewalls	301	shell/quad	192	**608**001	**608**192
609	T3_WRO_Fabric_Tread	301	shell/quad	64	**609**001	**609**064
610	T3_WLO_Fabric_Tread	301	shell/quad	64	**610**001	**610**064
611	T3_WRO_Sidewalls	103	shell/quad	192	**611**001	**611**192
612	T3_WLO_Sidewalls	103	shell/quad	192	**612**001	**612**192
613	T3_WRO_Tread	103	shell/quad	64	**613**001	**613**064
614	T3_WLO_Tread	103	shell/quad	64	**614**001	**614**064
654	T3_Discs_Inner	101	shell/tria	144	**654**001	**654**064

Table A.8. Detailed summary of complete FE model of the tractor-trailer (cont.)

Part ID	Part title	Material ID	Element type	Number of elements	Element ID minimum	Element ID maximum
655	T3_WRI_Rim	101	shell/quad	96	**655**001	**655**096
656	T3_WLI_Rim	101	shell/quad	96	**656**001	**656**096
657	T3_WRI_Fabric_Sidewalls	301	shell/quad	192	**657**001	**657**192
658	T3_WLI_Fabric_Sidewalls	301	shell/quad	192	**658**001	**658**192
659	T3_WRI_Fabric_Tread	301	shell/quad	64	**659**001	**659**064
660	T3_WLI_Fabric_Tread	301	shell/quad	64	**660**001	**660**064
661	T3_WRI_Sidewalls	103	shell/quad	192	**661**001	**661**192
662	T3_WLI_Sidewalls	103	shell/quad	192	**662**001	**662**192
663	T3_WRI_Tread	103	shell/quad	64	**663**001	**663**064
664	T3_WLI_Tread	103	shell/quad	64	**664**001	**664**064
700	Frame_Longitudinal	104	shell/quad	490	**700**001	**700**490
701	Frame_Longitudinal_Add	101	shell/quad	36	**701**001	**701**036
702	Frame_Transverse_Front	101	shell/quad	30	**702**001	**702**030
703	Frame_Engine_Support	101	shell/quad	44	**703**001	**703**044
704	Frame_Crossmembers	101	shell/quad	160	**704**001	**704**160
705	Frame_Crossmembers_Support	101	shell/quad	72	**705**001	**705**072
706	Frame_Crossmembers_Add	101	shell/quad	48	**706**001	**706**048
707	Frame_Transverse_Back	101	shell/quad	56	**707**001	**707**056
708	Frame_Back_Connectors	101	shell/quad	22	**708**001	**708**022
709	Frame_Cab_Support	101	shell/quad	40	**709**001	**709**040
710	Fifth_Wheel_Support_Plate	101	shell/quad	40	**710**001	**710**040
711	Fifth_Wheel_Base	201	solid/penta	8	**711**001	**711**008
712	Fifth_Wheel	207	solid/hexa	32	**712**001	**712**032
713	Fuel_Tanks	204	shell/quad	324	**713**001	**713**324
714	Front_Bumper	202	shell/quad	206	**714**001	**714**206
715	Engine	205	solid/hexa	96	**715**001	**715**096
720	Hood	203	shell/quad	598	**720**001	**720**598
721	Hood_Lamps	208	shell/quad	16	**721**001	**721**016
722	Mudflaps	203	shell/quad	110	**722**001	**722**110
730	Driver_Cab	206	shell/quad	640	**730**001	**730**640
731	Driver_Cab_Windows	208	shell/quad	142	**731**001	**731**142
800	Load_Deck_Main_Beams_V	105	shell/quad	1,256	**800**001	**801**256
802	Load_Deck_Main_Beams_H	106	shell/quad	1,076	**802**001	**803**076
804	Load_Deck_Side_Beams_V	101	shell/quad	672	**804**001	**804**672
805	Load_Deck_Side_Beams_H	101	shell/quad	468	**805**001	**805**468
806	Load_Deck_Transverse_Beam_V	101	shell/quad	252	**806**001	**806**252
807	Load_Deck_Transverse_Beam_H	101	shell/quad	1,008	**807**001	**808**008
810	Load_Deck_Transverse_Beam_Add_V	101	shell/quad	24	**810**001	**810**024
811	Load_Deck_Transverse_Beam_Add_H	101	shell/quad	48	**811**001	**811**048
812	Load_Deck_Plate	110	shell/quad	424	**812**001	**812**424
813	Load_Deck_Ramp_Connectors	101	shell/quad	28	**813**001	**813**028
814	Top_Deck_Side_Beams_V	101	shell/quad	270	**814**001	**814**270
815	Top_Deck_Side_Beams_H	101	shell/quad	176	**815**001	**815**176
816	Top_Deck_Transverse_Beams_V	101	shell/quad	96	**816**001	**816**096
817	Top_Deck_Transverse_Beams_H	101	shell/quad	192	**817**001	**817**192
818	Top_Deck_Plate	101	shell/quad	28	**818**001	**818**028
819	Top_Deck_Skid_Plate	101	shell/quad	98	**819**001	**819**098

Table A.8. Detailed summary of complete FE model of the tractor-trailer (cont.)

Part ID	Part title	Material ID	Element type	Number of elements	Element ID minimum	Element ID maximum
820	Ramp_Joints	201	beam	10	**820**001	**820**010
821	Ramp_Rods	201	beam	36	**821**001	**821**036
822	Ramp_Side_Beams_V	101	shell/quad	252	**822**001	**822**252
823	Ramp_Side_Beams_H	101	shell/quad	244	**823**001	**823**244
824	Ramp_Transverse_Beams_V	101	shell/quad	48	**824**001	**824**048
825	Ramp_Transverse_Beams_H	101	shell/quad	96	**825**001	**825**096
830	Load	219	solid/hexa	456	**830**001	**830**456
831	Load_1	220	solid/hexa	60	**831**001	**831**060
832	Load_2	221	solid/hexa	68	**832**001	**832**068
833	Load_3	222	solid/hexa	180	**833**001	**833**180
834	Load_4	223	solid/hexa	120	**834**001	**834**120
835	Load_4_Base	101	solid/hexa	92	**835**001	**835**092
851	Acc_Front_Right	218	solid/hexa	1	**851**001	**851**001
852	Acc_Front_Left	218	solid/hexa	1	**852**001	**852**001
853	Acc_Rear_Right	218	solid/hexa	1	**853**001	**853**001
854	Acc_Rear_Left	218	solid/hexa	1	**854**001	**854**001
855	Acc_Trailer_Right	218	solid/hexa	1	**855**001	**855**001
856	Acc_Trailer_Left	218	solid/hexa	1	**856**001	**856**001
857	Acc_Rear_Center	218	solid/hexa	2	**857**001	**857**002

Comments:
Part No. 830 applied in the option II of the tractor-trailer FE model only.
Parts No. 831 to 835 applied in the option III of the tractor-trailer FE model only.

Six different types of material models were applied in the FE model of the truck tractor and trailer, as presented in Table A.9. Detailed properties of each used material model were provided in Table A.10 through Table A.14. The data were presented in accordance with the values declared in the appropriate cards in the LS-DYNA code.

Table A.9. Material models used in the FE model of the tractor trailer (LS-DYNA Keyword User's Manual, 2007)

Material number	Material designation in LS-DYNA code	Material model description	Material IDs in FE model (number)
*MAT_001	*MAT_ELASTIC	Isotropic elastic material	101 to 110 (10)
*MAT_020	*MAT_RIGID	Rigid material (part made from this material are considered to belong to a rigid body)	201 to 223 (23)
*MAT_034	*MAT_FABRIC	Fabric material (stiffness for tension only)	301 (1)
*MAT_S01	*MAT_SPRING_ELASTIC	Linear material for discrete springs	11, 21 (2)
*MAT_S02	*MAT_DAMPER_VISCOUS	Linear material for discrete dampers	12, 22, 42 (3)
*MAT_S04	*MAT_SPRING_NONLINEAR_ELASTIC	Nonlinear material for discrete springs	41 (1)

Comments:
Material No. 219 applied in the II variant of the tractor-trailer FE model only.
Materials No. 220 to 223 applied in the III variant of the tractor-trailer FE model only.

Table A.10. Properties of the elastic material models used in the FE model of the tractor trailer

Material ID	Material title in FE model	RO (Mg/mm^3)	E (MPa)	PR (–)	Number of referenced parts
101	Elastic_Steel	$7.850 \cdot 10^{-9}$	$2.100 \cdot 10^{5}$	0.30	$45^{I,II}$ (46^{III})
102	Elastic_Aluminum	$2.700 \cdot 10^{-9}$	$7.000 \cdot 10^{4}$	0.35	15
103	Elastic_Rubber	$1.250 \cdot 10^{-9}$	$1.000 \cdot 10^{2}$	0.45	44
104	Elastic_Steel_Frame	• $1.961 \cdot 10^{-8}$	$2.100 \cdot 10^{5}$	0.30	1
105	Elastic_Steel_Trailer_Frame_V	• $1.463 \cdot 10^{-8}$	$2.100 \cdot 10^{5}$	0.30	1
106	Elastic_Steel_Trailer_Frame_H	• $1.201 \cdot 10^{-8}$	$2.100 \cdot 10^{5}$	0.30	1
107	Elastic_Front_Drums	• $3.866 \cdot 10^{-9}$	$2.100 \cdot 10^{5}$	0.30	1
108	Elastic_Rear_Drums	• $3.824 \cdot 10^{-9}$	$2.100 \cdot 10^{5}$	0.30	2
109	Elastic_Trailer_Drums	• $3.332 \cdot 10^{-9}$	$2.100 \cdot 10^{5}$	0.30	3
110	Elastic_Steel_Trailer_Plate	• $1.961 \cdot 10^{-8}$	$2.100 \cdot 10^{5}$	0.30	1

where:
RO — mass density, ρ
E — Young's modulus, E
PR — Poisson's Ratio, ν
• — density recalculated to obtain appropriate calculated mass of the FE model

Table A.11. Properties of the rigid material models used in the FE model of the tractor trailer

Material ID	Material title in FE model	RO (Mg/mm^3)	E (MPa)	PR (–)	Number of referenced parts
201	Rigid_Steel	$7.850 \cdot 10^{-9}$	$2.100 \cdot 10^{5}$	0.30	9
202	Rigid_Stainless_Steel	$8.000 \cdot 10^{-9}$	$1.930 \cdot 10^{5}$	0.29	1
203	Rigid_Composite	$1.445 \cdot 10^{-9}$	$2.180 \cdot 10^{4}$	0.40	2
204	Rigid_Aluminum	$2.700 \cdot 10^{-9}$	$7.000 \cdot 10^{4}$	0.35	1
205	Rigid_Engine	• $2.724 \cdot 10^{-9}$	$2.100 \cdot 10^{5}$	0.30	1
206	Rigid_Driver_Cab	• $7.618 \cdot 10^{-9}$	$2.100 \cdot 10^{5}$	0.30	1
207	Rigid_Fifth_Wheel	• $2.573 \cdot 10^{-9}$	$2.100 \cdot 10^{5}$	0.30	1
208	Rigid_Glass	• $2.500 \cdot 10^{-9}$	$7.600 \cdot 10^{4}$	0.30	2
209	Rigid_F_Axle_Cylindrical_Joint	• $6.032 \cdot 10^{-8}$	$2.100 \cdot 10^{5}$	0.30	1
210	Rigid_R_Axle_Cylindrical_Joint	• $1.527 \cdot 10^{-7}$	$2.100 \cdot 10^{5}$	0.30	2
211	Rigid_T_Axle_Cylindrical_Joint	• $8.310 \cdot 10^{-8}$	$2.100 \cdot 10^{5}$	0.30	3
212	Rigid_F_Axle_Non_Rotating	• $6.316 \cdot 10^{-9}$	$2.100 \cdot 10^{5}$	0.30	1
213	Rigid_R1_Axle_Non_Rotating	• $8.099 \cdot 10^{-9}$	$2.100 \cdot 10^{5}$	0.30	1
214	Rigid_R1_Axle_Non_Rotating	• $6.327 \cdot 10^{-9}$	$2.100 \cdot 10^{5}$	0.30	1
215	Rigid_T1_Axle_Non_Rotating	• $7.603 \cdot 10^{-9}$	$2.100 \cdot 10^{5}$	0.30	1
216	Rigid_T1_Axle_Non_Rotating	• $7.603 \cdot 10^{-9}$	$2.100 \cdot 10^{5}$	0.30	1
217	Rigid_T1_Axle_Non_Rotating	• $7.603 \cdot 10^{-9}$	$2.100 \cdot 10^{5}$	0.30	1
218	Rigid_Accelerometers	$7.850 \cdot 10^{-9}$	$2.100 \cdot 10^{5}$	0.30	7
219	Rigid_Load	• $7.603 \cdot 10^{-9}$	$2.100 \cdot 10^{5}$	0.30	1^{II}
220	Rigid_Load_1	• $6.140 \cdot 10^{-9}$	$2.100 \cdot 10^{5}$	0.30	1^{III}
221	Rigid_Load_2	• $7.150 \cdot 10^{-9}$	$2.100 \cdot 10^{5}$	0.30	1^{III}
222	Rigid_Load_3	• $6.222 \cdot 10^{-9}$	$2.100 \cdot 10^{5}$	0.30	1^{III}
223	Rigid_Load_4	• $6.195 \cdot 10^{-9}$	$2.100 \cdot 10^{5}$	0.30	1^{III}

where:
RO — mass density, ρ
E — Young's modulus, E
PR — Poisson's Ratio, ν
• — density recalculated to obtain appropriate calculated mass of the FE model

Table A.12. Properties of the fabric material model used in the FE model of the tractor trailer

Material ID	Material title in FE model	RO (Mg/mm^3)	EA (MPa)	PRBA (–)	Number of referenced parts
301	Fabric	$1.000 \cdot 10^{-9}$	$2.100 \cdot 10^{5}$	0.30	44

where:
RO — mass density, ρ
EA — Young's modulus in longitudinal direction, E_A
PRBA — Poisson's Ratio in *BA* direction, ν_{BA}

Comments
Young's modulus in transverse E_B and normal E_C direction equals zero.
Poisson's ratio in *CA* and *CB* direction equals zero.

Table A.13. Properties of the spring elastic material models used in the FE model of the tractor trailer

Material ID	Material title in FE model	K (N/mm)	Number of referenced parts
11	Front_Springs	280	1
21	Rear_Springs	305	1

where:
K — elastic stiffness, k

Table A.14. Properties of the damper viscous material models used in the FE model of the tractor trailer

Material ID	Material title in FE model	DC (N·s/mm)	Number of referenced parts
12	Front_Dampers	17	1
22	Rear_Dampers	22	1
42	Trailer_Dampers	40	1

where:
DC — damping constant, c

A.3. FE Model of the Terex Crane

Detailed summary of the complete FE model of the Terex crane is listed in Table A.15.

Table A.15. Detailed summary of complete FE model of the Terex crane

Part ID	Part title	Material ID	Element type	Number of elements	Element ID minimum	Element ID maximum
11	Front_Springs	11	discrete	2	**11**001	**11**002
21	Front_Dampers	21	discrete	2	**21**001	**21**002
100	F1_Vertical_Cylidrical_Joint	204	beam	28	**100**001	**100**028
101	F1_Axle_Rigid_Non_Rotating	201	beam	92	**101**001	**101**092
102	F1_Axle_Rigid_Pivots	201	beam	6	**102**001	**102**006
103	F1_WR_Drum	208	solid/penta	32	**103**001	**103**032
104	F1_WL_Drum	208	solid/penta	32	**104**001	**104**032
105	F1_WR_Disc	102	shell/tria	72	**105**001	**105**072
106	F1_WL_Disc	102	shell/tria	72	**106**001	**106**072
107	F1_WR_Rim	102	shell/quad	160	**107**001	**107**160
108	F1_WL_Rim	102	shell/quad	160	**108**001	**108**160
109	F1_WR_Fabric_Sidewalls	301	shell/quad	192	**109**001	**109**192
110	F1_WL_Fabric_Sidewalls	301	shell/quad	192	**110**001	**110**192
111	F1_WR_Fabric_Tread	301	shell/quad	64	**111**001	**111**064
112	F1_WL_Fabric_Tread	301	shell/quad	64	**112**001	**112**064
113	F1_WR_Sidewalls	103	shell/quad	192	**113**001	**113**192
114	F1_WL_Sidewalls	103	shell/quad	192	**114**001	**114**192
115	F1_WR_Tread	103	shell/quad	64	**115**001	**115**064
116	F1_WL_Tread	103	shell/quad	64	**116**001	**116**064
200	R1_Torque_Rod	206	beam	7	**200**001	**200**007
201	R1_Axle_Rigid_Non_Rotating	202	shell/quad	212	**201**001	**201**212
202	R1_Axle_Rigid_Rotating	206	beam	22	**202**001	**202**022
203	R1_WR_Drum	209	solid/penta	40	**203**001	**203**040
204	R1_WL_Drum	209	solid/penta	40	**204**001	**204**040
205	R1_WRO_Disc	102	shell/tria	72	**205**001	**205**072
206	R1_WLO_Disc	102	shell/tria	72	**206**001	**206**072
207	R1_WRO_Rim	102	shell/quad	96	**207**001	**207**096
208	R1_WLO_Rim	102	shell/quad	96	**208**001	**208**096
209	R1_WRO_Fabric_Sidewalls	301	shell/quad	192	**209**001	**209**192
210	R1_WLO_Fabric_Sidewalls	301	shell/quad	192	**210**001	**210**192
211	R1_WRO_Fabric_Tread	301	shell/quad	64	**211**001	**211**064
212	R1_WLO_Fabric_Tread	301	shell/quad	64	**212**001	**212**064
213	R1_WRO_Sidewalls	103	shell/quad	192	**213**001	**213**192
214	R1_WLO_Sidewalls	103	shell/quad	192	**214**001	**214**192
215	R1_WRO_Tread	103	shell/quad	64	**215**001	**215**064
216	R1_WLO_Tread	103	shell/quad	64	**216**001	**216**064
255	R1_WRI_Disc	102	shell/tria	72	**255**001	**255**072
256	R1_WLI_Disc	102	shell/tria	72	**256**001	**256**072
257	R1_WRI_Rim	102	shell/quad	96	**257**001	**257**096
258	R1_WLI_Rim	102	shell/quad	96	**258**001	**258**096
259	R1_WRI_Fabric_Sidewalls	301	shell/quad	192	**259**001	**259**192
260	R1_WLI_Fabric_Sidewalls	301	shell/quad	192	**260**001	**260**192
261	R1_WRI_Fabric_Tread	301	shell/quad	64	**261**001	**261**064
262	R1_WLI_Fabric_Tread	301	shell/quad	64	**262**001	**262**064

Table A.15. Detailed summary of complete FE model of the Terex crane (cont.)

Part ID	Part title	Material ID	Element type	Number of elements	Element ID minimum	Element ID maximum
263	R1_WRI_Sidewalls	103	shell/quad	192	**263**001	**263**192
264	R1_WLI_Sidewalls	103	shell/quad	192	**264**001	**264**192
265	R1_WRI_Tread	103	shell/quad	64	**265**001	**265**064
266	R1_WLI_Tread	103	shell/quad	64	**266**001	**266**064
300	R2_Torque_Rod	206	beam	7	**300**001	**300**007
301	R2_Axle_Rigid_Non_Rotating	203	shell/quad	212	**301**001	**301**212
302	R2_Axle_Rigid_Rotating	206	beam	22	**302**001	**302**022
303	R2_WR_Drum	209	solid/penta	40	**303**001	**303**040
304	R2_WL_Drum	209	solid/penta	40	**304**001	**304**040
305	R2_WRO_Disc	102	shell/tria	72	**305**001	**305**072
306	R2_WLO_Disc	102	shell/tria	72	**306**001	**306**072
307	R2_WRO_Rim	102	shell/quad	96	**307**001	**307**096
308	R2_WLO_Rim	102	shell/quad	96	**308**001	**308**096
309	R2_WRO_Fabric_Sidewalls	301	shell/quad	192	**309**001	**309**192
310	R2_WLO_Fabric_Sidewalls	301	shell/quad	192	**310**001	**310**192
311	R2_WRO_Fabric_Tread	301	shell/quad	64	**311**001	**311**064
312	R2_WLO_Fabric_Tread	301	shell/quad	64	**312**001	**312**064
313	R2_WRO_Sidewalls	103	shell/quad	192	**313**001	**313**192
314	R2_WLO_Sidewalls	103	shell/quad	192	**314**001	**314**192
315	R2_WRO_Tread	103	shell/quad	64	**315**001	**315**064
316	R2_WLO_Tread	103	shell/quad	64	**316**001	**316**064
355	R2_WRI_Disc	102	shell/tria	72	**355**001	**355**072
356	R2_WLI_Disc	102	shell/tria	72	**356**001	**356**072
357	R2_WRI_Rim	102	shell/quad	96	**357**001	**357**096
358	R2_WLI_Rim	102	shell/quad	96	**358**001	**358**096
359	R2_WRI_Fabric_Sidewalls	301	shell/quad	192	**359**001	**359**192
360	R2_WLI_Fabric_Sidewalls	301	shell/quad	192	**360**001	**360**192
361	R2_WRI_Fabric_Tread	301	shell/quad	64	**361**001	**361**064
362	R2_WLI_Fabric_Tread	301	shell/quad	64	**362**001	**362**064
363	R2_WRI_Sidewalls	103	shell/quad	192	**363**001	**363**192
364	R2_WLI_Sidewalls	103	shell/quad	192	**364**001	**364**192
365	R2_WRI_Tread	103	shell/quad	64	**365**001	**365**064
366	R2_WLI_Tread	103	shell/quad	64	**366**001	**366**064
401	Frame_Main	104	shell	500	**401**001	**401**500
402	Frame_Main_Bottom	104	shell/quad	144	**402**001	**402**144
403	Frame_Front	104	shell/quad	254	**403**001	**403**254
404	Frame_Front_Bottom	104	shell/quad	51	**404**001	**404**051
405	Frame_Front_Crossmember	101	shell/quad	115	**405**001	**405**115
406	Frame_Main_Support	101	shell/quad	60	**406**001	**406**060
407	Frame_Main_Top	101	shell	228	**407**001	**407**228
408	Deck_Complete	102	shell/quad	500	**408**001	**408**500
411	Swing_Joint	206	beam	25	**411**001	**411**025
412	Boom_Support	206	shell	292	**412**001	**412**292
413	Hydraulic_Fluid_Tank	206	shell/quad	172	**413**001	**413**172
414	Fuel_Tank	206	shell/quad	180	**414**001	**414**180
415	Hood	206	shell/quad	457	**415**001	**415**457
416	Engine_Support	206	shell/quad	30	**416**001	**416**030

Table A.15. Detailed summary of complete FE model of the Terex crane (cont.)

Part ID	Part title	Material ID	Element type	Number of elements	Element ID minimum	Element ID maximum
417	Engine	205	solid/hexa	96	**417**001	**417**096
418	Deck_Box1	210	shell/quad	90	**418**001	**418**090
419	Deck_Box2	210	shell/quad	39	**419**001	**419**039
420	Deck_Box3	210	shell/quad	96	**420**001	**420**096
421	Driver_Cab	206	shell/quad	500	**421**001	**421**500
422	Driver_Cab_Door	206	shell/quad	86	**422**001	**422**086
423	Driver_Cab_Windows	211	shell/quad	197	**423**001	**423**197
424	Driver_Cab_Door_Window	211	shell/quad	72	**424**001	**424**072
425	Front_Bumper	206	shell/quad	166	**425**001	**425**166
426	Front_Mass	207	shell/quad	130	**426**001	**426**130
431	Suspension_Frame	215	shell/quad	64	**431**001	**431**064
432	Suspension_Crosstubes	206	beam	8	**432**001	**432**008
433	Suspension_Saddles	206	shell/quad	24	**433**001	**433**024
434	Suspension_Rod_Connectors	206	shell/quad	8	**434**001	**434**008
435	Equalizer_Beam_Right	206	shell	168	**435**001	**435**168
436	Equalizer_Beam_Left	206	shell	168	**436**001	**436**168
437	Discrete_Springs_Equalizer_Beams	12	discrete	8	**437**001	**437**008
438	Discrete_Dampers_Equalizer_Beams	22	discrete	4	**438**001	**438**004
439	Discrete_Springs_Axles	13	discrete	8	**439**001	**439**008
440	Discrete_Dampers_Axles	23	discrete	4	**440**001	**440**004
441	Turntable_Base	216	shell	292	**441**001	**441**292
442	Turntable_Sidewalls	217	shell/quad	364	**442**001	**442**364
443	Turntable_Counterweight	218	shell/quad	252	**443**001	**443**252
444	Turntable_Cylinder_Joint	206	beam	3	**444**001	**444**003
445	Turntable_Boom_Joint	206	beam	3	**445**001	**445**003
446	Main_Cylinder	212	solid	272	**446**001	**446**272
447	Operator_Cab_Support	206	shell/quad	66	**447**001	**447**066
448	Operator_Cab	206	shell/quad	500	**448**001	**448**500
449	Operator_Cab_Door	206	shell/quad	168	**449**001	**449**168
450	Operator_Cab_Windows	211	shell/quad	376	**450**001	**450**376
451	Operator_Cab_Door_Window	211	shell/quad	79	**451**001	**451**079
452	Boom_Section_1	206	shell/quad	490	**452**001	**452**490
453	Boom_Section_2	206	shell/quad	396	**453**001	**453**396
454	Boom_Section_3	206	shell/quad	420	**454**001	**454**420
455	Boom_Section_4	206	shell/quad	500	**455**001	**455**500
456	Boom_Cylinder_Support	206	shell/quad	44	**456**001	**456**044
457	Boom_Cylinder_Support_Long	206	shell/quad	20	**457**001	**457**020
458	Main_Cylinder_Joint_U	206	beam	3	**458**001	**458**003
459	Boom_Cylinder_Inside	213	solid	128	**459**001	**459**128
501	Outriggers_Front_Case	206	shell/quad	400	**501**001	**501**400
502	Outriggers_Front_Case_Slides	206	shell/quad	48	**502**001	**502**048
503	Outriggers_Front_Case_Add	206	shell/quad	44	**503**001	**503**044
504	Outrigger_Front_Right	206	shell/quad	214	**504**001	**504**214
505	Outrigger_Front_Left	206	shell/quad	214	**505**001	**505**214
506	Outrigger_Front_Right_Cylinder_H	214	solid	40	**506**001	**506**040
507	Outrigger_Front_Left_Cylinder_H	214	solid	40	**507**001	**507**040
508	Outrigger_Front_Right_Cylinder_V	206	solid	96	**508**001	**508**096

Table A.15. Detailed summary of complete FE model of the Terex crane (cont.)

Part ID	Part title	Material ID	Element type	Number of elements	Element ID minimum	Element ID maximum
509	Outrigger_Front_Left_Cylinder_V	206	solid	96	**509**001	**509**096
521	Outriggers_Rear_Case	206	shell/quad	414	**521**001	**521**414
522	Outriggers_Rear_Case_Slides	206	shell/quad	36	**522**001	**522**048
523	Outriggers_Rear_Case_Add	206	shell/quad	44	**523**001	**523**044
524	Outrigger_Rear_Right	206	shell/quad	214	**524**001	**524**214
525	Outrigger_Rear_Left	206	shell/quad	214	**525**001	**525**214
526	Outrigger_Rear_Right_Cylinder_H	214	solid	40	**526**001	**526**040
527	Outrigger_Rear_Left_Cylinder_H	214	solid	40	**527**001	**527**040
528	Outrigger_Rear_Right_Cylinder_V	206	solid	96	**528**001	**528**096
529	Outrigger_Rear_Left_Cylinder_V	206	solid	96	**529**001	**529**096
548	Outrigger_5th_Cylinder_V	206	solid	72	**548**001	**548**072
551	Acc_meter_R	206	solid/hexa	2	**551**001	**551**002

Five different types of material models were applied in the FE model of the Terex crane, as presented in Table A.16. Detailed properties of each used material model were provided in Table A.17 through Table A.21. The data were presented in accordance with the values declared in the appropriate cards in the LS-DYNA code.

Table A.16. Material models used in the FE model of the Terex crane (LS-DYNA Keyword User's Manual, 2007)

Material number	Material designation in LS-DYNA code	Material model description	Material IDs in FE model (number)
*MAT_001	*MAT_ELASTIC	Isotropic elastic material	101 to 104 (4)
*MAT_020	*MAT_RIGID	Rigid material (part made from this material are considered to belong to a rigid body)	201 to 218 (18)
*MAT_034	*MAT_FABRIC	Fabric material (stiffness for tension only)	301 (1)
*MAT_S01	*MAT_SPRING_ELASTIC	Linear material for discrete springs	11, 12, 13 (3)
*MAT_S02	*MAT_DAMPER_VISCOUS	Linear material for discrete dampers	21, 22, 23 (3)

Table A.17. Properties of the elastic material models used in the FE model of the Terex crane

Material ID	Material title in FE model	RO (Mg/mm^3)	E (MPa)	PR (–)	Number of referenced parts
101	Elastic_Steel	$7.850 \cdot 10^{-9}$	$2.100 \cdot 10^{5}$	0.30	3
102	Elastic_Aluminum	$2.700 \cdot 10^{-9}$	$7.000 \cdot 10^{4}$	0.35	21
103	Elastic_Rubber	$1.250 \cdot 10^{-9}$	$1.000 \cdot 10^{2}$	0.45	20
104	Elastic_Steel_Frame	• $1.727 \cdot 10^{-8}$	$2.100 \cdot 10^{5}$	0.30	2

where:
RO — mass density, ρ
E — Young's modulus, E
PR — Poisson's Ratio, ν
• — density recalculated to obtain appropriate calculated mass of the FE model

Table A.18. Properties of the rigid material models used in the FE model of the Terex crane

Material ID	Material title in FE model	RO (Mg/mm^3)	E (MPa)	PR (–)	Number of referenced parts
201	Rigid_F_Axle_Non_Rotating	$7.850 \cdot 10^{-9}$	$2.100 \cdot 10^{5}$	0.30	2
202	Rigid_R1_Axle_Non_Rotating	• $1.186 \cdot 10^{-8}$	$2.100 \cdot 10^{5}$	0.30	1
203	Rigid_R2_Axle_Non_Rotating	• $7.753 \cdot 10^{-9}$	$2.100 \cdot 10^{5}$	0.30	1
204	Rigid_F_Cylindrical_Joints	• $1.879 \cdot 10^{-8}$	$7.000 \cdot 10^{4}$	0.35	1
205	Rigid_Engine	• $2.748 \cdot 10^{-9}$	$3.020 \cdot 10^{5}$	0.20	1
206	Rigid_Steel	$7.850 \cdot 10^{-9}$	$2.100 \cdot 10^{5}$	0.30	49
207	Rigid_Front_Mass	$7.850 \cdot 10^{-9}$	$2.100 \cdot 10^{5}$	0.30	1
208	Rigid_F_Drums	• $2.242 \cdot 10^{-9}$	$2.100 \cdot 10^{5}$	0.30	2
209	Rigid_R_Drums	• $2.709 \cdot 10^{-9}$	$2.100 \cdot 10^{5}$	0.30	4
210	Rigid_Aluminum	$2.700 \cdot 10^{-9}$	$7.000 \cdot 10^{4}$	0.35	3
211	Rigid_Glass	$2.500 \cdot 10^{-9}$	$7.600 \cdot 10^{4}$	0.30	4
212	Rigid_Main_Cylinder	• $2.462 \cdot 10^{-9}$	$2.100 \cdot 10^{5}$	0.30	1
213	Rigid_Boom_Cylinder	• $3.285 \cdot 10^{-9}$	$2.100 \cdot 10^{5}$	0.30	1
214	Rigid_Outrigger_Cylinders	• $1.388 \cdot 10^{-8}$	$2.100 \cdot 10^{5}$	0.30	4
215	Rigid_Suspension_Frame	• $5.786 \cdot 10^{-9}$	$2.100 \cdot 10^{5}$	0.30	1
216	Rigid_Turntable_Base	• $2.792 \cdot 10^{-8}$	$2.100 \cdot 10^{5}$	0.30	1
217	Rigid_Turntable_Sidewalls	• $2.071 \cdot 10^{-8}$	$2.100 \cdot 10^{5}$	0.30	1
218	Rigid_Turntable_Counterweigth	• $1.536 \cdot 10^{-8}$	$2.100 \cdot 10^{5}$	0.30	1

where:
RO — mass density, ρ
E — Young's modulus, E
PR — Poisson's Ratio, ν
• — density recalculated to obtain appropriate calculated mass of the Terex crane

Table A.19. Properties of the fabric material model used in the FE model of the tractor trailer

Material ID	Material title in FE model	RO (Mg/mm^3)	EA (MPa)	PRBA (–)	Number of referenced parts
301	Fabric	$1.000 \cdot 10^{-9}$	$2.100 \cdot 10^{5}$	0.30	20

where:
RO — mass density, ρ
EA — Young's modulus in longitudinal direction, E_A
PRBA — Poisson's Ratio in BA direction, ν_{BA}

Comments
Young's modulus in transverse E_B and normal E_C direction equals zero.
Poisson's ratio in CA and CB direction equals zero.

Table A.20. Properties of the spring elastic material models used in the FE model of the Terex crane

Material ID	Material title in FE model	K (N/mm)	Number of referenced parts
11	Front_Springs	560	1
12	Rear_Springs_Equalizer_Beams	5	1
13	Rear_Springs_Axles	5	1

where:
K — elastic stiffness, k

Table A.21. Properties of the damper viscous material models used in the FE model of the Terex crane

Material ID	Material title in FE model	DC (N·s/mm)	Number of referenced parts
21	Front_Dampers	20	1
22	Rear_Dampers_Equalizer_Beams	10	1
23	Rear_Dampers_Axles	10	1

where:
DC — damping constant, *c*

A.4. FE Model of the FDOT Truck

Detailed summary of the complete FE model of the FDOT Truck is listed in Table A.22.

Table A.22. Detailed summary of complete FE model of the FDOT Truck

Part ID	Part title	Material ID	Element type	Number of elements	Element ID minimum	Element ID maximum
100	F1_Axle_Rigid_Non_Rotating	201	beam	12	**100**001	**100**012
101	F1_Cylidrical_Joint	206	beam	4	**101**001	**101**004
102	F1_Shock_Absorber	21	discrete	2	**102**001	**102**002
103	F1_Drums	208	solid/penta	64	**103**001	**103**064
105	F1_WR_Disc	107	shell/tria	72	**105**001	**105**072
106	F1_WL_Disc	107	shell/tria	72	**106**001	**106**072
107	F1_WR_Rim	107	shell/quad	64	**107**001	**107**064
108	F1_WL_Rim	107	shell/quad	64	**108**001	**108**064
109	F1_WR_Fabric_Sidewalls	301	shell/quad	192	**109**001	**109**192
110	F1_WL_Fabric_Sidewalls	301	shell/quad	192	**110**001	**110**192
111	F1_WR_Fabric_Tread	301	shell/quad	64	**111**001	**111**064
112	F1_WL_Fabric_Tread	301	shell/quad	64	**112**001	**112**064
113	F1_WR_Sidewalls	106	shell/quad	192	**113**001	**113**192
114	F1_WL_Sidewalls	106	shell/quad	192	**114**001	**114**192
115	F1_WR_Tread	106	shell/quad	64	**115**001	**115**064
116	F1_WL_Tread	106	shell/quad	64	**116**001	**116**064
120	F1_Leaf_Spring	101	beam	140	**120**001	**120**140
121	F1_Spring_Support_Front	206	beam	12	**121**001	**121**012
122	F1_Spring_Support_Back	206	beam	16	**122**001	**122**016
123	F1_Spring_Connectors_Front	206	beam	4	**123**001	**123**004
124	F1_Spring_Connectors_Back	206	beam	4	**124**001	**124**004
200	R1_Axle_Rigid_Non_Rotating	202	beam	20	**200**001	**200**020
203	R1_Drums	209	solid/penta	80	**203**001	**203**080
205	R1_WRO_Disc	107	shell/tria	72	**205**001	**205**072
206	R1_WLO_Disc	107	shell/tria	72	**206**001	**206**072
207	R1_WRO_Rim	107	shell/quad	64	**207**001	**207**064
208	R1_WLO_Rim	107	shell/quad	64	**208**001	**208**064
209	R1_WRO_Fabric_Sidewalls	301	shell/quad	192	**209**001	**209**192
210	R1_WLO_Fabric_Sidewalls	301	shell/quad	192	**210**001	**210**192
211	R1_WRO_Fabric_Tread	301	shell/quad	64	**211**001	**211**064
212	R1_WLO_Fabric_Tread	301	shell/quad	64	**212**001	**212**064
213	R1_WRO_Sidewalls	106	shell/quad	192	**213**001	**213**192
214	R1_WLO_Sidewalls	106	shell/quad	192	**214**001	**214**192
215	R1_WRO_Tread	106	shell/quad	64	**215**001	**215**064
216	R1_WLO_Tread	106	shell/quad	64	**216**001	**216**064
221	R1_Torque_Rod	206	beam	8	**221**001	**221**008
222	R1_Equalizer_Beam_Connector	206	beam	8	**222**001	**222**008
255	R1_WRI_Disc	107	shell/tria	72	**255**001	**255**072
256	R1_WLI_Disc	107	shell/tria	72	**256**001	**256**072
257	R1_WRI_Rim	107	shell/quad	64	**257**001	**257**064
258	R1_WLI_Rim	107	shell/quad	64	**258**001	**258**064
259	R1_WRI_Fabric_Sidewalls	301	shell/quad	192	**259**001	**259**192
260	R1_WLI_Fabric_Sidewalls	301	shell/quad	192	**260**001	**260**192
261	R1_WRI_Fabric_Tread	301	shell/quad	64	**261**001	**261**064

Table A.22. Detailed summary of complete FE model of the FDOT Truck (cont.)

Part ID	Part title	Material ID	Element type	Number of elements	Element ID minimum	Element ID maximum
262	R1_WLI_Fabric_Tread	301	shell/quad	64	**262**001	**262**064
263	R1_WRI_Sidewalls	106	shell/quad	192	**263**001	**263**192
264	R1_WLI_Sidewalls	106	shell/quad	192	**264**001	**264**192
265	R1_WRI_Tread	106	shell/quad	64	**265**001	**265**064
266	R1_WLI_Tread	106	shell/quad	64	**266**001	**266**064
300	R2_Axle_Rigid_Non_Rotating	202	beam	20	**300**001	**300**020
303	R2_Drums	209	solid/penta	80	**303**001	**303**080
305	R2_WRO_Disc	107	shell/tria	72	**305**001	**305**072
306	R2_WLO_Disc	107	shell/tria	72	**306**001	**306**072
307	R2_WRO_Rim	107	shell/quad	64	**307**001	**307**064
308	R2_WLO_Rim	107	shell/quad	64	**308**001	**308**064
309	R2_WRO_Fabric_Sidewalls	301	shell/quad	192	**309**001	**309**192
310	R2_WLO_Fabric_Sidewalls	301	shell/quad	192	**310**001	**310**192
311	R2_WRO_Fabric_Tread	301	shell/quad	64	**311**001	**311**064
312	R2_WLO_Fabric_Tread	301	shell/quad	64	**312**001	**312**064
313	R2_WRO_Sidewalls	106	shell/quad	192	**313**001	**313**192
314	R2_WLO_Sidewalls	106	shell/quad	192	**314**001	**314**192
315	R2_WRO_Tread	106	shell/quad	64	**315**001	**315**064
316	R2_WLO_Tread	106	shell/quad	64	**316**001	**316**064
321	R2_Torque_Rod	206	beam	8	**321**001	**321**008
322	R2_Equalizer_Beam_Connector	206	beam	8	**322**001	**322**008
355	R2_WRI_Disc	107	shell/tria	72	**355**001	**355**072
356	R2_WLI_Disc	107	shell/tria	72	**356**001	**356**072
357	R2_WRI_Rim	107	shell/quad	64	**357**001	**357**064
358	R2_WLI_Rim	107	shell/quad	64	**358**001	**358**064
359	R2_WRI_Fabric_Sidewalls	301	shell/quad	192	**359**001	**359**192
360	R2_WLI_Fabric_Sidewalls	301	shell/quad	192	**360**001	**360**192
361	R2_WRI_Fabric_Tread	301	shell/quad	64	**361**001	**361**064
362	R2_WLI_Fabric_Tread	301	shell/quad	64	**362**001	**362**064
363	R2_WRI_Sidewalls	106	shell/quad	192	**363**001	**363**192
364	R2_WLI_Sidewalls	106	shell/quad	192	**364**001	**364**192
365	R2_WRI_Tread	106	shell/quad	64	**365**001	**365**064
366	R2_WLI_Tread	106	shell/quad	64	**366**001	**366**064
400	T1_Axle_Rigid_Non_Rotating	204	beam	20	**400**001	**400**020
403	T1_Drums	210	solid/penta	80	**403**001	**403**080
405	T1_WRO_Disc	108	shell/tria	72	**405**001	**405**072
406	T1_WLO_Disc	108	shell/tria	72	**406**001	**406**072
407	T1_WRO_Rim	108	shell/quad	64	**407**001	**407**064
408	T1_WLO_Rim	108	shell/quad	64	**408**001	**408**064
409	T1_WRO_Fabric_Sidewalls	301	shell/quad	192	**409**001	**409**192
410	T1_WLO_Fabric_Sidewalls	301	shell/quad	192	**410**001	**410**192
411	T1_WRO_Fabric_Tread	301	shell/quad	64	**411**001	**411**064
412	T1_WLO_Fabric_Tread	301	shell/quad	64	**412**001	**412**064
413	T1_WRO_Sidewalls	106	shell/quad	192	**413**001	**413**192
414	T1_WLO_Sidewalls	106	shell/quad	192	**414**001	**414**192
415	T1_WRO_Tread	106	shell/quad	64	**415**001	**415**064
416	T1_WLO_Tread	106	shell/quad	64	**416**001	**416**064

Table A.22. Detailed summary of complete FE model of the FDOT Truck (cont.)

Part ID	Part title	Material ID	Element type	Number of elements	Element ID minimum	Element ID maximum
421	T1_Torque_Rod	206	beam	8	**421**001	**421**008
422	T1_Equalizer_Beam_Connector	206	beam	8	**422**001	**422**008
455	T1_WRI_Disc	108	shell/tria	72	**455**001	**455**072
456	T1_WLI_Disc	108	shell/tria	72	**456**001	**456**072
457	T1_WRI_Rim	108	shell/quad	64	**457**001	**457**064
458	T1_WLI_Rim	108	shell/quad	64	**458**001	**458**064
459	T1_WRI_Fabric_Sidewalls	301	shell/quad	192	**459**001	**459**192
460	T1_WLI_Fabric_Sidewalls	301	shell/quad	192	**460**001	**460**192
461	T1_WRI_Fabric_Tread	301	shell/quad	64	**461**001	**461**064
462	T1_WLI_Fabric_Tread	301	shell/quad	64	**462**001	**462**064
463	T1_WRI_Sidewalls	106	shell/quad	192	**463**001	**463**192
464	T1_WLI_Sidewalls	106	shell/quad	192	**464**001	**464**192
465	T1_WRI_Tread	106	shell/quad	64	**465**001	**465**064
466	T1_WLI_Tread	106	shell/quad	64	**466**001	**466**064
500	T2_Axle_Rigid_Non_Rotating	204	beam	20	**500**001	**500**020
503	T2_Drums	210	solid/penta	80	**503**001	**503**080
505	T2_WRO_Disc	108	shell/tria	72	**505**001	**505**072
506	T2_WLO_Disc	108	shell/tria	72	**506**001	**506**072
507	T2_WRO_Rim	108	shell/quad	64	**507**001	**507**064
508	T2_WLO_Rim	108	shell/quad	64	**508**001	**508**064
509	T2_WRO_Fabric_Sidewalls	301	shell/quad	192	**509**001	**509**192
510	T2_WLO_Fabric_Sidewalls	301	shell/quad	192	**510**001	**510**192
511	T2_WRO_Fabric_Tread	301	shell/quad	64	**511**001	**511**064
512	T2_WLO_Fabric_Tread	301	shell/quad	64	**512**001	**512**064
513	T2_WRO_Sidewalls	106	shell/quad	192	**513**001	**513**192
514	T2_WLO_Sidewalls	106	shell/quad	192	**514**001	**514**192
515	T2_WRO_Tread	106	shell/quad	64	**515**001	**515**064
516	T2_WLO_Tread	106	shell/quad	64	**516**001	**516**064
521	T2_Torque_Rod	206	beam	8	**521**001	**521**008
522	T2_Equalizer_Beam_Connector	206	beam	8	**522**001	**522**008
555	T2_WRI_Disc	108	shell/tria	72	**555**001	**555**072
556	T2_WLI_Disc	108	shell/tria	72	**556**001	**556**072
557	T2_WRI_Rim	108	shell/quad	64	**557**001	**557**064
558	T2_WLI_Rim	108	shell/quad	64	**558**001	**558**064
559	T2_WRI_Fabric_Sidewalls	301	shell/quad	192	**559**001	**559**192
560	T2_WLI_Fabric_Sidewalls	301	shell/quad	192	**560**001	**560**192
561	T2_WRI_Fabric_Tread	301	shell/quad	64	**561**001	**561**064
562	T2_WLI_Fabric_Tread	301	shell/quad	64	**562**001	**562**064
563	T2_WRI_Sidewalls	106	shell/quad	192	**563**001	**563**192
564	T2_WLI_Sidewalls	106	shell/quad	192	**564**001	**564**192
565	T2_WRI_Tread	106	shell/quad	64	**565**001	**565**064
566	T2_WLI_Tread	106	shell/quad	64	**566**001	**566**064
601	Trailer_Main_Beams_V	105	shell/quad	434	**601**001	**601**434
602	Trailer_Main_Beams_H	105	shell/quad	500	**602**001	**602**500
603	Trailer_Front_Transverse_V	105	shell/quad	62	**603**001	**603**062
604	Trailer_Front_Transverse_H	105	shell/quad	116	**604**001	**604**116
605	Trailer_Middle_Transverse_V	105	shell/quad	50	**605**001	**605**050

Table A.22. Detailed summary of complete FE model of the FDOT Truck (cont.)

Part ID	Part title	Material ID	Element type	Number of elements	Element ID minimum	Element ID maximum
606	Trailer_Middle_Transverse_H	105	shell/quad	200	**606**001	**606**200
607	Trailer_Longitudinal_V	105	shell/quad	144	**607**001	**607**144
608	Trailer_Longitudinal_H	105	shell/quad	192	**608**001	**608**192
609	Trailer_Back_Transverse_V	105	shell/quad	56	**609**001	**609**056
610	Trailer_Back_Transverse_H	105	shell/quad	192	**610**001	**610**192
611	Trailer_Main_Transverse	105	shell/quad	168	**611**001	**611**168
612	Trailer_Suspension_Support	206	shell/quad	274	**612**001	**612**274
613	Trailer_Suspension_Connectors	206	beam	24	**613**001	**613**024
614	Trailer_Equalizer_Beam_R	206	beam	12	**614**001	**614**012
615	Trailer_Equalizer_Beam_L	206	beam	12	**615**001	**615**012
618	Trailer_Axle_Discrete_Springs	12	discrete	8	**618**001	**618**008
619	Trailer_Axle_Discrete_Dampers	22	discrete	4	**619**001	**619**004
620	Trailer_Beam_Discrete_Springs	13	discrete	8	**620**001	**620**008
621	Trailer_Beam_Discrete_Dampers	23	discrete	4	**621**001	**621**004
622	Trailer_Front_Plate	105	shell/quad	96	**622**001	**622**096
623	Trailer_Load_Deck	206	shell/quad	140	**623**001	**623**140
624	Trailer_Concrete_Blocks	207	solid/hexa	336	**624**001	**624**336
625	Trailer_Block_Columns	206	beam	4	**625**001	**625**004
701	Tractor_Frame_Longitudinal_23	105	shell/quad	194	**701**001	**701**194
702	Tractor_Frame_Longitudinal_16	105	shell/quad	176	**702**001	**702**176
703	Tractor_Frame_Transverse_Front	105	shell/quad	26	**703**001	**703**026
704	Tractor_Frame_Transverse_Middle	105	shell/quad	4	**704**001	**704**004
705	Tractor_Frame_Transverse_Rear	105	shell/quad	28	**705**001	**705**028
706	Tractor_Frame_Plate_Rear	105	shell/quad	36	**706**001	**706**036
707	Tractor_Frame_Transverse_Back	105	shell/quad	14	**707**001	**707**014
710	Tractor_Rubber_Pad_Plates	105	shell/quad	32	**710**001	**710**032
711	Tractor_Rubber_Pads	601	solid/hexa	20	**711**001	**711**020
712	Tractor_Suspension_Support	105	shell/quad	108	**712**001	**712**108
713	Tractor_Suspension_Connectors	206	beam	20	**713**001	**713**020
714	Tractor_Equalizer_Beam_R	206	beam	12	**714**001	**714**012
715	Tractor_Equalizer_Beam_L	206	beam	12	**715**001	**715**012
718	Tractor_Axle_Discrete_Springs	14	discrete	8	**718**001	**718**008
719	Tractor_Axle_Discrete_Dampers	24	discrete	4	**719**001	**719**004
720	Tractor_Beam_Discrete_Springs	15	discrete	8	**720**001	**720**008
721	Tractor_Beam_Discrete_Dampers	25	discrete	4	**721**001	**721**004
722	Tractor_Cylindrical_Joints	206	beam	8	**722**001	**722**008
723	Tractor_Cylindrical_Joints_Frame	206	beam	4	**723**001	**723**004
730	Tractor_Front_Bumper	206	shell/quad	142	**730**001	**730**142
731	Tractor_Driver_Cab	206	shell	500	**731**001	**731**500
733	Tractor_Driver_Cab_Window	206	shell	258	**733**001	**733**258
734	Tractor_Engine	205	solid/hexa	144	**734**001	**734**144
735	Tractor_5th_Wheel_Support	206	solid/hexa	12	**735**001	**735**012
736	Tractor_5th_Wheel	206	solid/hexa	30	**736**001	**736**030
737	Tractor_Torque_Rod_Support	206	shell/quad	13	**737**001	**737**013

Six different types of material models were applied in the FE model of the FDOT truck, as presented in Table A.23. Detailed properties of each used material model were provided in Table A.24 through Table A.29. The data were presented in accordance with the values declared in the appropriate cards in the LS-DYNA code.

Table A.23. Material models used in the FE model of the FDOT truck (LS-DYNA Keyword User's Manual, 2007)

Material number	Material designation in LS-DYNA code	Material model description	Material IDs in FE model (number)
*MAT_001	*MAT_ELASTIC	Isotropic elastic material	101, 105–108 (5)
*MAT_020	*MAT_RIGID	Rigid material (part made from this material are considered to belong to a rigid body)	201, 202 204 to 210 (9)
*MAT_006	*MAT_VISCOELASTIC	Viscoelastic material	601 (1)
*MAT_034	*MAT_FABRIC	Fabric material (stiffness for tension only)	301 (1)
*MAT_S01	*MAT_SPRING_ELASTIC	Linear material for discrete springs	12 to 15 (4)
*MAT_S02	*MAT_DAMPER_VISCOUS	Linear material for discrete dampers	21 to 25 (5)

Table A.24. Properties of the elastic material models used in the FE model of the FDOT truck

Material ID	Material title in FE model	RO (Mg/mm^3)	E (MPa)	PR (–)	Number of referenced parts
101	Elastic_Steel_Spring	$7.850 \cdot 10^{-9}$	$2.100 \cdot 10^{5}$	0.30	1
105	Elastic_Steel	$7.850 \cdot 10^{-9}$	$2.100 \cdot 10^{5}$	0.30	21
106	Elastic_Rubber	$1.174 \cdot 10^{-9}$	$1.000 \cdot 10^{2}$	0.45	36
107	Elastic_Tractor_Wheels	• $4.420 \cdot 10^{-9}$	$2.100 \cdot 10^{5}$	0.30	20
108	Elastic_Trailer_Wheels	• $5.170 \cdot 10^{-8}$	$2.100 \cdot 10^{5}$	0.30	16

where:
RO — mass density, ρ
E — Young's modulus, E
PR — Poisson's Ratio, ν
• — density recalculated to obtain appropriate calculated mass of the FE model

Table A.25. Properties of the rigid material models used in the FE model of the Terex crane

Material ID	Material title in FE model	RO (Mg/mm^3)	E (MPa)	PR (–)	Number of referenced parts
201	Rigid_F_Axle_Non_Rotating	• $3.103 \cdot 10^{-8}$	$2.100 \cdot 10^{5}$	0.30	1
202	Rigid_R_Axles_Non_Rotating	• $5.473 \cdot 10^{-8}$	$2.100 \cdot 10^{5}$	0.30	2
204	Rigid_T_Axles_Non_Rotating	• $2.317 \cdot 10^{-8}$	$2.100 \cdot 10^{5}$	0.30	2
205	Rigid_Engine	• $1.963 \cdot 10^{-9}$	$3.020 \cdot 10^{5}$	0.20	1
206	Rigid_Steel_General	$7.850 \cdot 10^{-9}$	$2.100 \cdot 10^{5}$	0.30	30
207	Rigid_Concrete	$2.585 \cdot 10^{-9}$	$3.750 \cdot 10^{4}$	0.22	1
208	Rigid_F_Drums	• $2.042 \cdot 10^{-9}$	$2.100 \cdot 10^{5}$	0.30	1
209	Rigid_R_Drums	• $2.441 \cdot 10^{-9}$	$2.100 \cdot 10^{5}$	0.30	2
210	Rigid_T_Drums	• $2.603 \cdot 10^{-9}$	$2.100 \cdot 10^{5}$	0.30	2

where:
RO — mass density, ρ
E — Young's modulus, E
PR — Poisson's Ratio, ν
• — density recalculated to obtain appropriate calculated mass of the Terex crane

Table A.26. Properties of the fabric material model used in the FE model of the tractor trailer

Material ID	Material title in FE model	RO (Mg/mm^3)	EA (MPa)	PRBA (–)	Number of referenced parts
301	Fabric	$1.000 \cdot 10^{-9}$	$2.100 \cdot 10^{5}$	0.30	36

where:
RO — mass density, ρ
EA — Young's modulus in longitudinal direction, E_A
PRBA — Poisson's Ratio in *BA* direction, ν_{BA}

Comments
Young's modulus in transverse E_B and normal E_C direction equals zero.
Poisson's ratio in *CA* and *CB* direction equals zero.

Table A.27. Properties of the viscoelastic material model used in the FE model of the bridge

Material ID	Material title in FE model	RO (Mg/mm^3)	BULK (MPa)	G0 (MPa)	G1 (MPa)	BETA (–)	Number of referenced parts
3601	Viscoelastic_Neoprene	$1.250 \cdot 10^{-9}$	26.67	1.0	0.8	1	1

where:
RO — mass density, ρ
BULK — elastic bulk modulus, K
G0 — short-time shear modulus, G_0
G1 — long-time (infinite) shear modulus, G_∞
BETA — decay constant, β

Table A.28. Properties of the spring elastic material models used in the FE model of the Terex crane

Material ID	Material title in FE model	K (N/mm)	Number of referenced parts
12	Trailer_Axle_Springs	10	1
13	Trailer_Beam_Springs	10	1
14	Tractor_Axle_Springs	10	1
15	Tractor_Beam_Springs	10	1

where:
K — elastic stiffness, k

Table A.29. Properties of the damper viscous material models used in the FE model of the Terex crane

Material ID	Material title in FE model	DC (N·s/mm)	Number of referenced parts
21	Front_Dampers	50	1
22	Trailer_Axle_Dampers	5	1
23	Trailer_Beam_Dampers	5	1
24	Tractor_Axle_Dampers	5	1
25	Tractor_Beam_Dampers	5	1

where:
DC — damping constant, c

Appendix B

COMPLETE RESULTS OF THE EXPERIMENTAL SUSPENSION TESTS FOR SELECTED VEHICLES

TABLE OF CONTENTS

B. COMPLETE RESULTS OF THE EXPERIMENTAL SUSPENSION TESTS FOR SELECTED VEHICLES

B.1. Suspension Tests of the Unloaded Tractor-Trailer

Suspension tests of the unloaded tractor-trailer included nine runs with three different velocities – 16, 24 and 32 km/h (10, 15, and 20 mph), as provided in Table B.1. Three runs were conducted for each speed to check the validity of obtained results. Complete results for each vehicle velocity of are presented in following parts. Time histories of accelerations and the changes in distance were limited to five-second periods – one second before the speed bump and four seconds after it for each suspension system. Positive direction of the acceleration is up – according to Z-axis of the global coordinate for the FE model.

Results of the suspension tests in the form of time histories are presented in Figure B.1 through Figure B.21 – for the velocity of 16 km/h (10 mph); Figure B.22 through Figure B.42 – for the velocity of 24 km/h (15 mph); and Figure B.43 through Figure B.63 – for the velocity of 32 km/h (20 mph). In some cases, the results are not complete due to signal failures or a damage of the gauge.

Table B.1. Summary of all considered cases for the suspension tests of the unloaded tractor-trailer

Run #	Pass #	Velocity	Vehicle configuration
01	1	16 km/h (10 mph)	unloaded
02	2		
03	3		
04	1	24 km/h (15 mph)	unloaded
05	2		
06	3		
07	1	32 km/h (20 mph)	unloaded
08	2		
09	3		

Velocity of 16 km/h (10 mph)

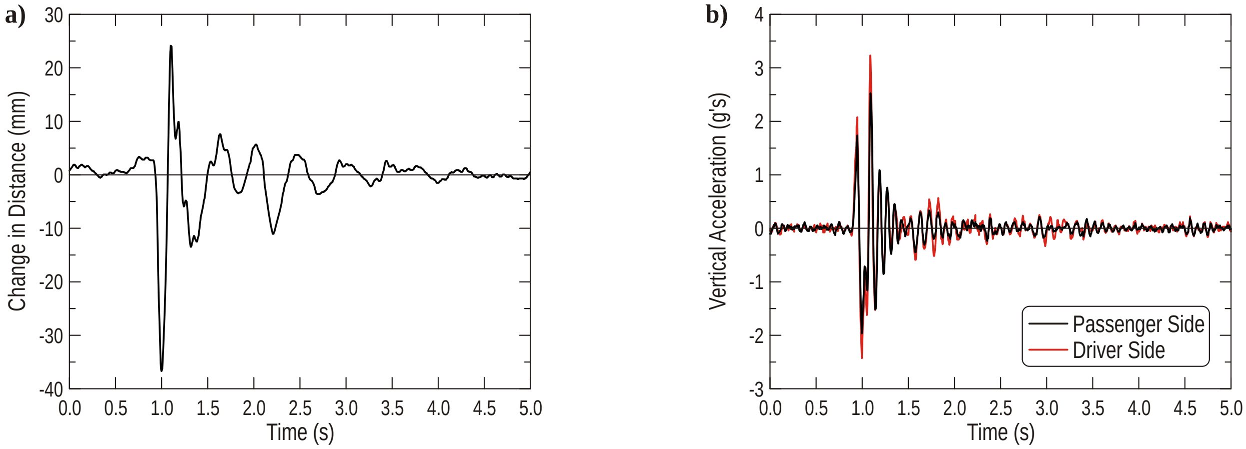

Figure B.1. Time histories for the front axle – velocity of 16 km/h (10 mph), run #01: a) change in distance, b) vertical acceleration

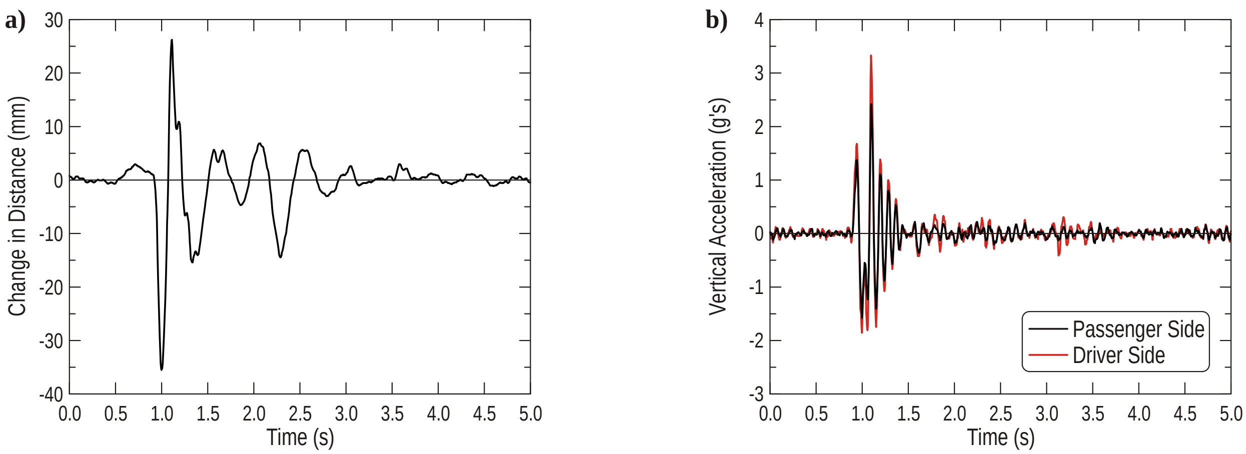

Figure B.2. Time histories for the front axle – velocity of 16 km/h (10 mph), run #02: a) change in distance, b) vertical acceleration

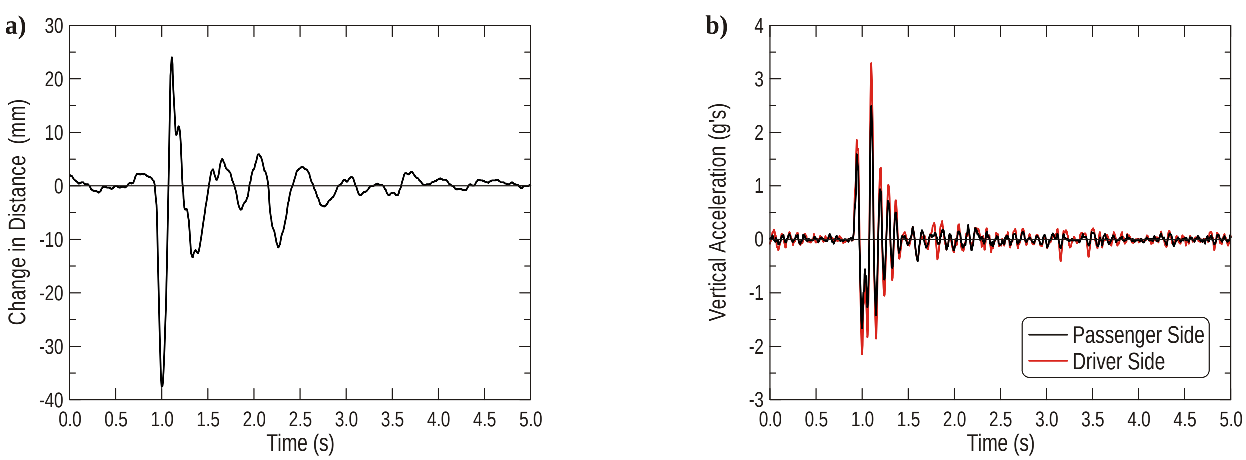

Figure B.3. Time histories for the front axle – velocity of 16 km/h (10 mph), run #03: a) change in distance, b) vertical acceleration

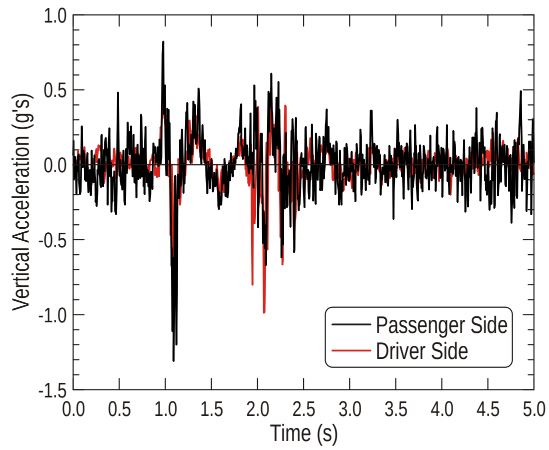

Figure B.4. Time history of vertical acceleration for points located on the frame above the front axle – velocity of 16 km/h (10 mph), run #01

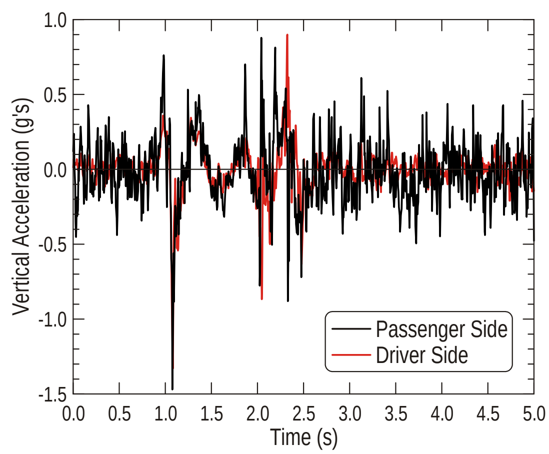

Figure B.5. Time history of vertical acceleration for points located on the frame above the front axle – velocity of 16 km/h (10 mph), run #02

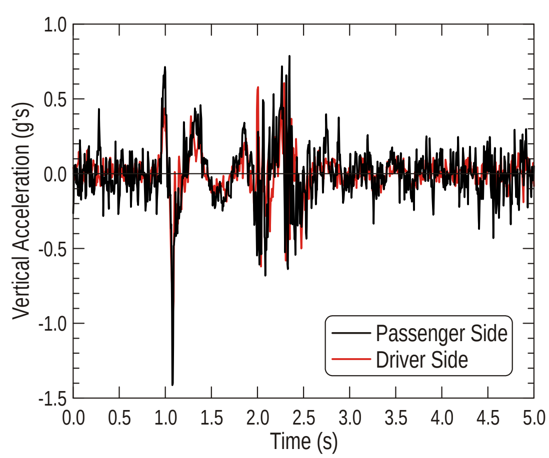

Figure B.6. Time history of vertical acceleration for points located on the frame above the front axle – velocity of 16 km/h (10 mph), run #03

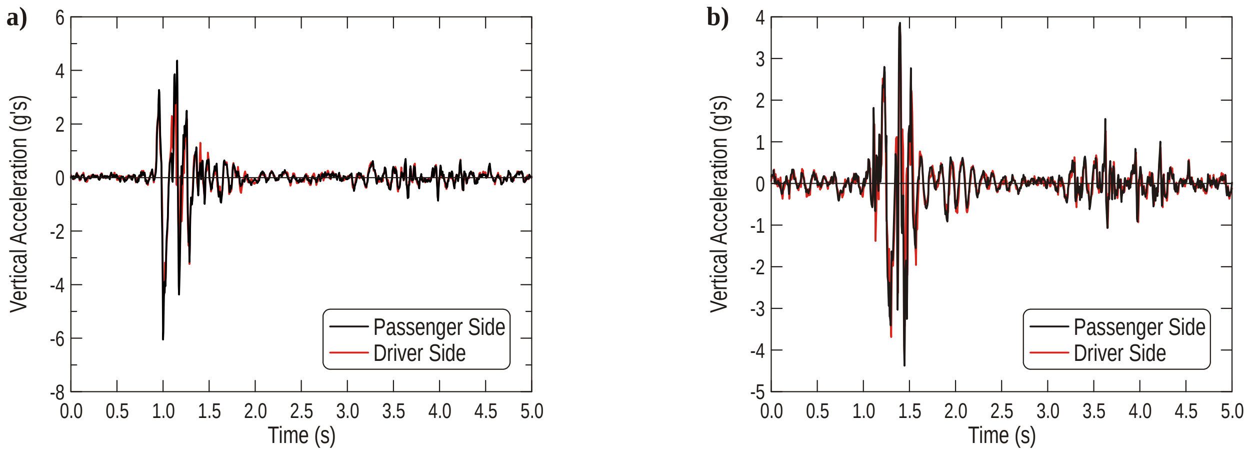

Figure B.7. Time histories of vertical acceleration for the rear tandem axles – velocity of 16 km/h (10 mph), run #01: a) forward axle, b) rear axle

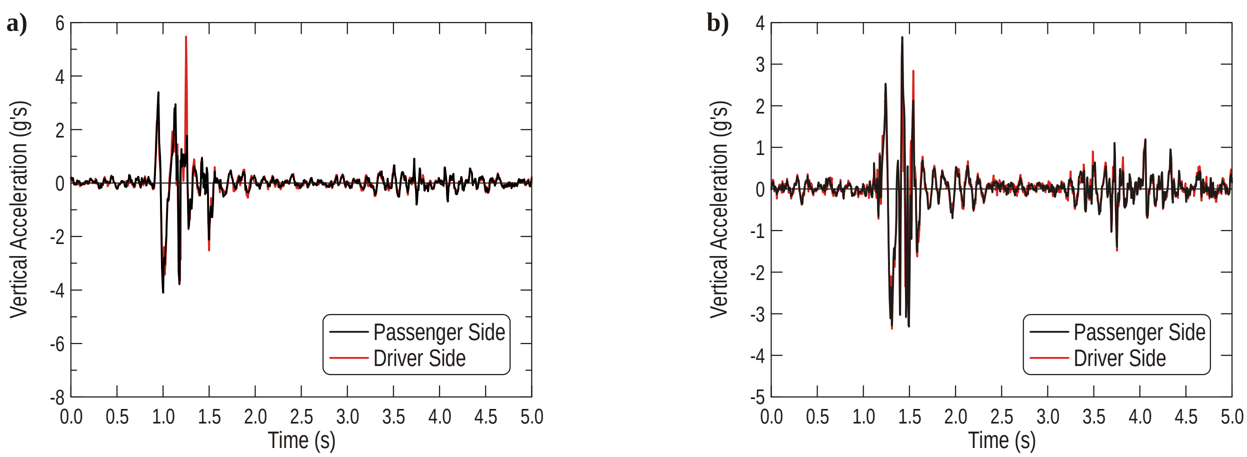

Figure B.8. Time histories of vertical acceleration for the rear tandem axles – velocity of 16 km/h (10 mph), run #02: a) forward axle, b) rear axle

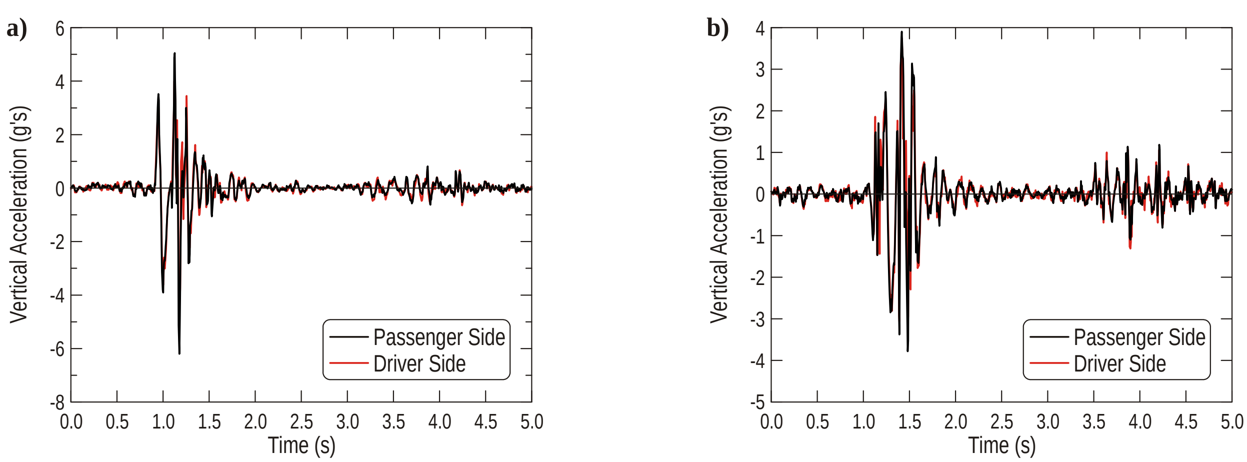

Figure B.9. Time histories of vertical acceleration for the rear tandem axles – velocity of 16 km/h (10 mph), run #03: a) forward axle, b) rear axle

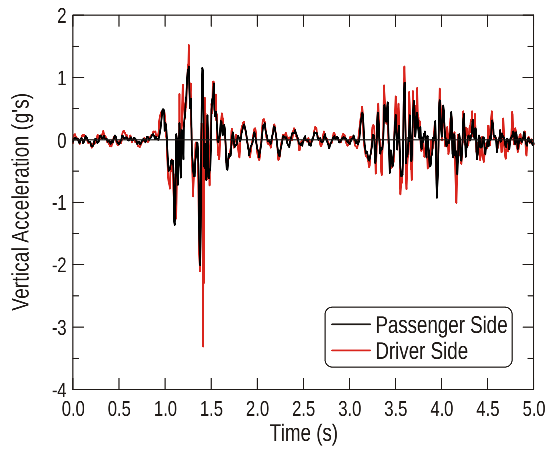

Figure B.10. Time histories of vertical acceleration for points located on the frame above the rear tandem axles – velocity of 16 km/h (10 mph), run #01

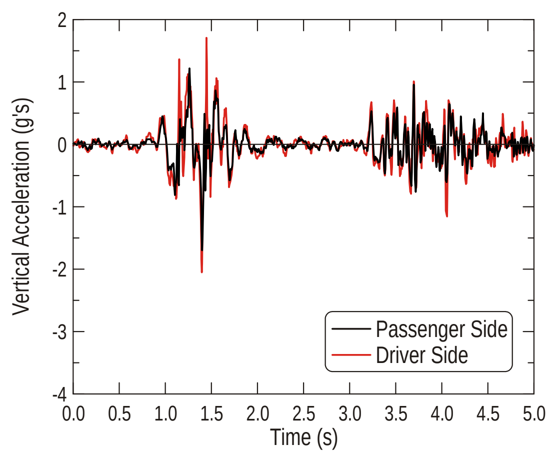

Figure B.11. Time histories of vertical acceleration for points located on the frame above the rear tandem axles – velocity of 16 km/h (10 mph), run #02

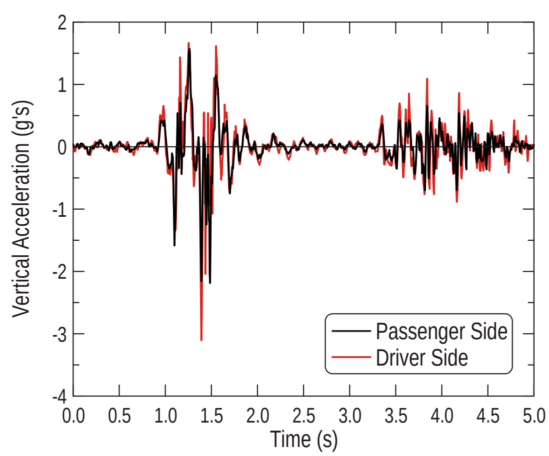

Figure B.12. Time histories of vertical acceleration for points located on the frame above the rear tandem axles – velocity of 16 km/h (10 mph), run #03

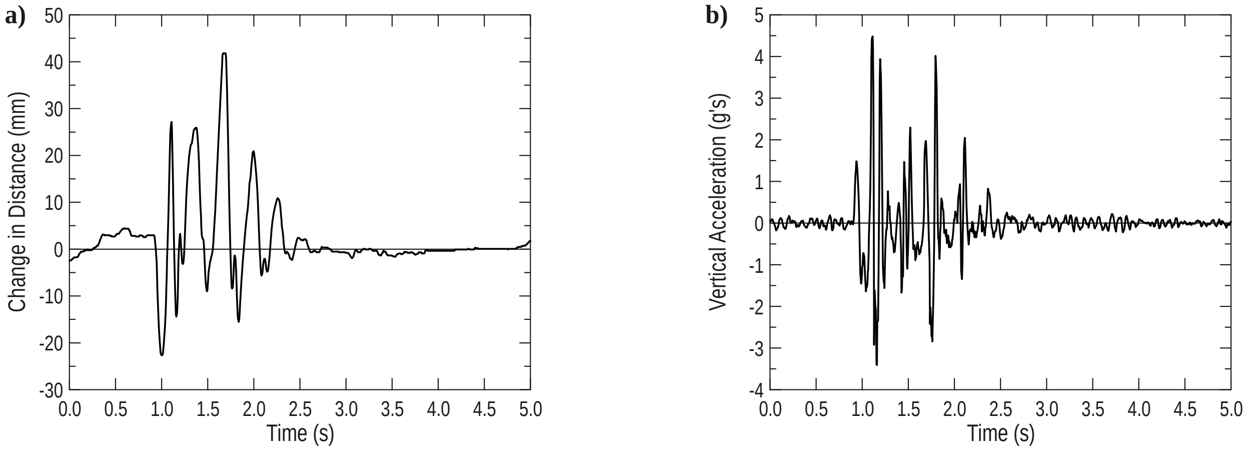

Figure B.13. Time histories for the first trailer axle – velocity of 16 km/h (10 mph), run #01: a) change in distance, b) vertical acceleration

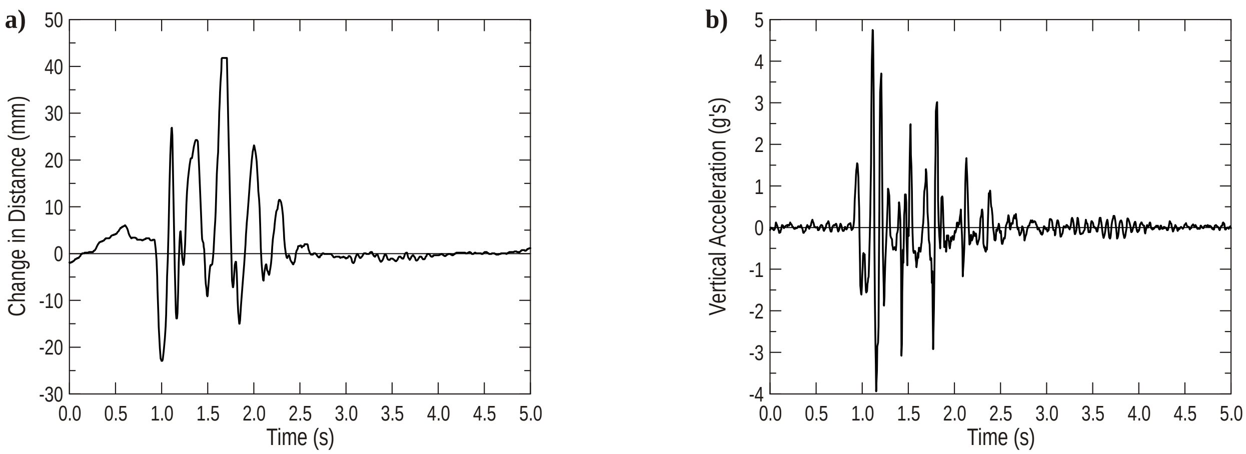

Figure B.14. Time histories for the first trailer axle – velocity of 16 km/h (10 mph), run #02: a) change in distance, b) vertical acceleration

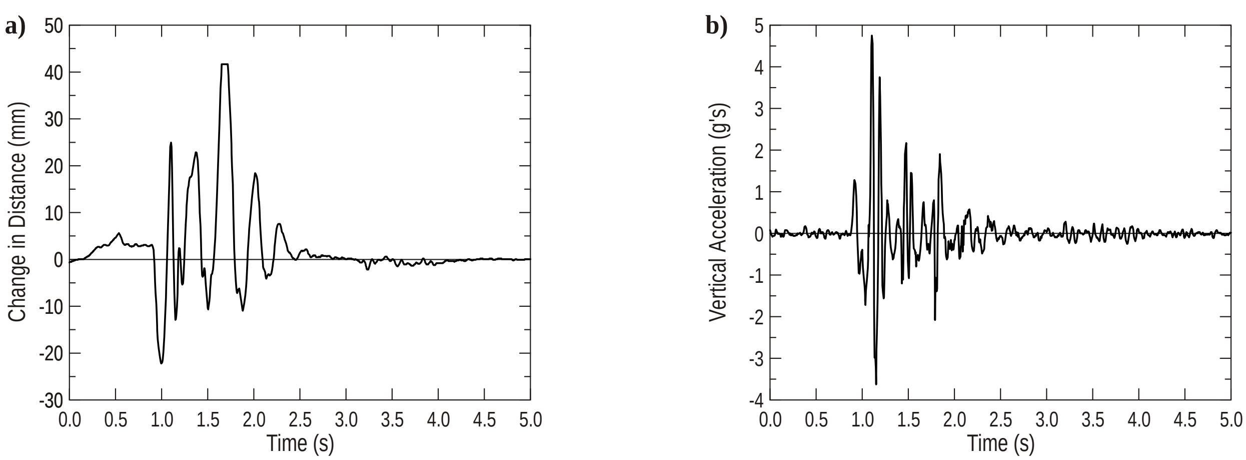

Figure B.15. Time histories for the first trailer axle – velocity of 16 km/h (10 mph), run #03: a) change in distance, b) vertical acceleration

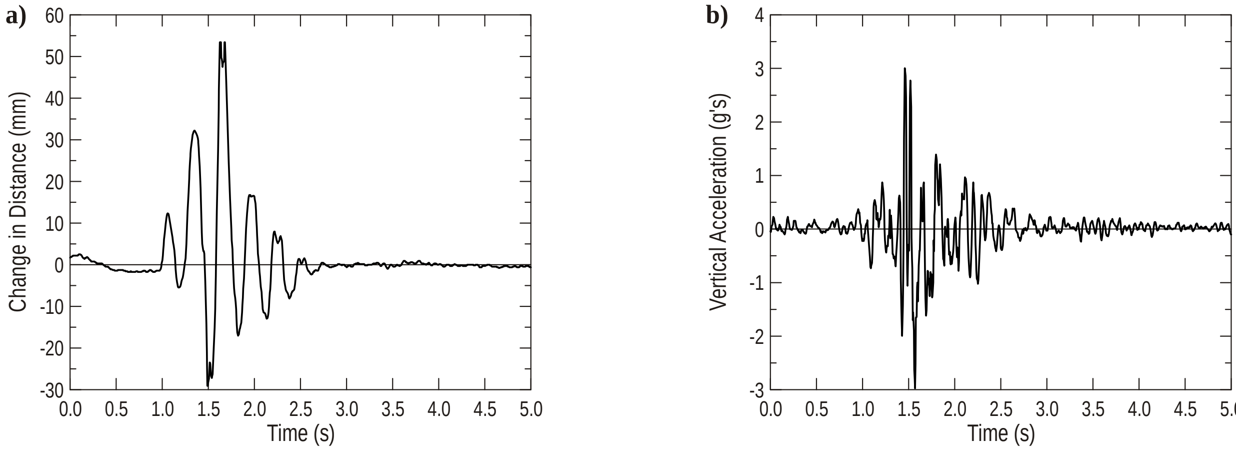

Figure B.16. Time histories for the third trailer axle – velocity of 16 km/h (10 mph), run #01: a) change in distance, b) vertical acceleration

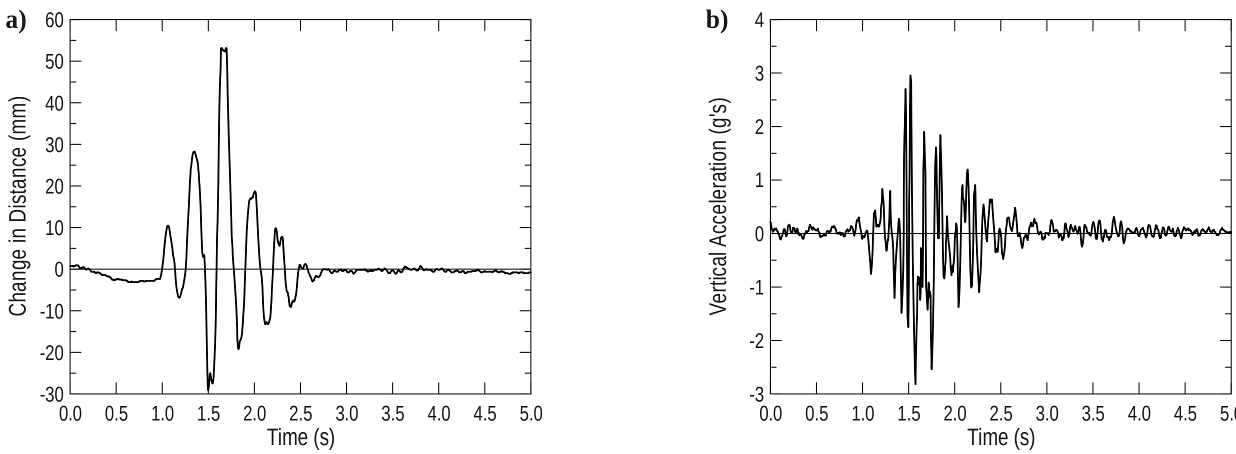

Figure B.17. Time histories for the third trailer axle – velocity of 16 km/h (10 mph), run #02: a) change in distance, b) vertical acceleration

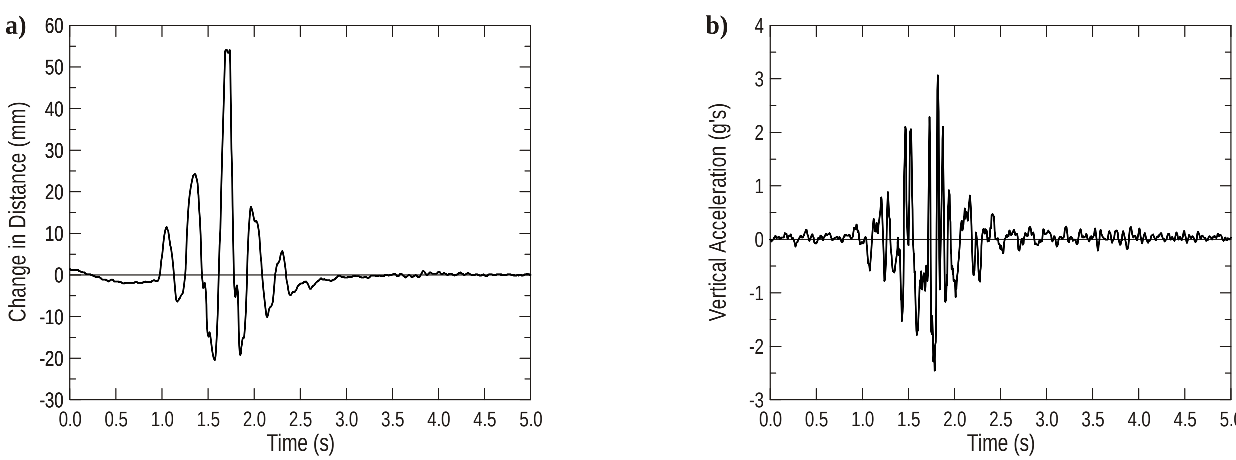

Figure B.18. Time histories for the third trailer axle – velocity of 16 km/h (10 mph), run #03: a) change in distance, b) vertical acceleration

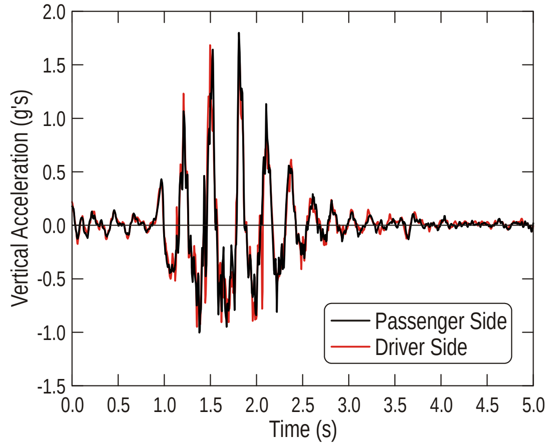

Figure B.19. Time histories of vertical acceleration for points located on the trailer deck above the first trailer axle – velocity of 16 km/h (10 mph), run #01

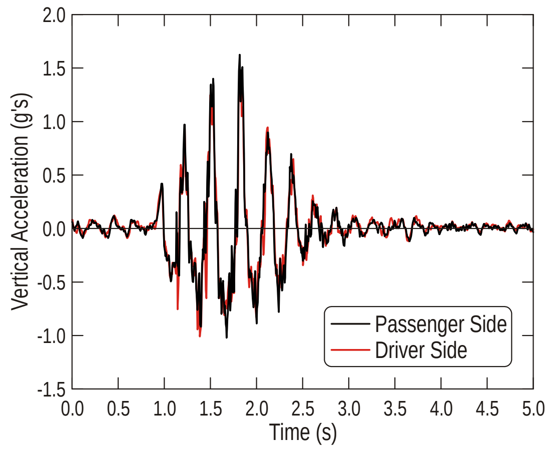

Figure B.20. Time histories of vertical acceleration for points located on the trailer deck above the first trailer axle – velocity of 16 km/h (10 mph), run #02

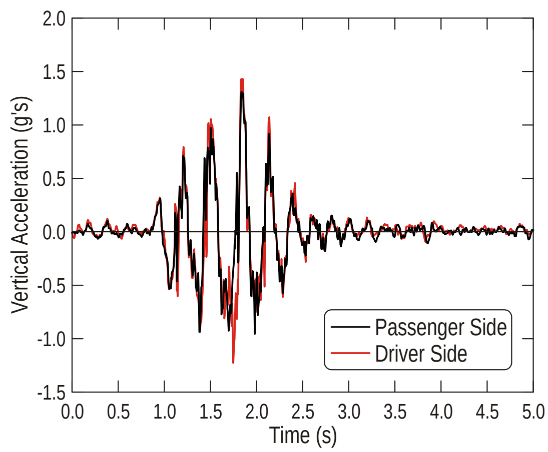

Figure B.21. Time histories of vertical acceleration for points located on the trailer deck above the first trailer axle – velocity of 16 km/h (10 mph), run #03

Velocity of 24 km/h (15 mph)

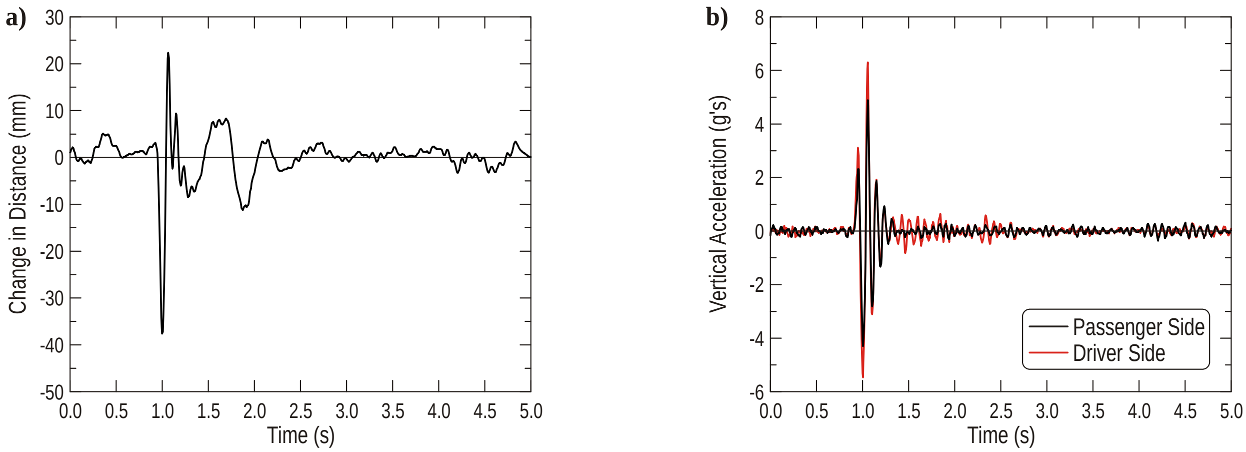

Figure B.22. Time histories for the front axle – velocity of 24 km/h (15 mph), run #04: a) change in distance, b) vertical acceleration

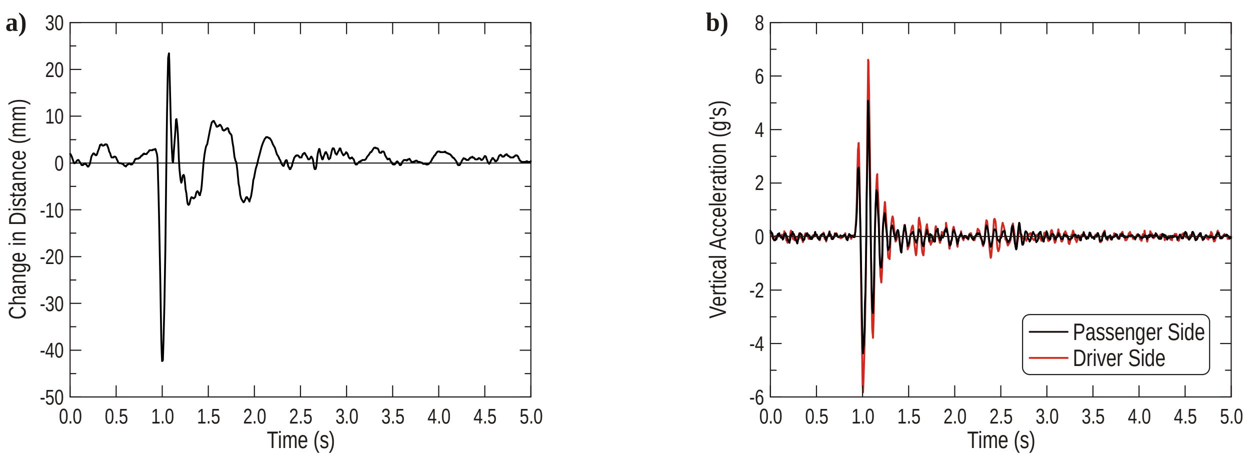

Figure B.23. Time histories for the front axle – velocity of 24 km/h (15 mph), run #05: a) change in distance, b) vertical acceleration

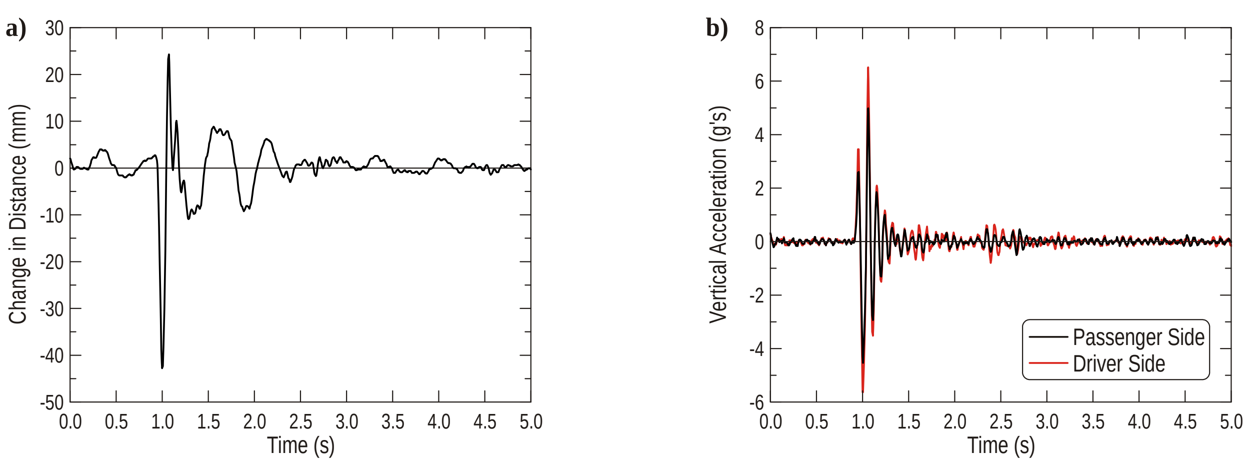

Figure B.24. Time histories for the front axle – velocity of 24 km/h (15 mph), run #06: a) change in distance, b) vertical acceleration

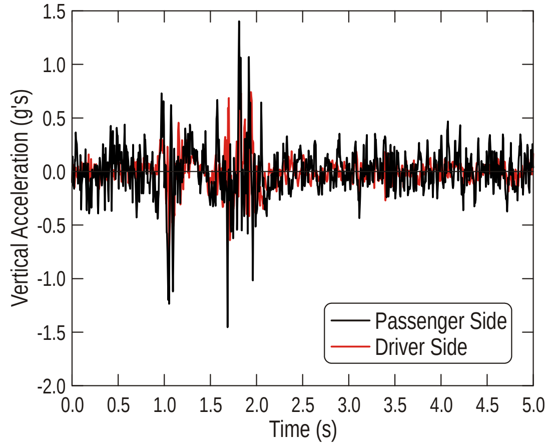

Figure B.25. Time history of vertical acceleration for points located on the frame above the front axle – velocity of 24 km/h (15 mph), run #04

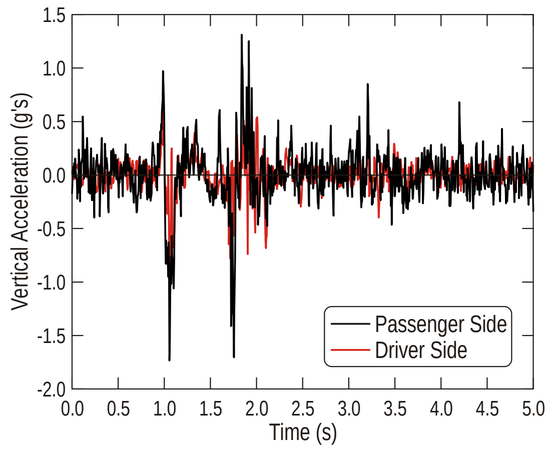

Figure B.26. Time history of vertical acceleration for points located on the frame above the front axle – velocity of 24 km/h (15 mph), run #05

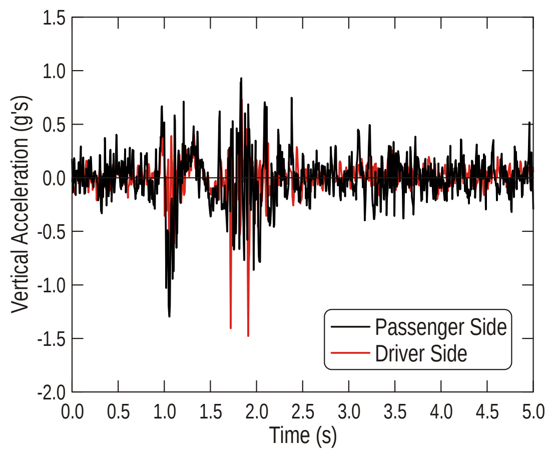

Figure B.27. Time history of vertical acceleration for points located on the frame above the front axle – velocity of 24 km/h (15 mph), run #06

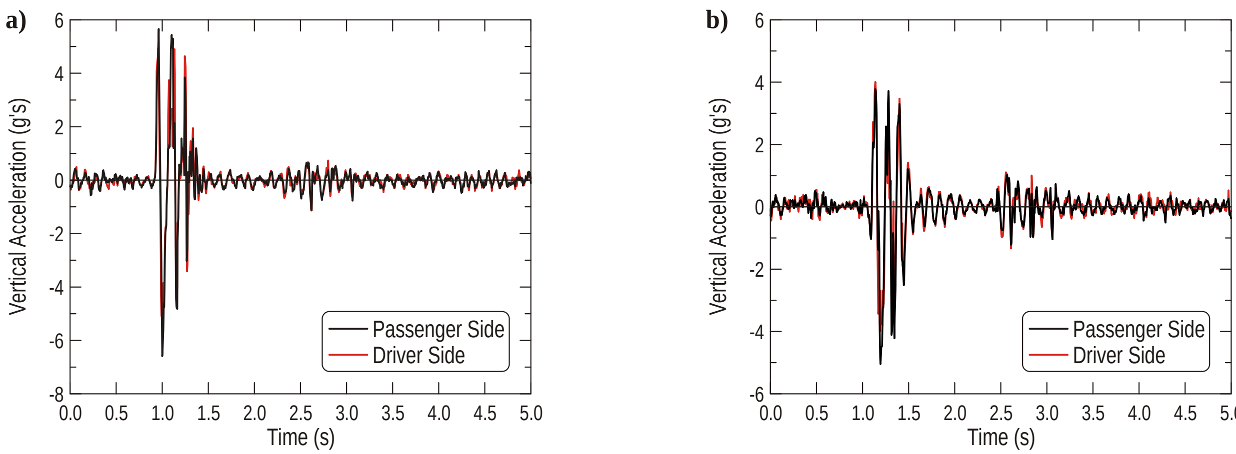

Figure B.28. Time histories of vertical acceleration for the rear tandem axles – velocity of 24 km/h (15 mph), run #04: a) forward axle, b) rear axle

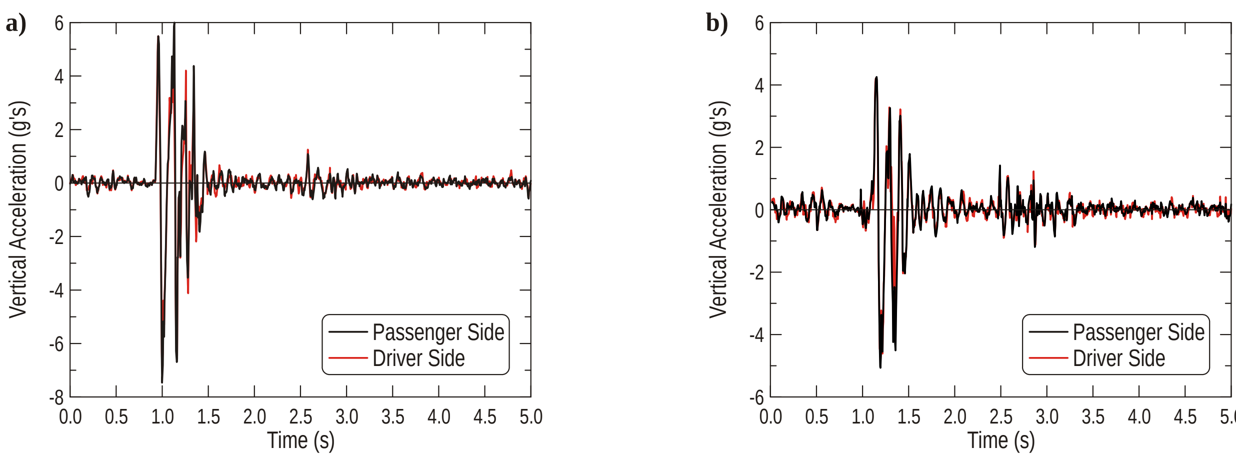

Figure B.29. Time histories of vertical acceleration for the rear tandem axles – velocity of 24 km/h (15 mph), run #05: a) forward axle, b) rear axle

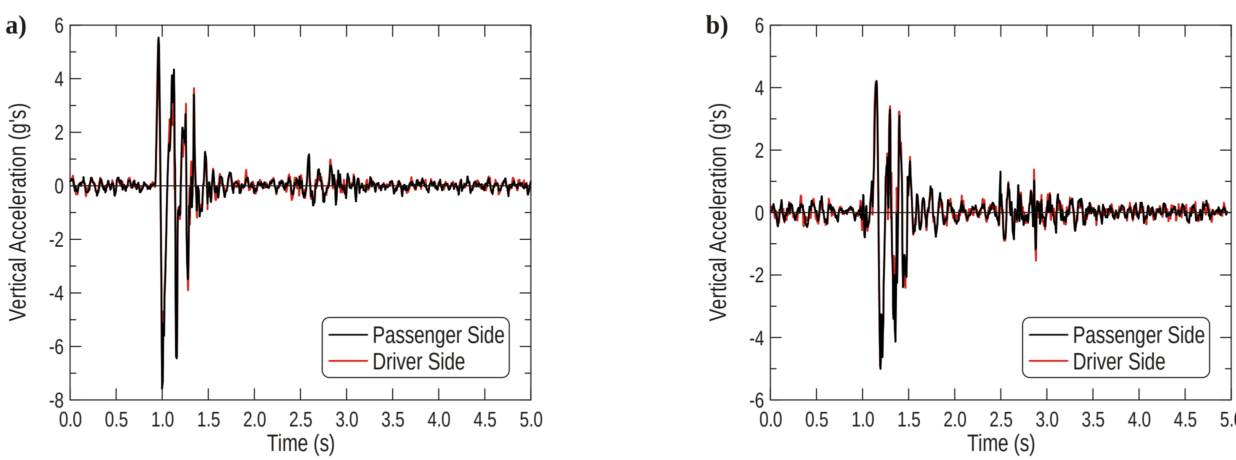

Figure B.30. Time histories of vertical acceleration for the rear tandem axles – velocity of 24 km/h (15 mph), run #06: a) forward axle, b) rear axle

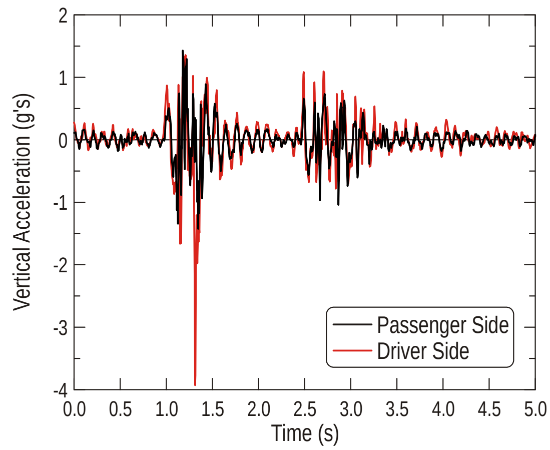

Figure B.31. Time histories of vertical acceleration for points located on the frame above the rear tandem axles – velocity of 24 km/h (15 mph), run #04

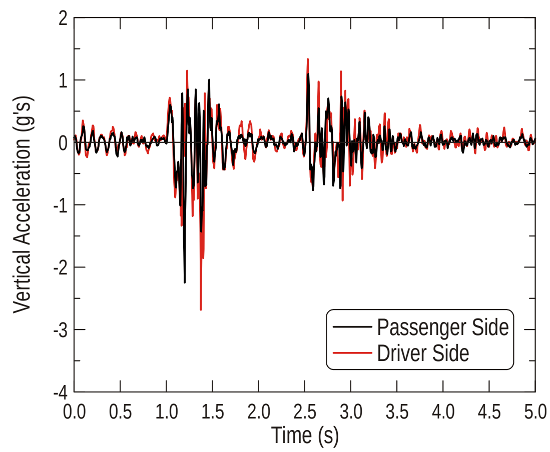

Figure B.32. Time histories of vertical acceleration for points located on the frame above the rear tandem axles – velocity of 24 km/h (15 mph), run #05

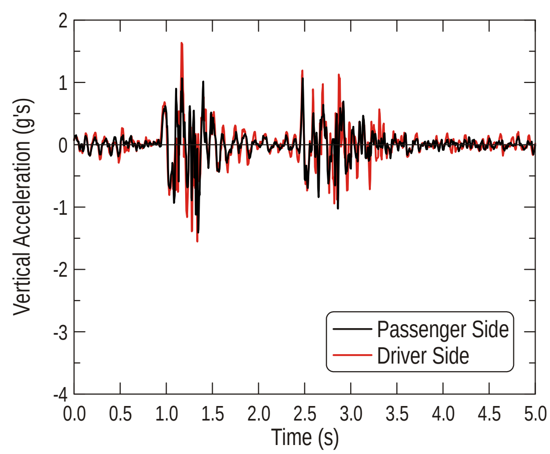

Figure B.33. Time histories of vertical acceleration for points located on the frame above the rear tandem axles – velocity of 24 km/h (15 mph), run #06

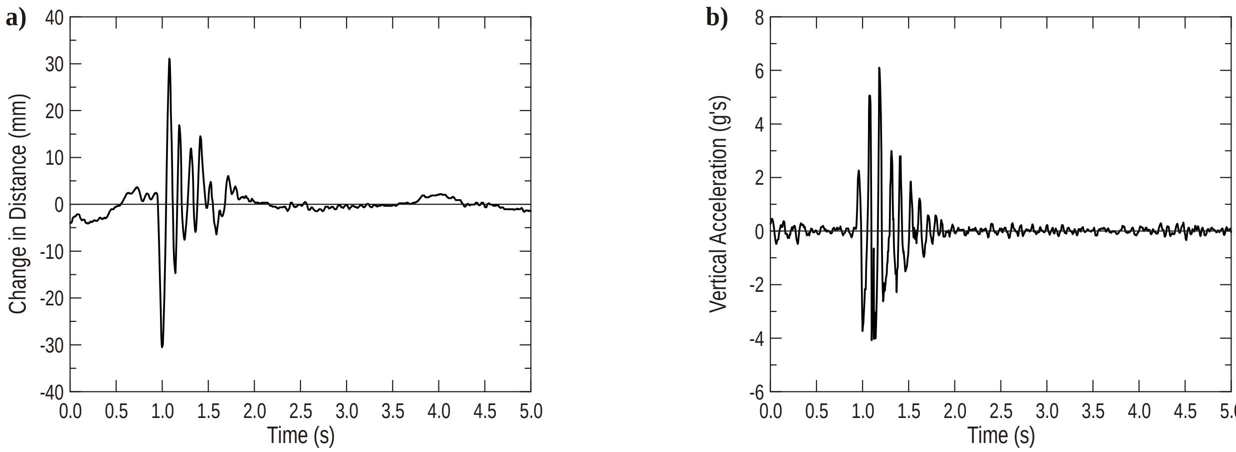

Figure B.34. Time histories for the first trailer axle – velocity of 24 km/h (15 mph), run #04: a) change in distance, b) vertical acceleration

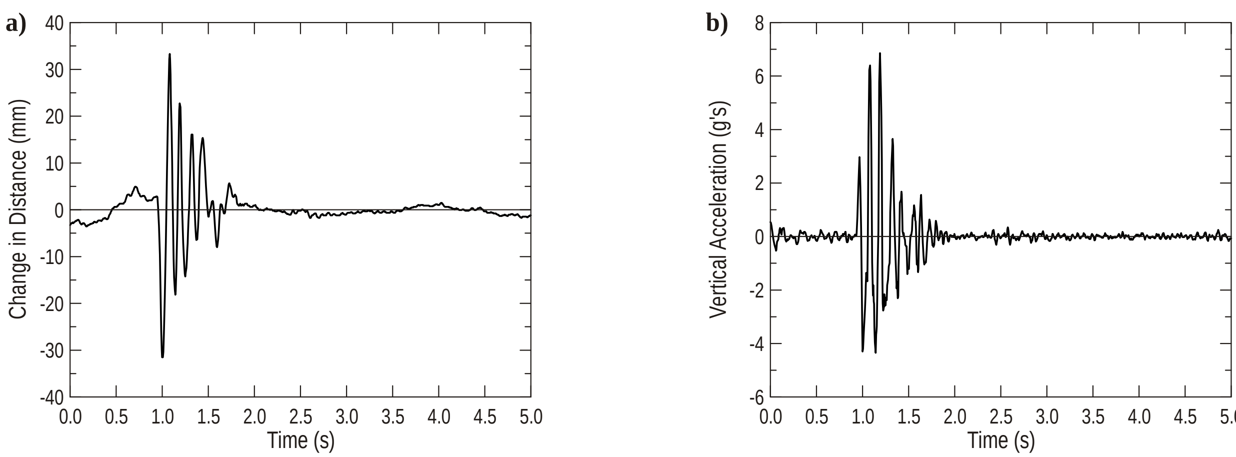

Figure B.35. Time histories for the first trailer axle – velocity of 24 km/h (15 mph), run #05: a) change in distance, b) vertical acceleration

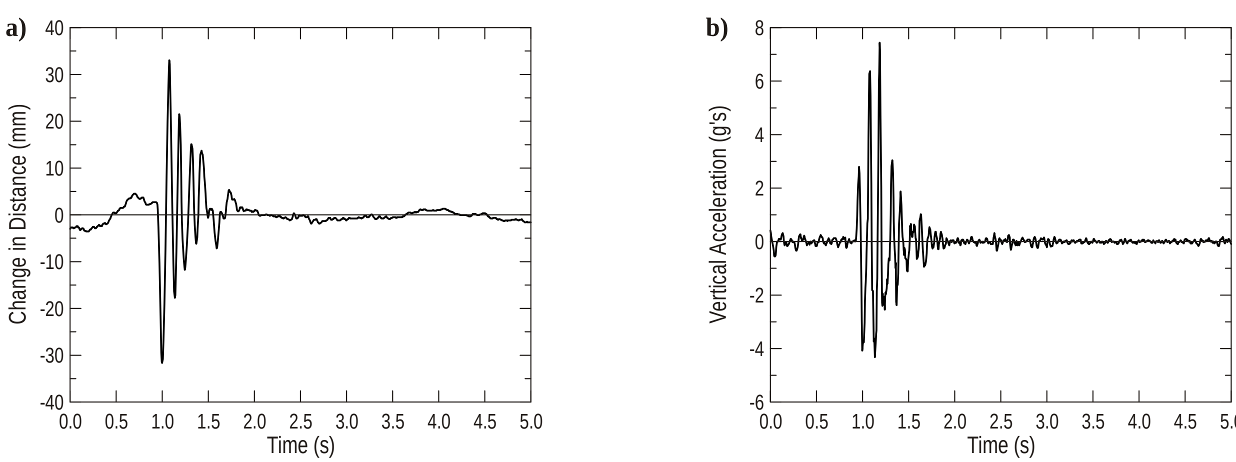

Figure B.36. Time histories for the first trailer axle – velocity of 24 km/h (15 mph), run #06: a) change in distance, b) vertical acceleration

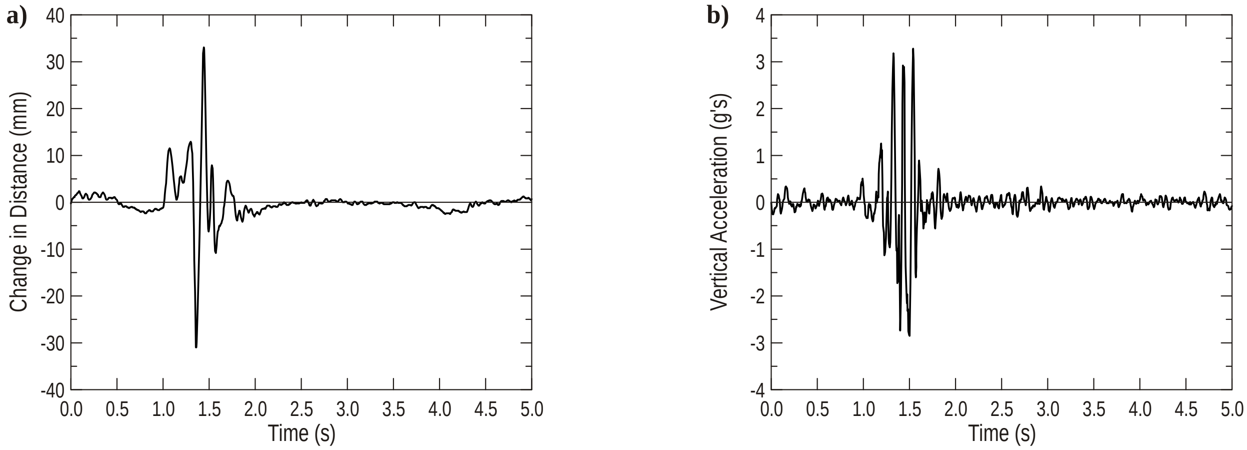

Figure B.37. Time histories for the third trailer axle – velocity of 24 km/h (15 mph), run #04: a) change in distance, b) vertical acceleration

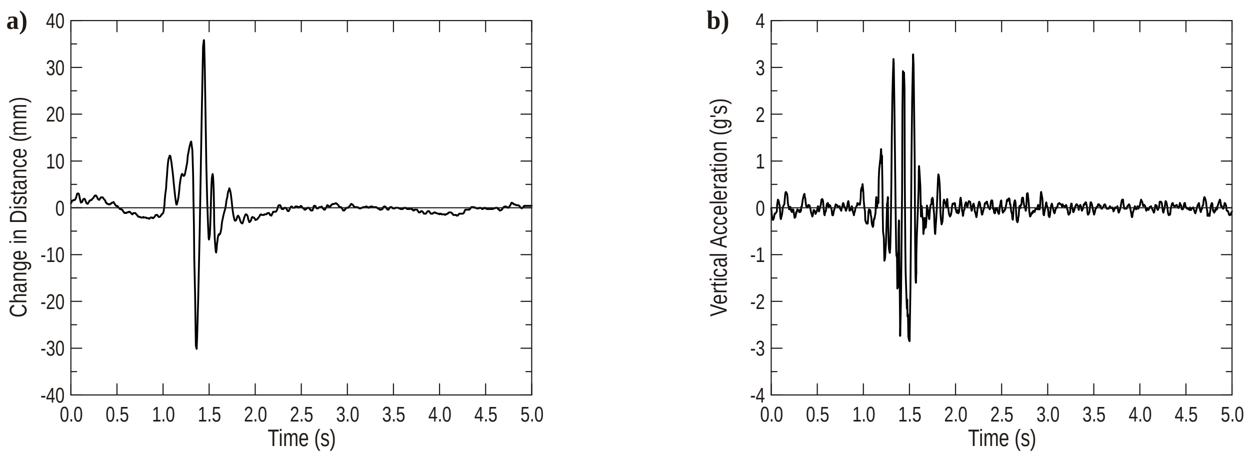

Figure B.38. Time histories for the third trailer axle – velocity of 24 km/h (15 mph), run #05: a) change in distance, b) vertical acceleration

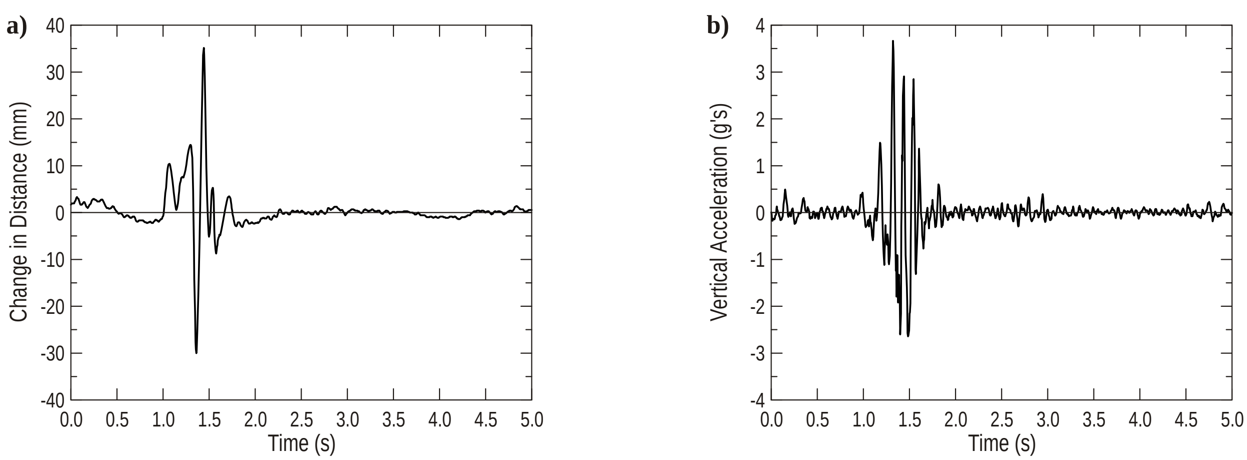

Figure B.39. Time histories for the third trailer axle – velocity of 24 km/h (15 mph), run #06: a) change in distance, b) vertical acceleration

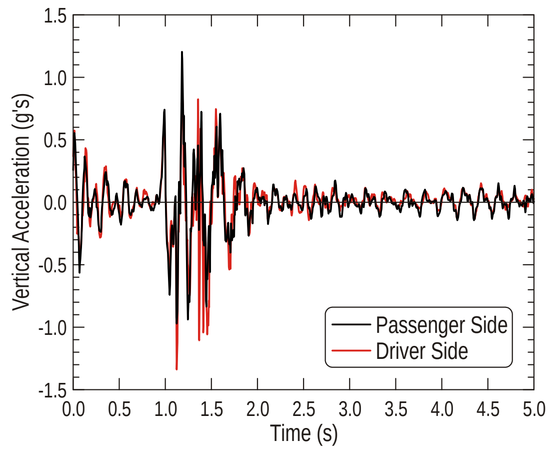

Figure B.40. Time histories of vertical acceleration for points located on the trailer deck above the first trailer axle – velocity of 24 km/h (15 mph), run #04

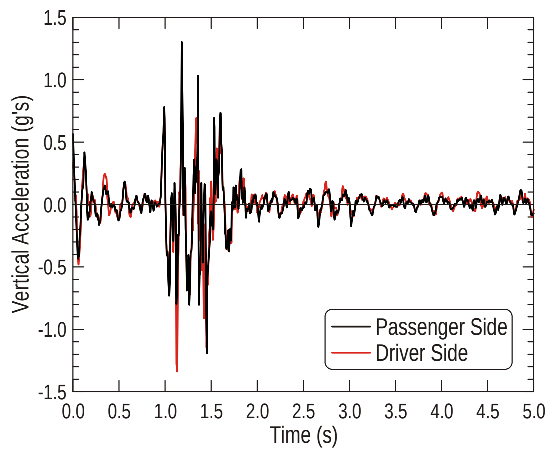

Figure B.41. Time histories of vertical acceleration for points located on the trailer deck above the first trailer axle – velocity of 24 km/h (15 mph), run #05

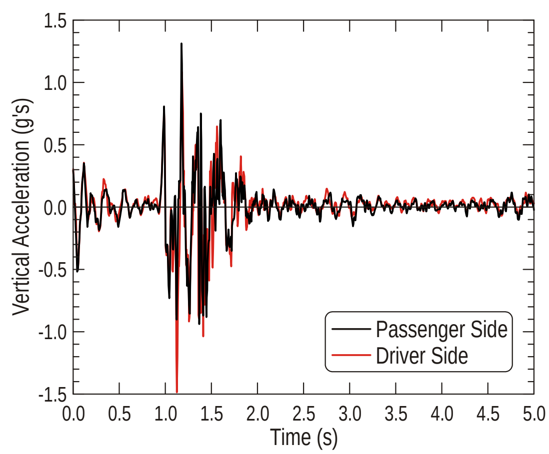

Figure B.42. Time histories of vertical acceleration for points located on the trailer deck above the first trailer axle – velocity of 24 km/h (15 mph), run #06

Velocity of 32 km/h (20 mph)

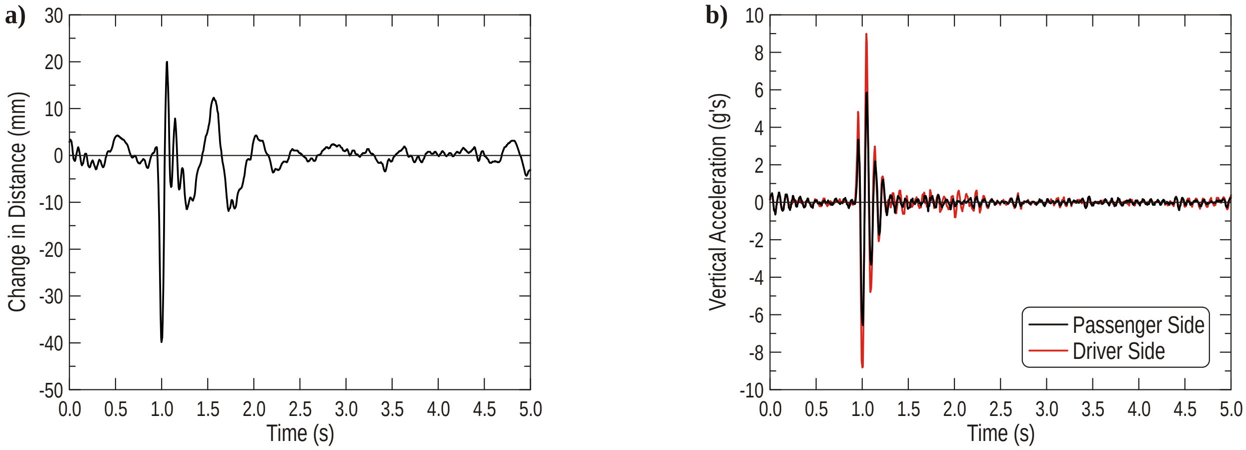

Figure B.43. Time histories for the front axle – velocity of 32 km/h (20 mph), run #07: a) change in distance, b) vertical acceleration

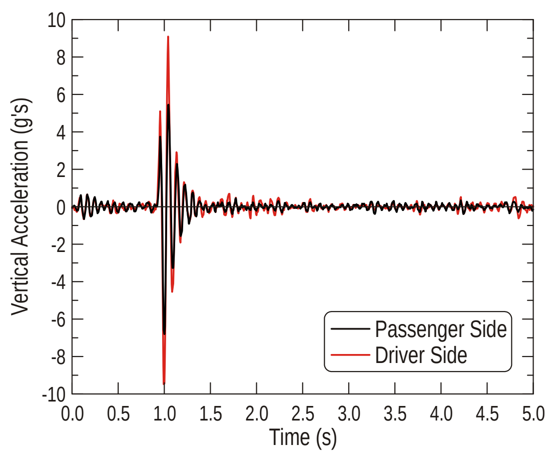

Figure B.44. Time histories of vertical acceleration for the front axle – velocity of 32 km/h (20 mph), run #08

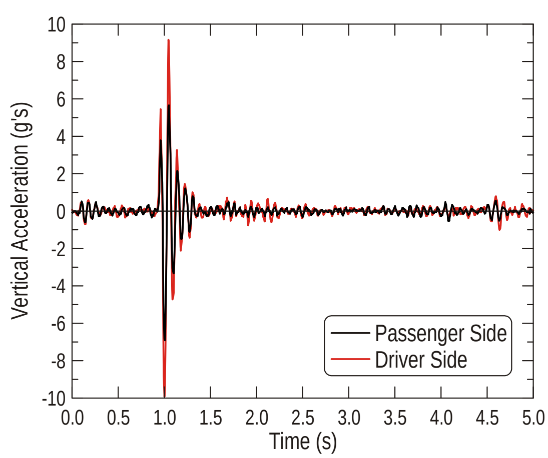

Figure B.45. Time histories of vertical acceleration for the front axle – velocity of 32 km/h (20 mph), run #09

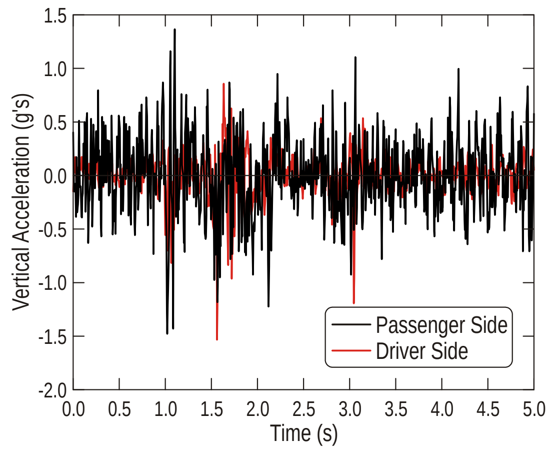

Figure B.46. Time history of vertical acceleration for points located on the frame above the front axle – velocity of 32 km/h (20 mph), run #07

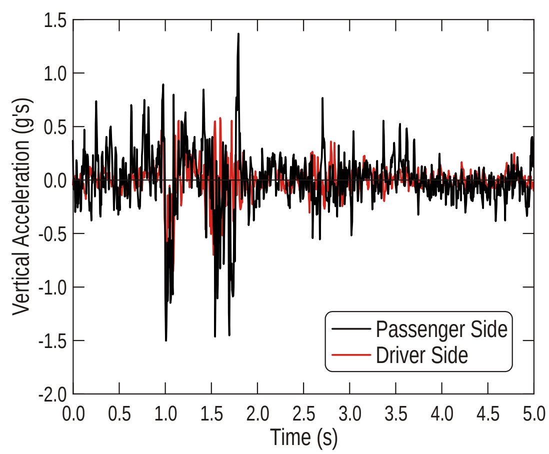

Figure B.47. Time history of vertical acceleration for points located on the frame above the front axle – velocity of 32 km/h (20 mph), run #08

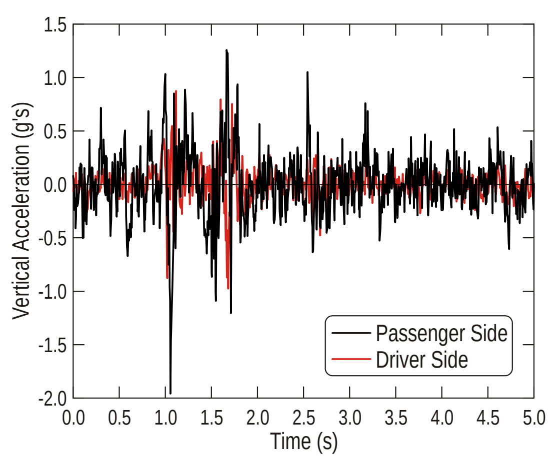

Figure B.48. Time history of vertical acceleration for points located on the frame above the front axle – velocity of 32 km/h (20 mph), run #09

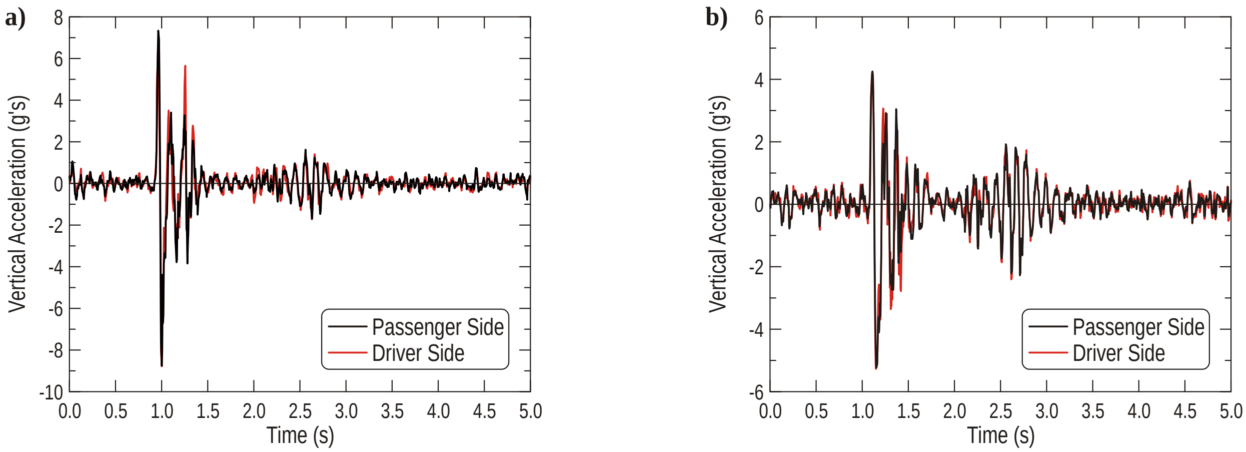

Figure B.49. Time histories of vertical acceleration for the rear tandem axles – velocity of 32 km/h (20 mph), run #07: a) forward axle, b) rear axle

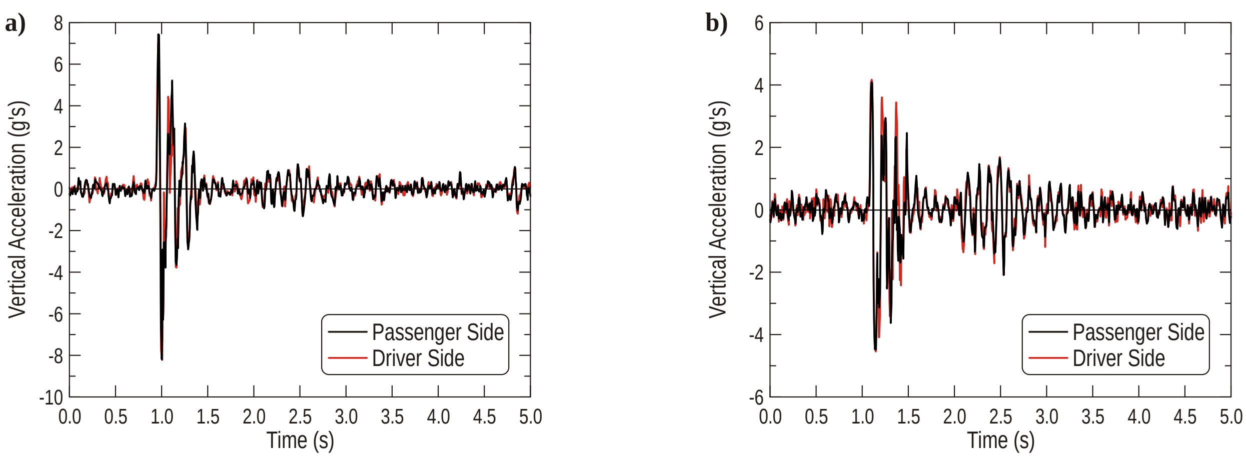

Figure B.50. Time histories of vertical acceleration for the rear tandem axles – velocity of 32 km/h (20 mph), run #08: a) forward axle, b) rear axle

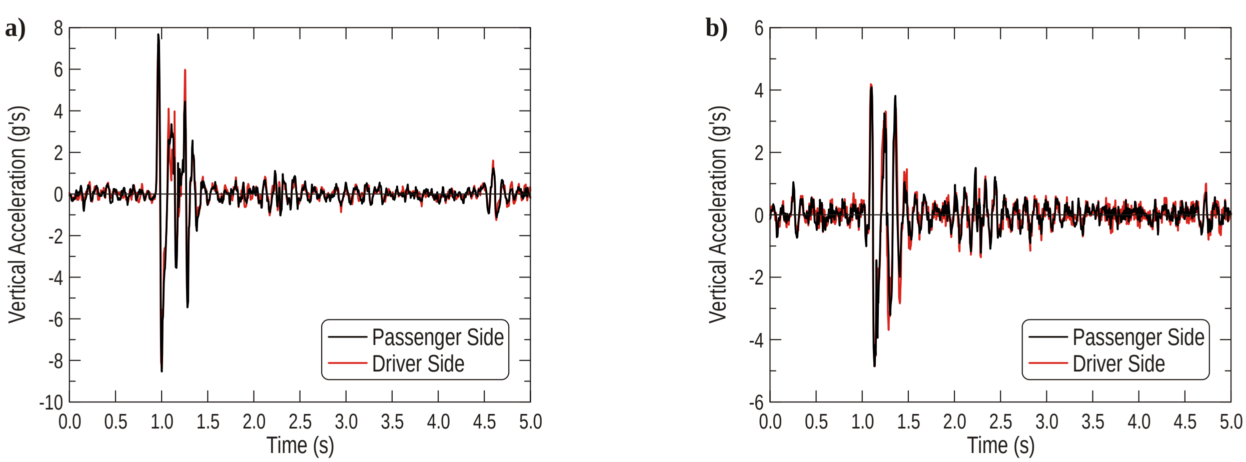

Figure B.51. Time histories of vertical acceleration for the rear tandem axles – velocity of 32 km/h (20 mph), run #09: a) forward axle, b) rear axle

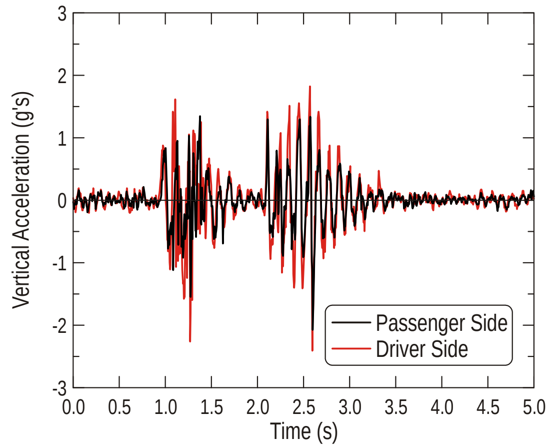

Figure B.52. Time histories of vertical acceleration for points located on the frame above the rear tandem axles – velocity of 32 km/h (20 mph), run #07

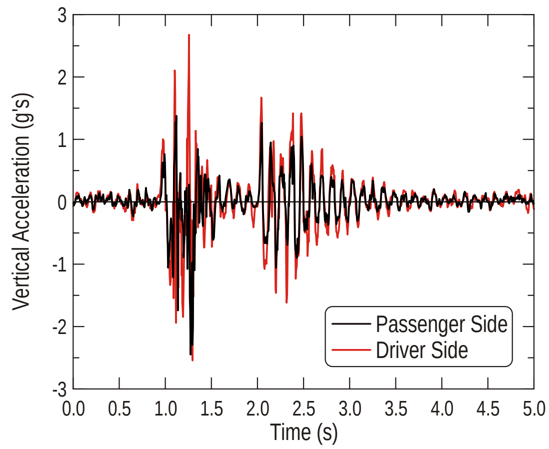

Figure B.53. Time histories of vertical acceleration for points located on the frame above the rear tandem axles – velocity of 32 km/h (20 mph), run #08

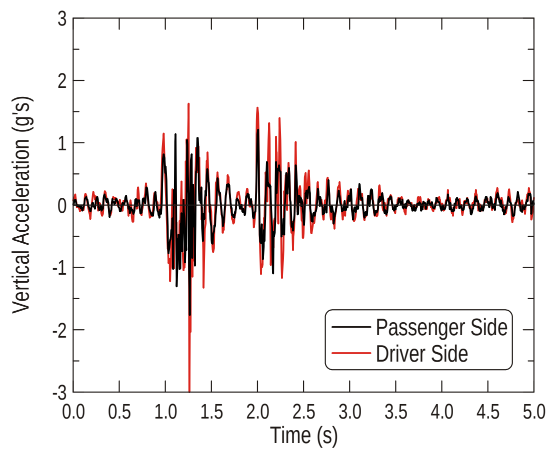

Figure B.54. Time histories of vertical acceleration for points located on the frame above the rear tandem axles – velocity of 32 km/h (20 mph), run #09

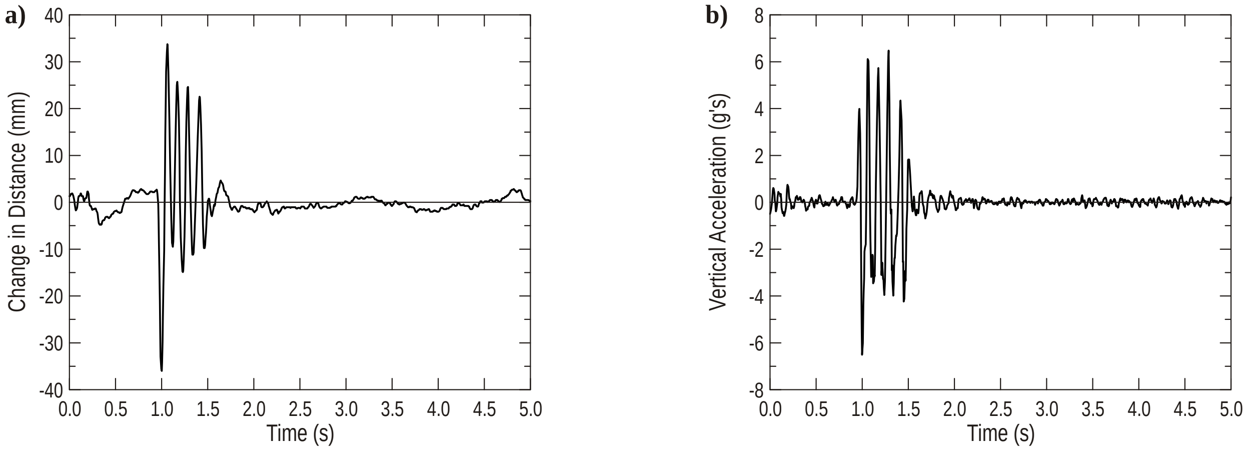

Figure B.55. Time histories for the first trailer axle – velocity of 32 km/h (20 mph), run #07: a) change in distance, b) vertical acceleration

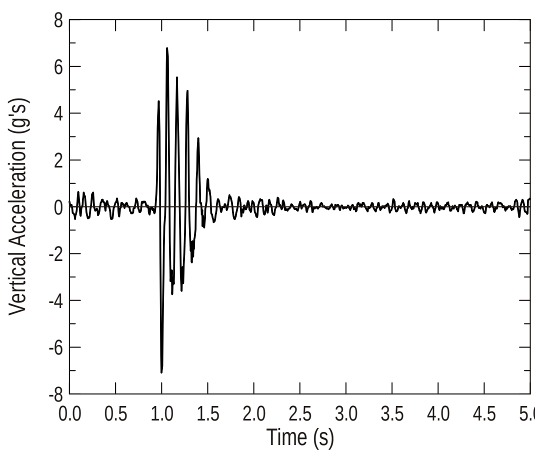

Figure B.56. Time histories of vertical acceleration for the first trailer axle – velocity of 32 km/h (20 mph), run #08

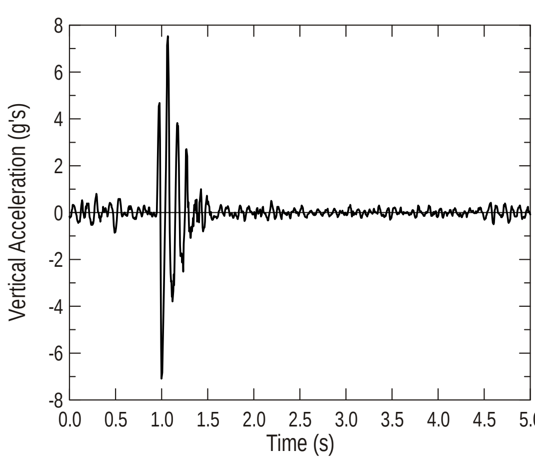

Figure B.57. Time histories of vertical acceleration for the first trailer axle – velocity of 32 km/h (20 mph), run #09

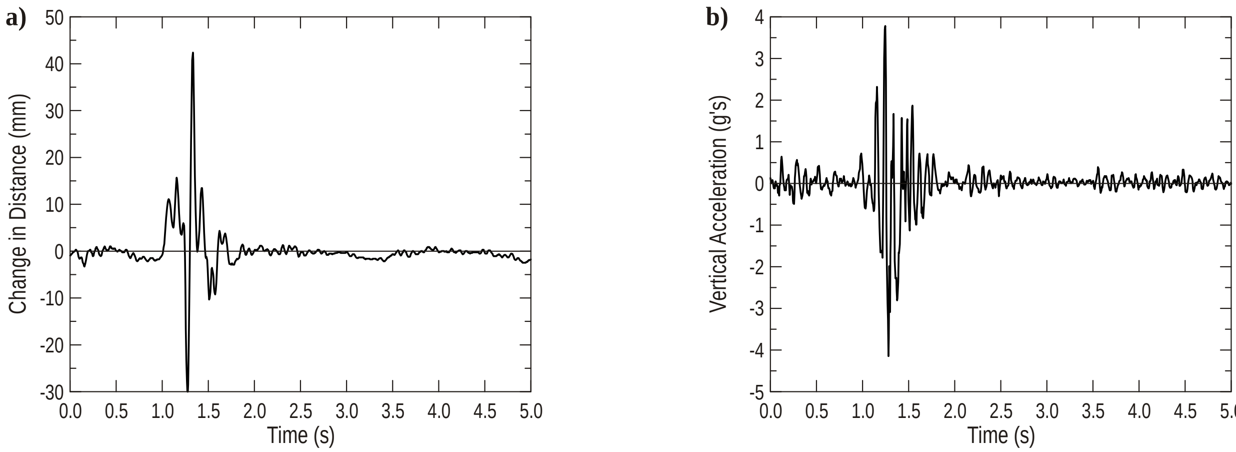

Figure B.58. Time histories for the third trailer axle – velocity of 32 km/h (20 mph), run #07: a) change in distance, b) vertical acceleration

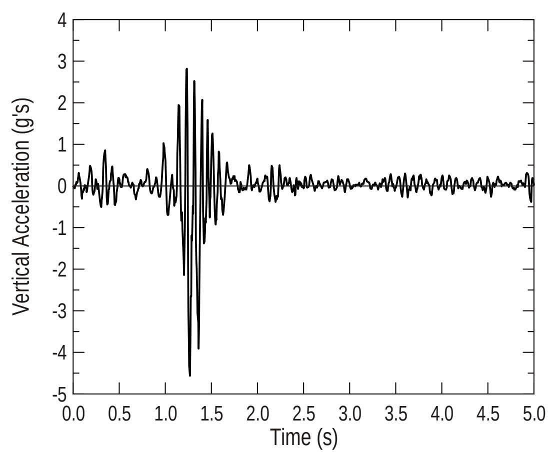

Figure B.59. Time histories of vertical acceleration for the third trailer axle – velocity of 32 km/h (20 mph), run #08

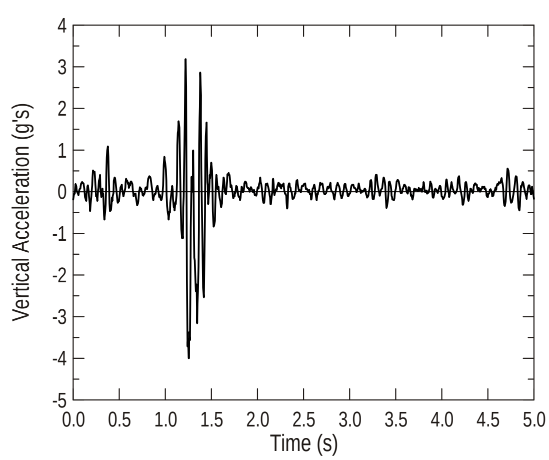

Figure B.60. Time histories of vertical acceleration for the third trailer axle – velocity of 32 km/h (20 mph), run #09

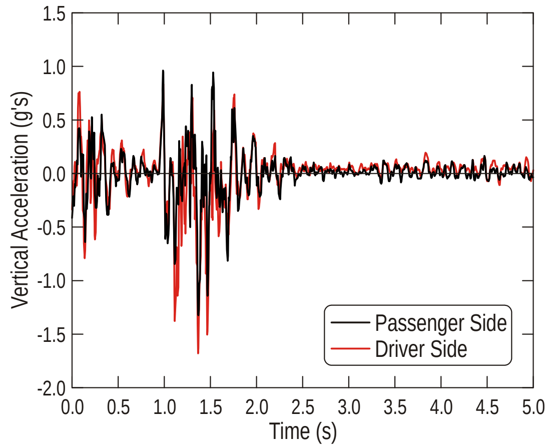

Figure B.61. Time histories of vertical acceleration for points located on the trailer deck above the first trailer axle – velocity of 32 km/h (20 mph), run #07

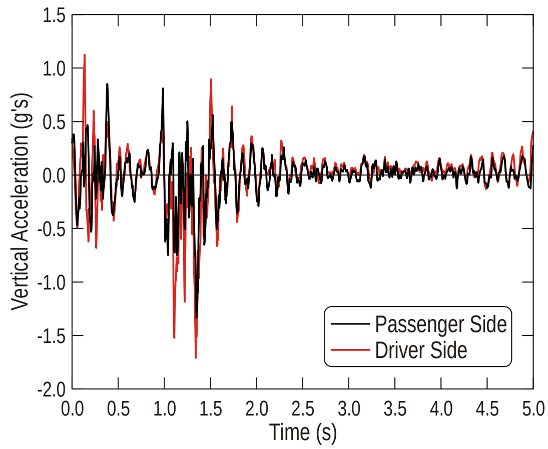

Figure B.62. Time histories of vertical acceleration for points located on the trailer deck above the first trailer axle – velocity of 32 km/h (20 mph), run #08

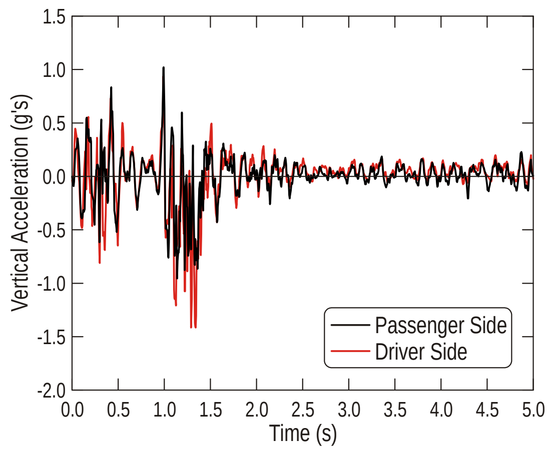

Figure B.63. Time histories of vertical acceleration for points located on the trailer deck above the first trailer axle – velocity of 32 km/h (20 mph), run #09

B.2. Suspension Tests of the Loaded Tractor-Trailer

Suspension tests of the fully loaded tractor-trailer included six runs with two different velocities – 8 and 16 km/h (5 and 10 mph), as provided in Table B.2. The results are presented in Figure B.64 through Figure B.84 – for the velocity of 8 km/h (5 mph) and Figure B.85 through Figure B.105 – for the velocity of 16 km/h (10 mph). In some cases, the results are not complete due to signal failure or/and damage of gauges.

Table B.2. Summary of all considered cases for the suspension tests of the loaded tractor-trailer

Run #	Pass #	Velocity	Vehicle configuration
10	1	8 km/h (5 mph)	loaded
11	2		
12	3		
13	1	16 km/h (10 mph)	loaded
14	2		
15	3		

Velocity of 8 km/h (5 mph)

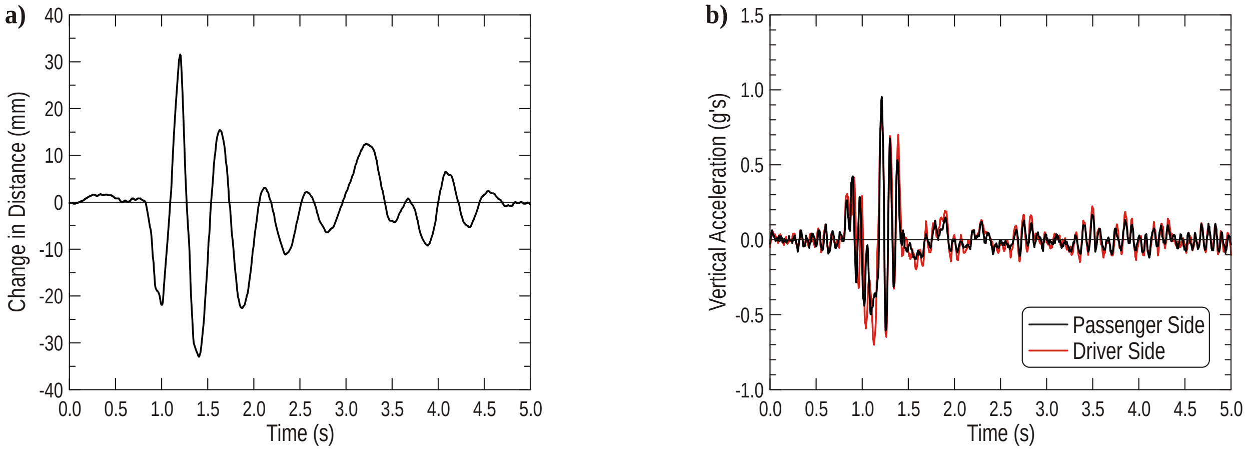

Figure B.64. Time histories for the front axle – velocity of 8 km/h (5 mph), run #10: a) change in distance, b) vertical acceleration

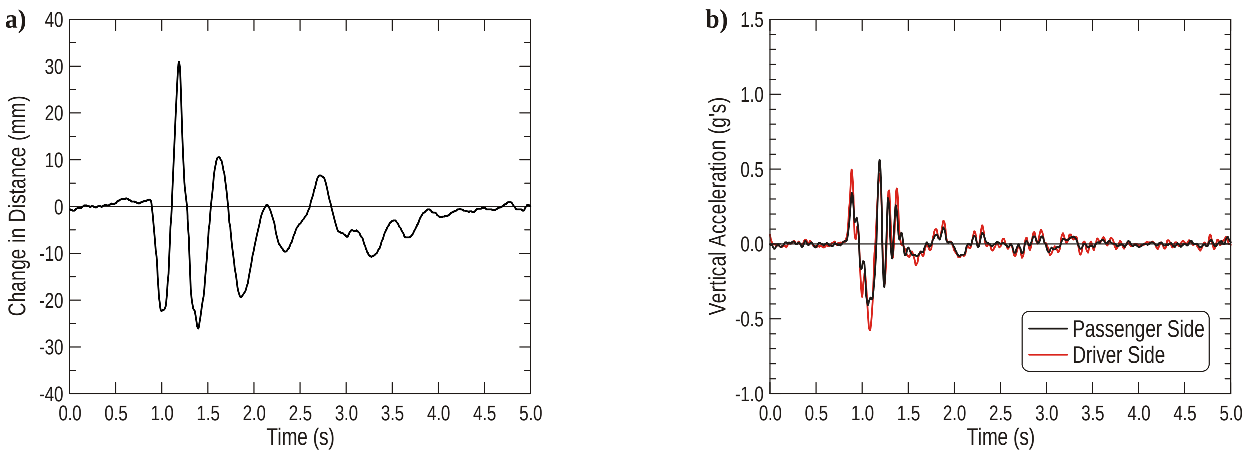

Figure B.65. Time histories for the front axle – velocity of 8 km/h (5 mph), run #11: a) change in distance, b) vertical acceleration

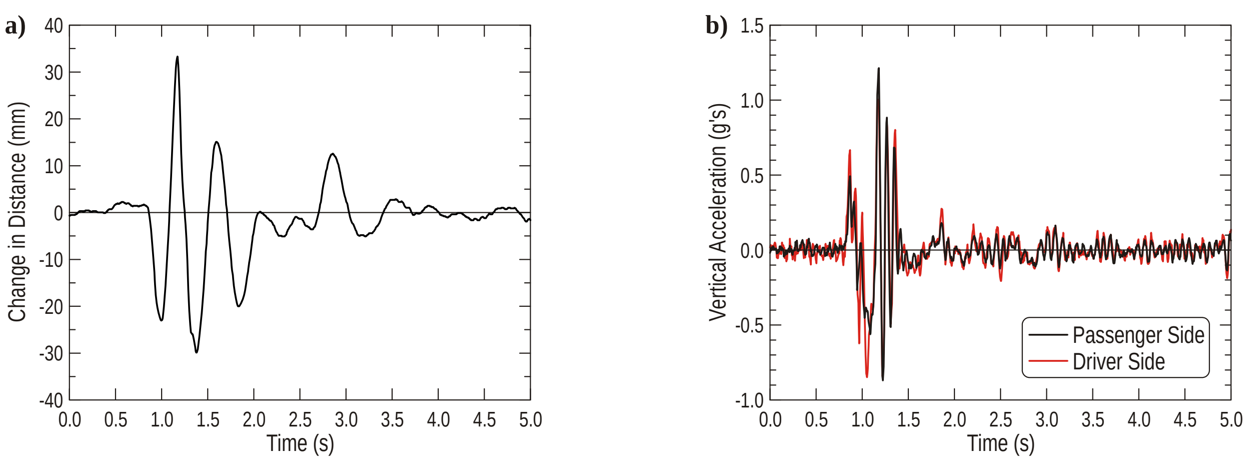

Figure B.66. Time histories for the front axle – velocity of 8 km/h (5 mph), run #12: a) change in distance, b) vertical acceleration

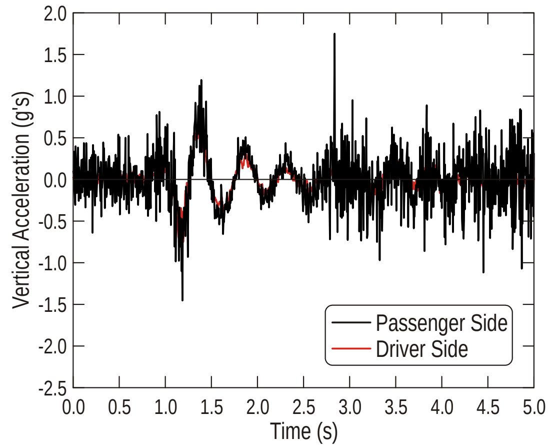

Figure B.67. Time history of vertical acceleration for points located on the frame above the front axle – velocity of 8 km/h (5 mph), run #10

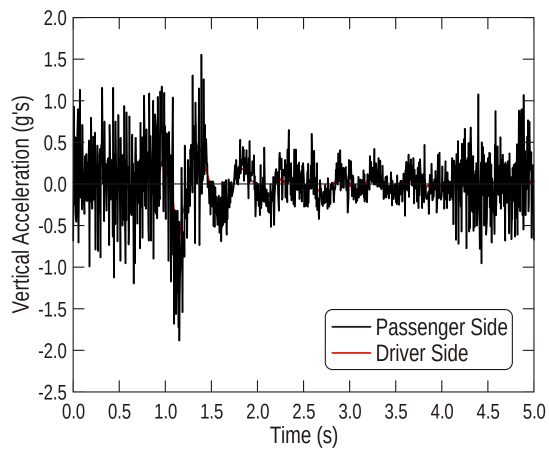

Figure B.68. Time history of vertical acceleration for points located on the frame above the front axle – velocity of 8 km/h (5 mph), run #11

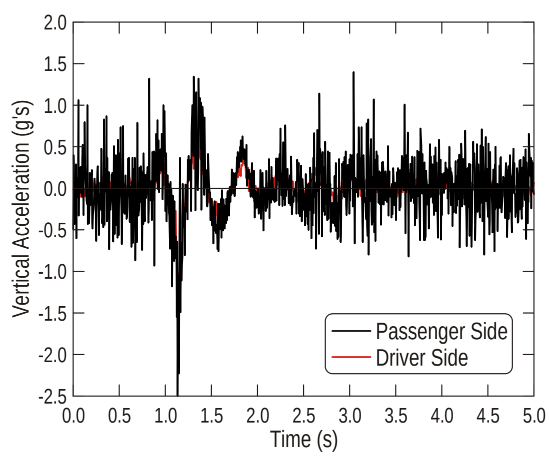

Figure B.69. Time history of vertical acceleration for points located on the frame above the front axle – velocity of 8 km/h (5 mph), run #12

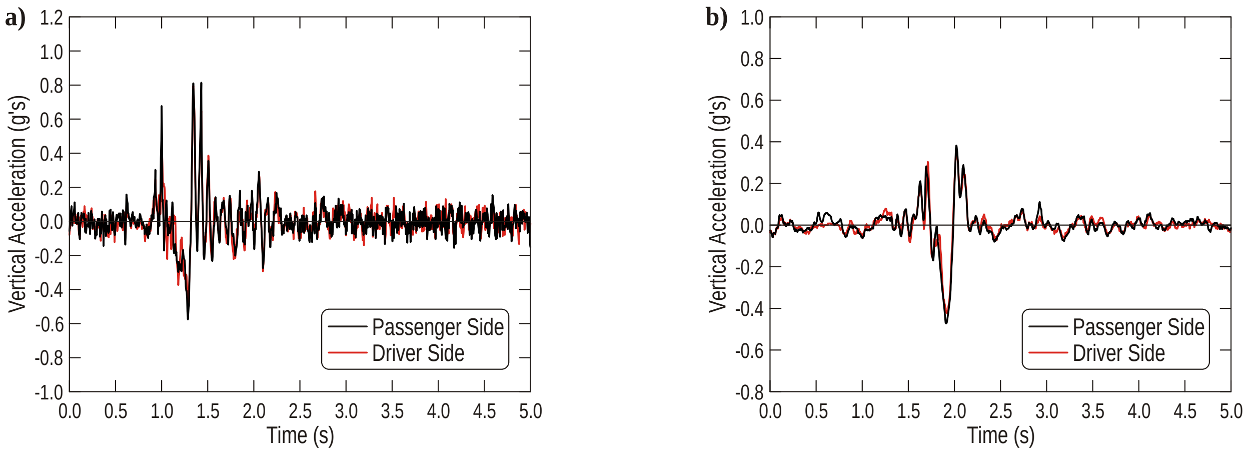

Figure B.70. Time histories of vertical acceleration for the rear tandem axles – velocity of 8 km/h (5 mph), run #10: a) forward axle, b) rear axle

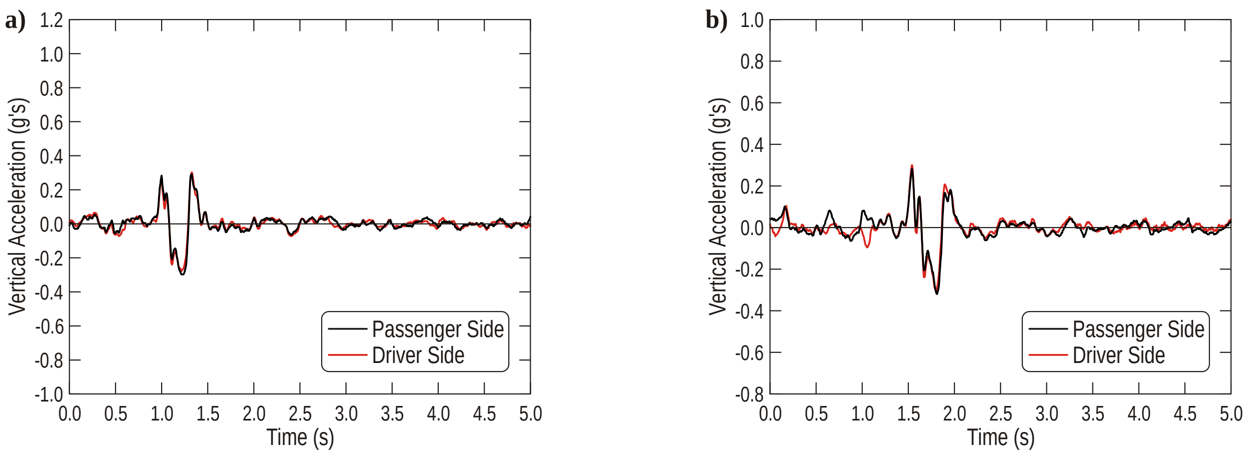

Figure B.71. Time histories of vertical acceleration for the rear tandem axles – velocity of 8 km/h (5 mph), run #11: a) forward axle, b) rear axle

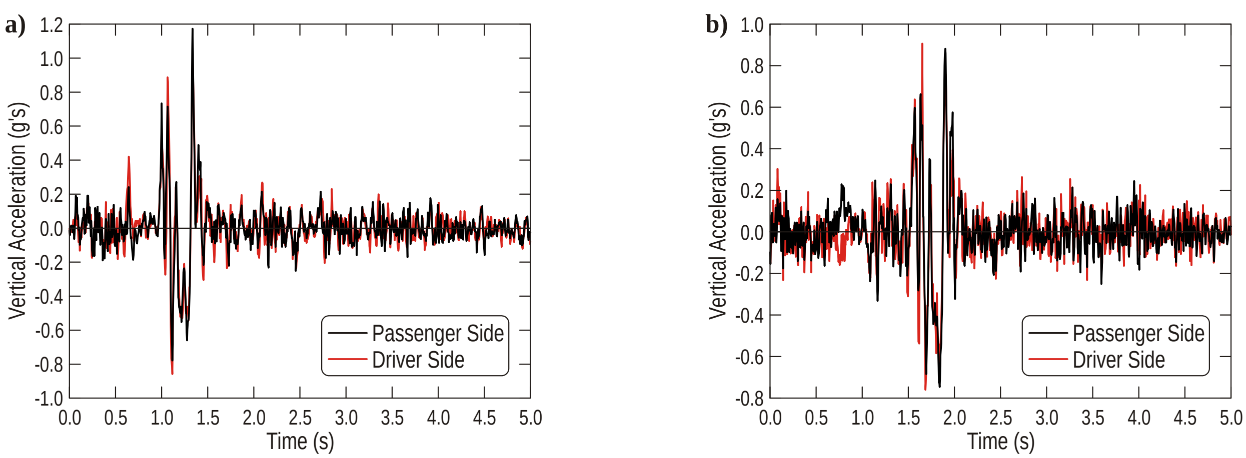

Figure B.72. Time histories of vertical acceleration for the rear tandem axles – velocity of 8 km/h (5 mph), run #12: a) forward axle, b) rear axle

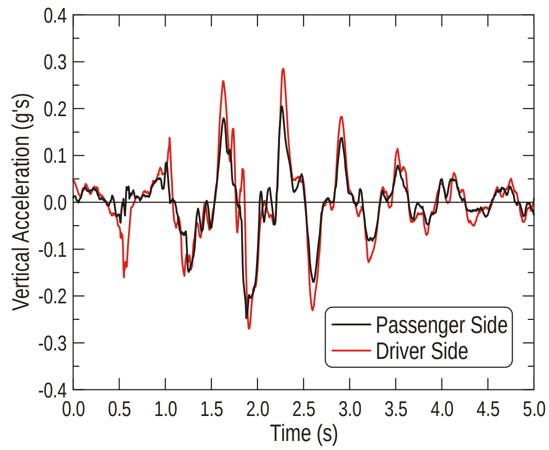

Figure B.73. Time histories of vertical acceleration for points located on the frame above the rear tandem axles – velocity of 8 km/h (5 mph), run #10

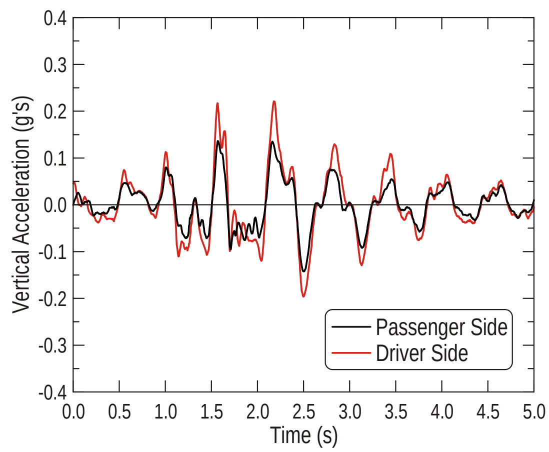

Figure B.74. Time histories of vertical acceleration for points located on the frame above the rear tandem axles – velocity of 8 km/h (5 mph), run #11

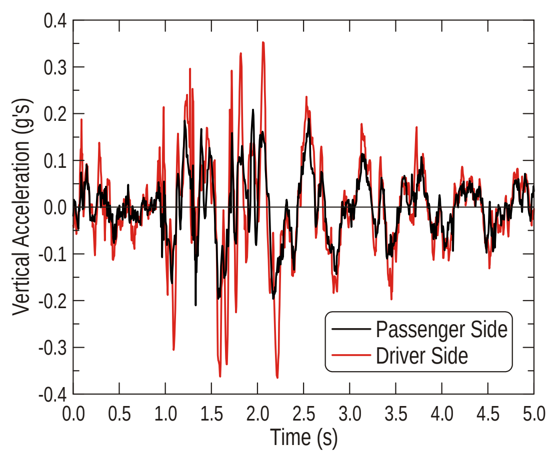

Figure B.75. Time histories of vertical acceleration for points located on the frame above the rear tandem axles – velocity of 8 km/h (5 mph), run #12

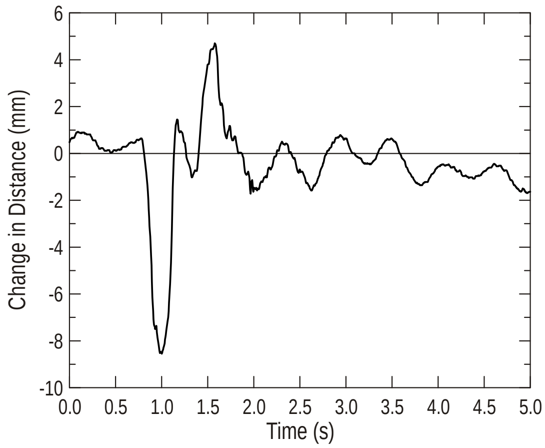

Figure B.76. Time histories of change in distance for the first trailer axle – velocity of 8 km/h (5 mph), run #10

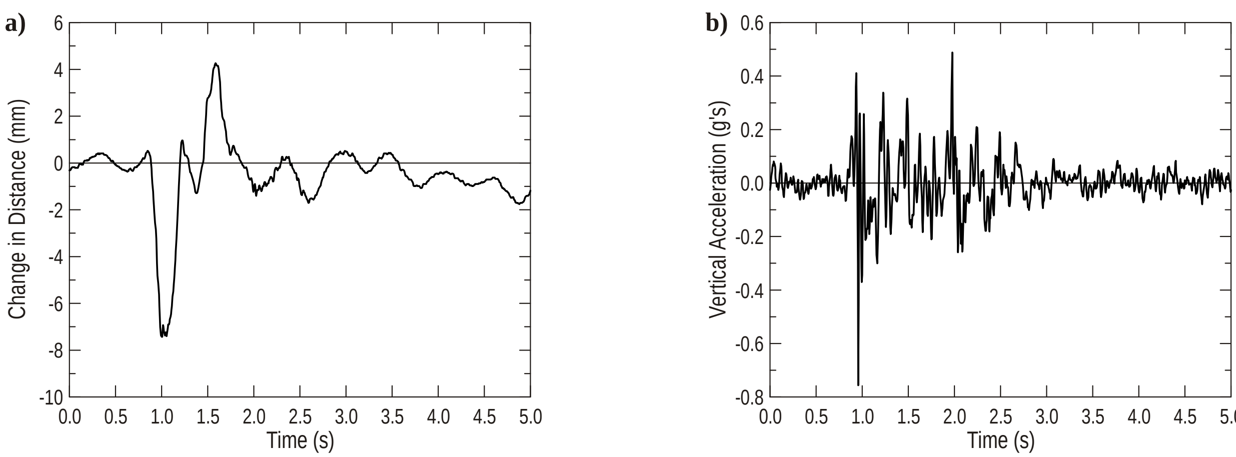

Figure B.77. Time histories for the first trailer axle – velocity of 8 km/h (5 mph), run #11: a) change in distance, b) vertical acceleration

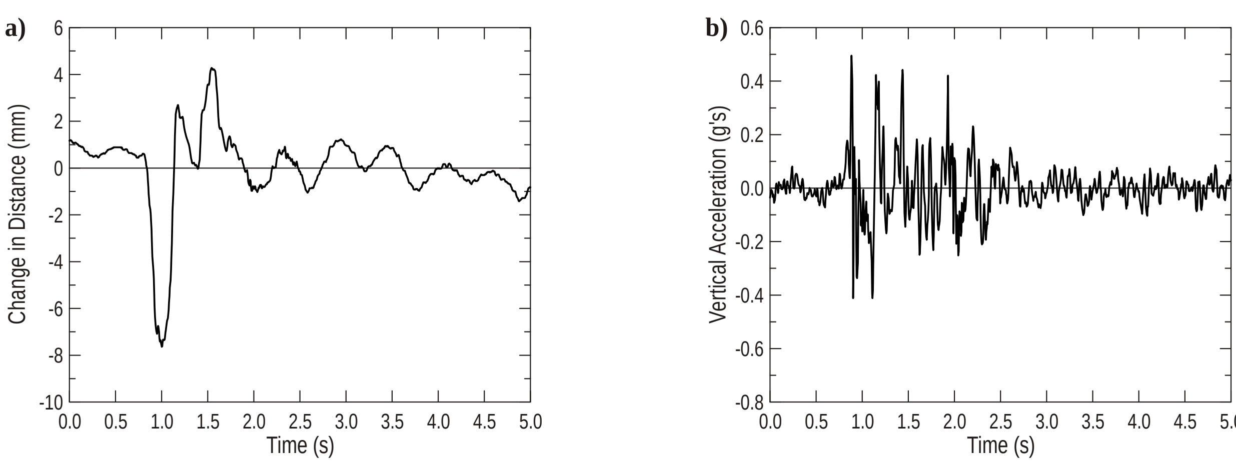

Figure B.78. Time histories for the first trailer axle – velocity of 8 km/h (5 mph), run #12: a) change in distance, b) vertical acceleration

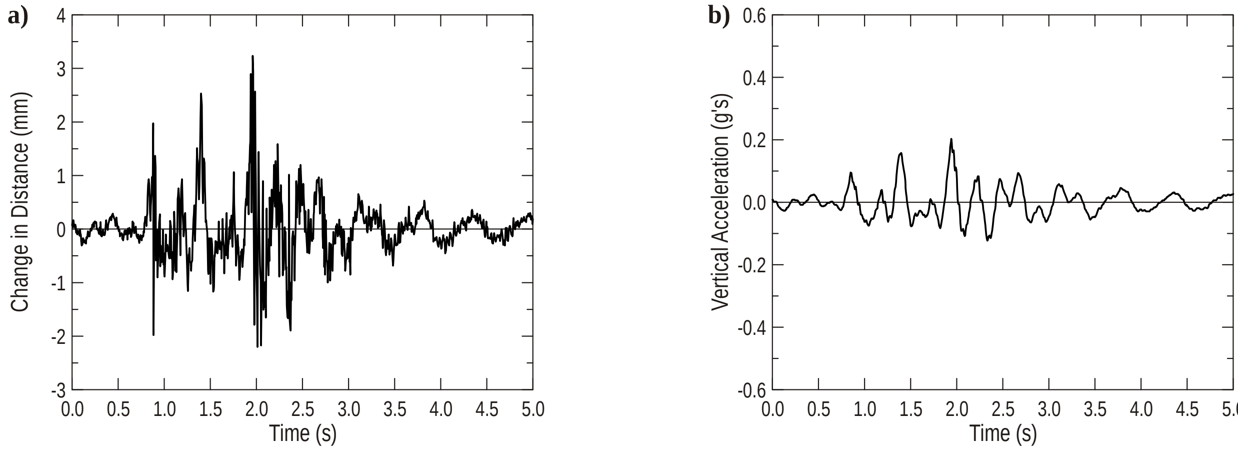

Figure B.79. Time histories for the third trailer axle – velocity of 8 km/h (5 mph), run #10: a) change in distance, b) vertical acceleration

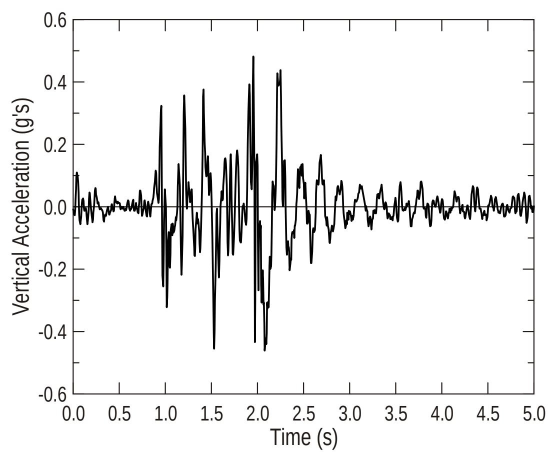

Figure B.80. Time histories of vertical acceleration for the third trailer axle – velocity of 8 km/h (5 mph), run #11

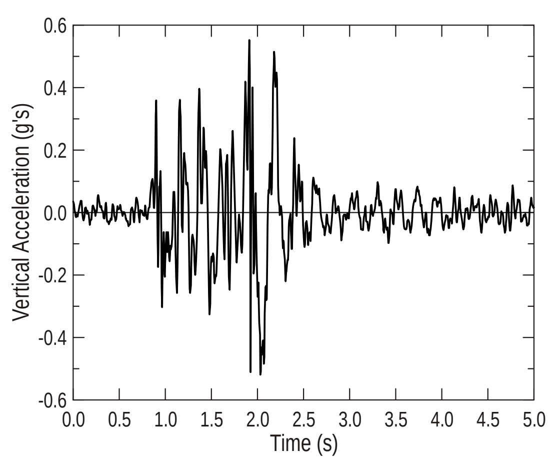

Figure B.81. Time histories of vertical acceleration for the third trailer axle – velocity of 8 km/h (5 mph), run #12

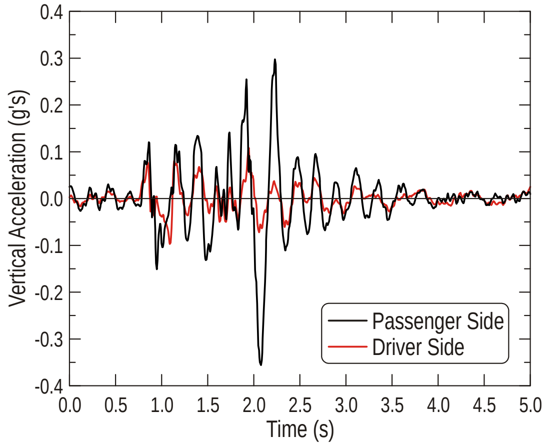

Figure B.82. Time histories of vertical acceleration for points located on the trailer deck above the first trailer axle – velocity of 8 km/h (5 mph), run #10

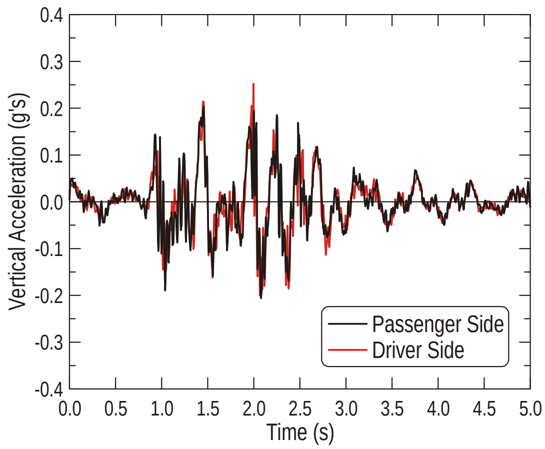

Figure B.83. Time histories of vertical acceleration for points located on the trailer deck above the first trailer axle – velocity of 8 km/h (5 mph), run #11

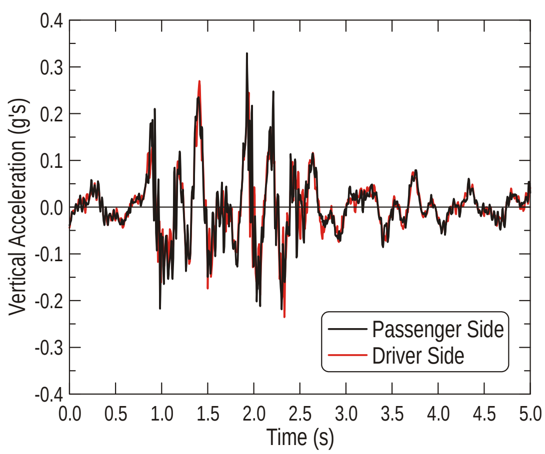

Figure B.84. Time histories of vertical acceleration for points located on the trailer deck above the first trailer axle – velocity of 8 km/h (5 mph), run #12

Velocity of 16 km/h (10 mph)

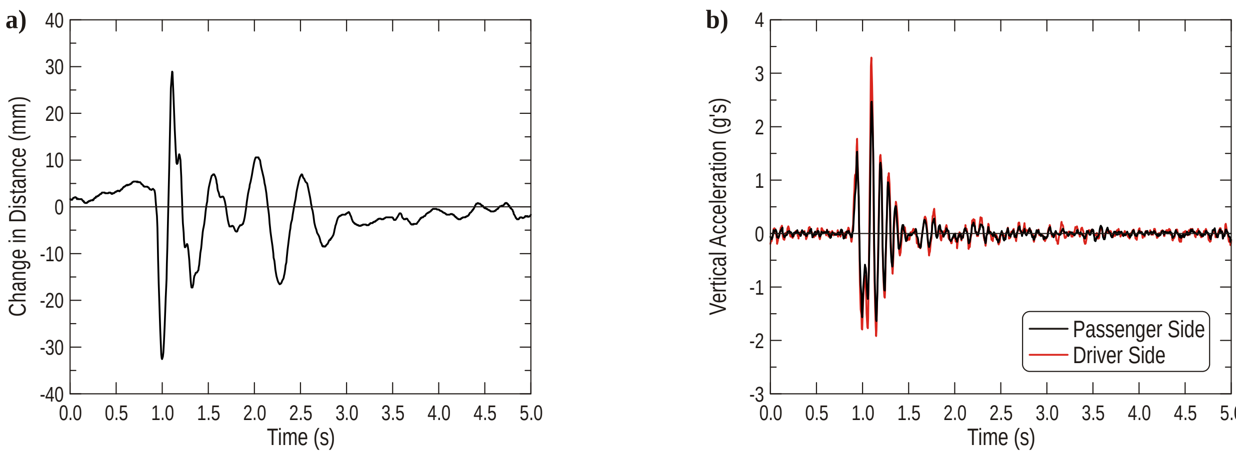

Figure B.85. Time histories for the front axle – velocity of 16 km/h (10 mph), run #13: a) change in distance, b) vertical acceleration

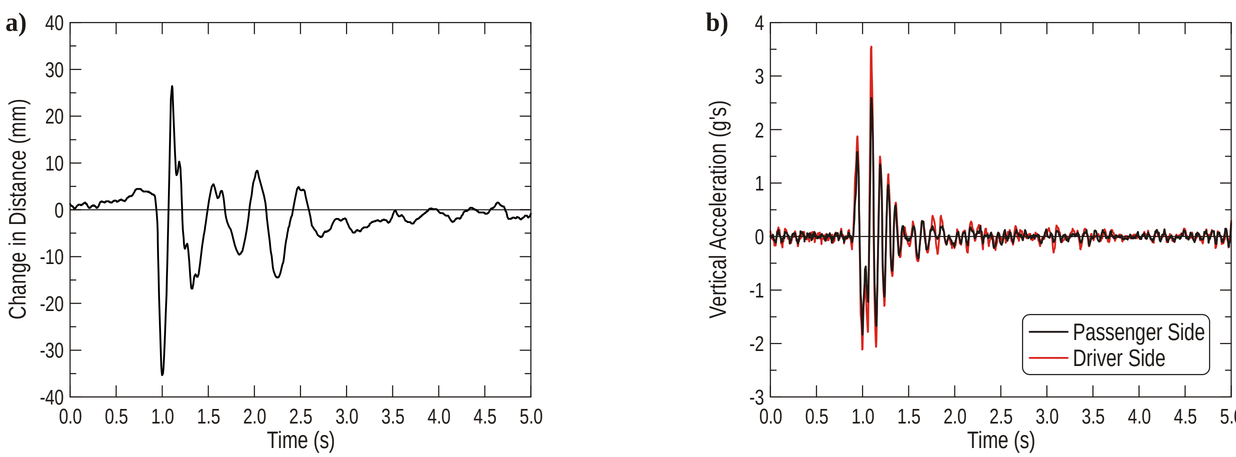

Figure B.86. Time histories for the front axle – velocity of 16 km/h (10 mph), run #14: a) change in distance, b) vertical acceleration

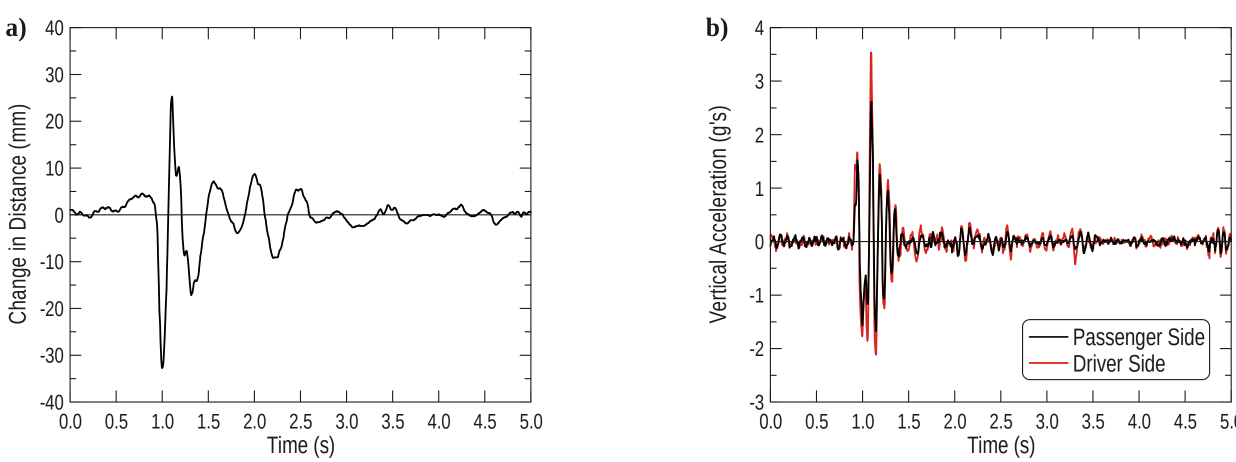

Figure B.87. Time histories for the front axle – velocity of 16 km/h (10 mph), run #15: a) change in distance, b) vertical acceleration

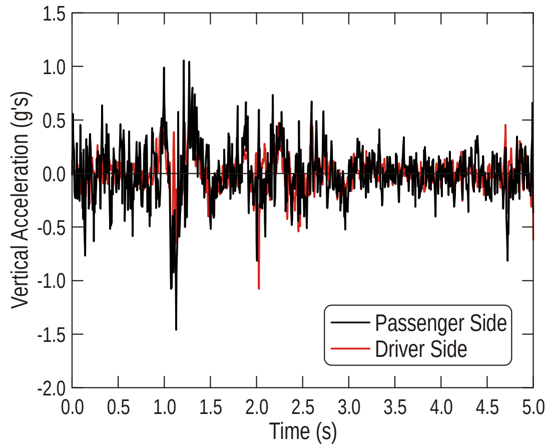

Figure B.88. Time history of vertical acceleration for points located on the frame above the front axle – velocity of 18 km/h (10 mph), run #13

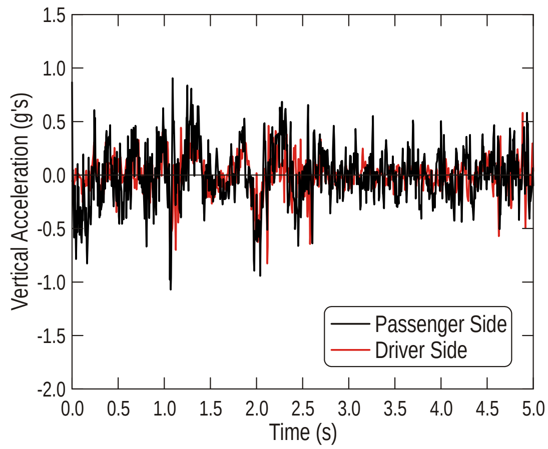

Figure B.89. Time history of vertical acceleration for points located on the frame above the front axle – velocity of 18 km/h (10 mph), run #14

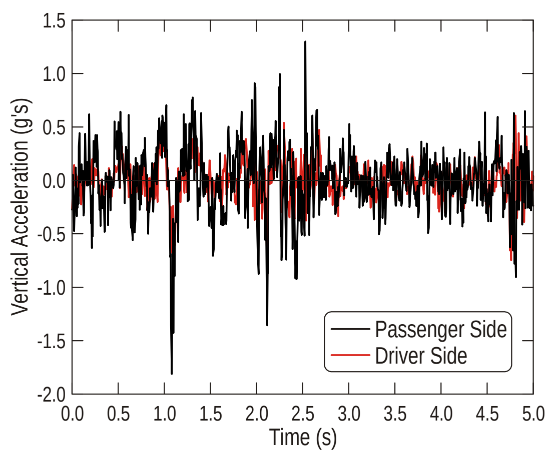

Figure B.90. Time history of vertical acceleration for points located on the frame above the front axle – velocity of 18 km/h (10 mph), run #15

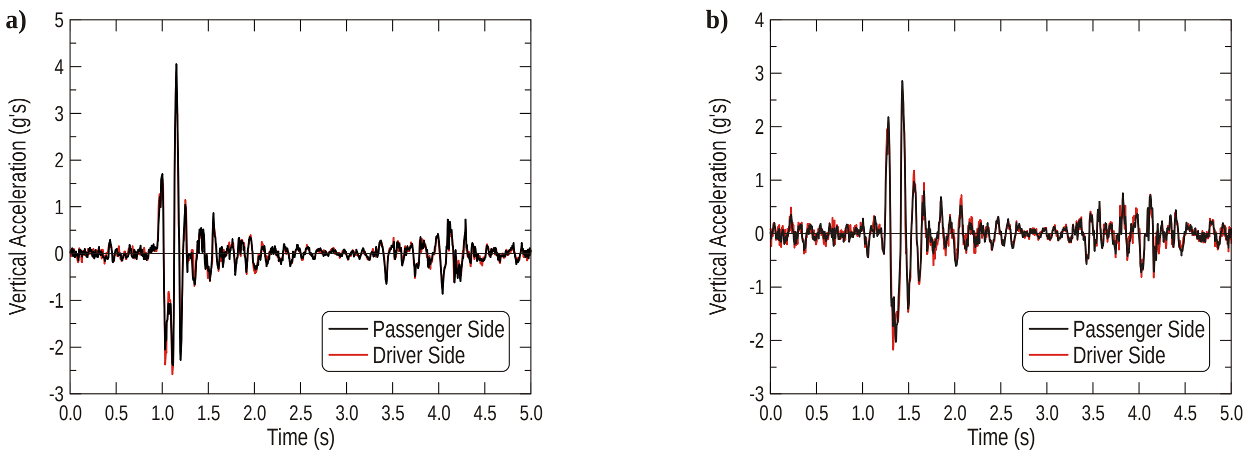

Figure B.91. Time histories of vertical acceleration for the rear tandem axles – velocity of 16 km/h (10 mph), run #13: a) forward axle, b) rear axle

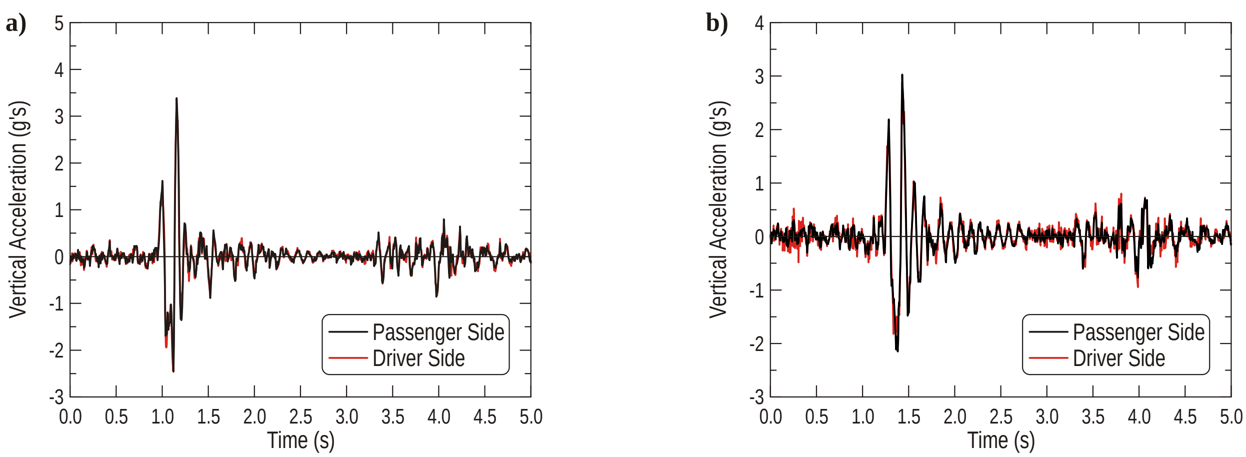

Figure B.92. Time histories of vertical acceleration for the rear tandem axles – velocity of 16 km/h (10 mph), run #14: a) forward axle, b) rear axle

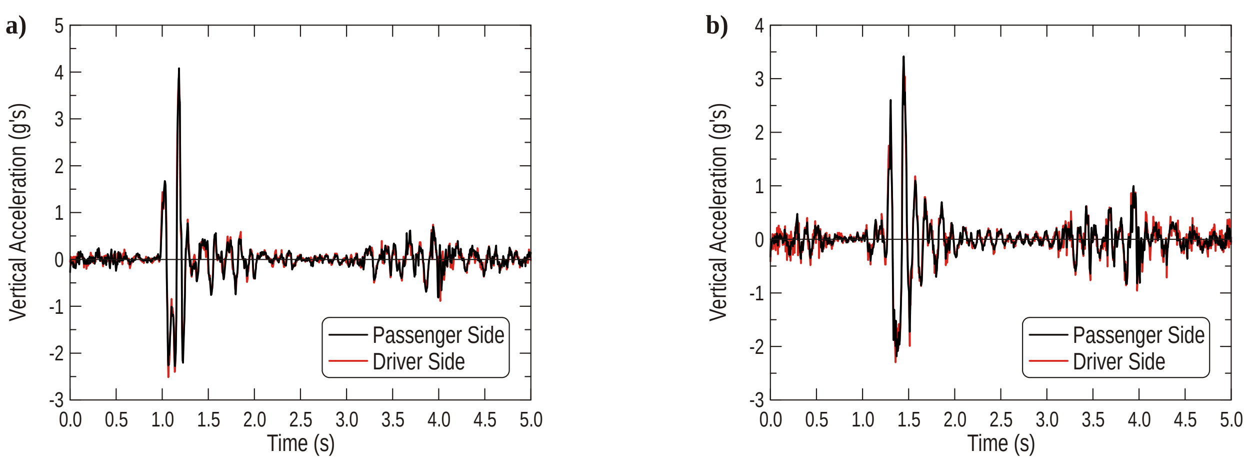

Figure B.93. Time histories of vertical acceleration for the rear tandem axles – velocity of 16 km/h (10 mph), run #15: a) forward axle, b) rear axle

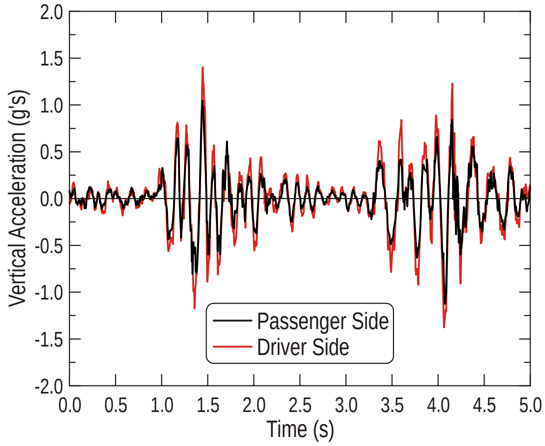

Figure B.94. Time histories of vertical acceleration for points located on the frame above the rear tandem axles – velocity of 16 km/h (10 mph), run #13

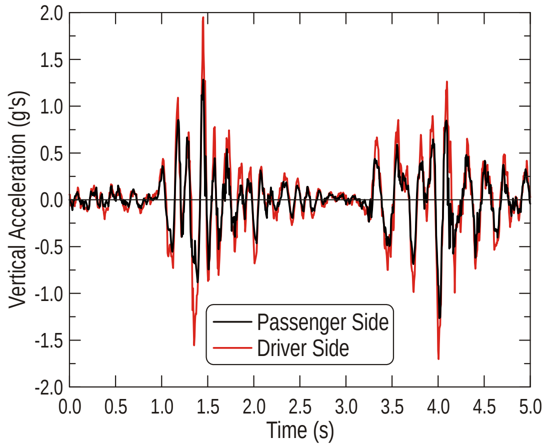

Figure B.95. Time histories of vertical acceleration for points located on the frame above the rear tandem axles – velocity of 16 km/h (10 mph), run #14

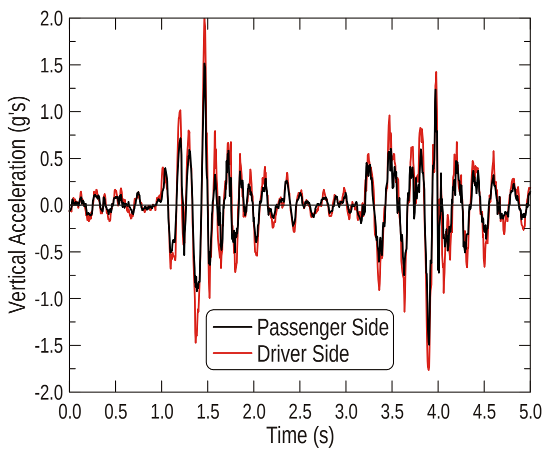

Figure B.96. Time histories of vertical acceleration for points located on the frame above the rear tandem axles – velocity of 16 km/h (10 mph), run #15

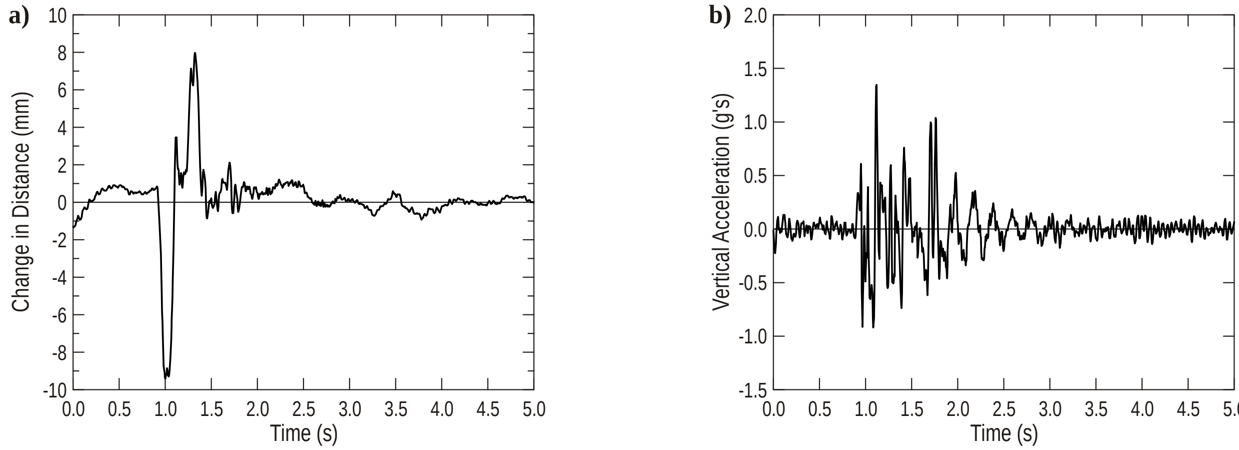

Figure B.97. Time histories for the third trailer axle – velocity of 16 km/h (10 mph), run #13: a) change in distance, b) vertical acceleration

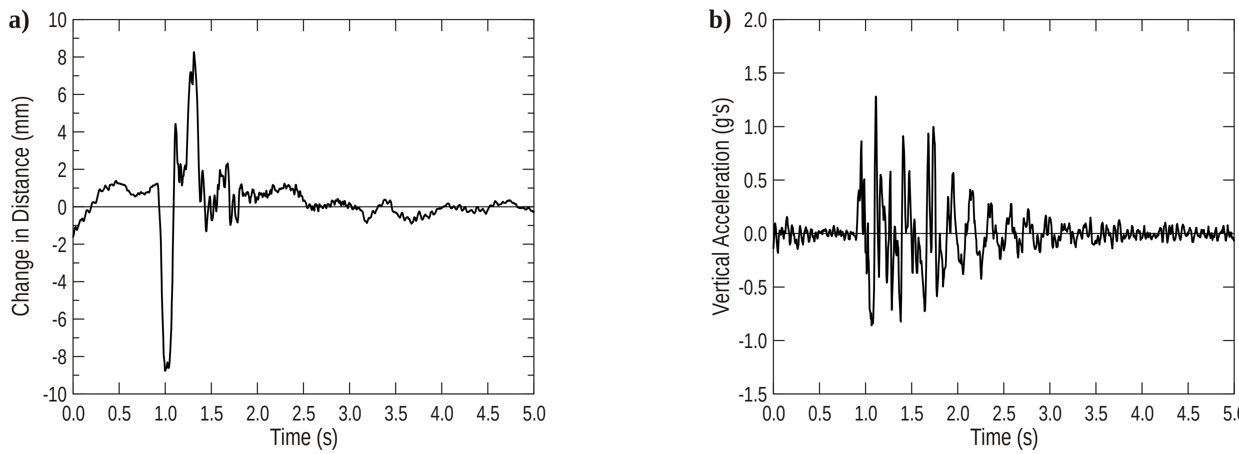

Figure B.98. Time histories for the third trailer axle – velocity of 16 km/h (10 mph), run #14: a) change in distance, b) vertical acceleration

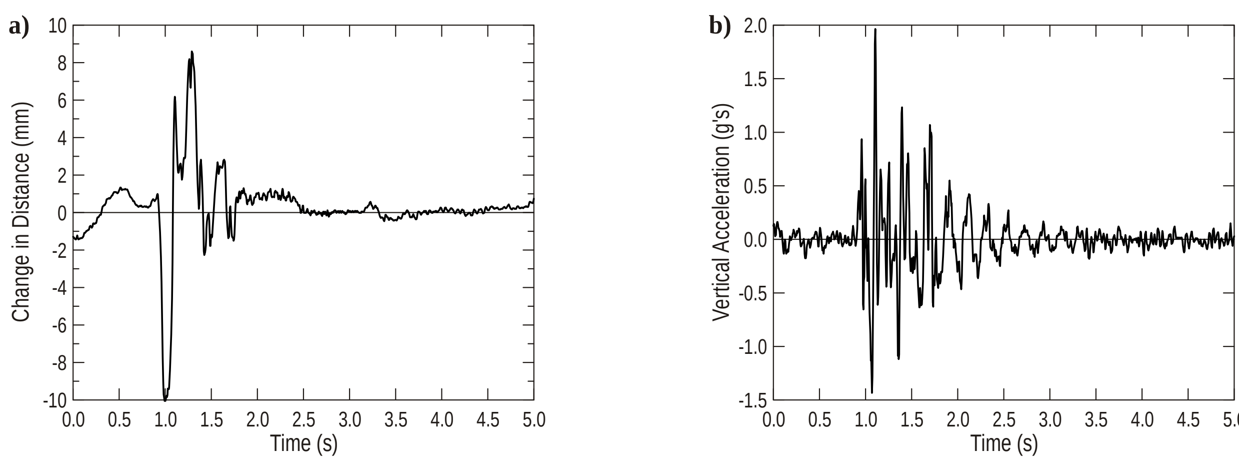

Figure B.99. Time histories for the third trailer axle – velocity of 16 km/h (10 mph), run #15: a) change in distance, b) vertical acceleration

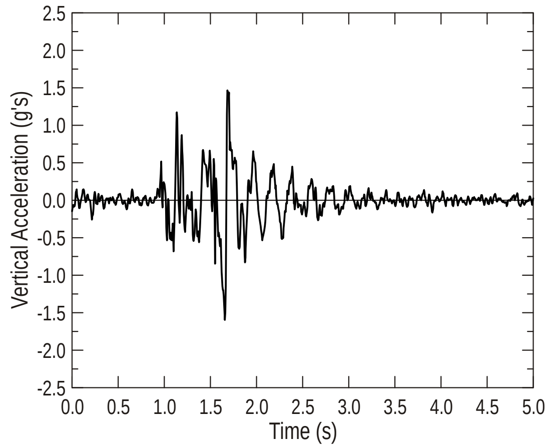

Figure B.100. Time histories of vertical acceleration for the third trailer axle – velocity of 16 km/h (10 mph), run #13

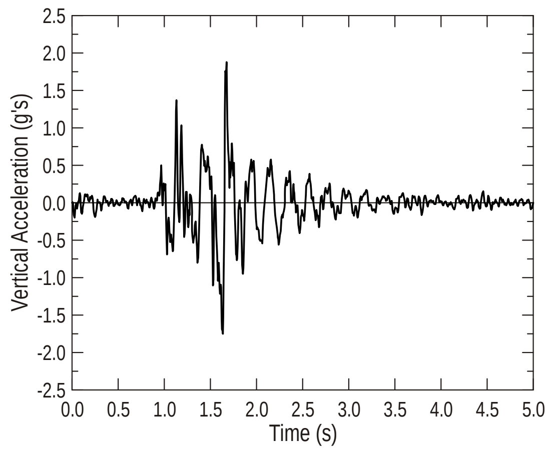

Figure B.101. Time histories of vertical acceleration for the third trailer axle – velocity of 16 km/h (10 mph), run #14

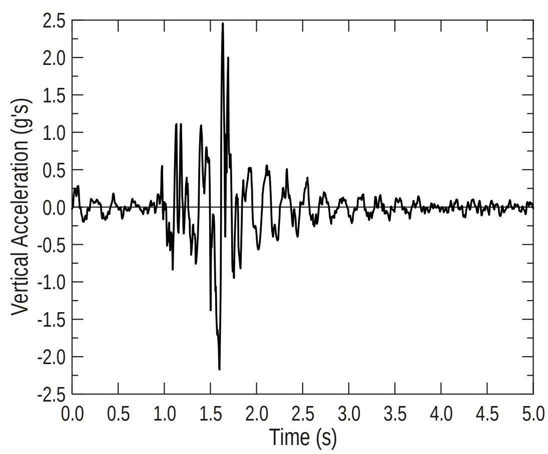

Figure B.102. Time histories of vertical acceleration for the third trailer axle – velocity of 16 km/h (10 mph), run #15

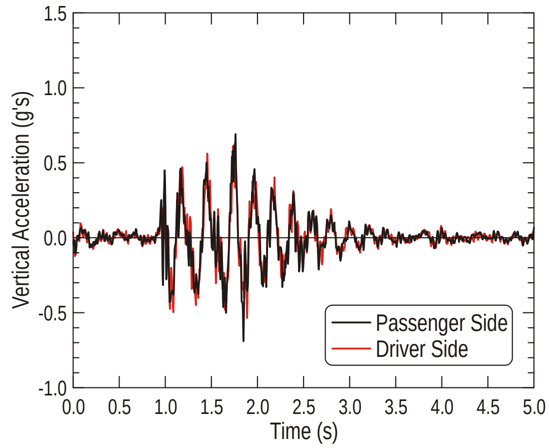

Figure B.103. Time histories of vertical acceleration for points located on the trailer deck above the first trailer axle – velocity of 16 km/h (10 mph), run #13

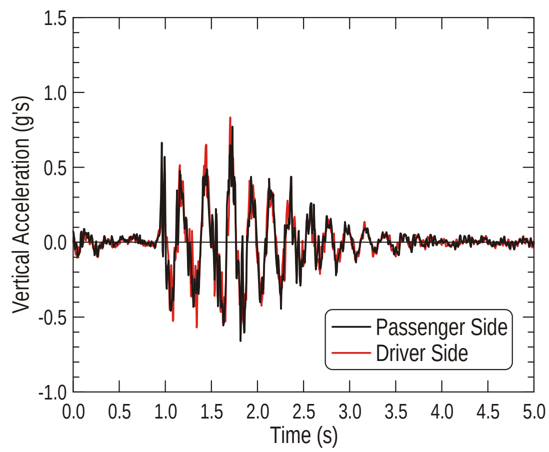

Figure B.104. Time histories of vertical acceleration for points located on the trailer deck above the first trailer axle – velocity of 16 km/h (10 mph), run #14

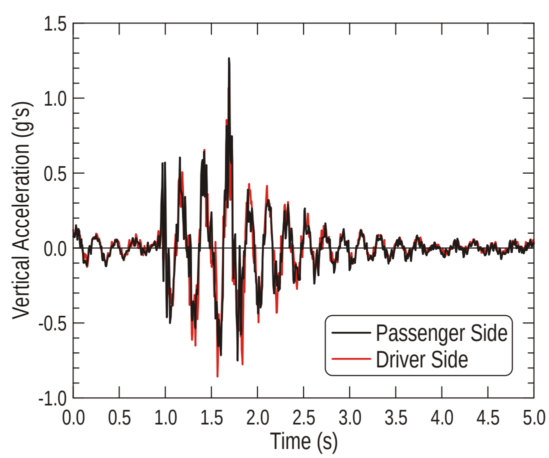

Figure B.105. Time histories of vertical acceleration for points located on the trailer deck above the first trailer axle – velocity of 16 km/h (10 mph), run #15

B.3. Suspension Tests of the Terex Crane

Suspension tests of the Terex crane included 12 runs with four different velocities – 8, 16, 24, and 32 km/h (5, 10, 15, and 20 mph) according to Table B.3. Results of the suspension tests in the form of time histories are presented in Figure B.106 through Figure B.117 – for the velocity of 8 km/h (5 mph); Figure B.118 through Figure B.129 – for the velocity of 16 km/h (10 mph); Figure B.130 through Figure B.141 – for the velocity of 24 km/h (15 mph); and Figure B.142 through Figure B.153 – for the velocity of 24 km/h (15 mph). Time histories of accelerations and the changes in distance were limited to five-second periods – one second before the front axle was driven over speed bump and four seconds after it.

Table B.3. Summary of all considered cases for the suspension tests of the Terex crane

Run #	Pass #	Velocity	Run #	Pass #	Velocity
01	1	8 km/h (5 mph)	07	1	24 km/h (15 mph)
02	2		08	2	
03	3		09	3	
04	1	16 km/h (10 mph)	10	1	32 km/h (20 mph)
05	2		11	2	
06	3		12	3	

Velocity of 8 km/h (5 mph)

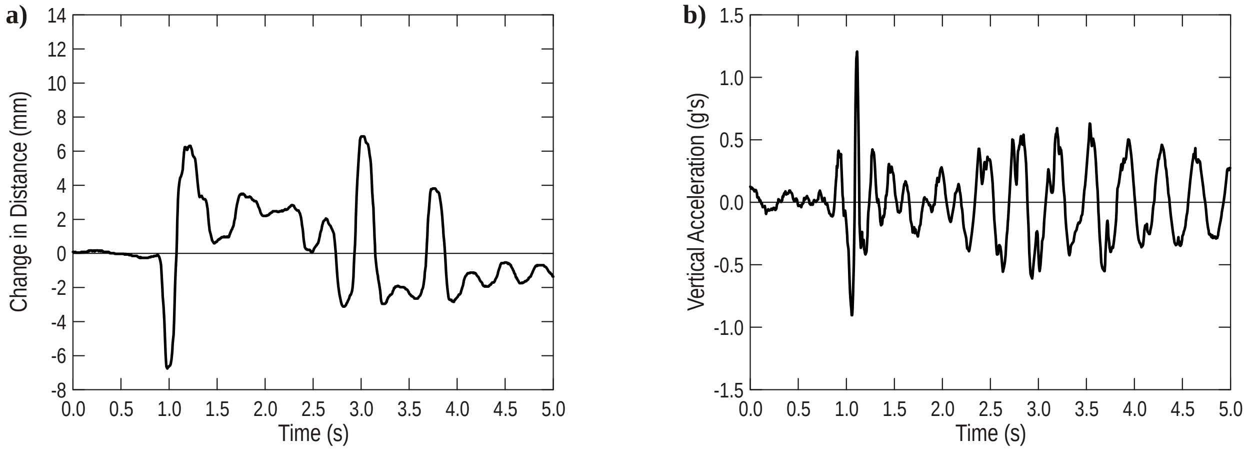

Figure B.106. Time histories for the front axle – velocity of 8 km/h (5 mph), run #01: a) change in distance, b) vertical acceleration

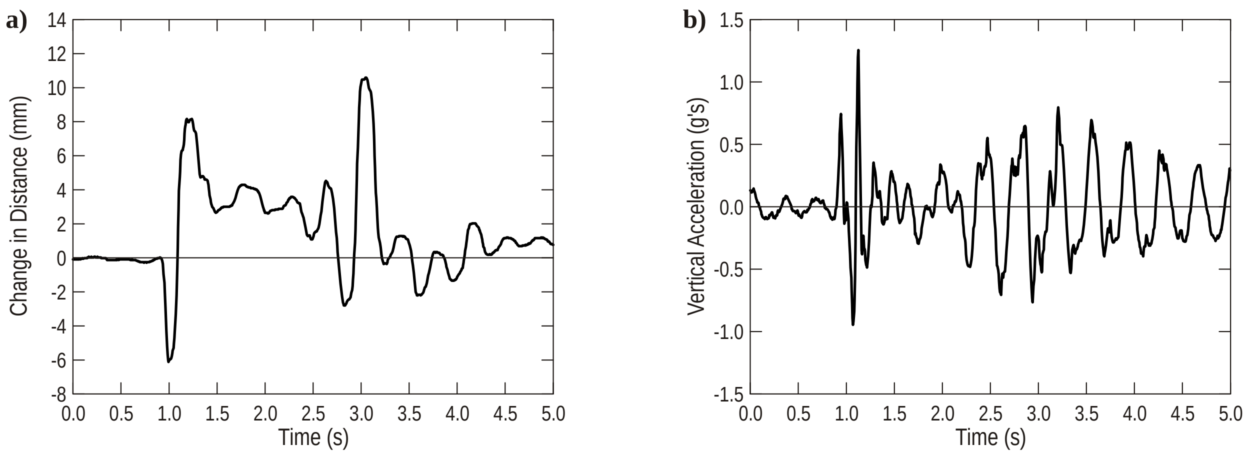

Figure B.107. Time histories for the front axle – velocity of 8 km/h (5 mph), run #02: a) change in distance, b) vertical acceleration

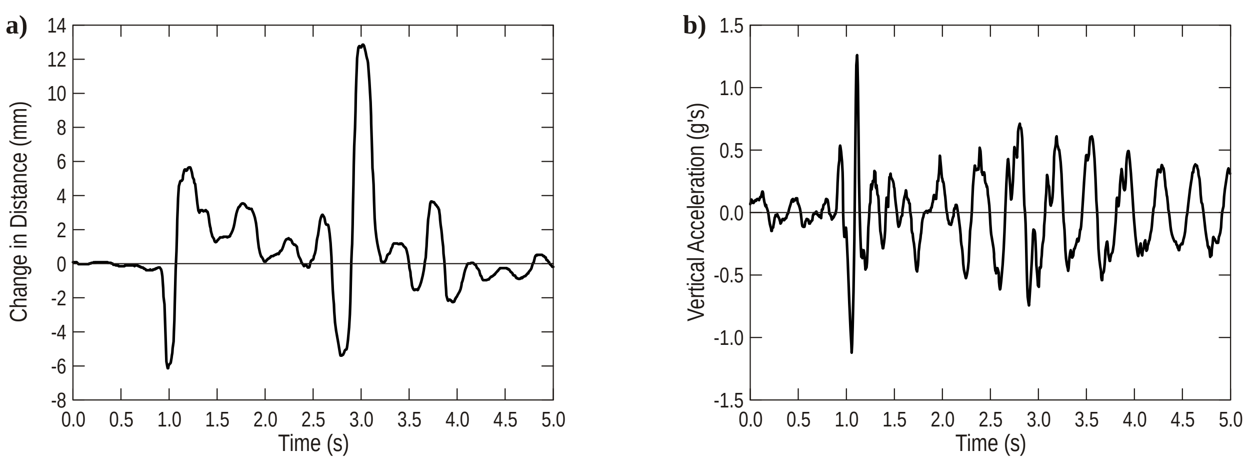

Figure B.108. Time histories for the front axle – velocity of 8 km/h (5 mph), run #03: a) change in distance, b) vertical acceleration

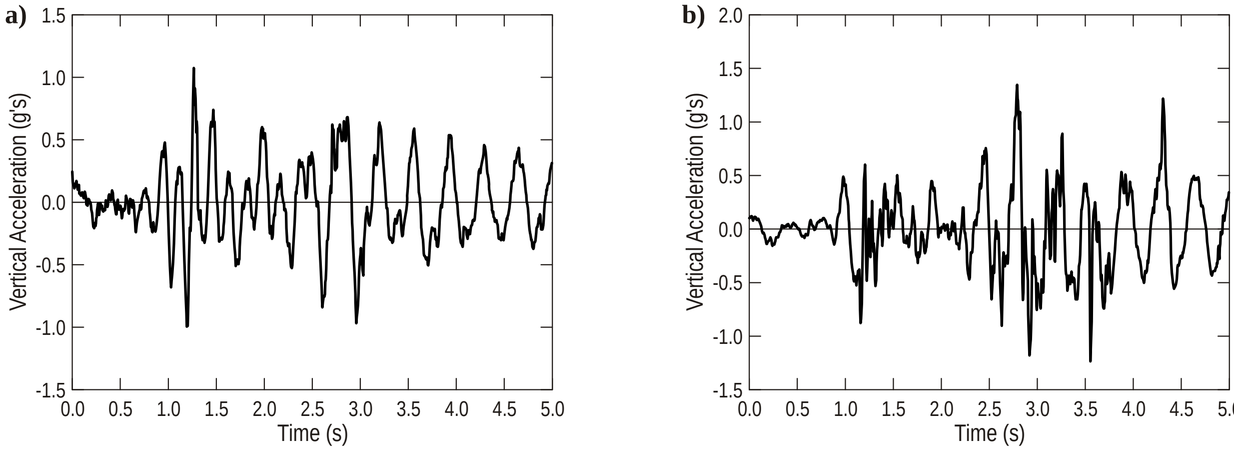

Figure B.109. Time histories for the points located in front of the crane – velocity of 8 km/h (5 mph), run #01: a) point on the front bumper, b) point on the boom above the front axle

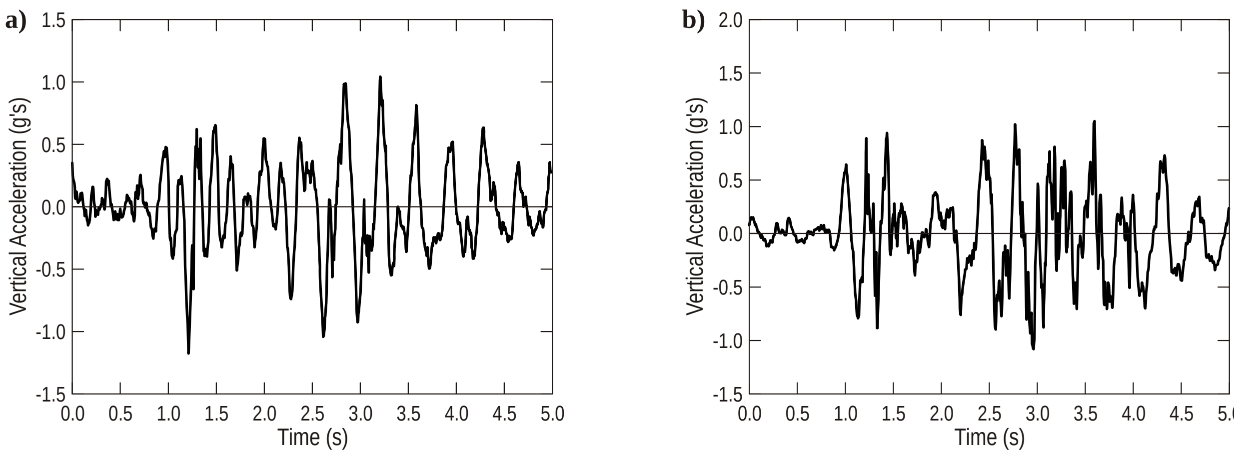

Figure B.110. Time histories for the points located in front of the crane – velocity of 8 km/h (5 mph), run #02: a) point on the front bumper, b) point on the boom above the front axle

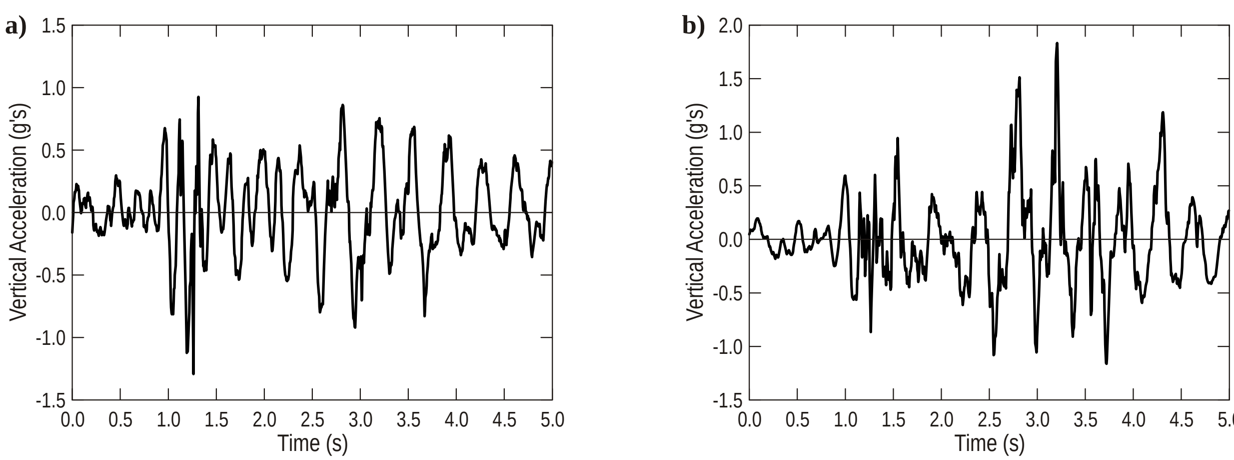

Figure B.111. Time histories for the points located in front of the crane – velocity of 8 km/h (5 mph), run #03: a) point on the front bumper, b) point on the boom above the front axle

a) 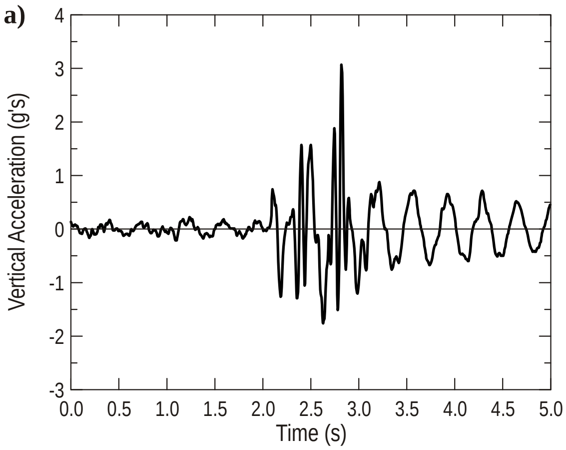

b) 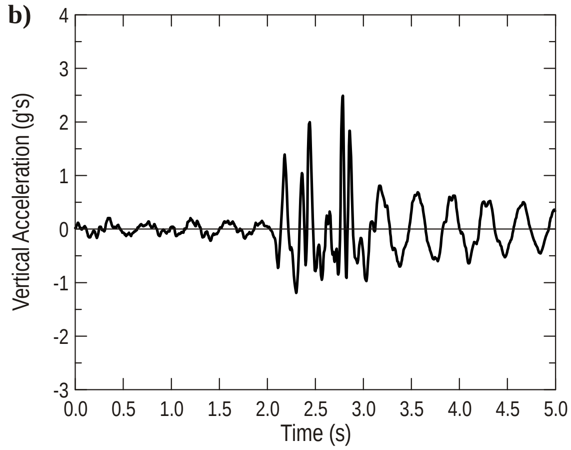

Figure B.112. Time histories for the points located on the rear tandem axles – velocity of 8 km/h (5 mph), run #01: a) forward axle, b) rear axle

a) 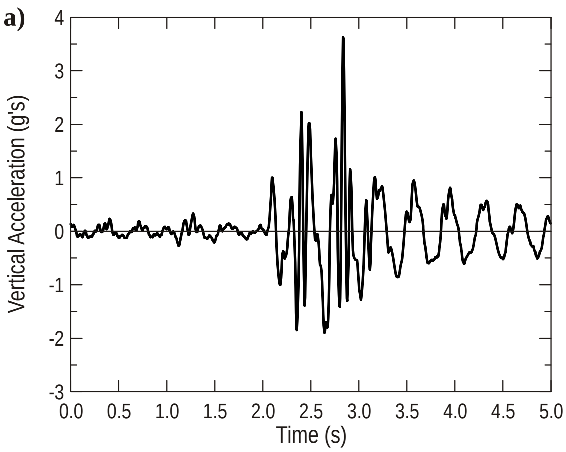

b) 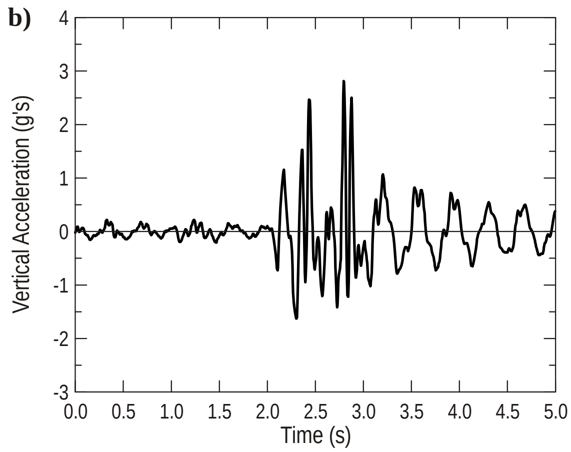

Figure B.113. Time histories for the points located on the rear tandem axles – velocity of 8 km/h (5 mph), run #02: a) forward axle, b) rear axle

a) 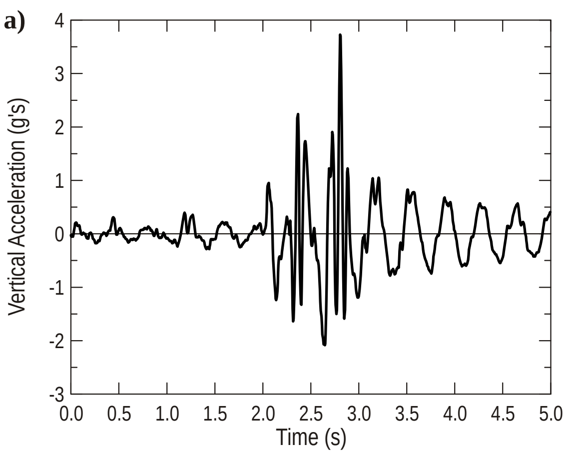

b) 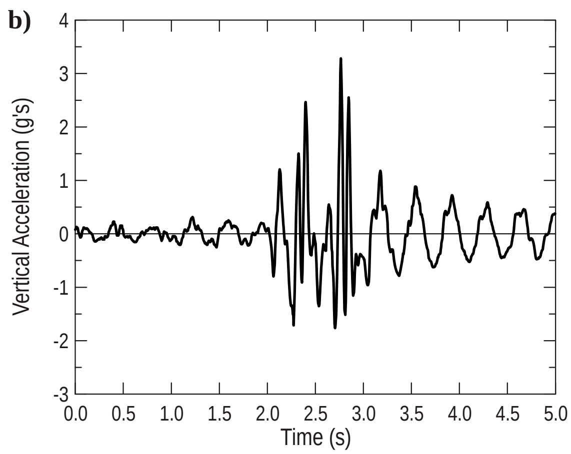

Figure B.114. Time histories for the points located on the rear tandem axles – velocity of 8 km/h (5 mph), run #03: a) forward axle, b) rear axle

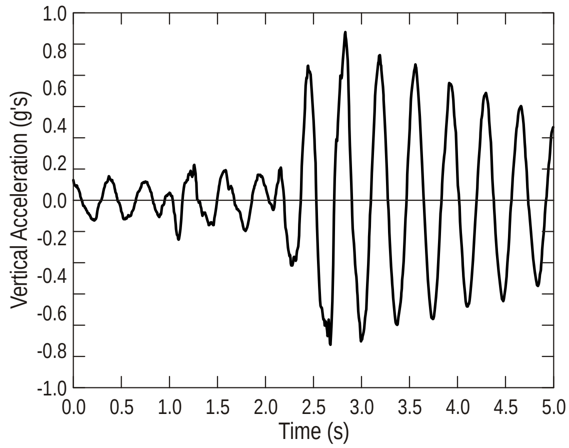

Figure B.115. Time histories for the point located on the frame above the rear tandem axles – velocity of 8 km/h (5 mph), run #01

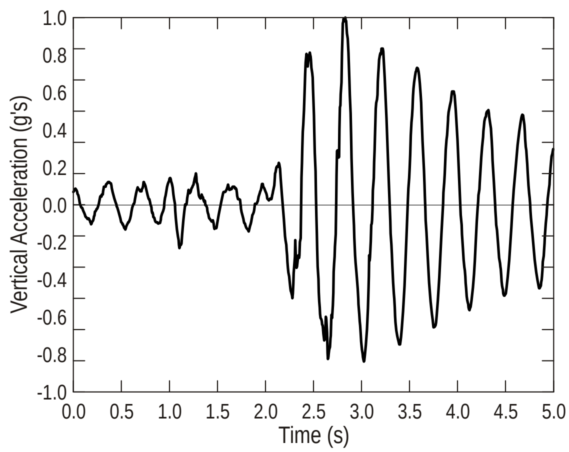

Figure B.116. Time histories for the point located on the frame above the rear tandem axles – velocity of 8 km/h (5 mph), run #02

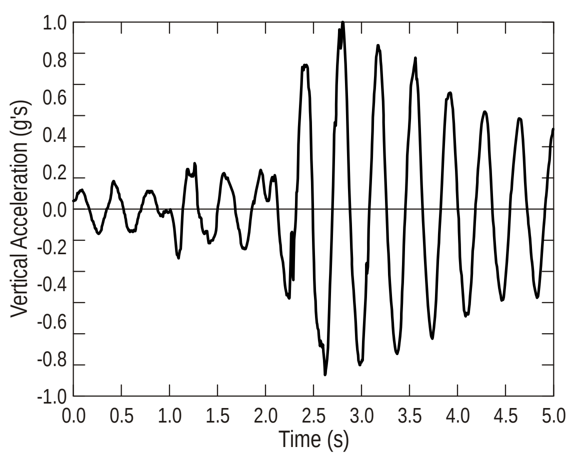

Figure B.117. Time histories for the point located on the frame above the rear tandem axles – velocity of 8 km/h (5 mph), run #03

Velocity of 16 km/h (10 mph)

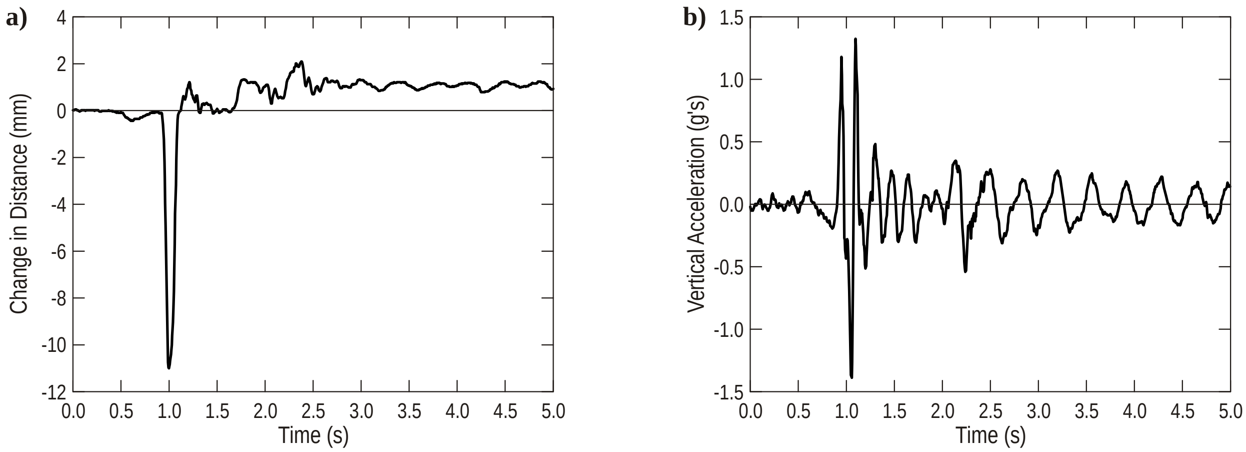

Figure B.118. Time histories for the front axle – velocity of 16 km/h (10 mph), run #04: a) change in distance, b) vertical acceleration

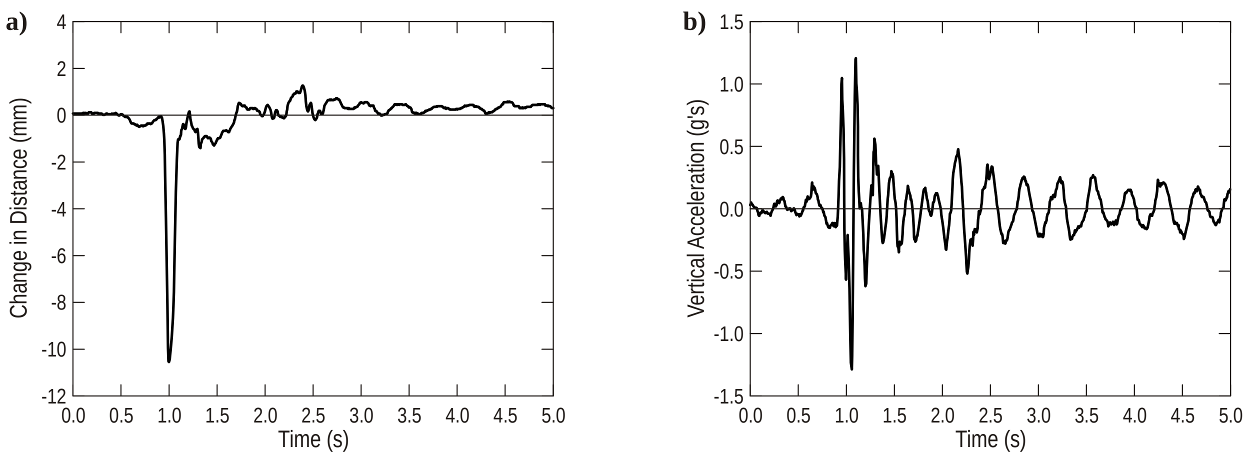

Figure B.119. Time histories for the front axle – velocity of 16 km/h (10 mph), run #05: a) change in distance, b) vertical acceleration

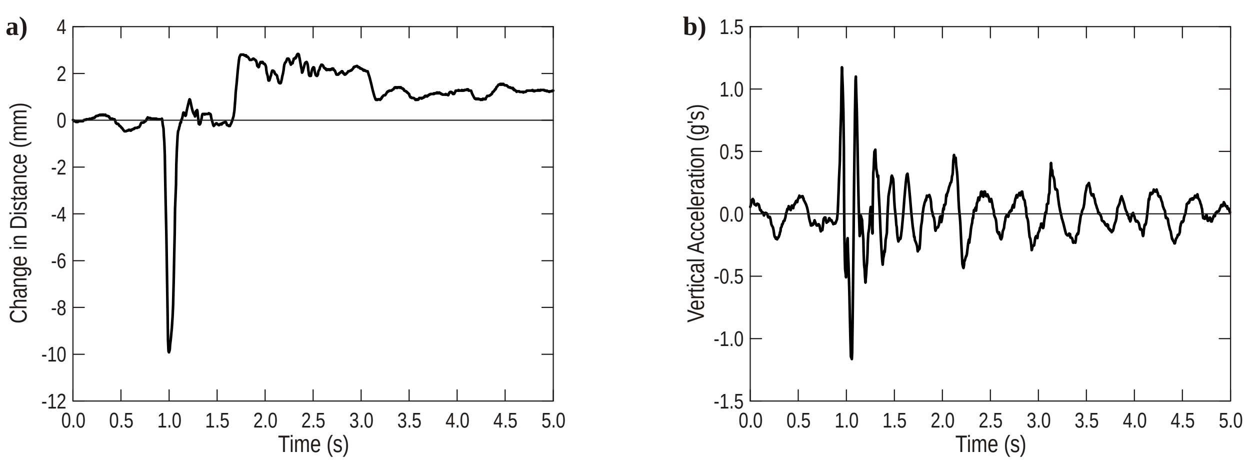

Figure B.120. Time histories for the front axle – velocity of 16 km/h (10 mph), run #06: a) change in distance, b) vertical acceleration

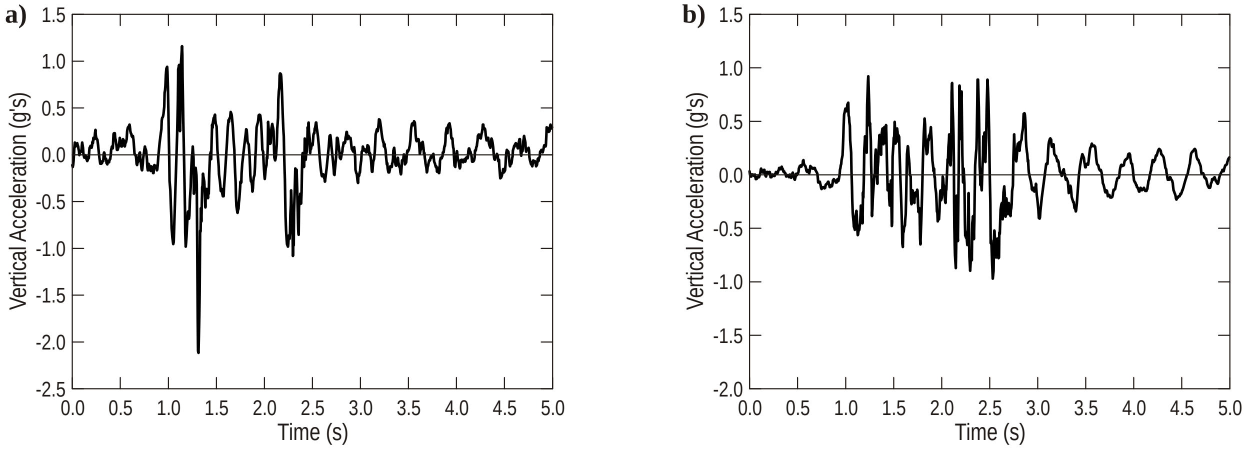

Figure B.121. Time histories for the points located in front of the crane – velocity of 16 km/h (10 mph), run #04: a) point on the front bumper, b) point on the boom above the front axle

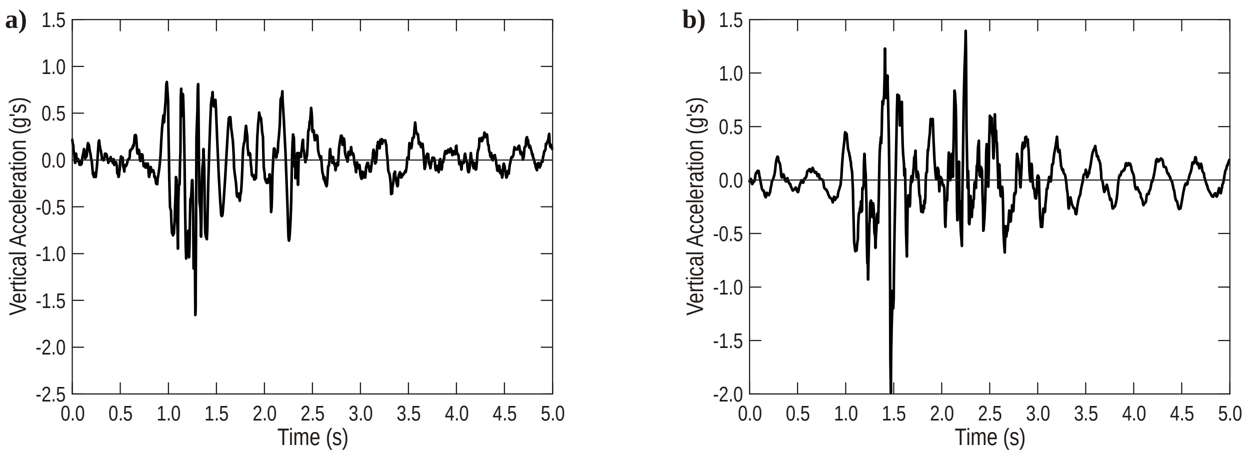

Figure B.122. Time histories for the points located in front of the crane – velocity of 16 km/h (10 mph), run #05: a) point on the front bumper, b) point on the boom above the front axle

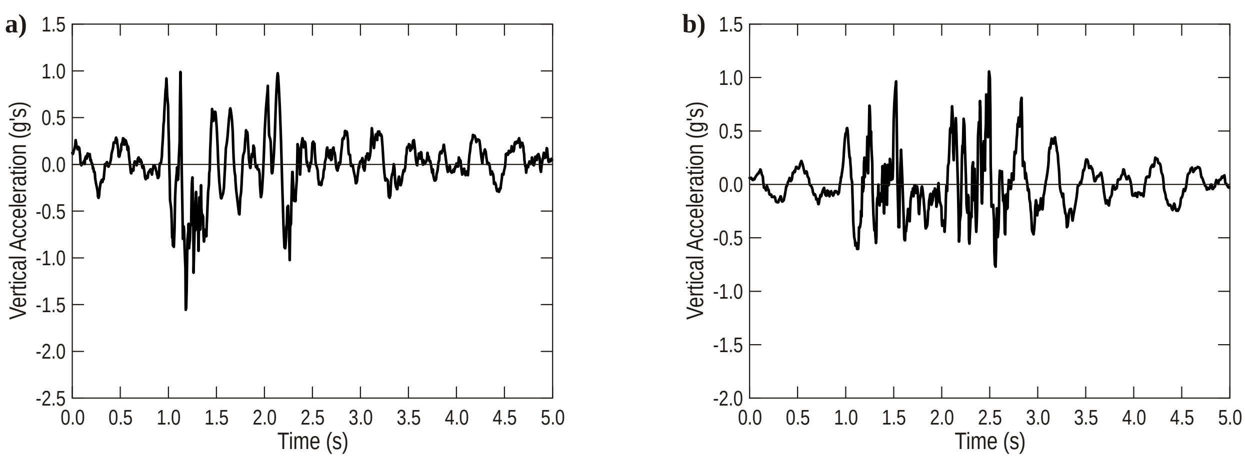

Figure B.123. Time histories for the points located in front of the crane – velocity of 16 km/h (10 mph), run #06: a) point on the front bumper, b) point on the boom above the front axle

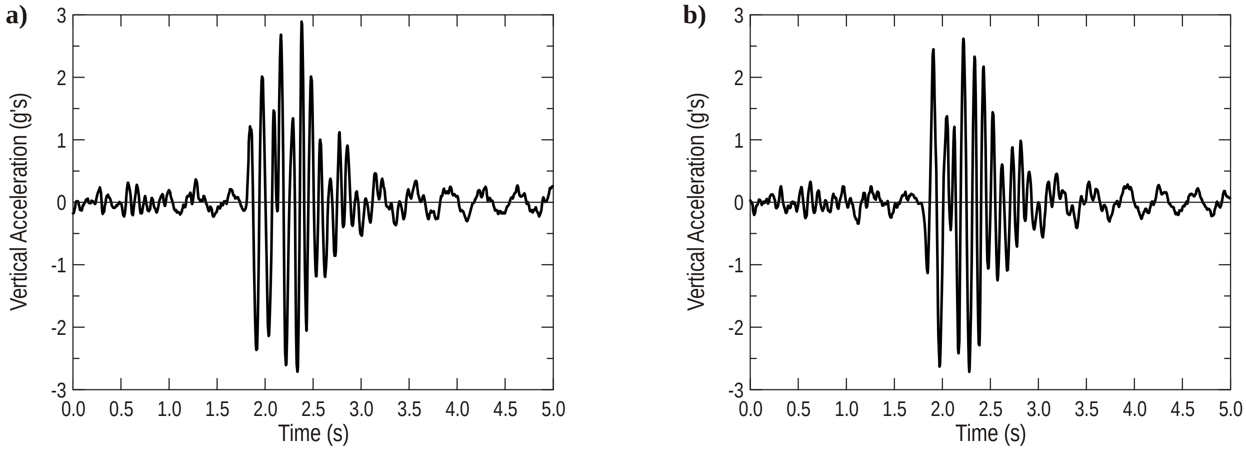

Figure B.124. Time histories for the points located on the rear tandem axles – velocity of 16 km/h (10 mph), run #04: a) forward axle, b) rear axle

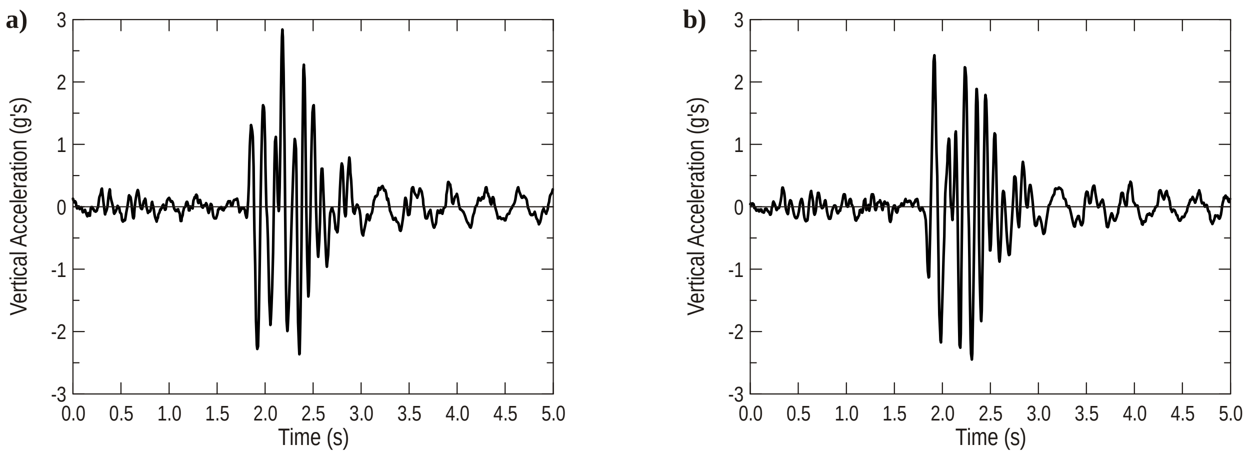

Figure B.125. Time histories for the points located on the rear tandem axles – velocity of 16 km/h (10 mph), run #05: a) forward axle, b) rear axle

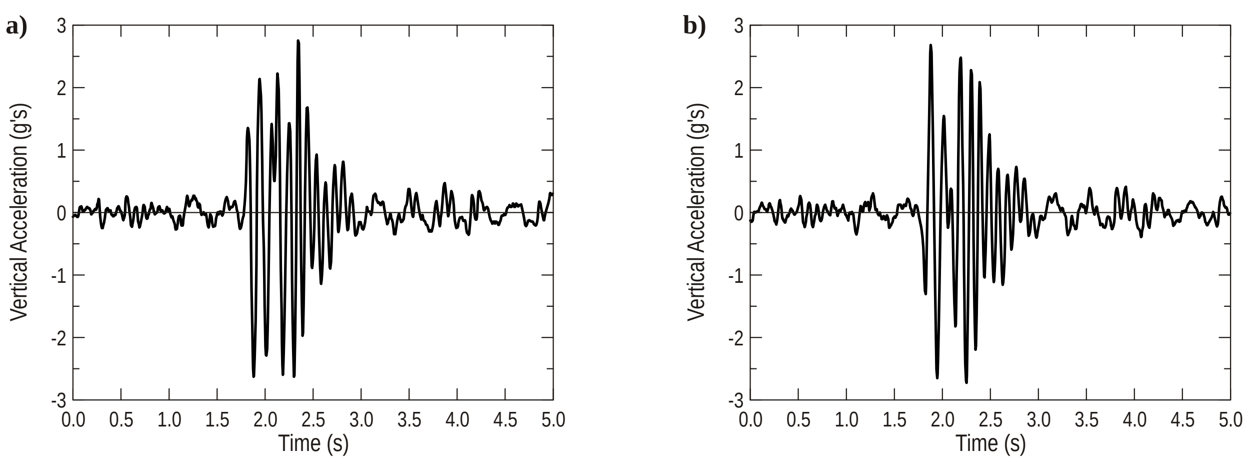

Figure B.126. Time histories for the points located on the rear tandem axles – velocity of 16 km/h (10 mph), run #06: a) forward axle, b) rear axle

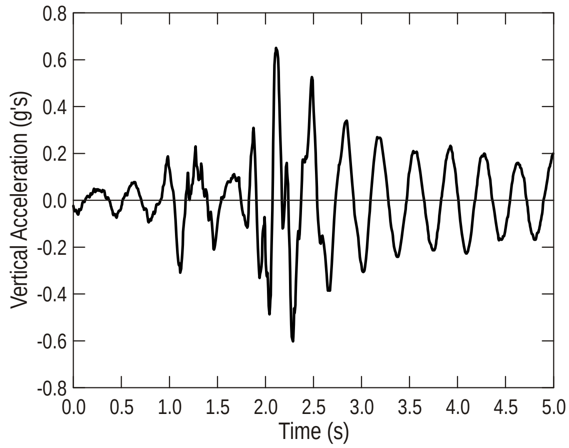

Figure B.127. Time histories for the point located on the frame above the rear tandem axles – velocity of 16 km/h (10 mph), run #04

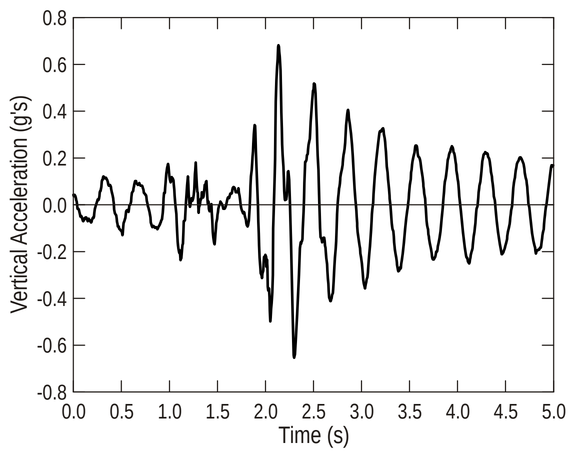

Figure B.128. Time histories for the point located on the frame above the rear tandem axles – velocity of 16 km/h (10 mph), run #05

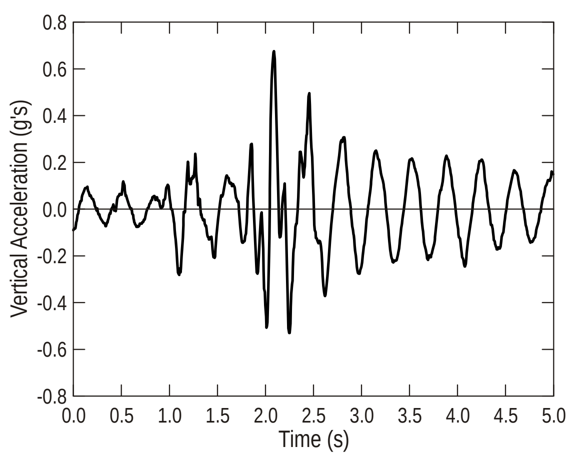

Figure B.129. Time histories for the point located on the frame above the rear tandem axles – velocity of 16 km/h (10 mph), run #06

Velocity of 24 km/h (15 mph)

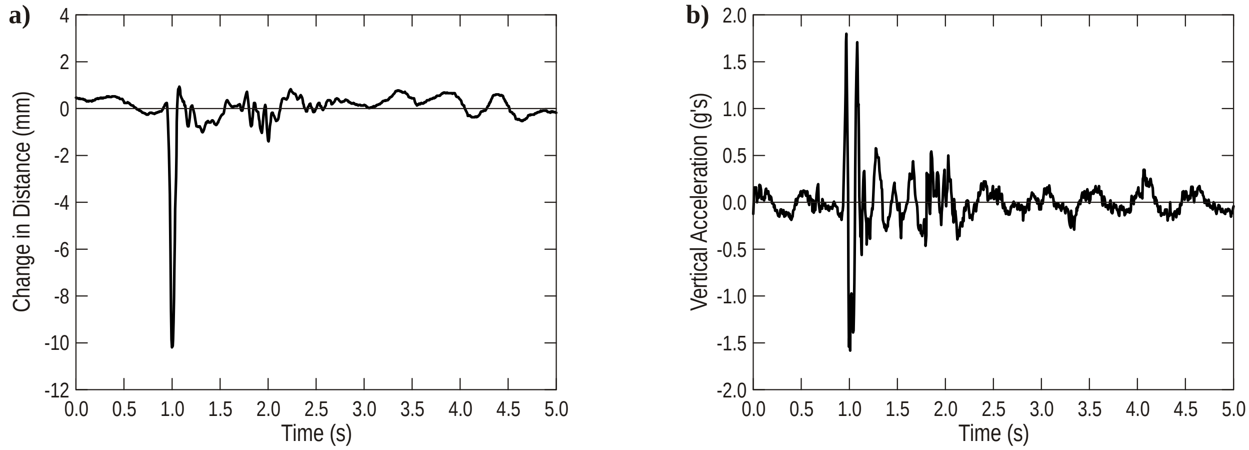

Figure B.130. Time histories for the front axle – velocity of 24 km/h (15 mph), run #07: a) change in distance, b) vertical acceleration

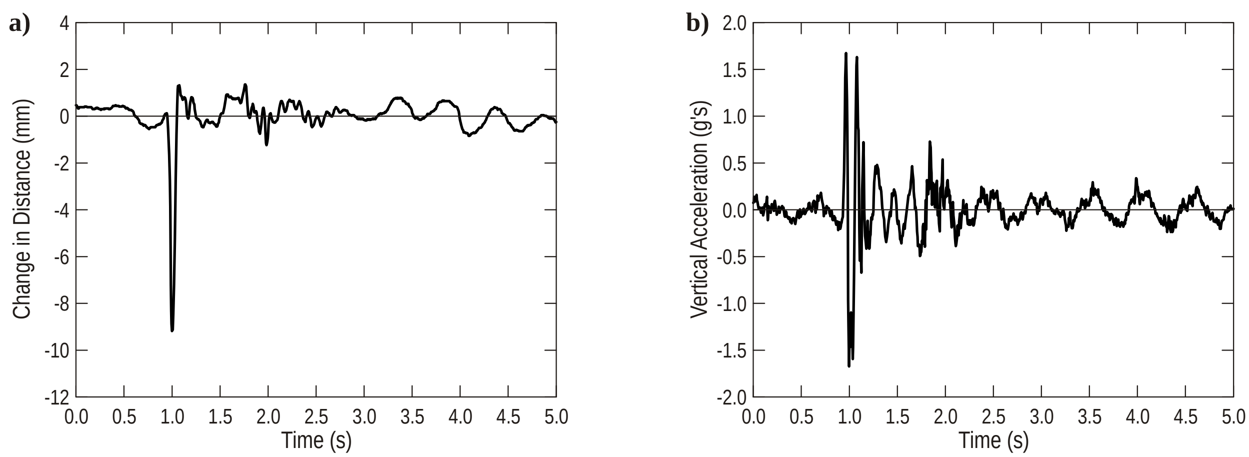

Figure B.131. Time histories for the front axle – velocity of 24 km/h (15 mph), run #08: a) change in distance, b) vertical acceleration

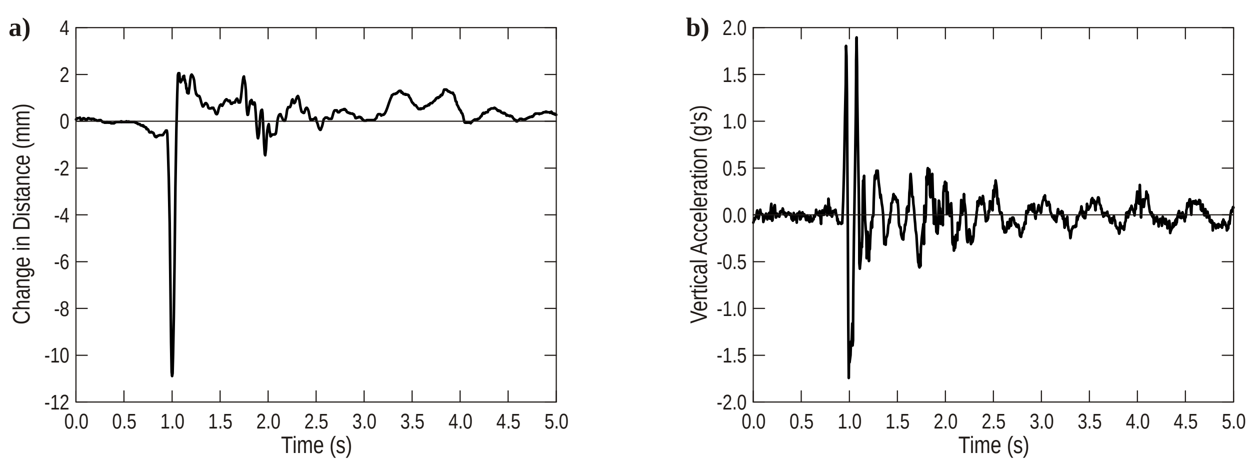

Figure B.132. Time histories for the front axle – velocity of 24 km/h (15 mph), run #09: a) change in distance, b) vertical acceleration

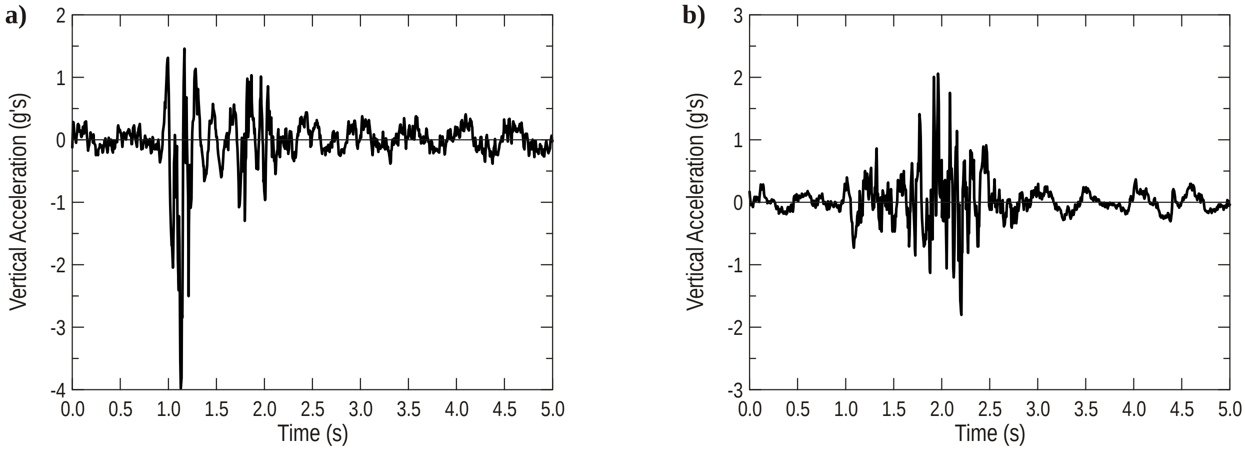

Figure B.133. Time histories for the points located in front of the crane – velocity of 24 km/h (15 mph), run #07: a) point on the front bumper, b) point on the boom above the front axle

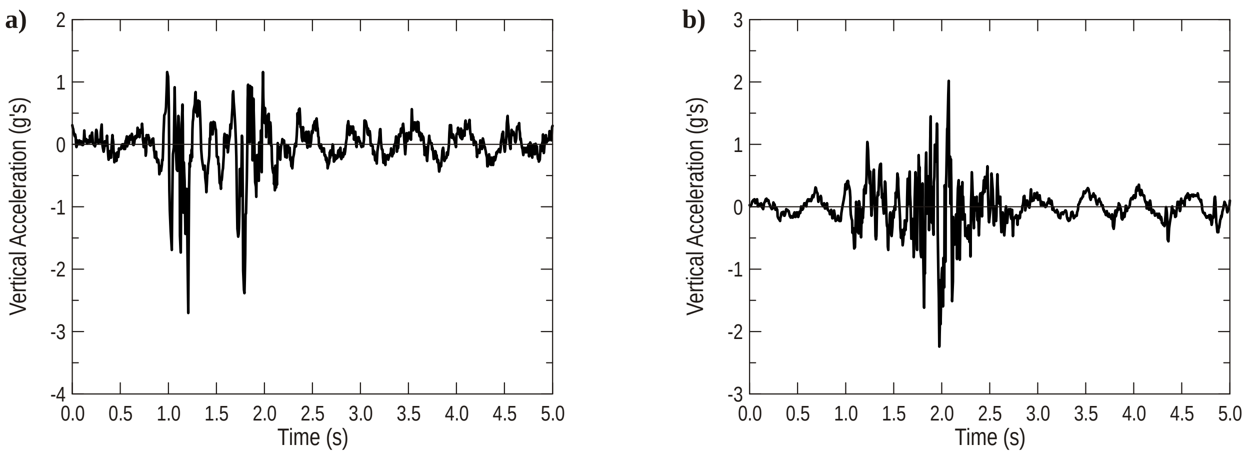

Figure B.134. Time histories for the points located in front of the crane – velocity of 24 km/h (15 mph), run #08: a) point on the front bumper, b) point on the boom above the front axle

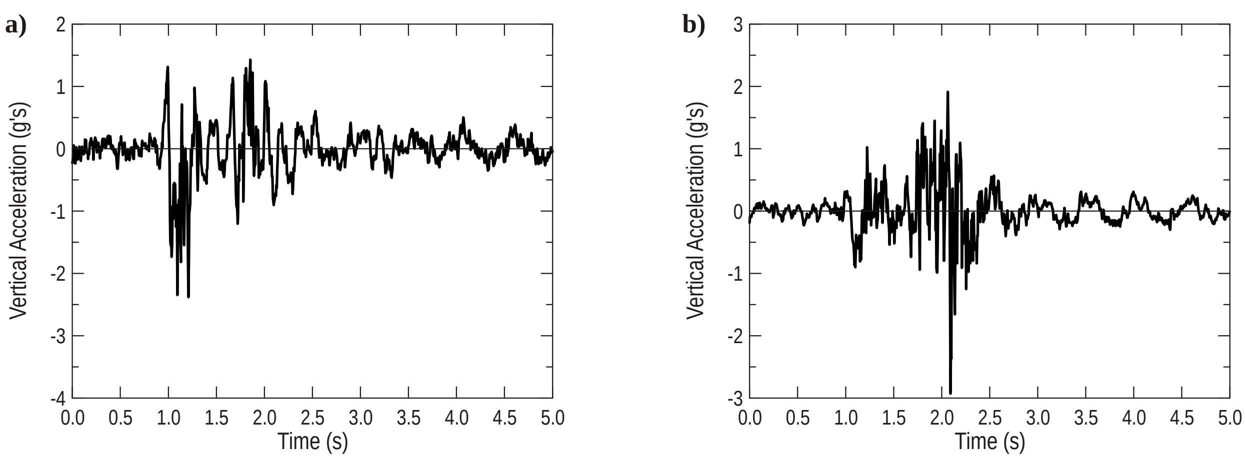

Figure B.135. Time histories for the points located in front of the crane – velocity of 24 km/h (15 mph), run #09: a) point on the front bumper, b) point on the boom above the front axle

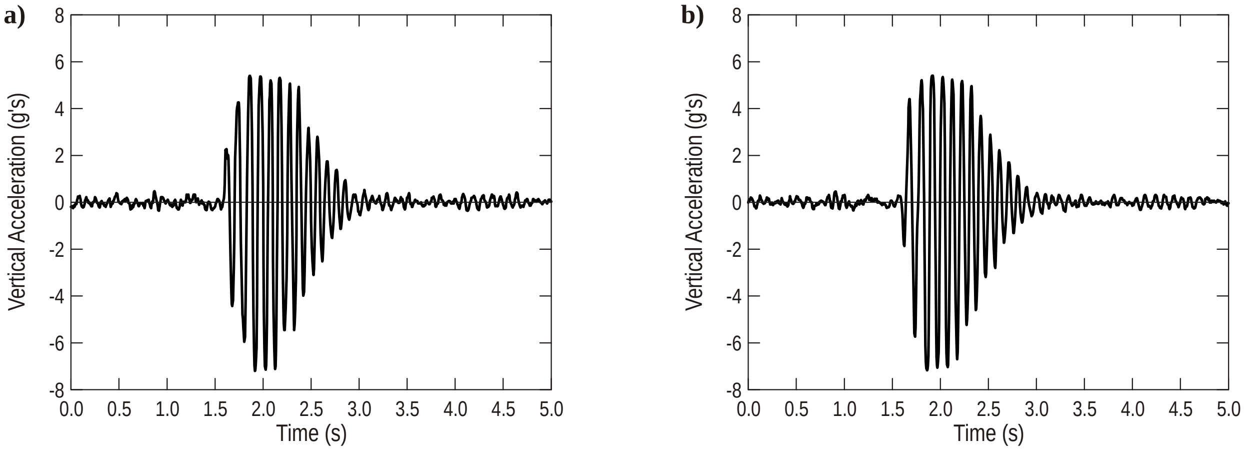

Figure B.136. Time histories for the points located on the rear tandem axles – velocity of 24 km/h (15 mph), run #07: a) forward axle, b) rear axle

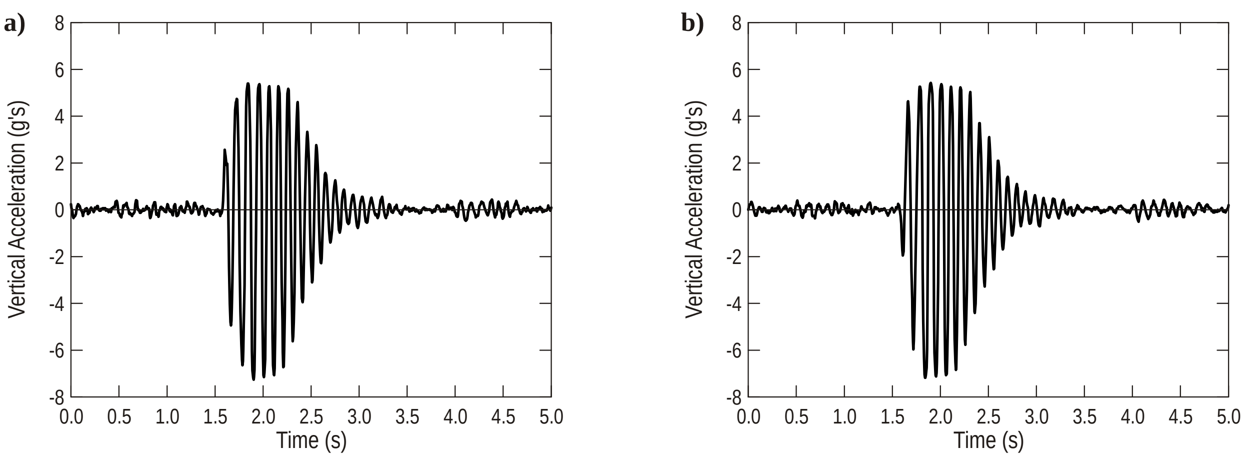

Figure B.137. Time histories for the points located on the rear tandem axles – velocity of 24 km/h (15 mph), run #08: a) forward axle, b) rear axle

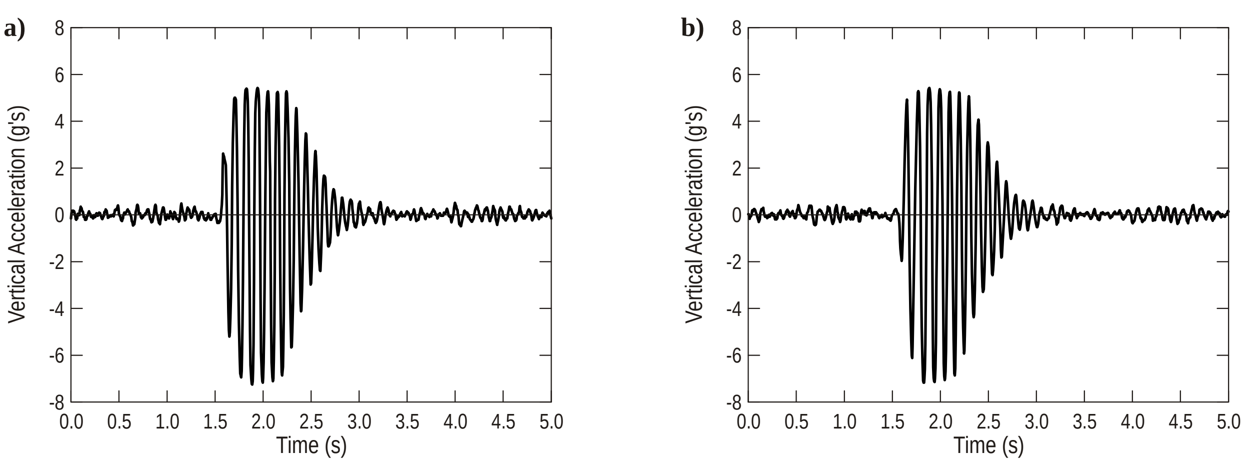

Figure B.138. Time histories for the points located on the rear tandem axles – velocity of 24 km/h (15 mph), run #09: a) forward axle, b) rear axle

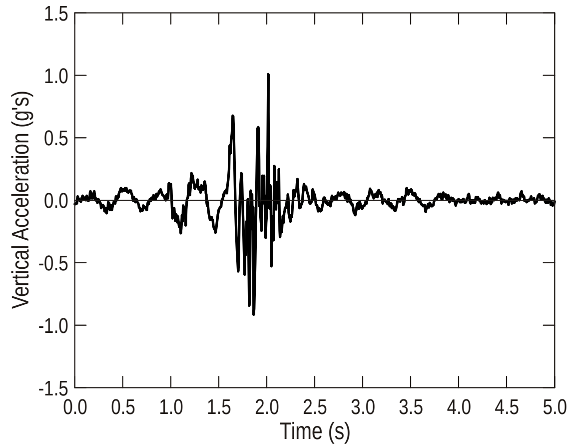

Figure B.139. Time histories for the point located on the frame above the rear tandem axles – velocity of 24 km/h (15 mph), run #07

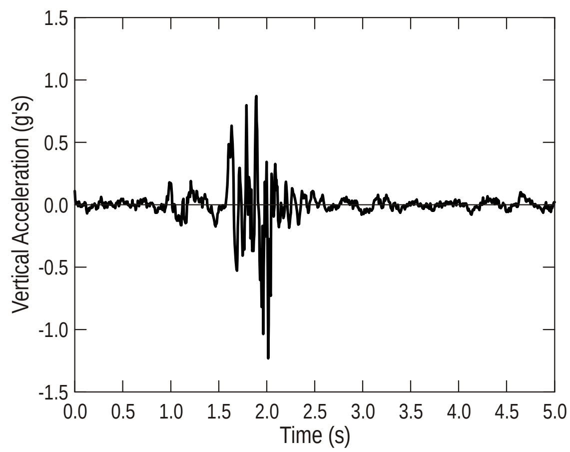

Figure B.140. Time histories for the point located on the frame above the rear tandem axles – velocity of 24 km/h (15 mph), run #08

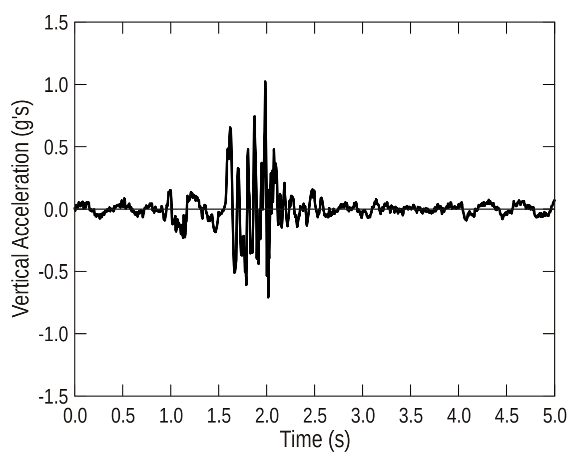

Figure B.141. Time histories for the point located on the frame above the rear tandem axles – velocity of 24 km/h (15 mph), run #09

Velocity of 32 km/h (20 mph)

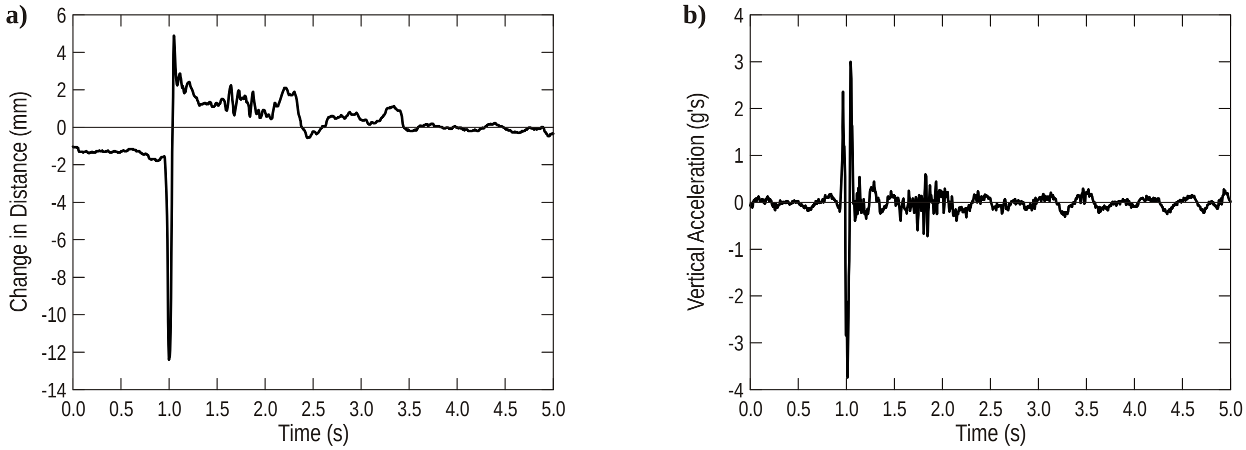

Figure B.142. Time histories for the front axle – velocity of 32 km/h (20 mph), run #10: a) change in distance, b) vertical acceleration

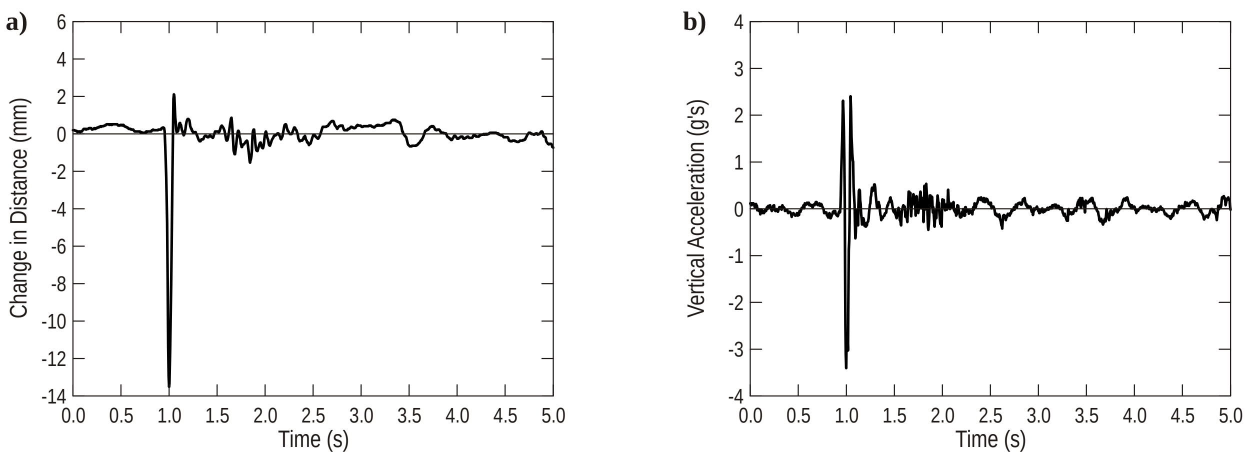

Figure B.143. Time histories for the front axle – velocity of 32 km/h (20 mph), run #11: a) change in distance, b) vertical acceleration

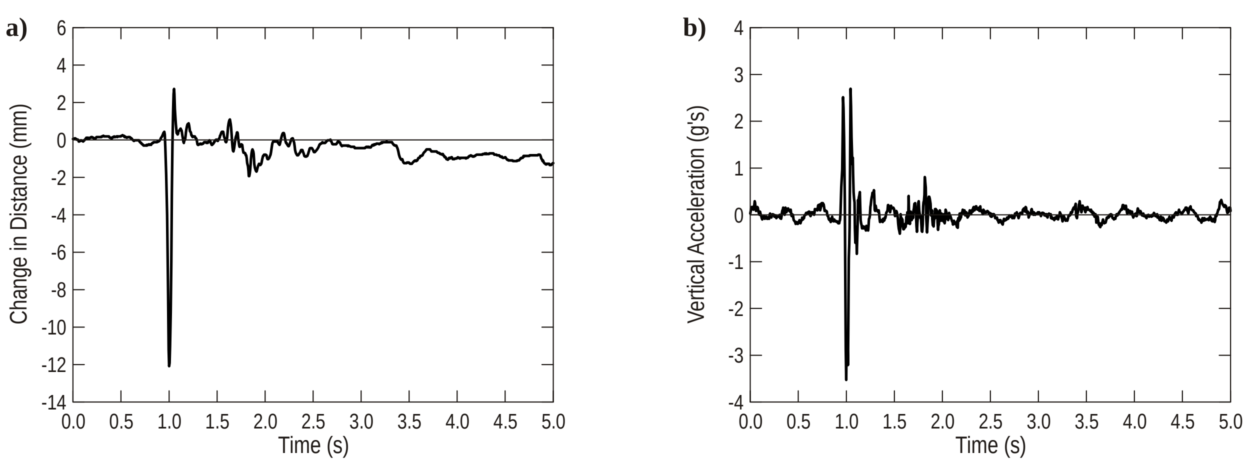

Figure B.144. Time histories for the front axle – velocity of 32 km/h (20 mph), run #12: a) change in distance, b) vertical acceleration

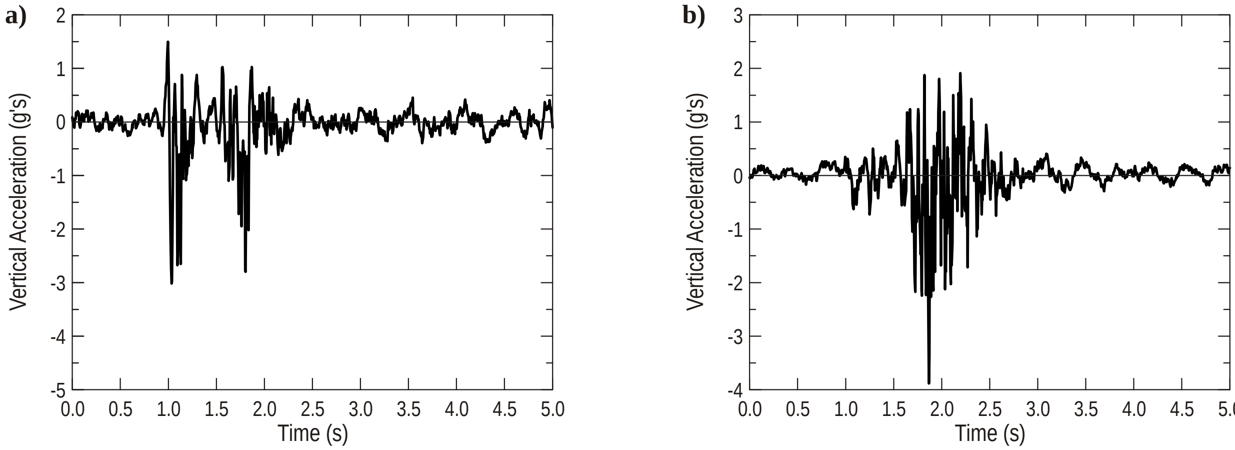

Figure B.145. Time histories for the points located in front of the crane – velocity of 32 km/h (20 mph), run #10: a) point on the front bumper, b) point on the boom above the front axle

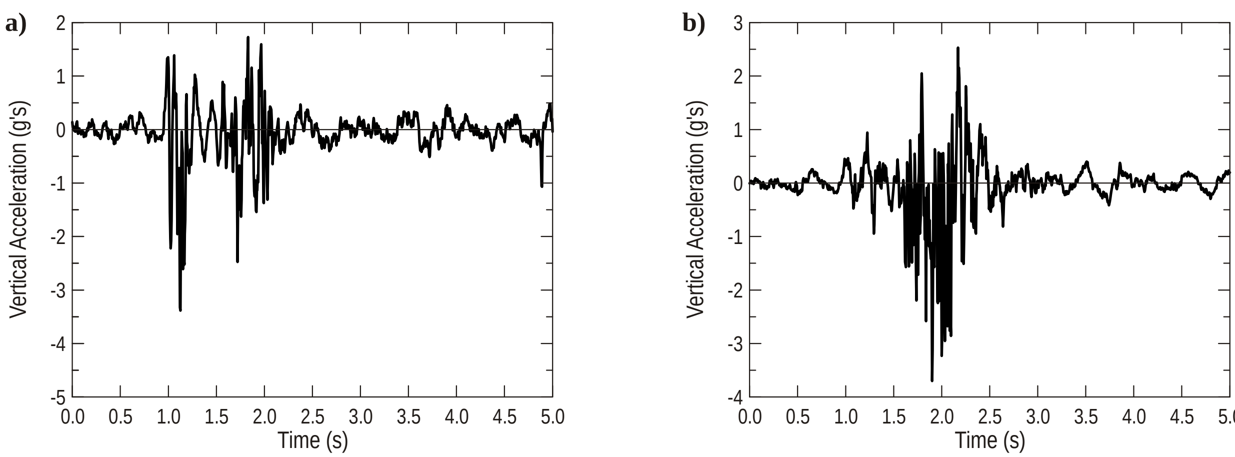

Figure B.146. Time histories for the points located in front of the crane – velocity of 32 km/h (20 mph), run #11: a) point on the front bumper, b) point on the boom above the front axle

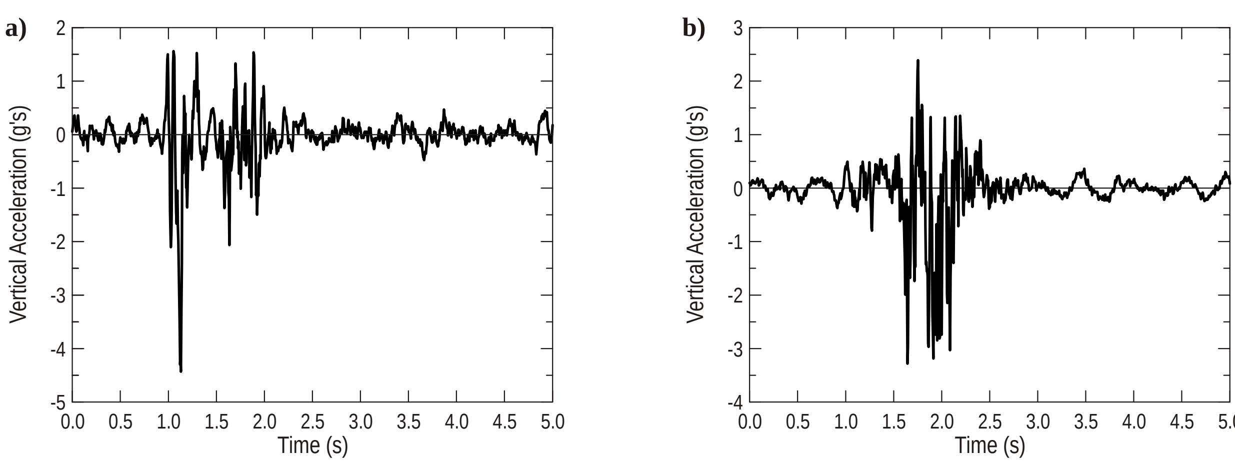

Figure B.147. Time histories for the points located in front of the crane – velocity of 32 km/h (20 mph), run #12: a) point on the front bumper, b) point on the boom above the front axle

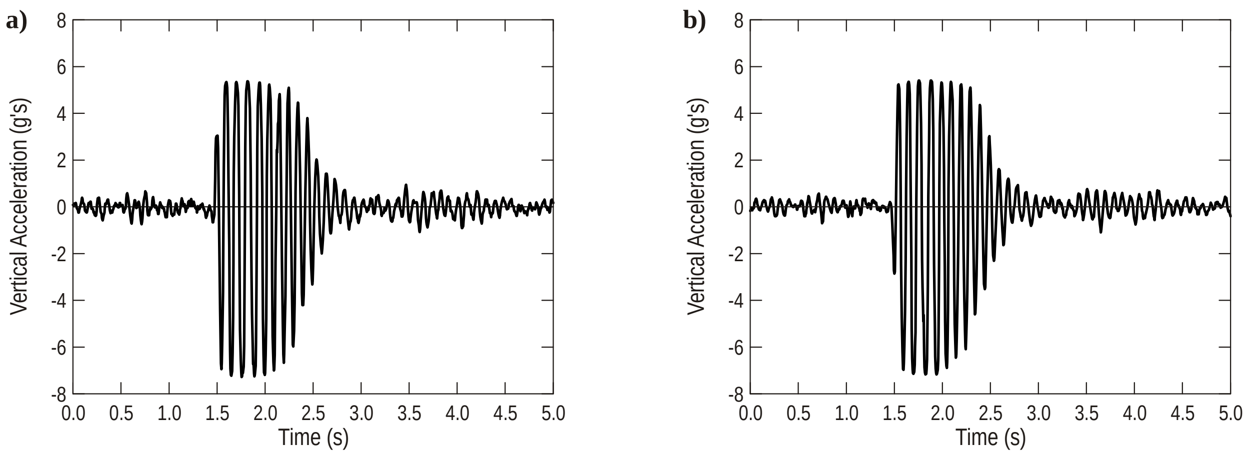

Figure B.148. Time histories for the points located on the rear tandem axles – velocity of 32 km/h (20 mph), run #10: a) forward axle, b) rear axle

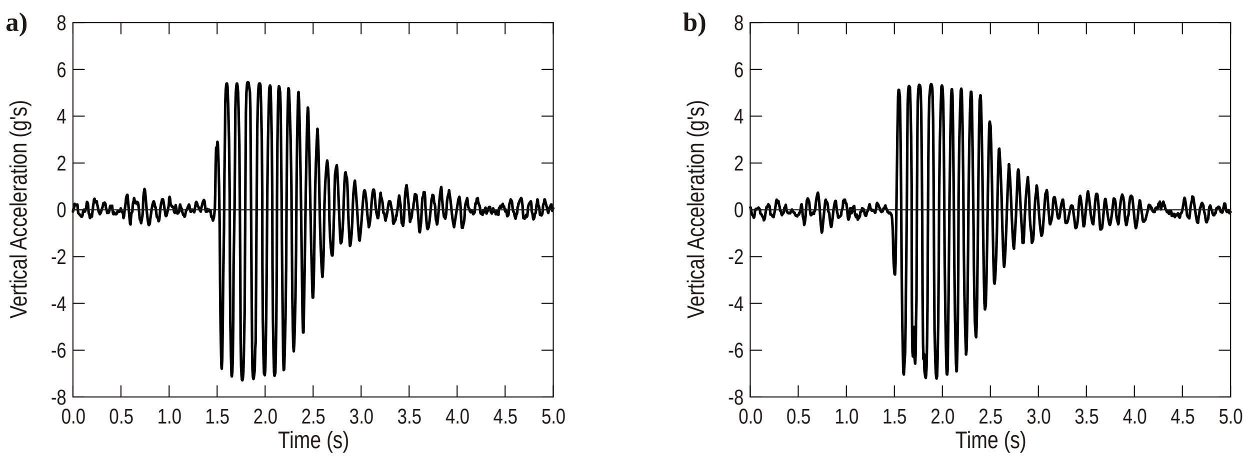

Figure B.149. Time histories for the points located on the rear tandem axles – velocity of 32 km/h (20 mph), run #11: a) forward axle, b) rear axle

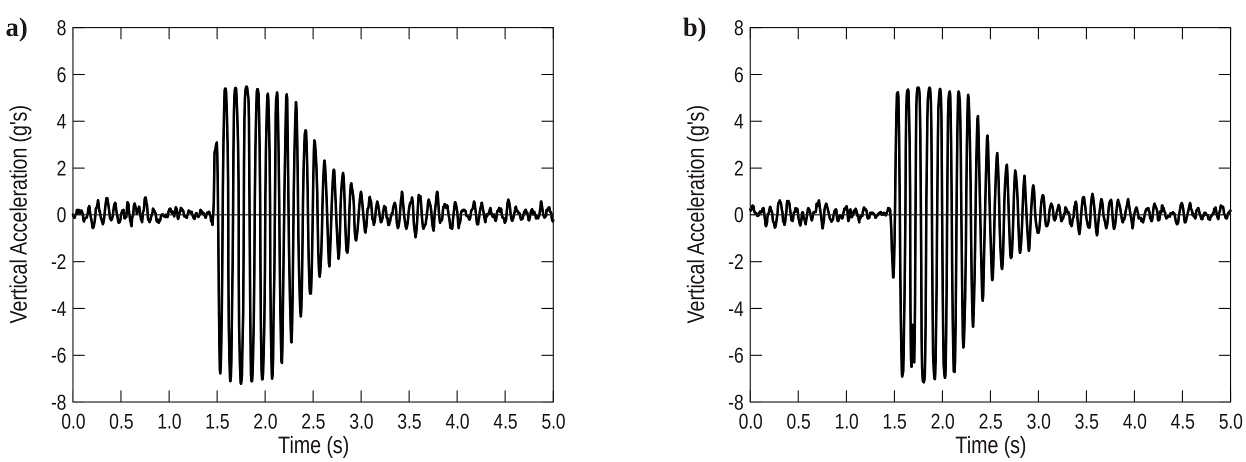

Figure B.150. Time histories for the points located on the rear tandem axles – velocity of 32 km/h (20 mph), run #12: a) forward axle, b) rear axle

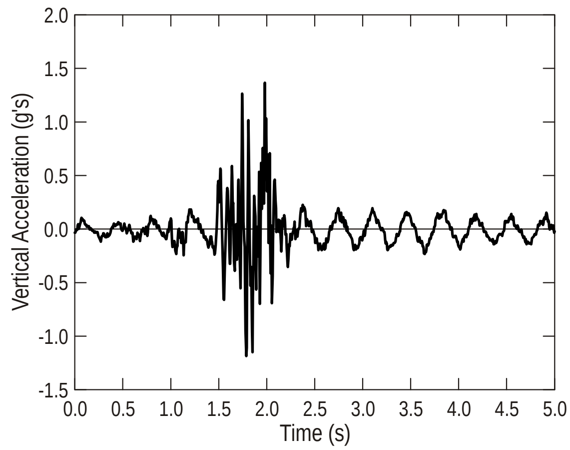

Figure B.151. Time histories for the point located on the frame above the rear tandem axles – velocity of 32 km/h (20 mph), run #10

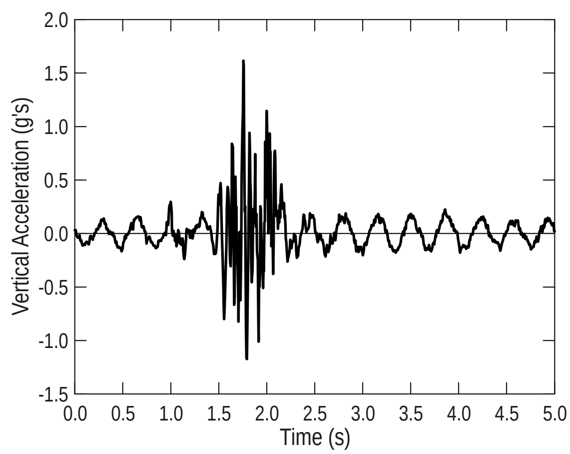

Figure B.152. Time histories for the point located on the frame above the rear tandem axles – velocity of 32 km/h (20 mph), run #11

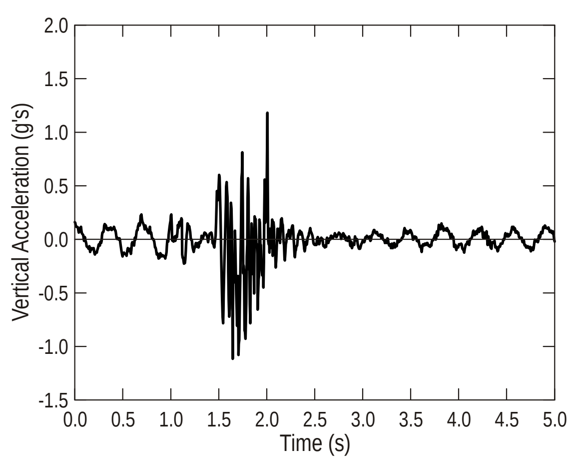

Figure B.153. Time histories for the point located on the frame above the rear tandem axles – velocity of 32 km/h (20 mph), run #12